ABSTRACT

Title of dissertation:	THE TILTS AND SPINS OF PLANETS AND MOONS
	Zeeve Rogoszinski Doctor of Philosophy, 2020
Dissertation directed by:	Professor Douglas Hamilton Department of Astronomy

The planets' spin states, specifically their tilts and spins, can provide useful constraints to planetary formation as they evolve and interact with their surroundings. In this thesis, we explore the spin dynamics required to reproduce Uranus's and Neptune's spin states through collisions, gas accretion, and secular spin-orbit resonances, and discuss the role these processes play in the greater context of solar system formation. Gas accretion is the likely source for their similar spin periods, yet a simple 2D accretion model with gas flowing to the planet's equator yields planets spinning at near break-up speeds. We confirm this using numerical simulations, further supporting the idea that a combination of magnetic effects and polar accretion are responsible for the gas planets' slower spin periods. Gas accretion should also drive obliquities to $0°$, but both Uranus and Neptune are tilted to $98°$ and $30°$ respectively. The leading hypothesis for their large obliquities is giant collisions, where for Uranus an Earth mass impactor struck the planet's North pole, while Neptune was struck by an impactor closer to the mass of Mars. Generating

two nearly identically sized planets with widely different tilts yet very similar spins is, however, a low probability event, as the planets would likely remain near their initial spin states. We compare different collisional models for tilted, untilted, spinning, and non-spinning planets, and find that two $0.5\,M_\oplus$ impacts produce better likelihoods than a single $M_\oplus$ strike. We can noticeably improve these statistics if the planet was already tilted beyond 40° by a spin-orbit resonance, and an initial tilt of 70° can increase the likelihood by an order of magnitude, compared to a pure collision scenario, while also halving the mass of the required subsequent impactor.

Tilting a planet without altering its spin period or inner satellite system is possible with a secular spin-orbit resonance, a coupling between spin and orbit precession frequencies, yet neither Uranus's nor Neptune's spin axes are precessing fast enough to match any present-day orbital precession rates. Here, we seek conditions in the past that could have augmented the ice giant's spin precession rates enough to excite their obliquities. First, we explore the possibility of Uranus forming closer to the Sun, as solar tides near 7 au can increase spin precession rates enough to match another planet's orbital precession rate located beyond Saturn. We show using numerical simulations that Uranus can be tilted to 90° on 100 Myr timescales, but leaving Uranus between Jupiter and Saturn for that long is unstable. While resonance kicks can tilt the planet to $\sim 40°$ on 10 Myr timescales, conditions need to be ideal. Another way to increase the ice giants' spin precession rates is if they harbored circumplanetary disks 3-10 times the mass of their satellite systems. We find that the presence of a massive disk moves the Laplace radius significantly outwards from its classical value, resulting in more of the disk contributing to the planet's pole

precession. In this case, the planets would resonate with their own orbits during the lifetime of the disk (~ 1 Myr), and Uranus can potentially be tilted to as high as 70°. Neptune, by contrast, can be tilted all the way to 30°, eliminating the need for collisions altogether.

Lastly, in the spirit of collisions and spin dynamics, we explore a collisional origin to the spin rates of the irregular satellites around Saturn, and show the conditions required to also vary the satellites' orbits. Irregular satellites are located far away from the planet on highly eccentric and inclined orbits, and recently reported Cassini observations show that the satellites that orbit retrograde spin on average faster than satellites that orbit prograde to Saturn's spin. Generating the spin rates of both prograde and retrograde populations, sans Phoebe, through collisions requires an initial population of $10^4 - 10^5$ particles more massive than 10^9 kg, and have more than half of them orbit in the retrograde direction. Spinning up Phoebe to its current spin rate requires imparting about 10% of its mass with giant collisions, which is enough to significantly alter its orbital parameters. As such, Phoebe may have scattered the inner prograde irregular satellites to more eccentric orbits, but this signature may also be a result of observation bias.

THE TILTS AND SPINS OF
PLANETS AND MOONS

by

Zeeve Rogoszinski

Dissertation submitted to the Faculty of the Graduate School of the
University of Maryland, College Park in partial fulfillment
of the requirements for the degree of
Doctor of Philosophy
2020

Advisory Committee:
Professor Douglas Hamilton, Chair/Advisor
Professor M. Coleman Miller
Professor Derek Richardson
Dr. Geoffrey Ryan
Professor Brett Gladman, External Examiner
Professor Thomas Cohen, Dean's Representative

Preface

The research presented in Chapters 2, 4, and 5 of this dissertation has been published or is currently under review, and is presented here with minimal modification.

Most of Chapter 2 and the entirety of Chapter 4 has been submitted for publication in the *Planetary Science Journal* under the title: "*Tilting Uranus: Collisions vs. Spin-Orbit Resonance*". It is currently under review.

Chapter 5 and portions from Chapters 2 and 3 have been published in: "*Tilting Ice Giants with a Spin-Orbit Resonance*", *The Astrophysical Journal*, Volume 888, Issue 2, Article ID. 60, 12 pp. (2020).

Chapter 3 is a hydrodynamics project aimed to explore and understand the method and difficulty of researching the origin of gas giants' spin rates, and Chapter 6 is currently in preparation for publication.

Dedication

To my family and friends

Acknowledgments

First, I thank my advisor, Doug Hamilton, because he is the reason why I chose to study planetary dynamics. His enthusiasm made our discussions and meetings enjoyable, and his mentorship has been extremely valuable to me as a doctoral student. When my research hit what seemed to be dead ends, I knew I could count on talking to Doug to help me see over these barriers and push onward. I also want to thank Geoff Ryan for his endless support and guidance in helping me understand the complexities of hydrodynamics simulations. What started out as a small side-project has evolved to a wonderful chapter that illuminated a necessary component to my thesis.

My time here would not have been nearly as wonderful if not for all of my friends in the department. Amy, Dana, Pradip, and Thomas, I could not have asked for better classmates. Thomas, it has been an absolute pleasure sharing an advisor and attending meetings all over the country and world with you. Pradip, I really enjoyed your company in our PSC office, and our conversations about physics problems, whether research or homework related, were some of the most valuable I had here. Dana, thank you for opening your home to us, organizing all the gatherings, and for being a great friend. Amy, it is such a pleasure to have gotten to know you since our summer in Williams College, and I am glad to share a birthday with you. Thank you also to Scott, Alex, Kyle, Drew, Laura, Liz, Milena, Ramsey, Teal, Becca, Jegug, Sara, Ginny, and Carrie for the fun times at UMD. I also need to thank again everyone who helped me organize the solar eclipse trip back in August

2017. Liz, Nick, Laura, Petr, Thomas, Bernadette, Pradip, Jialu, and Jiali, thank you all for helping me make this possible. Driving through national parks to see a solar eclipse has been one of my most memorable trips, a highlight of my time as a doctoral student, and I am so glad to have shared it with all of you. Finally, Blake and Myra, thank you both for being my closest friends here. It was wonderful having someone to go to the gym and eat dinner with almost every evening. I look forward to our future poker games, whiskey tastings, and trips to Florida.

I want to also thank the department's professional staff who have made submitting grant proposals and filling out travel expense forms as smooth as possible. Mona, Susan, Dorinda, and Adrienne, thank you all so much for your help and guidance.

Pursuing an interest in astronomy research would not have been possible had it not have been for my undergraduate professors and high school teachers who helped inspire me. Thank you Leonard Itzkowitz, Debra Elmegreen, Fred Chromey, and Jay Pasachoff for everything.

Lastly, I want to thank my girlfriend Lauren for her love and support as I complete this thesis. She heard me talk about planets and satellites more so than any non-astronomer should, and I am very grateful for her reassurance and encouragement when times were stressful.

Table of Contents

List of Tables

List of Figures

Chapter 1:   Introduction

1.1   The Origins of Planetary Tilts

The axial tilts of the planets in our solar system span the entire spectrum from 0° to 180°, and the histories of these obliquities, the angle between the planet's spin axis and the normal to the orbital plane, are unique to each planet. This places valuable constraints to their formation and evolution when placed in the broader context of solar system formation. Planetary tilts are affected by tides, collisions, gas accretion, and spin-orbit resonances, and combinations of these effects have shaped the spin architecture of the solar system that we observe today.

Collisions tend to be the primary explanation for large planetary tilts, at least among the terrestrial planets. Earth is thought to have been struck by a Mars-sized impactor during the early stages of planetary formation (Canup & Asphaug, 2001), resulting in the formation of our Moon. This strike could have initially tilted Earth to as high as 70°, and then as the Moon migrated outwards, the planet's obliquity and spin rate slowly decreased simultaneously until reaching its present day 23.5° tilt and 24 hour spin period (Ćuk et al., 2016). Mercury's and Venus's primordial obliquities (now 0° and 178°), however, were almost certainly erased by solar tides (Goldreich & Peale, 1970; Ingersoll & Dobrovolskis, 1978), so their anti-

parallel tilts simply imply initial obliquities below and above 90°, respectively. These primordial tilts can be explained by collisions, or through chaotic behavior when the planets' possibly fast initial precession and rotation rates drop concurrently via tidal dissipation (Laskar & Robutel, 1993). The Moon stabilizes the Earth to such chaotic oscillations (Laskar et al., 1993), but Mars's obliquity varies between 0° and $\sim 60°$ either chaotically (Laskar & Robutel, 1993), or by drifting in and out of a spin-orbit resonance with Venus over $10^5 - 10^7$ yr timescales as its quadrupole moment, J_2, fluctuates as a result of geologic activity (e.g. differentiation) (Ward, 1973; Ward et al., 1979; Ward & Rudy, 1991; Touma & Wisdom, 1993).

The gas giants' obliquities, on the other hand, are less prone to stochasticity. Gas from the circumstellar disk accretes onto the forming planet and carries with it angular momentum pointing normal to the planet's orbital plane. As such, obliquities are driven towards 0°, but this is not what we observe. Saturn, for instance, is tilted at a high 27° obliquity, and the impactor responsible would need to be $6 - 7.2\, M_\oplus$ (Parisi & Brunini, 2002). Juno mission observations of Jupiter's gravitational field suggest that the planet's core is diluted of heavy-elements (Wahl et al., 2017; Debras & Chabrier, 2019), and Liu et al. (2019) posit that a $5\, M_\oplus$ impact can mix these metals within the planet's inner envelope. This model implies that such collisions could be common in the early solar system, but in situ explanations, such as erosion of the core from convective mixing (Guillot et al., 2004; Wilson & Militzer, 2012) or planetesimal enrichment (Hori & Ikoma, 2011; Lozovsky et al., 2017), are still viable alternatives and do not require stochastic cataclysmic events. Instead, Saturn's obliquity can best be explained by a secular spin-orbit resonance

between the precession frequencies of Saturn's spin axis and Neptune's orbital pole (Ward & Hamilton, 2004; Hamilton & Ward, 2004; Boué et al., 2009; Brasser & Lee, 2015; Vokrouhlický & Nesvorný, 2015). And even Jupiter's small 3° tilt may have resulted from a resonance with either Uranus or Neptune (Ward & Canup, 2006; Vokrouhlický & Nesvorný, 2015; Saillenfest et al., 2020). Additional giant planets in the early solar system could complicate the situation, and while solutions are still possible, we do not expect them to change considerably.

1.2   The Tilts of Ice Giants

Uranus and Neptune are ice giants as they are composed of mostly ice and rock, but about 10% of their mass is hydrogen and helium gas (Hubbard et al., 1991; Podolak et al., 1995, 2000). This places these planets in an awkward position between gas giants and terrestrial planets. Since the bulk of their mass was a byproduct of the accumulation of solid material, collisions must have played an important role in their formation. It should therefore be obvious that Uranus's unique 98° obliquity is simply a result of a giant impact from an Earth-mass impactor (Benz et al., 1989; Korycansky et al., 1990; Slattery et al., 1992; Parisi & Brunini, 1997; Morbidelli et al., 2012; Izidoro et al., 2015; Kegerreis et al., 2018, 2019; Kurosaki & Inutsuka, 2019; Reinhardt et al., 2020; Ida et al., 2020), but there are some major caveats that need to be addressed.

First, such large impacts could significantly alter the planet's primordial spin rate, yet both Uranus and Neptune spin at similar periods ($T_U = 17.2$ hr, $T_N = 16.1$

hr). These periods were found by measuring the rotation of the planets' magnetic fields (Desch et al., 1986; Ness et al., 1986, 1989), and by observing variability in the planets' radio emission from the Voyager 2 mission (Desch et al., 1986; Warwick et al., 1986, 1989); however, these measurements assume solid-body rotation and their magnetic field rotation periods may vary with time just as they do with Saturn (Gurnett et al., 2009). Accounting for differential rotation to their inferred oblateness when minimizing their wind velocities still yields similar spin periods but with Uranus instead spinning faster than Neptune ($T_U = 16.6$ hr, $T_N = 17.5$ hr) (Helled et al., 2010). Regardless, and just as with Jupiter and Saturn, the two ice giants likely acquired their fast and nearly identical spin rates while accreting their massive gaseous atmospheres from a circumplanetary disk (Szulágyi et al., 2018; Batygin, 2018; Bryan et al., 2018). This may also explain the fact that Uranus's regular satellites are very similar in relative sizes and spacings to the Galilean satellites despite Jupiter's and Uranus's contrasting obliquities. Note that the total mass of Uranus's satellites is about 10^{-4} times the mass of Uranus, and the total mass of Jupiter's and Saturn's satellites are about 2×10^{-4} times the mass of their host planets.

Second, if Uranus's regular satellites were formed from a circumplanetary disk, then multiple impacts, which are less likely than a single strike, are required to explain their equatorial prograde orbits (Morbidelli et al., 2012). Tilting from $0°$ to $98°$ with a single impact would lead to nodal precession of the satellites, and their orbits would sweep out a torus around the tilted spin-axis. The satellites would then find themselves on crossing orbits and undergo mutual collisions. These collisions

would allow the satellite system to eventually realign to the planet's equatorial plane; however, the resulting proto-satellite disk would preserve its pre-impact angular momentum and hence would form retrograde satellites. Thus, at least two collisions are required. Neptune's satellites, on the other hand, were disrupted by capturing Triton (Agnor & Hamilton, 2006; Li & Christou, 2020), but it is likely that its primordial satellite system was somewhat similar to that of Uranus (Rufu & Canup, 2017). Neptune's obliquity, however, is only 30°, so the direction of its satellites' motions is not affected by giant impacts.

Ida et al. (2020) circumvent this multi-collision issue by suggesting that the Uranian satellite system was a byproduct of debris from an ice-rich giant impact. Previous simulations showed that a debris disk from a single rocky impactor would generate a disk 100 times more massive and 10 times smaller in size than the current Uranian satellite system (Slattery et al., 1992; Kegerreis et al., 2018, 2019; Kurosaki & Inutsuka, 2019; Reinhardt et al., 2020). This impact could likely evaporate the ices from the ejecta debris disk (Mousis, 2004) suggesting rock-dominated compositions when in fact the satellites are abundant in water ice. Ida et al. (2020) showed that an icy impactor would eject a water-vapor-rich disk that viscously evolves until particles re-condense to ice. Nearly all of the debris falls back onto Uranus, but the remaining 1% of the disk spreads to 10 times the size of the initial debris disk and could form the equatorial satellite system observed today.

It is not known whether the Uranian satellites formed from a classic circumplanetary disk or from an impact generated disk. If the Uranian satellites were indeed formed from a circumplanetary disk (Szulágyi et al., 2018) rather than a de-

bris disk (Ishizawa et al., 2019; Ida et al., 2020), then exciting Uranus's pre-impact tilt through some mechanism other than collisions, like a spin-orbit resonance, would reduce the number of impacts required by Morbidelli et al. (2012) back to one.

1.3 Spin-Orbit Resonances

An external torque from the Sun on an oblate planet causes slow uniform regression (negative precession) of the planet's spin axis at a rate α about the normal to its orbital plane (Colombo, 1966). Similarly, torques from the surrounding giant planets cause a planet's orbit to regress about the normal to the invariable plane at a rate g. One of the simplest spin-orbit resonances occurs when these two precession frequencies are commensurate (Figure 1.1). Here the spin axis and orbital pole remain at fixed angles relative to the pole of the planet's orbit and the total angular momentum of the solar system, respectively, and the two vectors precess uniformly. The normal to the total angular momentum vector is the invariable plane, and the angle between the projection of the two precessing vectors into the invariable plane is the resonance angle given by

$$\Psi = \phi_\alpha - \phi_g. \tag{1.1}$$

Here ϕ_α and ϕ_g are the longitudes measured from a reference direction to the projections of the spin axis and nodal pole onto the invariable plane, respectively (Hamilton & Ward, 2004).

In reality, a planet's orbital precession frequency is not uniform as it is the sum
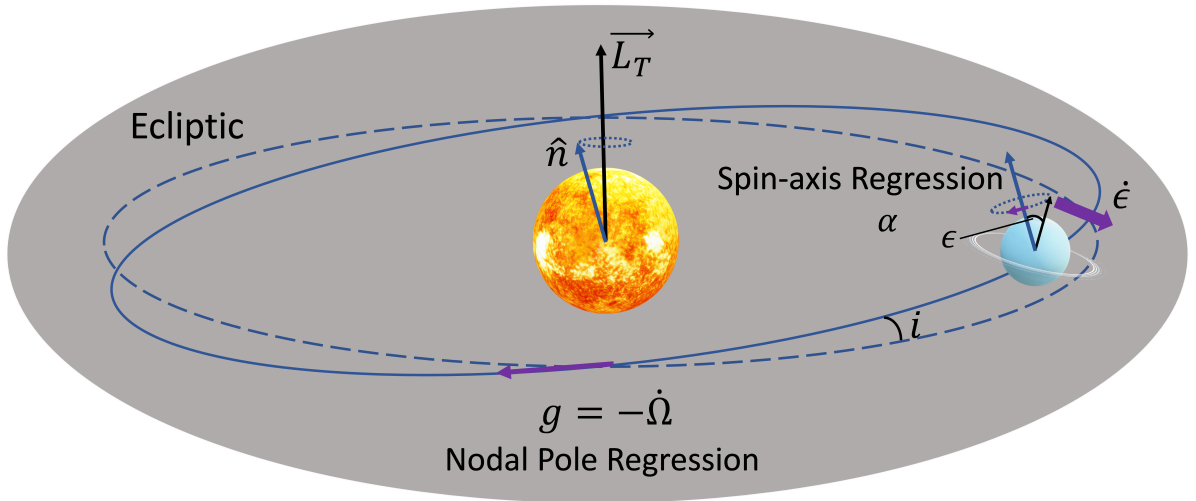
Figure 1.1: A diagram of an obliquity (ϵ) excitation from a secular spin-orbit resonance. Uranus's nodal pole ($\hat{n}$) regresses about the normal to the ecliptic at a rate g due to torques from the surrounding planets and protoplanetary disk. Uranus's spin-axis regresses about the orbit normal at a rate α due to torques from the Sun and satellite system. For reference, the planet spins and orbits in the counter-clockwise direction, while the spin and orbital axes regress in the clockwise direction.

of all the frequencies induced by the other giant planets. Most of these terms are rapid, so they tend to average out over time and can be safely ignored. This leaves only the slower and weaker near-resonant terms, which instead accrue significant amplitude changes to the planet's orbit (Murray & Dermott, 1999). Following a resonance capture, the resonance angle (Equation 1.1) varies slowly resulting in a gradual increase to the planet's obliquity if a dissipative force is active (Ward, 1974). However, capturing into a secular spin-orbit resonance requires not only nearly identical precession frequencies, but also a configuration of coplanar vectors.

The orientation of this vector pair near resonance determines the configuration's stability and longevity, but imagining which states for secular spin-orbit resonances are unstable is not obvious. To highlight how the relative orientation of two orbits near resonance determines the system's stability, we can imagine a 2:1 mean-motion resonance between Jupiter on an outer circular orbit and an asteroid on an inner eccentric orbit (Murray & Dermott, 1999, pg. 321). In this case, if the closest approach occurs before the asteroid reaches pericenter, then the two bodies diverge immediately afterwards with the asteroid speeding up. The tangential force Jupiter imparts onto the asteroid is therefore stronger and longer lasting before conjunction, which in turn increases the angular momentum of the asteroid's orbit and drives the point of closest approach towards pericenter. If the close encounter instead happens after the asteroid passes through pericenter but before it reaches its apocenter, then the asteroid is slowing down and the impulse from Jupiter decreases angular momentum and drives conjunction also closer to pericenter. Thus, encounters near pericenter are stable, while encounters near apocenter, where the

asteroid's longitude of pericenter is rotated by 180°, are unstable. Just like in this example and any other pendulum models, there are certain spin-orbit nodal alignments that are stable, and we seek ones that can sustain long term libration and excite obliquities.

Solutions for spin-orbit vector orientations that yield equilibria about which the resonance angle can librate are called "Cassini states" (Colombo, 1966; Peale, 1969; Ward, 1975; Ward & Hamilton, 2004), and there are four of them. Cassini states 1 and 4 have both axial vectors co-precessing on the same side of the normal to the invariable plane (Figure 1.2), but Cassini state 4 is an unstable solution and librations about Cassini state 1 drive obliquities towards 0°. A resonance argument like Equation 1.1 that librates about Cassini state 2, which is a stable equilibrium point where the spin axis and orbital pole co-precess on opposite sides of the normal to the invariable plane (Figure 1.2), is capable of obliquity excitations from initially near-zero tilts, and the strongest such resonance occurs when the planet's spin precession frequency matches its own nodal precession frequency. We will be focusing on this state to tilt ice giants. Lastly, Cassini state 3 is stable but only exists if the vectors precess in the opposite directions, which is not relevant here.

Quillen et al. (2018) also included mean-motion terms in their resonance arguments, and they demonstrated that the corresponding torques from these terms can be as large as their secular counterparts. Planets located near a mean-motion resonance have altered orbital precession frequencies that might also induce a spin-orbit resonance (Millholland & Laughlin, 2019). Since there is a rich variety of formation scenarios for Uranus and Neptune, with some starting in or eventually entering into
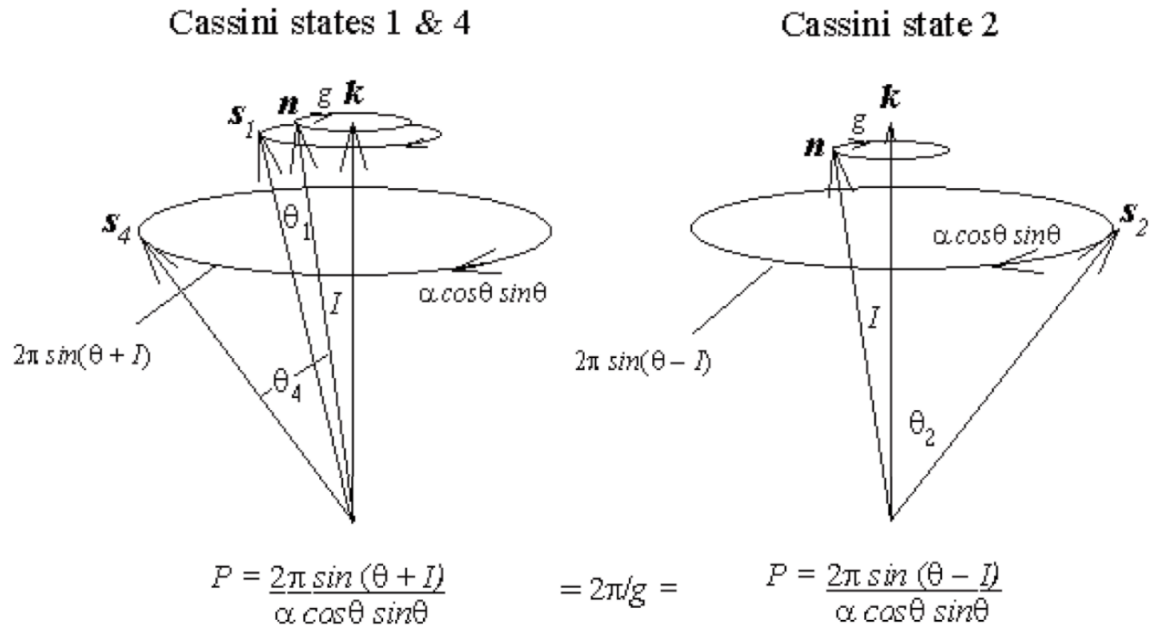
Figure 1.2: A diagram from Ward & Hamilton (2004) (Fig. 1) showing the orientation of vectors for different Cassini states. $\mathbf{s}_i$ is the Cassini state position of the planet's spin-axis relative to the orbit normal $\mathbf{n}$ and normal to the invariable plane $\mathbf{k}$. Here θ is the obliquity, and I is the inclination.

different resonance chains with the other giant planets (e.g. Morbidelli et al., 2007, 2009; Levison et al., 2011; Nesvorný & Morbidelli, 2012; Deienno et al., 2017), it is not clear which, if any, of these resonances were important in the past.

One way to facilitate a frequency match is if Uranus once harbored a satellite larger than the Moon (Boué & Laskar, 2010). This could augment the planet's gravitational quadrupole moment enough to speed up its spin precession frequency and generate a resonance on a timescale on the order of 10^6 yr. However, this model suffers from the same problem as the giant impact hypothesis in that the moon would need to be implausibly large, placed at a large distance from the planet, and would also need to be removed without exciting the rest of the satellite system. Perhaps there are other ways to speed up Uranus's spin precession rate and generate the planet's large obliquity.

1.4   Outline of Thesis

The primary motivation of this dissertation is to expand and expound the origin of the ice giants' spin states through a variety of spin dynamics. To provide a baseline for comparison, we revisit the giant impact model in the next chapter by exploring the probabilities of different collisional scenarios. If a spin-orbit resonance can tilt Uranus all the way to 98°, then no impacts are required. Furthermore, raising Uranus's tilt significantly is also equally valuable. Next, one cannot discuss the evolution of a planet's tilt without addressing the evolution of its spin rate. It is not obvious what Uranus's primordial spin rate was, but gas accretion is likely the

primary source. Understanding all of the subtleties of gas accretion is beyond the scope of this dissertation, but Chapter 3 explores the tools and theory necessary to attempt to understand why gas giants do not spin at near break up speeds. Lastly, Chapters 4 and 5 investigate alternate spin-orbit resonance scenarios to tilt Uranus over.

Capitalizing on tools developed to investigate planetary spins, Chapter 6 is focused on satellites' spin rates. Here we examine whether the spins and orbits of irregular satellites around Saturn can be explained as byproducts of collisions. We evaluate the conditions required for collisions to produce the satellite spin states observed by the Cassini spacecraft, and discuss how these constraints play into the greater context of irregular satellite formation around giant planets.

Chapter 2:   A Re-examination of the Collision Model

2.1   Conditions for Collisions

The leading explanation for Uranus's 98° tilt is a single Earth-mass impactor striking the planet's polar region (Benz et al., 1989; Korycansky et al., 1990; Slattery et al., 1992; Parisi & Brunini, 1997; Morbidelli et al., 2012; Izidoro et al., 2015; Kegerreis et al., 2018, 2019; Kurosaki & Inutsuka, 2019; Reinhardt et al., 2020; Ida et al., 2020), but if Uranus's regular satellites originated in a circumplanetary disk (Szulágyi et al., 2018) instead of a debris disk (Ida et al., 2020), then Morbidelli et al. (2012) argue for two or more collisions. Although two successive giant impacts are less likely to occur than just one strike, it may be easier to generate Uranus's spin state with smaller impactors. This chapter re-examines the collision model by deriving probability distributions of Uranus's final spin state for different scenarios, and then comparing them.

To do this, we use a collisional code that builds up a planet by summing the angular momentum of the planet and impactors, and we assume some reasonable approximations about the impactors' trajectories. Here, the impactors are assumed to originate within the protoplanetary disk, they approach a random location on the planet's surface on trajectories that parallel its orbital plane, and all the mass is

absorbed upon impact. This is a sufficient approximation because we assume small inclinations and less than $0.1\,M_\oplus$ of material is expected to be ejected from the system after an Earth-mass strike (Kegerreis et al., 2018, 2019). Because nearly every object in the Solar System orbits in the same direction, the impactors' relative speed would be almost 40% of Uranus's orbital speed if they traveled on nearly parabolic orbits. Since we expect most impactors to follow orbits with lower eccentricities, the relative velocities are sampled between 0 and 0.4 times Uranus's circular speed (6.8 km/s) (Hamilton & Burns, 1994). Finally, after running this for a half million randomized instances, we can generate distributions of the planet's spin state.

Considering that the impactor's relative speed is small compared to the planet's escape speed (21.4 km/s), gravitational focusing is also important. For cases where gravitational focusing is strong, the impact cross section is large and the impactor is focused to a hyperbolic trajectory aimed more closely towards the planet's center. Since head-on collisions do not impart any angular momentum, the planet's spin state is expected to be more difficult to change when focusing is included. The impact geometry is shown in Figure 2.1, with the impactor initially traveling in the $+\hat{y}$ direction. The impact parameter is the shortest distance between the two bodies if they both traveled on straight lines, and is given as

$$b_{\mathrm{max}}^2 = R_P^2(1 + (V_{\mathrm{esc}}/V_{\mathrm{rel}})^2). \tag{2.1}$$

The impactor passes through a random point on the effective collision cross sectional area (b^2), strikes the corresponding point on the planet's surface, and transmits
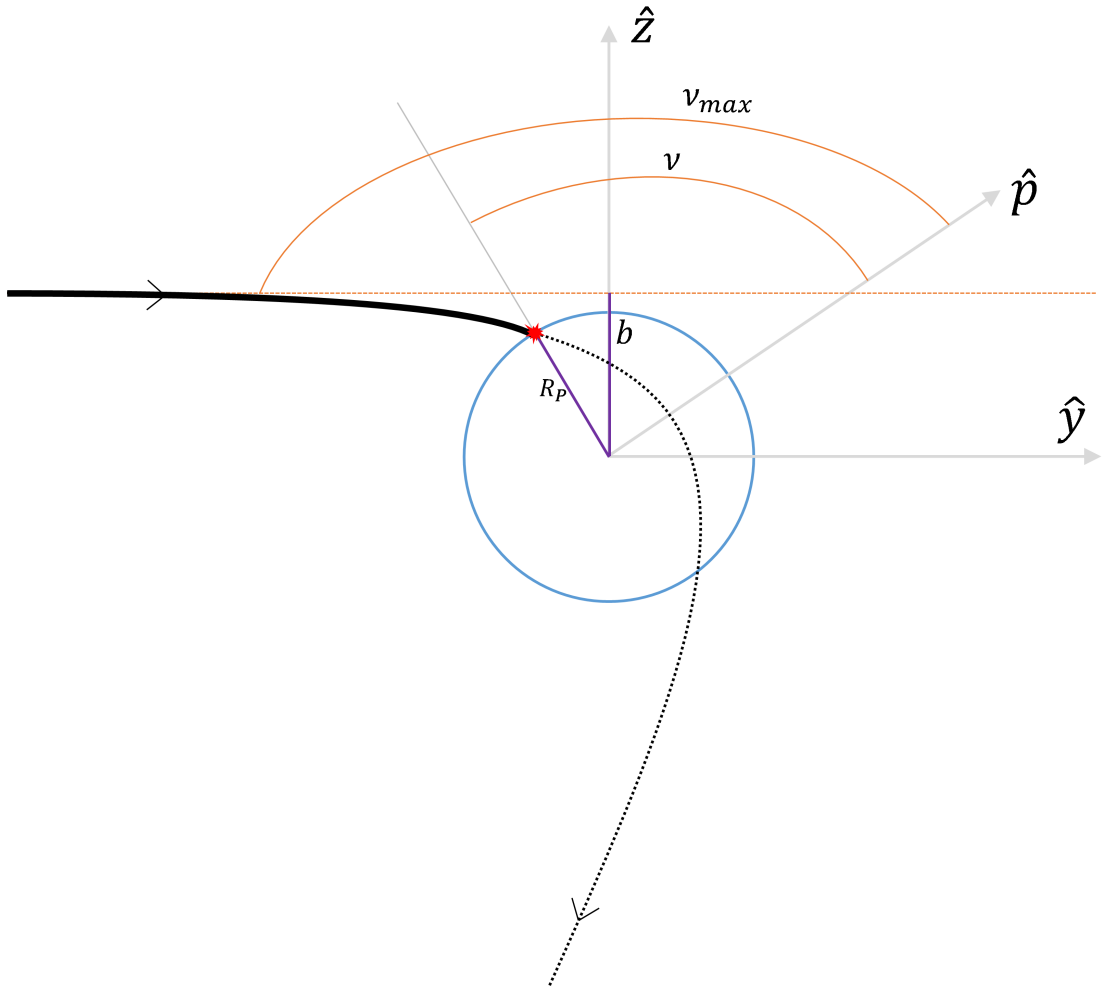
Figure 2.1: A diagram for gravitational focusing. Here a particle with a low relative speed is focused onto a hyperbolic trajectory towards the planet's center. The blue circle is the planet's cross section described by its radius R_P, and the particle is initially traveling in the $+\hat{y}$ direction. ν is the true anomaly, $\nu_{\max} = \cos^{-1}(-1/e)$ is the angle between the asymptote and pericenter, b is the impact parameter, $\hat{p}$ points in the direction of pericenter, the planet spins along $+\hat{z}$, and $+\hat{x}$ goes out of the page.

angular momentum $\vec{L} = m\vec{r} \times \vec{v}$. Only the tangential component contributes to the imparted angular momentum, so $\vec{L} = L_\theta(-\sin(\phi)\hat{x} + \cos(\phi)\hat{z})$, where $\phi = \tan^{-1}(z/x)$ is the azimuthal angle of the impactor on the planet's cross sectional area, $L_\theta = mR_P V_\theta$, and

$$V_\theta = \sqrt{\frac{GM_P}{a(1-e^2)}}(1 + e\cos(\nu)) = \sqrt{\frac{GM_P a(1-e^2)}{R_P^2}} \tag{2.2}$$

with impactor striking the planet at a distance $R_P = a(1 - e^2)/(1 + e\cos(\nu))$. Here, R_P is the planet's radius, m is the mass of the impactor, M_P is the mass of the planet, and $a = -GM_P/V_{\mathrm{rel}}^2$ for a hyperbolic orbit. From the definition of a hyperbola, the length of the line segment from the focus to the intersection of the asymptote (along the axis $\hat{p}$ in Figure 2.1) is ae (Danby, 1992), and the angle of approach is given as $\nu_{\max} = \cos^{-1}(-1/e)$. Thus, $\sin(\pi - \nu_{\max}) = \sqrt{1 - e^{-2}} = b_r/ae$, and the eccentricity of the impactor's trajectory is then $e = \sqrt{(b/a)^2 + 1}$, which is greater than 1. Figure 2.1 shows an example of an impact strike at $\phi = 0$, which imparts angular momentum only in the $\hat{z}$ direction, speeds up the planet's spin rate and drives obliquities to $0°$.

Also, since we do not know how the density profile changes between impacts, we maintain the dimensionless moment of inertia at $K \equiv \frac{I}{MR_P^2} = 0.225$, but vary the planet's radius by assuming a constant density profile. Although these assumptions are mildly inconsistent, we find that even large impacts incident on a mostly formed Uranus yield just small changes in radius, and that the final spin rates changes by only about 10% for other mass-radius relations. Finally, Podolak & Helled (2012)

suggest a maximum impact boundary of around 0.95 R_P as beyond this the impactor simply grazes the planet's atmosphere and departs almost unaffected. For simplicity, and in the spirit of approximation, this subtlety is ignored.

2.2   Accretion onto a Slowly Spinning Planet

In Figures 2.2a and 2.2b, we assume that the planet's initial spin rate was low to highlight the angular momentum imparted by impacts. Since $V_{\rm esc}^2 = 2GM_P/R_P$, the impact cross section $b^2 \propto R$ for $V_{\rm rel} \ll V_{\rm esc}$ (Equation 2.1). The corresponding probability density distribution of impact locations is $\frac{d(\pi b^2)}{dR}$, which is constant; therefore, the spin distribution induced from a single collision is flat (Figure 2.2a). However, if the impactor's relative speed is instead much greater than the planet's escape speed, then gravitational focusing is weak and the impactors will be traveling on nearly straight lines. In this case a single collision produces a spin distribution that increases linearly with the planet's radius, as there is an equal chance of striking anywhere on the planet's surface. The obliquity distribution for a single impact, with or without gravitational focusing, is uniform because an initially non-spinning planet has no obliquity and every outcome is equally likely. A Uranian core formed from the accretion of many small objects, by contrast, would likely have a very low spin rate (Lissauer & Kary, 1991; Dones & Tremaine, 1993a,b; Agnor et al., 1999), since each successive strike likely cancels out at least some of the angular momentum imparted from the previous impact (Figures 2.2c and 2.2d). The planet would also have a narrower range of likely obliquities because the phase space available for low
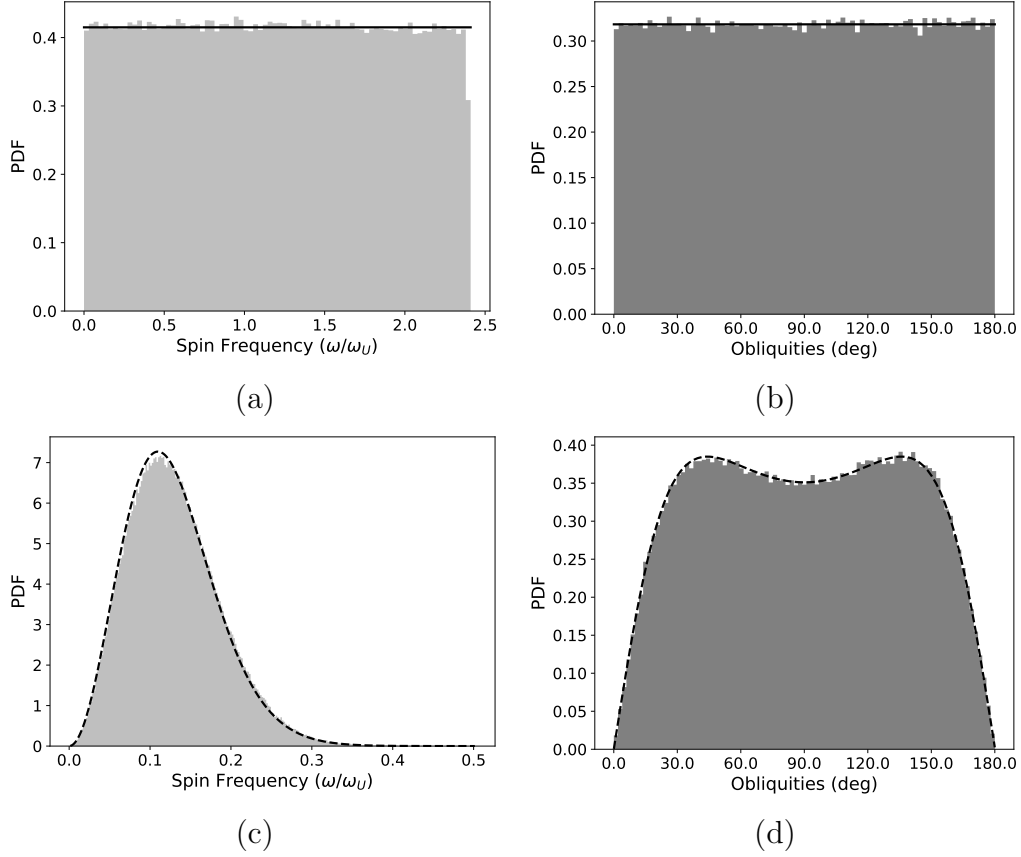
Figure 2.2: (a) The spin distribution for 5×10^5 realizations of a single impact ($m_i = 1\, M_\oplus$) on a non-spinning proto-Uranus with initial mass $13.5\, M_\oplus$ including the effects of gravitational focusing. ω_U is the current uranian spin angular frequency, and all of the following distributions are normalized so that the shaded areas equal 1 (with the obliquities in radians); therefore, the solid line that fits the distribution is the probability distribution function (PDF) $P = \omega_U/\omega_{\max}$. (b) The corresponding obliquity distribution (depicted in degrees) with the solid line given by $P = 1/\pi$. (c) The spin distribution for 100 impacts of equal mass ($m_i = 0.01\, M_\oplus$). (d) The corresponding obliquity distribution for 100 impacts. The dashed lines tracing the distributions in both of these figures are the analytic results (Equation 2.3, 2.4), and a detailed analysis can be found in Appendix A.

18

tilts is small.

The calculation for the planet's final spin state for many impacts behaves similarly to a random walk, so from the central limit theorem, each directional component of the imparted angular momentum can be described by a normal distribution. The theoretical curve of Figure 2.2c is given by the probability distribution $f_L(l)$, which describes the probability that L, the magnitude of the planet's spin angular momentum $L = \sqrt{L_X^2 + L_Y^2 + L_Z^2}$, takes the value l:

$$f_L(l) = \frac{2l^2 e^{-l^2/2\sigma^2}}{\sqrt{2\pi}\,\sigma^2\sigma_z}\,\Phi(0.5; 1.5; -\beta l^2) \tag{2.3}$$

(Dones & Tremaine, 1993a, Eq. 109). Here σ is the standard deviation for the components of the planet's spin angular momentum that lie in the orbital plane, σ_z is the standard deviation for the component perpendicular to the orbital plane, and $\beta = \frac{\sigma^2 - \sigma_z^2}{2\sigma^2\sigma_z^2}$. The angular momentum imparted is always perpendicular to the plane of the impactor's trajectory. After multiple impacts, standard deviations are related by $\sigma_z \approx \sqrt{2}\sigma$, so $\beta < 0$. Finally, $\Phi(0.5; 1.5; \beta l^2)$ is the confluent hypergeometric function of the first kind. The corresponding obliquity probability distribution is:

$$f_\epsilon(\varepsilon) = \left| \frac{1}{4\sqrt{2}\,\sigma^2\sigma_z} \frac{\tan(\varepsilon)}{\cos^2(\varepsilon)} \left(\frac{\tan^2(\varepsilon)}{2\sigma^2} + \frac{1}{2\sigma_z^2} \right)^{-3/2} \right| \tag{2.4}$$

(Dones & Tremaine, 1993a, Eq. 111), and derivations can be found in Appendix A. Notice how well these calculations agree with the numerical result for many impacts (Figures 2.2c and 2.2d). Consequentially, keeping the total mass imparted constant

and increasing the number of impactors in Figure 2.2c from 100 to 1000 would shift the peak to slower spin rates by a factor of $\sqrt{10}$. Because Uranus's spin period is quite fast, its spin state could not have simply been a byproduct of myriad small collisions.

We will now consider the intermediary cases with only a few impactors incident on a slow spinning planet. Figure 2.3 shows the product of two equal sized hits, and the resulting distributions interestingly resemble the limit of multiple collisions. If the masses of the two impactors differ significantly, however, the corresponding spin and obliquity distributions are more similar to the single impact case (Figure 2.4). Therefore, while the planet's obliquity distribution may be more or less flat, its spin rate strongly depends on both the number of strikes and the total mass.

Table 2.1 shows a range of possible collisions onto a non-spinning planet. This shows that the smallest amount of mass necessary to push Uranus toward its observed spin state is about $0.4\,M_{\oplus}$, regardless of the number of impacts. The odds of this happening decreases for each additional collision because each impact needs to hit at exactly the right location. The last section of Table 2.1 also provides statistics for impactors much greater than an Earth-mass. Impactors this massive would likely violate the no mass-loss assumption, yet the odds of generating Uranus's current spin state is still low. A more detailed analysis of these impacts is beyond the scope of this paper; however, see Kegerreis et al. (2018, 2019) for a smoothed-particle hydrodynamics analysis on the effects impacts have on Uranus's rotation rate and internal structure.
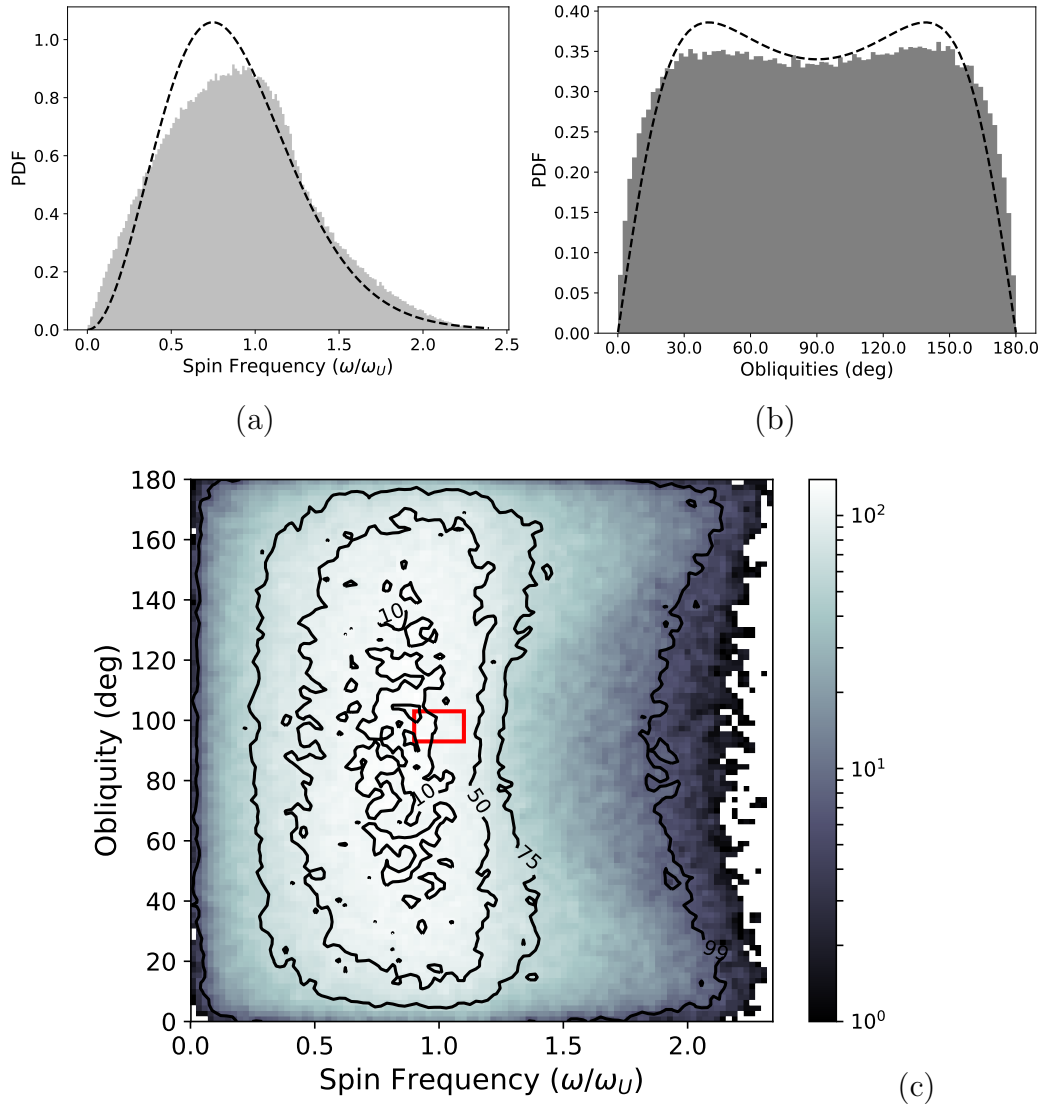
Figure 2.3: (a) The spin distribution for two impacts of equal mass ($m_i = 0.5\,M_\oplus$) onto an initially non-spinning Uranus. (b) The corresponding obliquity distribution for two equal impacts. The dashed line is the analytic result for the limit of an Earth mass distributed amongst a large number of particles. (c) A density plot of the spin frequency vs. obliquity where the value of each pixel is the number of iterations that yielded that result. Values within 10% of Uranus's current obliquity and spin rate are contained within the red rectangle. The top 10, 50, 75, and 99 percent of iterations fall within the contour lines. The probability of falling within this rectangle compared to a similar space around the peak of this distribution is 0.96, meaning that the current state is a likely outcome.
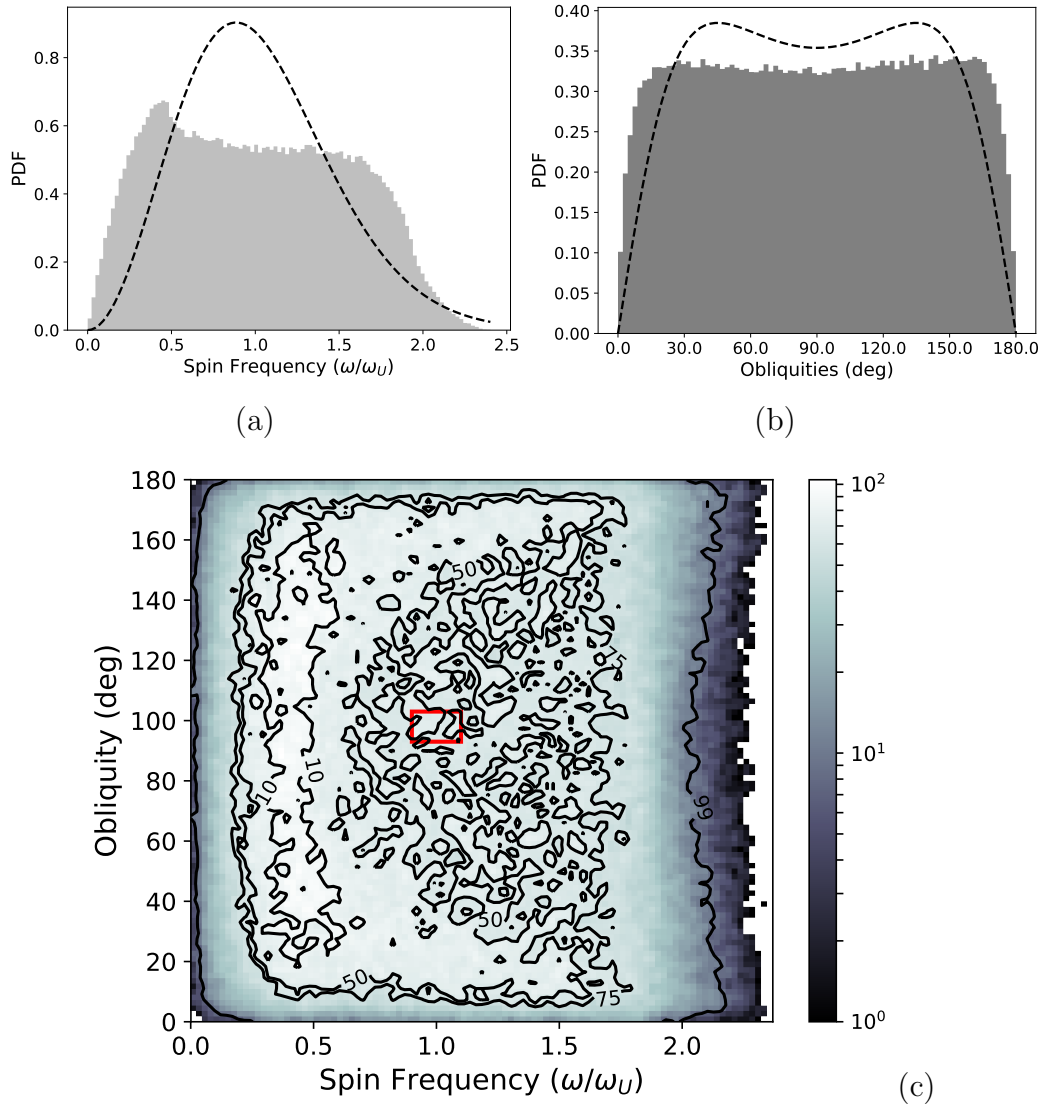
Figure 2.4: (a) The spin distribution for two impacts of masses $0.8\,M_\oplus$ and $0.2\,M_\oplus$ onto a non-spinning planet. (b) The corresponding obliquity distribution for these two unequal impacts. The dashed line is the analytic result for the limit of an Earth mass distributed amongst a large number of particles. (c) A density plot of the spin frequency vs. obliquity where each pixel is the number of iterations that yielded those values. Values within 10% of Uranus's current obliquity and spin rate are contained within the red rectangle. The likelihood of falling within 10% of the planet's current spin state is $l_U = 0.0062$, 0.76 times that of falling within 10% of the most likely value.

N	M_i	M_T	Probability (l_U)	Normalized Probability
1	1	1.0	5.0×10^{-3}	1.00
2	0.5	1.0	1.1×10^{-2}	2.20
3	0.333	1.0	7.1×10^{-3}	1.42
4	0.25	1.0	4.5×10^{-3}	0.90
7	0.142	1.0	6.4×10^{-4}	0.13
100	0.01	1.0	0	0
2	0.8, 0.2	1.0	6.2×10^{-3}	1.24
1	0.41	0.41	5.2×10^{-3}	1.04
2	0.205	0.41	4.4×10^{-5}	0.001
3	0.137	0.41	2.0×10^{-6}	~ 0
1	3.4	3.4	1.6×10^{-3}	0.32
2	1.7	3.4	2.3×10^{-3}	0.46

Table 2.1: This table shows the probability of a number of collisions (N) each with mass M_i totaling to M_T (in Earth masses) simultaneously generating a spin rate and tilt within 10% of Uranus's current spin state. The target spin rates are between $0.9 < \omega/\omega_U < 1.1$ and the target obliquities are between $93° < \epsilon < 103°$ out of 5×10^5 realizations. In this data set, Uranus is initially non-spinning with an obliquity of $0°$, and in general, probabilities decrease with more impactors. The final column divides the probability by the odds of generating Uranus's current state from a single Earth-mass impactor (first entry).

We also explored cases with multiple unequal sized impactors and discovered that the order of the impacts does not matter, as expected, and that the odds improve for similar sized impactors. An example of this can be seen in Figures 2.3a & 2.4a where for the same total mass the spin distribution for two equally sized impactors is concentrated near Uranus's current spin state, whereas the distribution is flatter for two unequal sized impacts. The result is that a small number of equal impacts totaling to about $1\,M_\oplus$ is the most likely explanation for Uranus's spin state if the planet was initially non-spinning.

2.3 With the Effects of Gas Accretion

2.3.1 An Initial Spin Period of 68.8 hours

N	M_i	M_T	ϵ_i	Probability (l_U)	Normalized Probability
1	1.0	1.0	0°	4.5×10^{-3}	0.90
2	0.2	0.5	0°	5.4×10^{-4}	0.11
2	0.5	1.0	0°	1.0×10^{-2}	2.00
2	1.0	2.0	0°	4.7×10^{-3}	0.94
2	1.5	3.0	0°	2.5×10^{-3}	0.50
1	1.0	1.0	40°	4.7×10^{-3}	0.94
2	0.25	0.5	40°	9.0×10^{-4}	0.18
2	0.5	1.0	40°	1.0×10^{-2}	2.00
2	1.0	2.0	40°	5.0×10^{-3}	1.00
2	1.5	3.0	40°	2.7×10^{-3}	0.54
1	1.0	1.0	70°	4.8×10^{-3}	0.96
2	0.25	0.5	70°	1.7×10^{-3}	0.34
2	0.5	1.0	70°	1.0×10^{-2}	2.00
2	1.0	2.0	70°	5.0×10^{-3}	1.00
2	1.5	3.0	70°	2.7×10^{-3}	0.54

Table 2.2: This table shows the same calculations as in Table 2.1, but with the planet having an initial spin period of 68.8 hrs. ϵ_i is Uranus's initial obliquity. The normalized probability column divides the Probability by 5×10^{-3} as in Table 2.1.

Gas accretion almost certainly provides a significant source of angular momentum, so much so that we might expect the giant planets to be spinning at near break-up velocities if they accreted gas from an inviscid thin circumplanetary disk (Bodenheimer & Pollack, 1986; Lissauer et al., 2009; Ward & Canup, 2010); instead, we observe the gas giants to be spinning several times slower. The mechanism responsible for removing excess angular momentum is likely a combination of polar accretion and magnetic interactions between the planet and the disk (e.g. Fendt, 2003; Tanigawa et al., 2012; Batygin, 2018, see Chapter 3.2.2 for more detail). This

Figure 2.5: Density plot showing two impacts of equal mass ($m_i = 1.0\,M_\oplus$) incident on Uranus with $T_i = 68.8$ hours and $\epsilon_i = 40°$. The probability of Uranus's spin state falling within 10% of the maximum value is 1.4 times that of the planet's current state.

may explain Uranus's and Neptune's similar fast spin rates, and so the planet's initial obliquities should be near 0° as the angular momentum imparted by accretion is normal to the planet's orbital plane.

First, we explore cases where the planet initially spins slowly. In Figure 2.5 we have Uranus's initial spin period four times slower than its current value, tilted to 40°, and the planet was struck by two Earth-mass impactors. In this case, even if Uranus was tilted initially by another method, the odds of generating Uranus's current spin state are about the same as if the planet was untilted. This is shown in Table 2.2, and the entries show similar likelihoods to the non-spinning case. However, both the non-spinning and slow spinning cases are improbable for two reasons. First, the mechanism responsible for removing excess angular momentum during gas accretion needs to be extremely efficient. And second, the odds that both Uranus and Neptune were spun up similarly by impacts requires significant fine tuning.

2.3.2   An Initial Spin Period of 17.2 hours

Accordingly, we investigate the effects of gas accretion by considering impacts onto an untilted fast spinning Uranus. Note that since we are adding angular momentum vectors, the order does not matter; therefore, striking Uranus with a giant impactor before the planet accretes gas will yield the same probability distributions as the reverse case considered here. For an initial spin period near Uranus's current value, the minimum impactor mass increases by $\sqrt{2}$ from $\sim 0.4\,M_\oplus$ to $0.55\,M_\oplus$ over
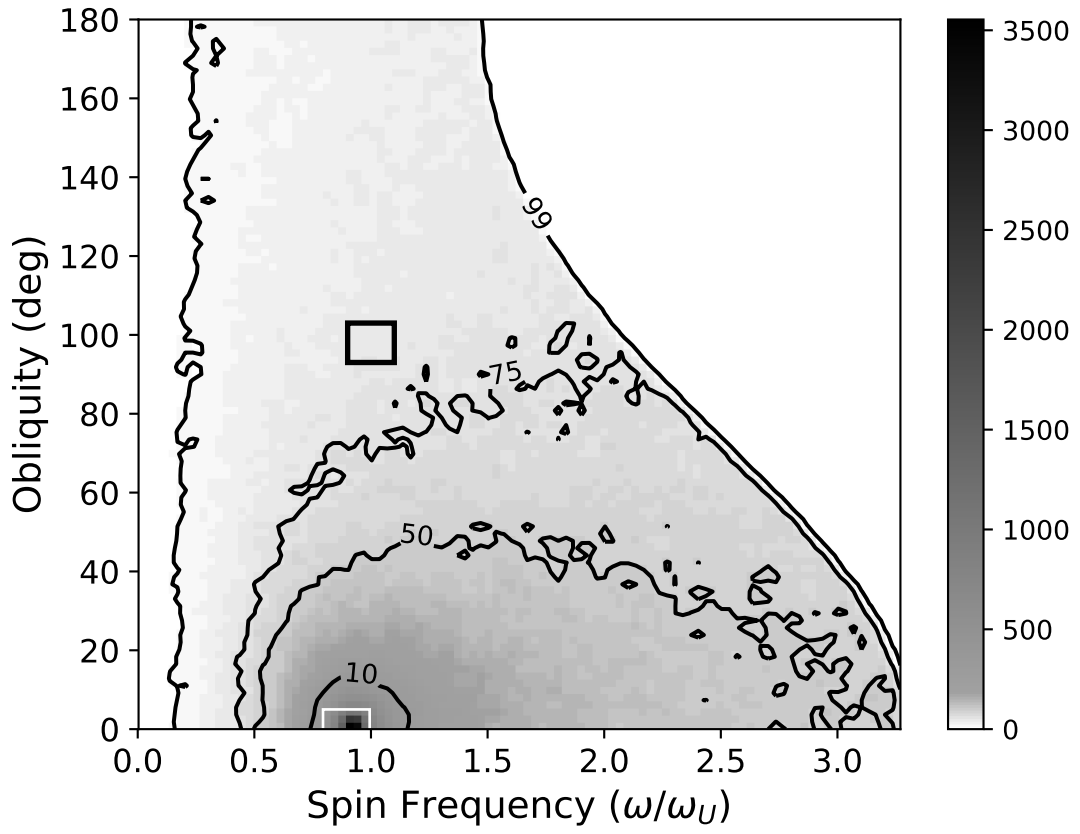
Figure 2.6: Density plot of Uranus's obliquity and spin rate after a 1 $M_\oplus$ strike if its initial spin period is $T_i = 16$ hr at $\epsilon_i = 0°$ obliquity (Rogoszinski & Hamilton, 2020a). Values within 10% of Uranus's current obliquity and spin rate are contained inside the black box; the equivalent white box surrounds the peak of distribution. The color bar shows the number of instances for that value, and the contour lines contain the values within which a percentage of instances are found. The likelihood, l, of the planet's final spin state being within 10% of its initial value is about 25 times greater than finding the planet within 10% of Uranus's current spin state (l_U=0.0033).
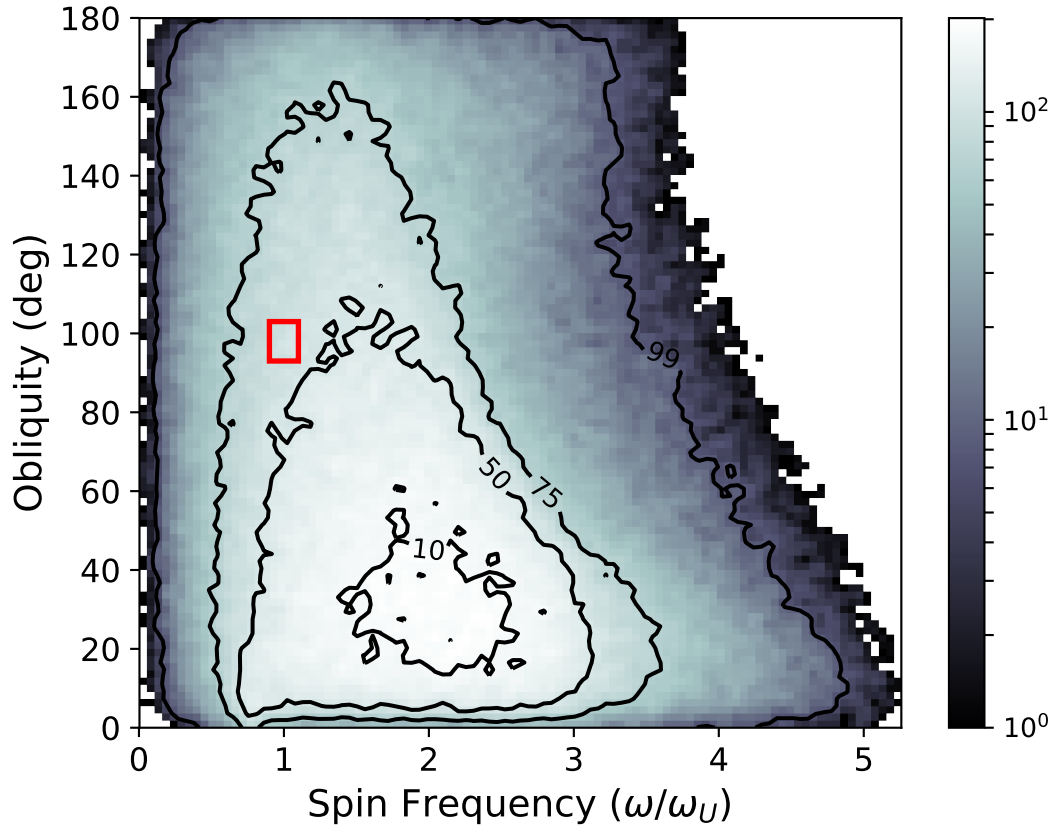
Figure 2.7: Density plot for collisions incident on Uranus with gravitational focusing. Two impacts of equal mass ($m_i = 1.0\,M_\oplus$) incident on Uranus with $T_i =$17.2 hours and $\epsilon_i =$0°. The color bar shows the number of realizations for that value, and the contour lines contain the values within which a percentage of realizations are found. The red box contains the space within 10% of Uranus's current obliquity and spin rate. Uranus having a spin of $2\,\omega_U$ and $\epsilon = 30°$ is twice as likely as its current state ($l_U = 0.0042$).

N	M_i	M_T	ϵ_i	Probability (l_U)	Normalized Probability
1	1.0	1.0	0°	3.4×10^{-3}	0.68
2	0.25	0.5	0°	0	0
2	0.5	1.0	0°	3.7×10^{-3}	0.74
2	1.0	2.0	0°	4.1×10^{-3}	0.82
2	1.5	3.0	0°	2.6×10^{-3}	0.52
5	0.6	3.0	0°	6.1×10^{-3}	1.22
10	0.3	3.0	0°	7.5×10^{-3}	1.50
15	0.2	3.0	0°	6.0×10^{-3}	1.20
1	1.0	1.0	40°	4.5×10^{-3}	0.90
2	0.25	0.5	40°	1.3×10^{-3}	0.26
2	0.5	1.0	40°	7.4×10^{-3}	1.48
2	1.0	2.0	40°	4.7×10^{-3}	0.94
2	1.5	3.0	40°	2.6×10^{-3}	0.52
1	1.0	1.0	70°	8.3×10^{-3}	1.66
2	0.25	0.5	70°	2.6×10^{-2}	5.20
2	0.5	1.0	70°	1.4×10^{-2}	2.80
2	1.0	2.0	70°	5.7×10^{-3}	1.14
2	1.5	3.0	70°	2.7×10^{-3}	0.54

Table 2.3: This table shows the same calculations as in Table 2.1, but with the planet having an initial spin period of 17.2 hrs. ϵ_i is Uranus's initial obliquity. The final column normalizes the probability column by 5×10^{-3} as in Table 2.1.

the non-spinning case because the planet already has the correct $|\vec{L}|$ which must be rotated by $\sim 90°$ by the impact. However, while the non-spinning and slowly-spinning cases have relatively flat obliquity distributions, a fast spinning planet is more resistant to change. For example, striking this planet with a 1 $M_\oplus$ object will most likely yield little to no change to the planet's spin state (Figure 2.6). Introducing more impactors does not change this conclusion appreciably; the planet still tends to remain with a low tilt and similar spin period. Figure 2.7 demonstrates this with the most favorable case of two 1 $M_\oplus$ strikes onto an untilted planet already spinning with a 17.2 hrs period. Additional cases are reported in Table 2.3.

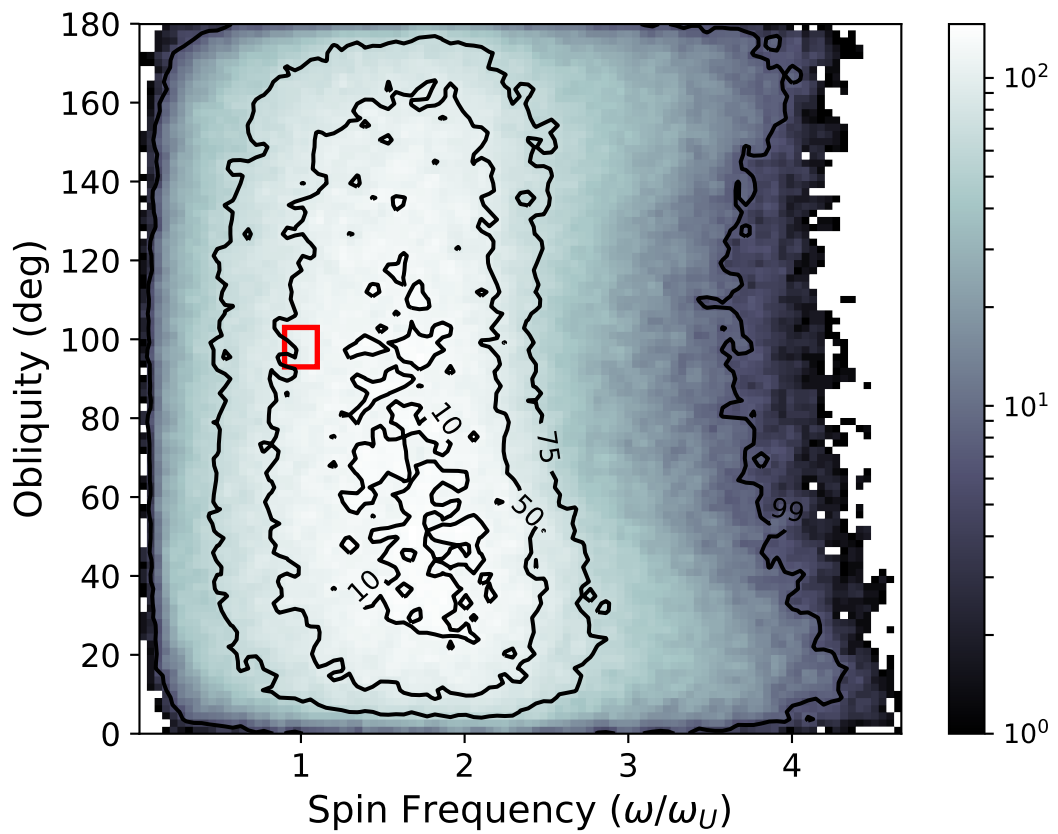If Uranus was initially tilted by a 40° resonance kick, its rapid rotation ensures
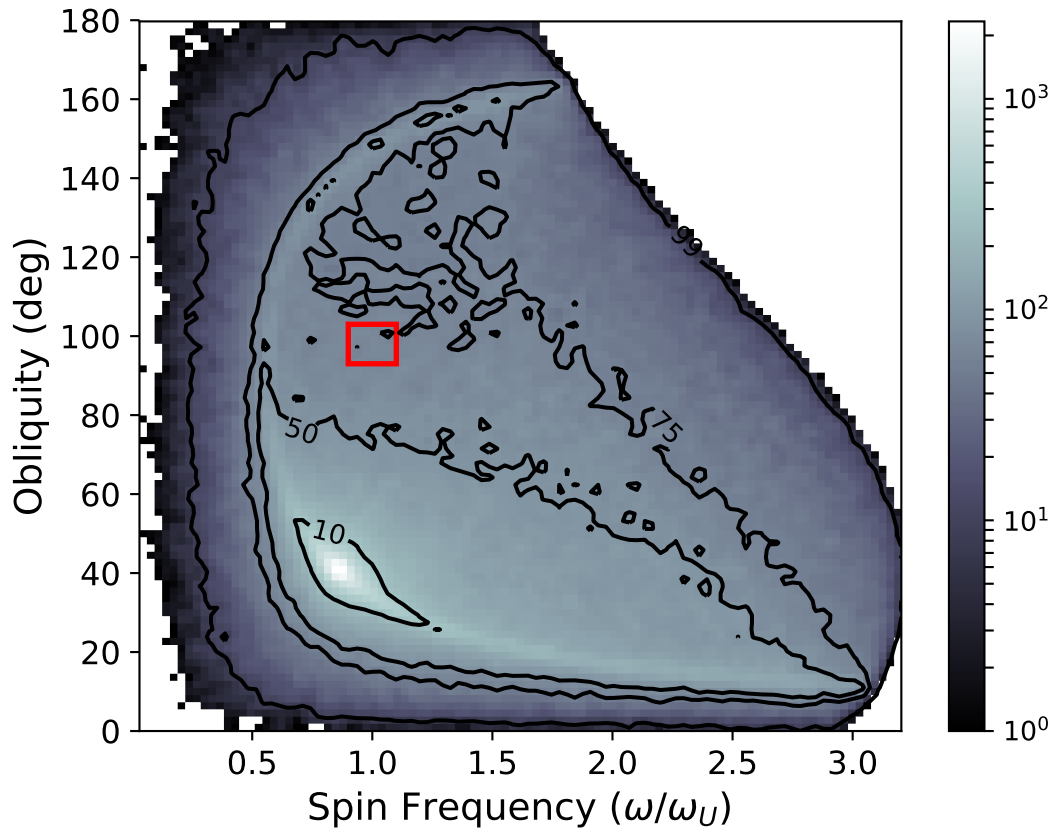
Figure 2.8: Density plot showing one impact ($m_i = 1.0\,M_\oplus$) incident on Uranus with $T_i =$17.2 hours and $\epsilon_i =$40°. It is 17.5 times more likely to fall within 10% of the initial state than Uranus's current spin state ($l_U = 0.0045$). Notice the sharp spike of over 2000 counts near the planet's initial spin state.
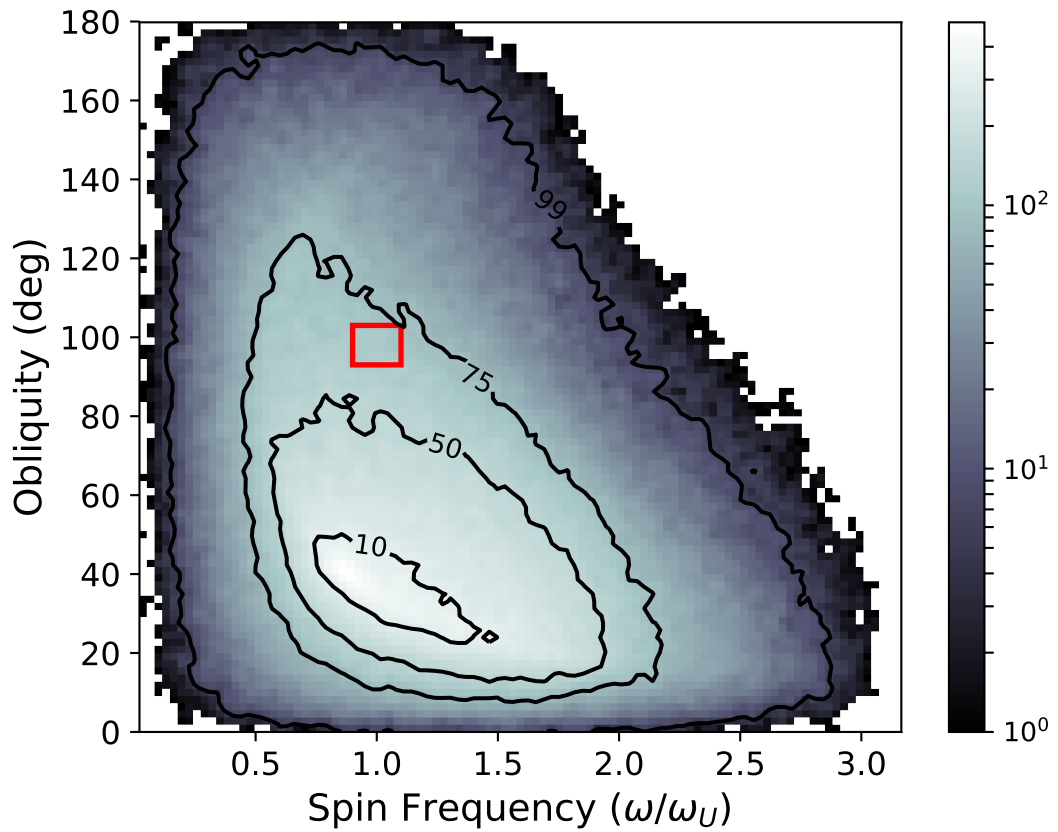
Figure 2.9: Density plot showing two impacts ($m_i = 0.5\,M_{\oplus}$) incident on Uranus with T_i =17.2 hours and ϵ_i =40°. The probability of Uranus's spin state falling within 10% of the maximum value is 3.5 times that of the planet's current state ($l_U = 0.0075$).

Figure 2.10: Density plot showing two impacts ($m_i = 0.5\,M_\oplus$) incident on Uranus with T_i =17.2 hours and ϵ_i =70°. The probability of Uranus's spin state falling within 10% of the maximum value is 1.8 times that of the planet's current state ($l_U = 0.014$).

Figure 2.11: Here, $T_i = 16$ hr and $\epsilon_i = 75°$. Values within 10% of Uranus's current obliquity and spin rate are contained inside the black box; the equivalent white box surrounds the peak of distribution. Uranus is struck by two 0.25 $M_\oplus$ objects. In this case, it is 2.1 times more likely to find the planet near the maximum value than finding Uranus within 10% of its current spin state (l_U=0.038).

that its spin state will tend to remain relatively unaffected by subsequent impacts. This can be seen in Figure 2.8 with a 1 $M_\oplus$ strike, where the probability of tilting Uranus to 98° is only 4.5×10^{-3}. The odds do improve if the number of impacts increases (Figure 2.9), but they are not better than the non-spinning case. However, if Uranus was initially tilted by 70° via a spin-orbit resonance (Rogoszinski & Hamilton, 2020a), then two 0.5 Earth-mass strikes generates a favorable result (Figure 2.10). Also, only in this case will two 0.25 $M_\oplus$ strikes yield even better likelihoods (Figure 2.11). Therefore, if Uranus's and Neptune's current spin rates were a byproduct of gas accretion, then a large resonance kick can significantly reduce the mass needed in later impacts.

2.3.3   An Initial Spin Period of 8.6 hours

Finally, the mechanism that removes angular momentum during gas accretion could have been very weak and Uranus would have been initially spinning very fast. In this case, slowing down Uranus's spin rate and tilting the planet over would require very massive impacts. As discussed in the previous subsection, changing the planet's spin state with many impactors requires more impacting mass to compensate for partial cancellations of impact effects. Table 2.4 shows that ten impacts totaling to 4 $M_\oplus$ produce plausible outcomes. However, it is unclear how gas accretion would transport the optimal amount of angular momentum to the ice giants but not to the gas giants, nor is it expected that the massive impactors required in this scenario would spin both Uranus and Neptune down similarly. While their obliquity

N	M_i	M_T	ϵ_i	Probability (l_U)	Normalized Probability
1	1.0	1.0	0°	2.3×10^{-3}	0.46
2	0.25	0.5	0°	0	0.00
2	0.5	1.0	0°	2.6×10^{-4}	0.05
2	1.0	2.0	0°	2.7×10^{-3}	0.54
2	1.5	3.0	0°	2.0×10^{-3}	0.40
1	1.0	1.0	40°	4.1×10^{-3}	0.82
2	0.25	0.5	40°	0	0
2	0.5	1.0	40°	2.0×10^{-3}	0.40
2	1.0	2.0	40°	4.1×10^{-3}	0.82
2	1.5	3.0	40°	2.5×10^{-3}	0.50
1	1.0	1.0	70°	2.1×10^{-3}	0.42
2	0.25	0.5	70°	1.2×10^{-4}	0.02
2	0.5	1.0	70°	3.3×10^{-3}	0.66
2	1.0	2.0	70°	3.0×10^{-3}	0.60
2	1.5	3.0	70°	2.4×10^{-3}	0.48
5	0.8	4.0	0°	3.4×10^{-3}	0.68
10	0.4	4.0	0°	5.0×10^{-3}	1.00
15	0.2667	4.0	0°	4.4×10^{-3}	0.88

Table 2.4: This table shows the same calculations as in the previous tables, but the planet is spinning with a period of 8.6 hrs. The final column has been normalized as in Table 2.1.

distributions peaks at around 30°, which favors a Neptune formation scenario, the planets would still likely be spinning twice as fast as they are today (Figure 2.12). Additionally, ten independent strikes is less probable than only two, while also requiring the solar system to have been populated with many massive rogue planetary cores.

2.4 Conclusion

We have shown here that it is difficult for a $1\,M_\oplus$ collision to reproduce Uranus's current spin state if Uranus was initially untilted and spinning near its current rate. Since there is a higher concentration of radial impacts near the planet's
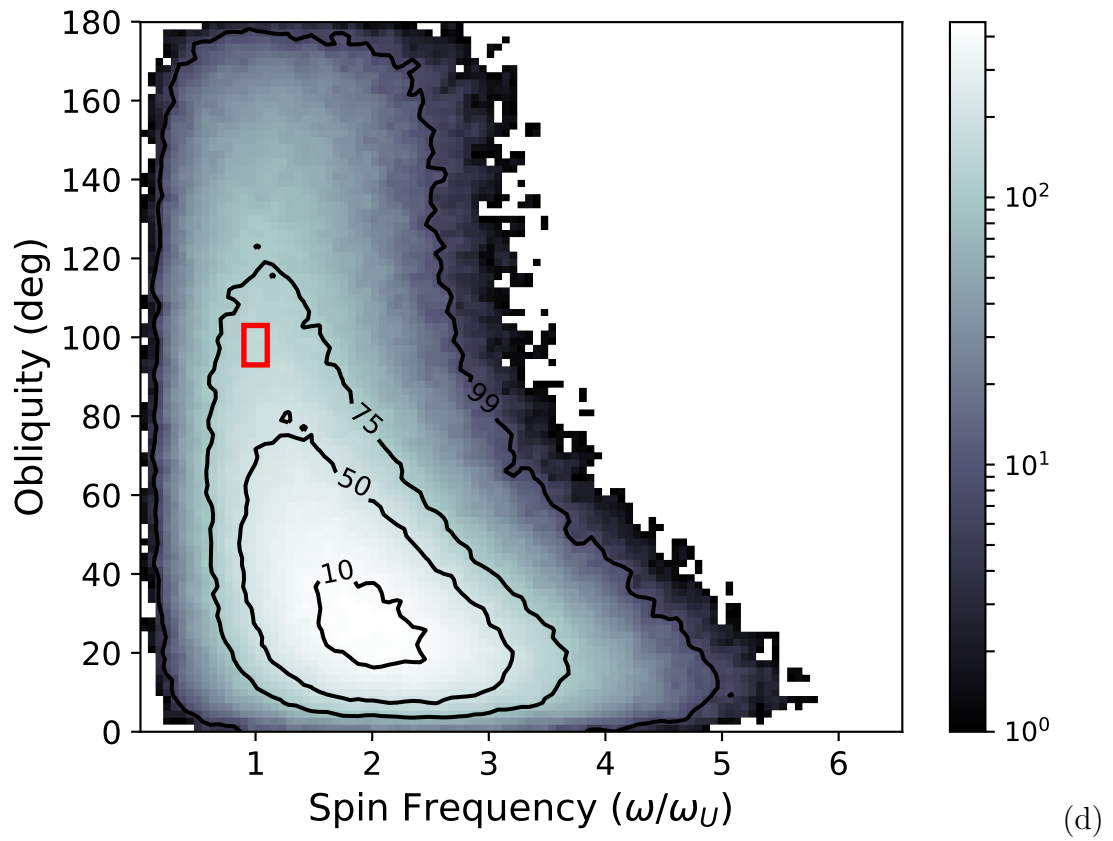
Figure 2.12: Density plot showing ten impacts of equal mass ($m_i = 0.4\,M_\oplus$) incident on Uranus with $T_i =$8.6 hours and $\epsilon_i =$0°. The probability of Uranus's spin state falling within 10% of the maximum value is 2.9 times higher than falling near the planet's current state ($l_U = 0.005$), as shown in the red box.
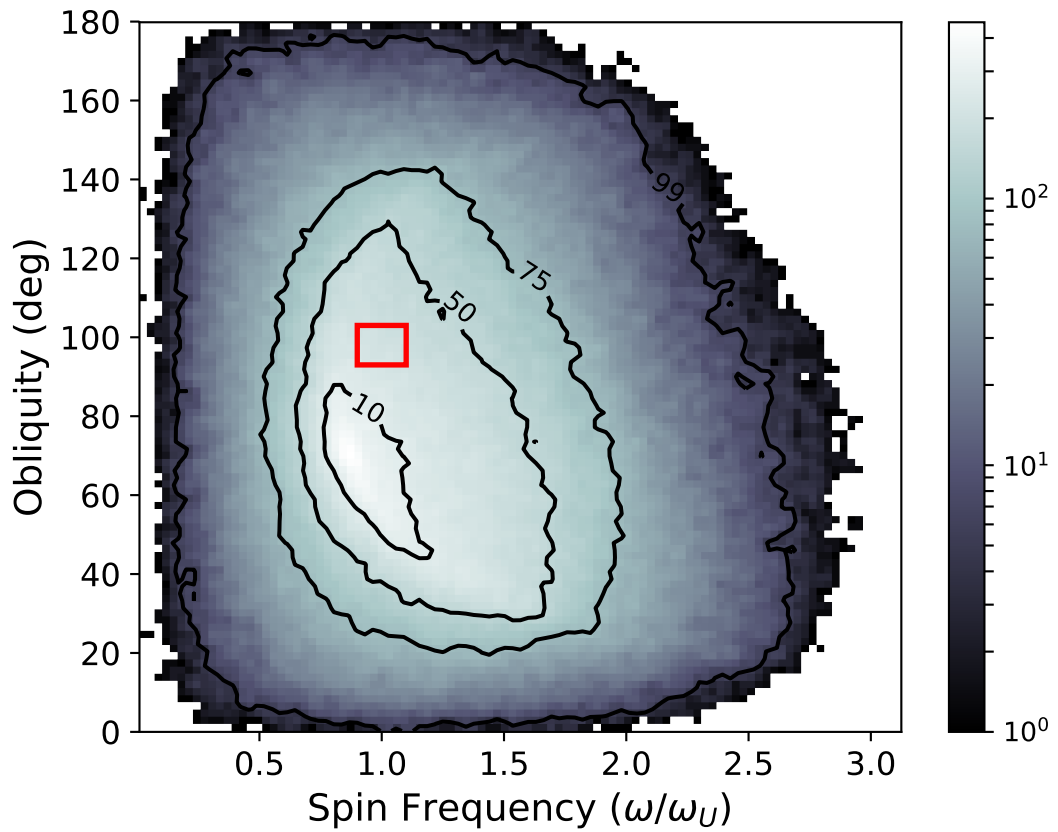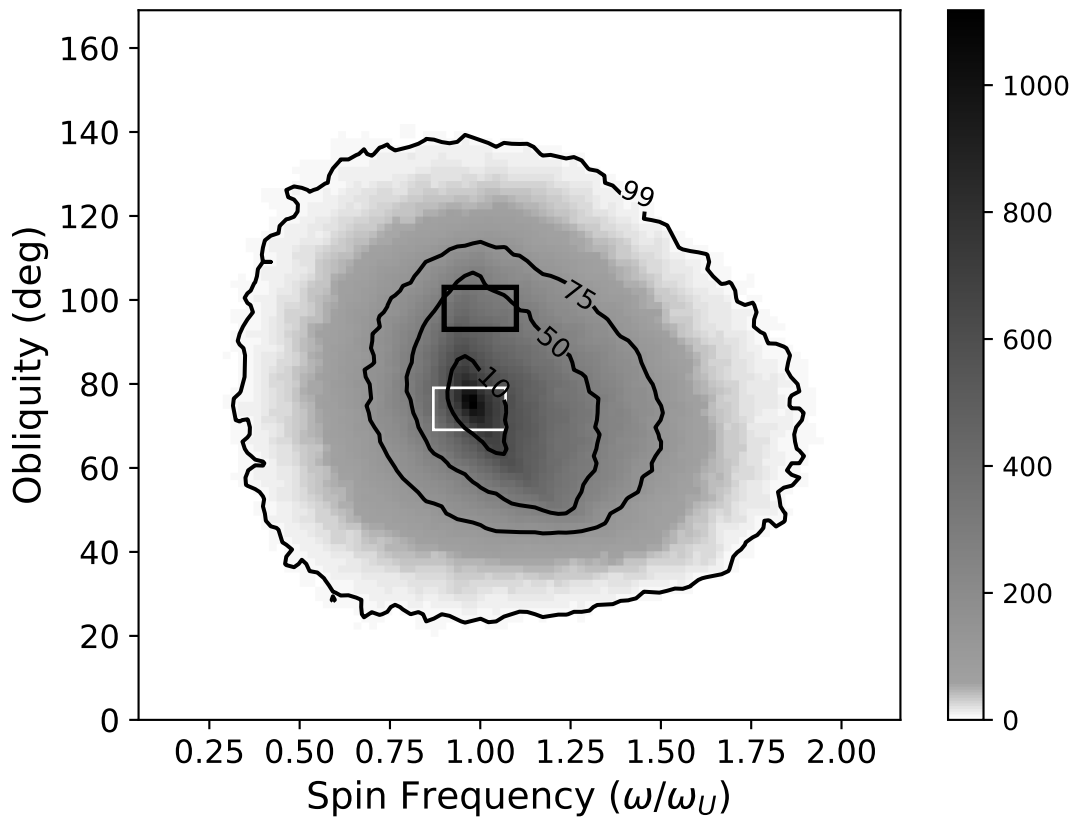
center, the angular momentum imparted is likely to be small, and the distribution peaks strongly near the planet's initial state. Two strikes are an improvement, and we find that two $0.5\,M_\oplus$ yield the best likelihoods. These likelihoods also improve if the planet was initially spinning slower than its current rate, but the mechanism responsible for removing a giant planet's angular momentum would then need to be more efficient for ice giants despite their more limited atmospheres. Since there is little justification for this, a pure giant collision scenario seems less likely.

The best case scenario is if Uranus was initially tilted higher than $70°$ and then later struck by one or more Mars-sized impactors. Pebble accretion models predict an abundance of Mars-to-Earth-sized planets that have since disappeared (Levison et al., 2015a,b), so it is entirely possible that a few rogue planetary cores struck the ice giants. This increases the likelihood from the $1\,M_\oplus$ strike onto an untilted fast spinning planet by an order of magnitude. The smallest obliquity excitations required to obtain favorable statistical improvements to the pure collisional model is $40°$, which would also eliminate one of the required impactors from Morbidelli et al. (2012)'s accretion model. A secular spin-orbit resonance can increase a planet's obliquity without altering its primordial spin rate, and in the following Chapters we explore how successful they are at tilting Uranus. However, before we delve deeply into these models, we digress briefly to the evolution of a gas planet's spin rate, as the origin and evolution of the planet's spin and obliquity are intimately related.

Chapter 3:   The Origin of Giant Planets' Spin Rates

3.1   Motivation

Giant planet formation models generally focus on gas giants because gas ac-
cretion onto a negligibly low-mass core is easier to model. Ice giants, with their com-
paratively smaller gaseous atmospheres and non-negligible cores, have not achieved
runaway gas accretion, so their formation processes are more complex. For instance,
while Uranus and Neptune are similar in many ways (e.g. mass, size and spin), their
differences suggest dissimilar evolutionary pathways (Podolak & Helled, 2012). The
most obvious difference is their obliquities, with Uranus tilted at 98° and Neptune at
a lower 30°. Other differences include Neptune's interior being more centrally dense
than Uranus despite Neptune having a more massive core (Podolak et al., 1995,
2000), and Uranus being the coldest planet in the solar system (Hanel et al., 1986;
Sromovsky & Fry, 2005). In fact, Uranus's albedo is expected for reflected sunlight
at that distance (Pearl et al., 1990), while Neptune is still radiating its internal heat
at more than twice that it receives from the Sun (Pearl & Conrath, 1991). These
unique characteristics could be explained exclusively or in part by giant impacts
(Reinhardt et al., 2020), their local environments near their respective birthplaces
in the circumstellar disk (Helled & Bodenheimer, 2014; Helled & Fortney, 2020;

Rogoszinski & Hamilton, 2020a), or other internal convection mechanisms (Pearl et al., 1990; Lunine, 1993; Podolak et al., 1995).

As such, it would be naïve to assume that ice giant formation is simply one step shy of gas giant formation; however, calculating the growth of ice giants is exceptionally difficult because one needs to seriously consider the interface between in-falling gas and a relatively massive magnetized core. Modeling this problem is crucial for better understanding planetary evolution, especially since the plurality of observed exoplanets are Neptune analogues[1]. A primary focus of this dissertation is to better understand the evolution of an ice giant's spin state, and, as discussed in the previous chapter, the evolution of the ice giants' obliquities depends on the planets' initial spin rate. In this Chapter we explore how to set up a simple two-dimensional giant planet formation model to study the planet's spin evolution. We focus on Jupiter analogues here because there is extensive literature on the subject to compare and contrast. Most simulations do not explicitly track a gas giant's spin evolution, and 2D dynamics are interesting and quick enough to warrant simulations as the motion of gas under the influence of multiple gravitational fields will be complex. It is also not obvious how trustworthy simple analytic arguments will be. Even if the results agree with the analytics, this work can provide a framework for future expansions (e.g. 3D magnetohydrodynamics and planet-disk interactions), which can eventually be applied to ice giant formation.

---

[1]1457 Neptune-like planets have been discovered out of a total 4284 confirmed exoplanets as of completing this dissertation (`https://exoplanets.nasa.gov/exoplanet-catalog/`).

3.2 Background

3.2.1 Growing Gas Giants vs. Ice Giants

Giant planets are formed from the accumulation of gas and dust inside proto-planetary disks (Kant, 1755; de Laplace, 1796), and the classic gas giant formation process can be broken into three stages (Bodenheimer & Pollack, 1986; Pollack et al., 1996; Lissauer et al., 2009). In stage 1, the core forms from the aggregation of pebbles and planetesimals. During stage 2, core accretion slows as the planetary core exceeds several Earth masses and becomes capable of capturing an atmosphere as its escape velocity exceeds the thermal velocity of the nearby gas. The planet distorts the surrounding disk as it accretes, and the corresponding gravitational torques lead to shocked wave fronts that carve out a gap (Lin & Papaloizou, 1979; Goldreich & Tremaine, 1979, 1980; Lin & Papaloizou, 1986; Kley & Nelson, 2012; Duffell, 2015). The gas flows from the circumstellar disk onto a circumplanetary envelope or disk before accreting onto the planet. Regular satellites around gas giants are formed here (Lunine & Stevenson, 1982; Canup & Ward, 2002; Mosqueira & Estrada, 2003; Alibert et al., 2005; Canup & Ward, 2006; Heller & Pudritz, 2015; Szulágyi et al., 2018). The transition between planar disks and more spherical envelopes depends on the planet's temperature: the hotter the planet, the greater the thermal pressure and the more spherical the circumplanetary gas is (Szulágyi et al., 2016). For Uranus and Neptune near their current locations, this transitional planet temperature is about 500 K (Szulágyi et al., 2018).

Stage 2 lasts a few Myr as the planet slowly accretes gas and planetesimals. Once the protoplanet's gaseous atmosphere becomes more massive than its core, the planet undergoes runaway gas accretion (stage 3), and it can gain about a Jupiter's worth of mass in just 10^4 yr. There are several competing explanations for why Uranus and Neptune have not accreted enough gas to achieve runaway gas accretion. The standard explanation by Pollack et al. (1996) suggests that Uranus and Neptune were simply not able to accrete enough solids near their current locations before the entire protoplanetary disk dissipated. Pebble accretion, however, reduces the ice giants' growth timescale and allows gas giants to form more rapidly at greater distances (Lambrechts & Johansen, 2012), but when the core is massive enough to gravitationally perturb the surrounding gas disk, it creates a pressure barrier to isolate it from further pebble accretion (Lambrechts et al., 2014). Alternatively, Thommes et al. (1999, 2002, 2003) posited that Uranus and Neptune formed between Jupiter and Saturn, and that Jupiter's and Saturn's cores happened to be more massive, allowing them to accrete most of the surrounding gas. When the solid-to-gas ratio in the circumstellar disk reached unity, there was not enough gas to damp the eccentricities and inclinations of the growing protoplanets, so dynamical instability is then triggered and the ice giants scattered outward.

These models all assume Uranus and Neptune formed in a massive circumstellar disk. Frelikh & Murray-Clay (2017) argued that if Uranus's and Neptune's cores were formed close to Jupiter and Saturn later in solar system evolution, then the ice giants could have accreted their atmospheres in an already depleted circumstellar disk after they had been scattered and reached close to their current locations. If

only 1% ($\sim 0.1 M_J$) of the original circumstellar disk remained after the cores migrated outward, then there would have been just enough gas near the ice giants to form their atmospheres. This reduction implies a gas accretion duration for Uranus and Neptune on the order of 10^5 yr given a nominal gas loss rate of $7 \times 10^{-10} M_\odot \, \mathrm{yr}^{-1}$ (Alexander et al., 2005), but 2D and 3D gas accretion models suggest that some gas also crosses through the gap, bypassing the planets altogether (Bryden et al., 1999; Tanigawa et al., 2012; Batygin, 2018). Therefore, if less than half of the gas within the planet's vicinity is actually accreted (Morbidelli et al., 2014; Cridland, 2018), then there needed to have been more gas to compensate, and we could expect a longer gas accretion timescale perhaps closer to 1 Myr.

3.2.2   Why do Gas Giants Spin So Slowly?

Circumplanetary disks regulate not only the growth rate of giant planets but also their spin rates (Bodenheimer & Pollack, 1986; Lissauer et al., 2009; Ward & Canup, 2010). We expect the planets to be spinning at near-breakup velocities if we only consider the hydrodynamics arising in an inviscid thin disk (Machida et al., 2008). We instead observe the giant planets, including the first giant exoplanet with a measured spin rate, β Pictoris b (Snellen et al., 2014), spinning several times slower than their breakup rates; therefore, there must be some mechanism responsible for removing excess angular momentum. The solution may be a combination of magnetic braking caused by the coupling of a magnetized planet to an ionized disk (Lovelace et al., 2011; Batygin, 2018), polar inflows and additional outflows

from a thick disk profile (Tanigawa et al., 2012; Szulágyi et al., 2014), acoustic waves from planet-disk interactions (Belyaev et al., 2013), and magnetically driven outflows (Quillen & Trilling, 1998; Fendt, 2003; Lubow & Martin, 2012; Gressel et al., 2013); regardless, gas accretion is a significant source of angular momentum. It is therefore possible that the planets' spin rates prior to gas accretion were indeed slow, especially if their cores were made up of the accumulation of many small bodies striking randomly at the planet's surface (Lissauer & Kary, 1991; Dones & Tremaine, 1993a,b; Agnor et al., 1999), but pebble accretion may also contribute a significant amount of prograde spin (Visser et al., 2020).

3.3 Using DISCO to Calculate the Spin Rates of Gas Giants

3.3.1 Equations of Hydrodynamics

Calculating the spin evolution of a gas giant requires evaluating the amount of angular momentum that is transfered to the planet from the circumplanetary disk. We model the circumplanetary disk as a two dimensional flow in the orbital plane governed by the Navier-Stokes equations using the hydrodynamics code DISCO. The relevant compressible Navier-Stokes equations without magnetic fields are

$$\partial_t(\Sigma) + \vec{\nabla}\cdot(\Sigma\vec{v}) = 0 \qquad \text{(Continuity Equation)} \qquad (3.1)$$

$$\partial_t(\Sigma\vec{v}) + \vec{\nabla}\cdot(\Sigma\vec{v}\vec{v} + \vec{P} - 2\Sigma\nu\overleftrightarrow{\sigma}) = \Sigma\vec{g} \qquad \text{(Conservation of Angular Momentum)}.$$

$$(3.2)$$

In cylindrical coordinates centered on Jupiter, including the viscous source terms (Landau & Lifshitz, 1959), they take the form

$$\partial_t \Sigma + \frac{1}{r}\partial_r(r\Sigma v) + \partial_\phi(\Sigma\Omega) = 0 \tag{3.3}$$

$$\partial_t(\Sigma v) + \frac{1}{r}\partial_r(r\Sigma v^2 + r\Pi - 2r\Sigma\nu\sigma_r^r) + \partial_\phi(\Sigma v\Omega - 2\Sigma\nu\sigma_r^\phi) = R\Sigma\Omega^2 + \frac{\Pi}{r} - \frac{2}{r}\Sigma\nu\sigma_\phi^\phi + \Sigma g_r, \tag{3.4}$$

$$\partial_t(\Sigma r^2\Omega) + \frac{1}{r}\partial_r(r\Sigma r^2\Omega v - 2r\Sigma\nu\sigma_\phi^r) + \partial_\phi(\Sigma r^2\Omega^2 + \Pi - 2\Sigma\nu\sigma_\phi^\phi) = \Sigma g_\phi, \tag{3.5}$$

where Equations 3.4 and 3.5 are the radial and azimuthal components of Equation 3.2,

$$g_R = -\partial_r(\Phi(r,\phi) + \Phi_C(r,\phi)) \tag{3.6}$$

$$g_\phi = -\partial_\phi(\Phi(r,\phi) + \Phi_C(r,\phi)) \tag{3.7}$$

are the external gravitational acceleration, $\Phi(r,\phi) = -\frac{GM_J}{r} - \frac{GM_\odot}{R}$ is the total gravitational potential, $\Phi_C(r,\phi) = rd\cos(\phi - \Omega t)\Omega^2$ is the centrifugal potential in a non-rotating orbiting frame[2], Σ is the surface density, r is the position, d is the distance the planet is from the Sun, R is the position with respect to the Sun, v is the radial velocity, Ω is the angular velocity, t is time, ϕ is the azimuthal angle, Π is the surface pressure (also called the vertical pressure, $\Pi = \int P dz$), and ν is the kinematic viscosity which we can model with the Shakura-Sunyaev α-prescription (Shakura & Sunyaev, 1973): $\nu = \alpha c_s H = \alpha c_s^2/\Omega$, where c_s is the sound speed and

---

[2]The simulations take place in the rotating frame, and DISCO automatically handles the additional fictitious forces.

α is a constant between 0 and 1. Finally,

$$\sigma_r^r = \partial_r v - \frac{1}{3}\vec{\nabla}\cdot\vec{v} \tag{3.8}$$

$$\sigma_r^\phi = \frac{1}{2}\left(\partial_r\Omega + \frac{1}{r^2}\partial_\phi v\right) \tag{3.9}$$

$$\sigma_\phi^r = r^2\sigma_r^\phi \tag{3.10}$$

$$\sigma_\phi^\phi = \partial_\phi\Omega + \frac{v}{r} - \frac{1}{3}\vec{\nabla}\cdot\vec{v} \tag{3.11}$$

are the viscous source terms.

3.3.2   Angular Momentum Transport in a Hydrodynamic Flow

Circumplanetary disks accrete because kinetic energy and angular momentum are lost due to internal processes within the gas flow. The source of this viscosity in circumplanetary disks is the magnetic interactions between the gaseous particles, but the details remain unclear. Turner et al. (2014) posit that the surface of circumplanetary disks can be ionized by X-rays so that the disk's surface is susceptible to magnetorotational instability (MRI), which increases the disk's magnetic field strength, generates small scale magnetically induced turbulence, and drives accretion (Shakura & Sunyaev, 1973); however, Fujii et al. (2011, 2014) argue that the ionized layer is too thin to contribute. Magnetic braking (Keith & Wardle, 2014; Lovelace et al., 2011) or magnetically driven outflows (Quillen & Trilling, 1998; Fendt, 2003) may also contribute to instability and induce accretion; however, the strength and evolution of the magnetic field of a forming planet is unknown. Non-

magnetic induced accretion has also been explored in the form of shocked spiral density waves produced by tidal torques from the central star (Martin & Lubow, 2011; Belyaev et al., 2013; Szulágyi et al., 2014; Ju et al., 2016; Zhu et al., 2016), and these density waves can increase dissipation and induce accretion.

To better understand how angular momentum moves through the disk, we can consider the azimuthally integrated equations, as denoted by angular brackets. The azimuthal terms fall out leaving the modified continuity equation

$$\partial_t \langle \Sigma \rangle + \frac{1}{r} \partial_r \langle r \Sigma v \rangle = 0, \tag{3.12}$$

and the modified angular momentum equation

$$\partial_t \langle \Sigma r^2 \Omega \rangle + \frac{1}{r} \partial_r (r \langle \Sigma r^2 \Omega v \rangle + r \langle \Sigma \nu r^2 \partial_r \Omega \rangle) = \langle \Sigma g_\phi \rangle. \tag{3.13}$$

The radial component of the gas's angular momentum does not contribute to the planet's spin, so we can ignore this for now. The first term in Equation 3.13 is the change in angular momentum in a fluid, and we want to solve for this at the disk's inner boundary. The other terms describe how the angular momentum changes in the disk as the gas accretes onto the planet. The total gravitational torque acting on gas within a radius R is

$$T_g = \int_0^R \int_0^{2\pi} r \Sigma g_\phi d\phi dr. \tag{3.14}$$

The corresponding advection flux, which characterizes bulk motion through the disk,

and viscous flux are also integrated from 0 to R, and are respectively $F_{\mathrm{adv}} = \langle \Sigma r^3 \Omega v \rangle$ and $F_{\mathrm{visc}} = \langle \Sigma \nu r^3 \partial_r \Omega \rangle$.

The angular momentum accreted should be equal to the sum of these torques, but individually these fluxes can account for how angular momentum is transported through the disk. The advective flux contains contributions from both the bulk flow of gas as well as waves in the disk. We can decompose these by considering the Reynolds flux (Ju et al., 2017; Ryan & MacFadyen, 2017). Let l be the mass-weighted average specific angular momentum

$$l = \frac{\langle \Sigma r^2 \Omega \rangle}{\langle \Sigma \rangle}, \tag{3.15}$$

and $\dot{M} = -\langle r \Sigma v \rangle$ be the total mass accretion rate at radius r. $F_{\dot{M}} = -\dot{M} l$ is then the corresponding mean angular momentum accretion flux, and the Reynolds flux is the difference

$$F_{\mathrm{Re}} = \langle \Sigma r^3 \Omega v \rangle + \dot{M} l = F_{\mathrm{adv}} - F_{\dot{M}}. \tag{3.16}$$

In other words, $F_{\dot{M}}$ accounts for the amount of axisymmetric flux moving through the disk, while F_{Re} account for non-axisymmetric flux due to transport from spiral arms. Finally, the total angular momentum accretion rate is

$$\dot{J} = T_g - F_{\mathrm{visc}} - F_{\mathrm{Re}} - F_{\dot{M}}. \tag{3.17}$$

for fluxes evaluated at the inner boundary.

The general setup for calculating the evolution of the planet's angular mo-

mentum is straightforward: calculate the rate angular momentum is accreting onto the planet for increasing central masses, and then integrate to get the total angular momentum imparted. This is given simply as

$$\Delta J = \int_{t_0}^{t_1} \dot{J} \, dt = \int_{M_0}^{M_1} \dot{J} \frac{dM}{\dot{M}} = \int_{M_0}^{M_1} \widetilde{l} \, dM \tag{3.18}$$

where $\widetilde{l} = \dot{J}/\dot{M}$ is the effective specific angular momentum. Generating the data, however, will require using a sophisticated hydrodynamics software.

3.3.3 DISCO

DISCO (Duffell, 2016) is a 3D moving-mesh magnetohydrodynamics code designed to study astrophysical disks. Disks can be found in any gaseous orbiting system that loses orbital energy much faster than it loses angular momentum, whether they are located around a black hole, star, or a planet. It is therefore important that a code dedicated to simulating disks can model a wide range of scales accurately and efficiently, and DISCO has already been used extensively to study planetary migration and gap openings in circumstellar disks (Duffell & MacFadyen, 2012, 2013; Duffell et al., 2014; Duffell, 2020).

What separates DISCO from other hydrodynamic codes is its moving-mesh grid. Standard hydrodynamics codes calculate the flow of gas by keeping the coordinate system fixed, which, although easier to implement, can lead to some numerical inefficiencies. Resolving gas that reaches supersonic speeds using a fixed grid requires finer timesteps, which can be expensive. A moving-mesh grid, on the other

hand, follows the orbital path of the gas even as it exceeds supersonic speeds, which can reduce the integration time by orders of magnitude. Also, though not unique to DISCO, the code is built to be parallelized, which also greatly reduces the total runtime. For example, the integration time of one of the simulations where gas is accreting onto a $150\,M_\oplus$ core is four times longer if the moving mesh grid is turned off, which would take one month to complete instead of about a week.

Another advantage of a moving-mesh grid is that since the grid follows the gas flow, it maintains contact discontinuities. Shock waves yield discontinuities in density and pressure, and it is important to preserve this feature as the shock front propagates. A fixed grid would smooth out the discontinuity, which leads to artificial diffusion and a less accurate model.

One simple test to show that DISCO can model the evolution of a disk is to place a ring of matter around a central body and include viscosity. Viscosity causes the gas particles in the disk to lose energy which leads to accretion; however, if an external torque is not present, then the total angular momentum of the system remains fixed. So if some gas falls inwards, then about an equal amount of gas should spread outwards. Figure 3.1 shows just that for a gaseous ring with a small amount of viscosity.
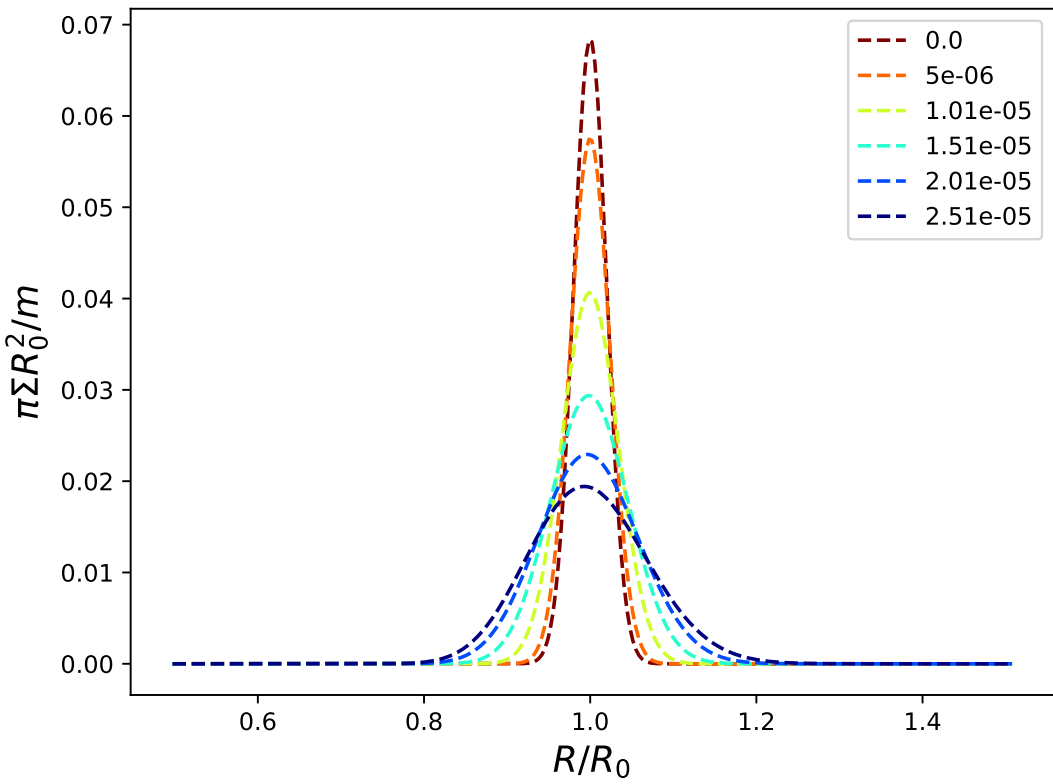
Figure 3.1: A DISCO run of a ring of gas with mass m and surface density Σ located at $R = R_0$ spreads out due to viscous torques. Here the kinematic viscosity is set to 10^{-5} in code units. The legend shows time in units of R_0^2/ν. A movie of this can be found here: https://github.com/zrogoszinski/Dissertation/blob/master/movies/visc_test_density.mp4.

3.3.4 Initial Conditions and Setup

3.3.4.1 Physical Conditions

We model gas accretion onto a forming Jupiter as a two dimensional viscous gaseous disk with an isothermal equation of state and viscosity set by the Shakura & Sunyaev alpha-prescription (Shakura & Sunyaev, 1973). We perform the simulation in cylindrical coordinates in a co-rotating frame centered on Jupiter.

We set the disk's equation of state to be isothermal, where temperature is fixed everywhere and the disk's pressure is a simple function of the sound speed and density. An isothermal equation of state is simple to implement as it depends on the fewest number of parameters, and it implies that the disk is continuously cooling. This is expected, but the cooling rate is entirely artificial. A more realistic disk would instead be modeled with an adiabatic equation of state to account for heat trapped in by the gas, and a cooling function to account for heat radiated by the disk as its vertical scale height expands. Implementing this requires additional badly constrained parameters such as opacity (Ayliffe & Bate, 2009b,a; Bitsch et al., 2013), but this can be explored further in future studies. Zhu et al. (2016) find that the α-viscosity parameter associated with spiral shock waves ranges from 0.001-0.02, so we set $\alpha = 0.01$ as the base case. Furthermore, we set the scale height of the gas in the circumplanetary disk to $H/R = 0.05$ (or a Mach number of $\mathcal{M} = 20$), for a fixed radius in the disk as calculated by Zhu et al. (2016) for an isothermal equation of state. This scale height is also consistent with other circumplanetary

disk simulations (e.g. Szulágyi et al., 2014). Since the temperature is constant throughout the domain, so is the sound speed (0.05 in code units).

We use a zero-gradient boundary condition on all fluid variables at the inner radial boundary, which is considered to be the planet's surface, with an additional restriction that the radial velocity must be inwards. This allows gas and waves to accrete onto the planet while preventing gas from recycling back into the circumplanetary disk. The outer boundary of the simulation is fixed to the initial condition. The layout is log scaled, and the number of radial zones is set to 320 with higher resolution runs at 640 radial zones. The width of the innermost annulus ranges from about 1300 km to 6500 km depending on the size of the inner radius. We use the HLLC Riemann solver to evaluate the flux between cells (Toro et al., 1994), and a total variation diminishing second-order Runge-Kutta time stepper (Gottlieb & Shu, 1998) with a CFL (Courant–Friedrichs–Lewy condition) of 0.3. To ensure stability when solving the fluid equations, the time-step is set to a fraction of the viscous or sound crossing time (whichever is smaller), and that multiplier is the CFL number. For the code to be second-order accurate in space, it needs to calculate the gradient in each cell; however, this is unstable when shocks form because gradients at the shock fronts are infinite. DISCO uses a piecewise linear reconstruction with a generalized minmod slope limiter to correct for slopes near shocks or discontinuities (Duffell, 2016).

3.3.4.2 Surface Density Gap Profile

As the planet accretes matter, it distorts the surrounding gas and creates a gap. The density profile of this gap has been studied and refined over time either numerically or analytically by carefully examining the torque induced by the planet onto the circumstellar disk for a variety of disk properties, such as the planet's mass and viscosity (Varnière et al., 2004; Crida et al., 2006; Duffell & MacFadyen, 2013; Fung et al., 2014; Duffell, 2015; Kanagawa et al., 2017). The surface density gap profile used in this project is the latest iteration by Duffell (2020). Here the surface density profile is given as

$$\Sigma(r) = \frac{\Sigma_0}{1 + \frac{0.45}{3\pi}\frac{\widetilde{q}(R)^2 \mathcal{M}^5}{\alpha}\delta(\widetilde{q}(R))}, \tag{3.19}$$

where

$$\widetilde{q}(R) = \frac{q}{(1 + D^3((R/a)^{1/6} - 1)^6)^{1/3}}, \tag{3.20}$$

$$D = 7\mathcal{M}^{3/2}/\alpha^{1/4}, \tag{3.21}$$

and

$$\delta(q) = \begin{cases} 1 & q < q_{NL} \\ (q/q_{NL})^{-1/2} + (q/q_w)^3 & q > q_{NL}. \end{cases} \tag{3.22}$$

q is the mass ratio of the planet to the central star, $q_{NL} = 1.04\mathcal{M}^3$ is the mass ratio threshold where spiral waves begin to show strong nonlinearity in their evolution, $q_w = 34q_{NL}(\alpha\mathcal{M})^{1/2}$ is the mass ratio when the gap depth scaling changes due to

excitation of torque at the gap walls (Ginzburg & Sari, 2018; Duffell, 2020), R is the distance to the central star, a is the radius of the planet's orbit, and Σ_0 is the central surface density.

We now need to set the initial velocity of the disk. The gap should be approximately in hydrostatic equilibrium before the gas accretes onto the planet. By definition if the gas is in a steady state, then all time derivatives in the fluid equations should be zero. Let's assume axial symmetry, ignore the gravity of the planet as the gas outside the gap is located beyond the planet's Hill radius, and set $\Pi = \Sigma c_s^2/\gamma$ to be the surface pressure where γ is the adiabatic index. To a first approximation we assume the protoplanetary disk is not viscous nor is it accreting, so $v = \sigma_\phi^R = \sigma_R^R = 0$. This is fine if the accretion rate is small. The fluid equations (Equations 3.3–3.5) in the Sun-centered frame are now

$$\partial_t \Sigma = \partial_t \Sigma R^2 \Omega = 0 \tag{3.23}$$

and

$$\frac{1}{R}\partial_R(R\Pi) = R\Sigma\Omega^2 + \frac{\Pi}{R} - \frac{GM_\odot}{R^2}\Sigma. \tag{3.24}$$

Notice that the continuity equation and the angular momentum of the gas are already in a steady state. Since we are assuming a steady state, the first term in the radial momentum equation is zero, and solving for the angular velocity yields

$$\Omega^2 = \frac{GM_\odot}{R^3} - \frac{1}{R}\frac{c_s^2}{\gamma}\frac{1}{\Sigma}\partial_R\Sigma. \tag{3.25}$$

Figure 3.2 shows plots of the gas's radial velocity and density, both inside the gap and out, surrounding a Jupiter mass core. The simulations take place in the planet's rotating frame, and the transformation to this coordinate system can be found in Appendix B. Here the Sun is located to the right at $x = 1$, and the planet orbits counterclockwise. Therefore, since gas located within the planet's orbit moves faster than the planet, the gas ahead of the planet is moving away from the planet while gas behind the planet is moving towards the planet. The situation is flipped for gas located farther away from the planet. The gap profile shown in the bottom plot of Figure 3.2 is consistent with Duffell (2020), however, shocks from the initial inflows onto the planet's surface can yield extremely high density gradients, large velocities, and violent interactions with the inner boundary. While DISCO is meant to handle these singularities, the runtime for such high resolution runs become extremely slow at least when the spiral arms begin to form. We therefore place a small disk around the planet to cushion the inflowing gas from the protoplanet disk, and allow the circumplanetary disk to begin forming. Since the planet must have accreted some matter before the gap profile opens anyway, this placement is not entirely ad hoc.

3.4   Results

3.4.1   Gas Flow Through the Circumplanetary Disk

This project is aimed towards understanding how gas is transported to the planet, and measuring the amount of angular momentum the planet accretes as-
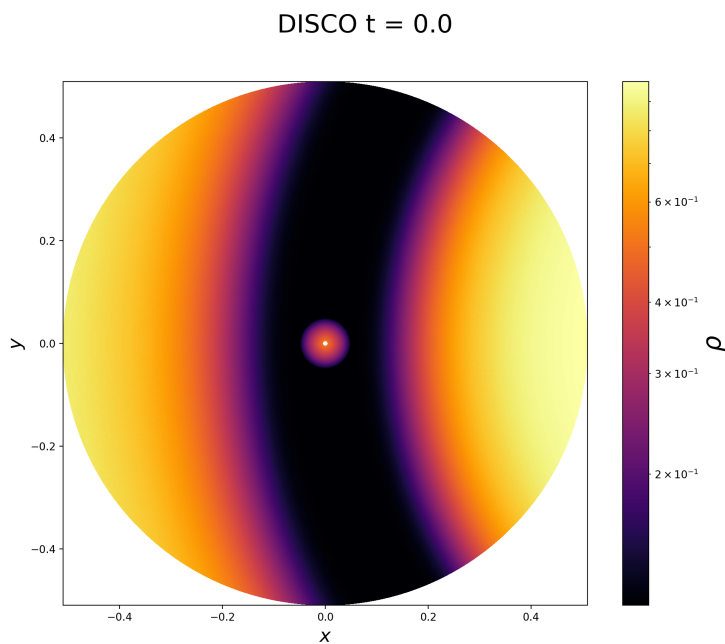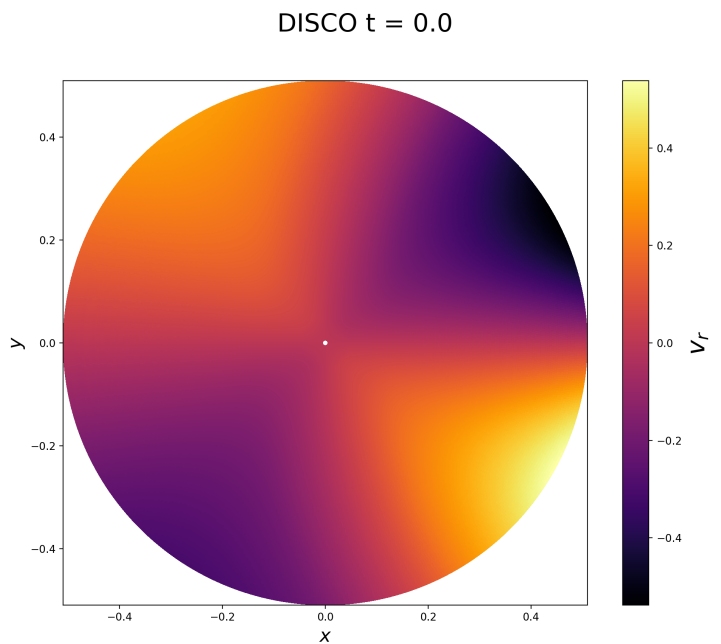
Figure 3.2: (top) A plot of the radial velocity in code units of gas surrounding the central M_J core. (bottom) A plot of the density of the surrounding gas around the core. The Sun is located to the right at $x = 1$.
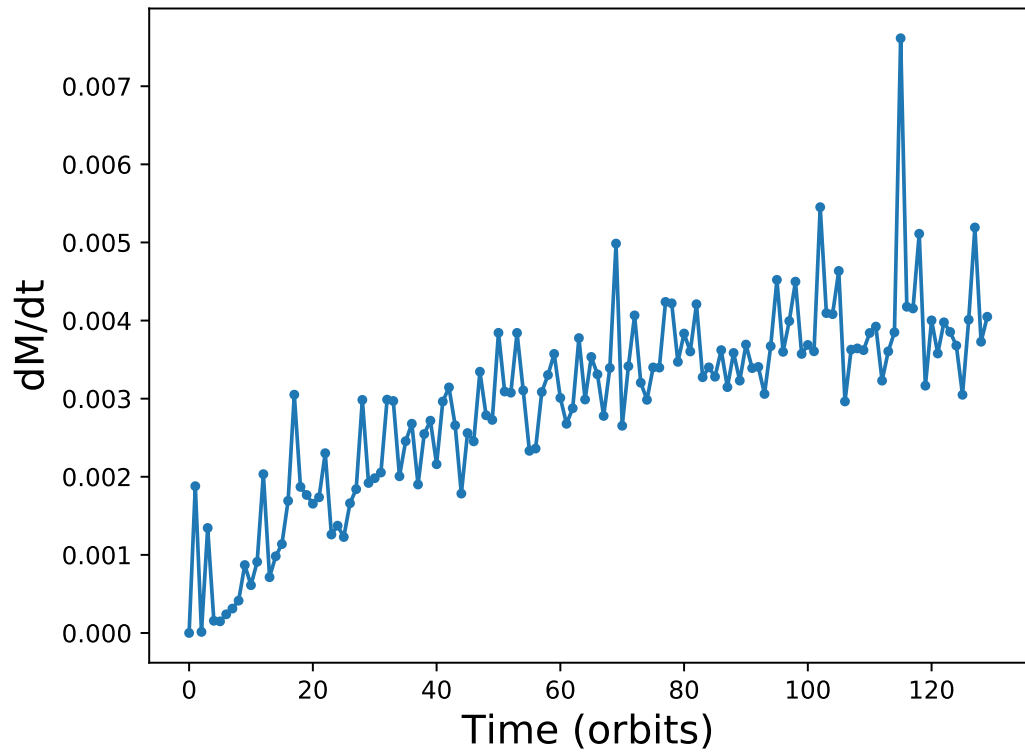
Figure 3.3: An example of the evolution of the mass accretion rate at the inner radius. In this simulation a Jupiter mass core is accreting gas for 130 orbits, and the resolution is set to 640 cells per annulus. The units for the mass accretion rate are in code units.

suming 2D accretion. Unfortunately, we cannot simulate a growing Jupiter at a high resolution within a reasonable time-frame, so instead we assume the growth rate is smooth and take snapshots of the mass accretion rate at different central masses. In the beginning of each simulation we let the gas fall onto an increasingly more massive central mass from the protoplanetary disk, so at least in the beginning of each run the mass accretion rate is highly variable. We therefore need to let each simulation evolve until the system reaches a steady state, and then measure the mass accretion rate at the inner boundary. Figure 3.3 shows the evolution of the mass accretion rate at the inner radius for one of the more expensive higher mass simulations, and, although the evolution of the mass accretion rate is not smooth, the average $\dot{M}$ stabilizes near 130 orbits. This particular run has gas accreting onto a Jupiter mass core with the resolution set to 640 radial zones per annulus, and it took 40,000 CPU-hours to complete.

Here we run simulations for a growing Jupiter-like planet starting at a tenth of a Jupiter mass because at around this point the planet begins to undergo runaway gas accretion (Lissauer et al., 2009). The top figures of Figure 3.4 show the final checkpoint for gas accreting onto this small core, and the bottom figures show gas accreting onto a Jupiter mass core. In both cases the inner radius is set to $10R_J$ because the planet is initially hot and its size expands by about this amount (Bodenheimer & Pollack, 1986; Lissauer et al., 2009). Also, for a more practical reason, it is the smallest value where the simulation can finish on reasonable timescales at high central masses and at the desired resolution of 640 cells per annulus. DISCO can still produce relatively inexpensive simulations for smaller sizes and masses at a

(a)

(b)

(c)

(d)
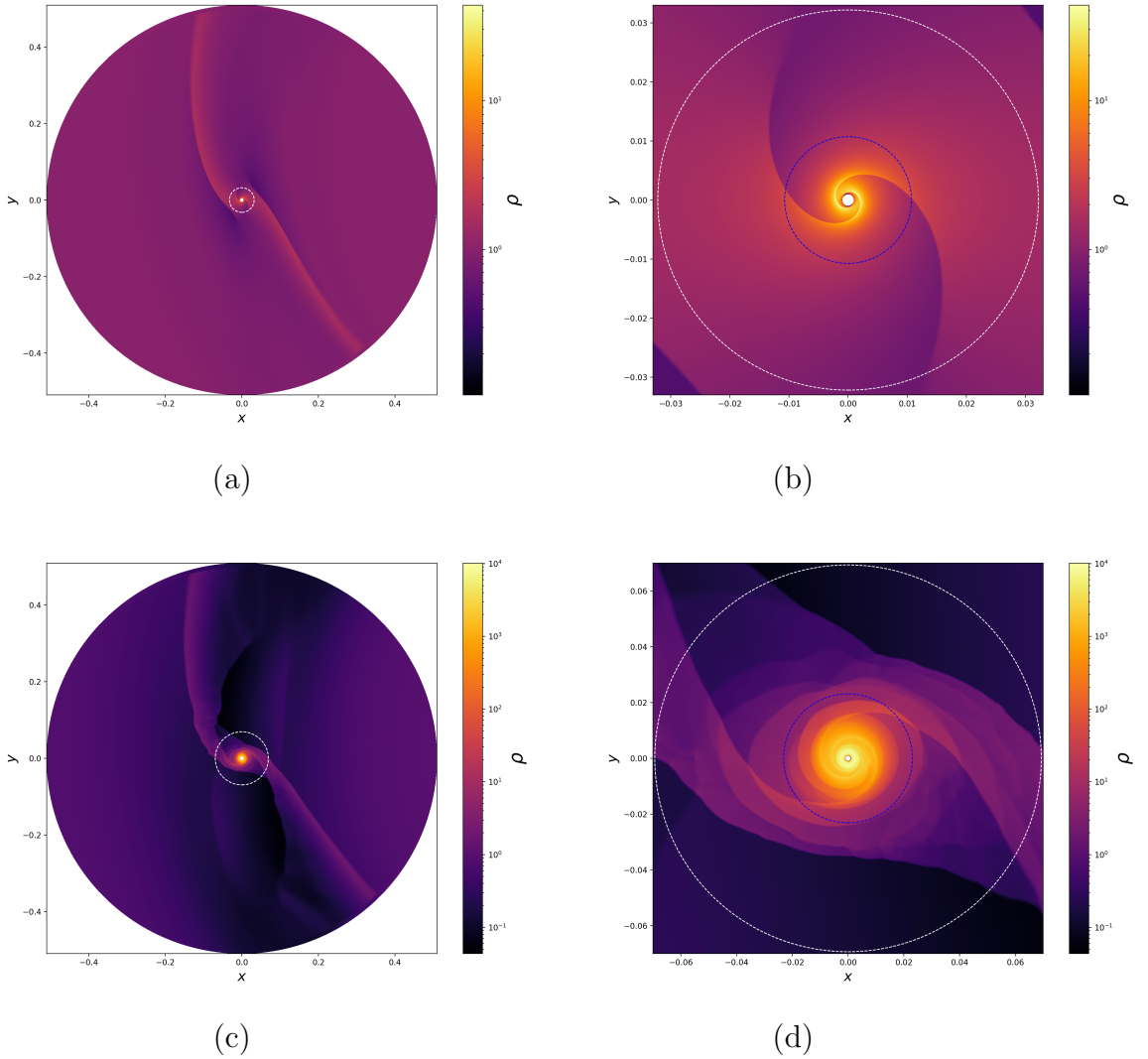
Figure 3.4: (a) A plot showing gas accreting onto a $0.1\,M_J$ core at a high resolution of 640 cells per annulus. Here the inner radius is set to 10 Jupiter radii. The white dashed circle is the planet's hill radius. (c) The same simulation but with a M_J core. (b) & (d) Zoomed into the planet's Hill radius. The blue dashed circle is a third of the planet's Hill radius. Movies of both runs can be found here: `https://github.com/zrogoszinski/Dissertation/blob/master/movies/`

lower resolution, and we will discuss these later. Note that in the planet's reference frame it is the Coriolis force that places the gas on a counter-clockwise orbit, and so all gas giants initially spin in the same orientation as their orbit (prograde).

Figures 3.5 and 3.6 show the corresponding fluid variables, azimuthally averaged around the disk. Notice that the gas's density and pressure begins to increase once it crosses the planet's Hill radius, and the gas also begins to circularize when the gas crosses $\sim R_{\mathrm{Hill}}/3$. This is in line with numerical estimates of a circumplanetary disk's outer boundary around a Jupiter analogue (Quillen & Trilling, 1998; Ayliffe & Bate, 2009a, 2012; Machida, 2009; Ward & Canup, 2010; Martin & Lubow, 2011; Tanigawa et al., 2012; Szulágyi et al., 2014; Zhu et al., 2016), though in these cases they explored three-dimensional models. Machida (2009) argue that the peak surface density is due to a centrifugal barrier, where the centrifugal force balances the planet's force of gravity. This is around the pericenter of the gas's trajectory after crossing through the planet's Lagrange point. Gas is thought to pile up here and then spread once the pressure increases. Using analytic and numerical estimates of a protoplanetary system's specific angular momentum (Lissauer, 1995; Machida et al., 2008), Machida (2009) measure a centrifugal radius around Jupiter of $\sim 0.03 R_{\mathrm{Hill}}$, which is consistent with Figure 3.6 but not Figure 3.5. Here the centrifugal radius is smaller than the inner boundary, so in-falling gas is simply piling up near the planet's surface. If the inner boundary instead decreased to about the radius of Jupiter, then the centrifugal radius lies near the peak of the gas's surface density. To better understand how the gas is transported, though, we must break down the angular momentum fluxes in the disk.
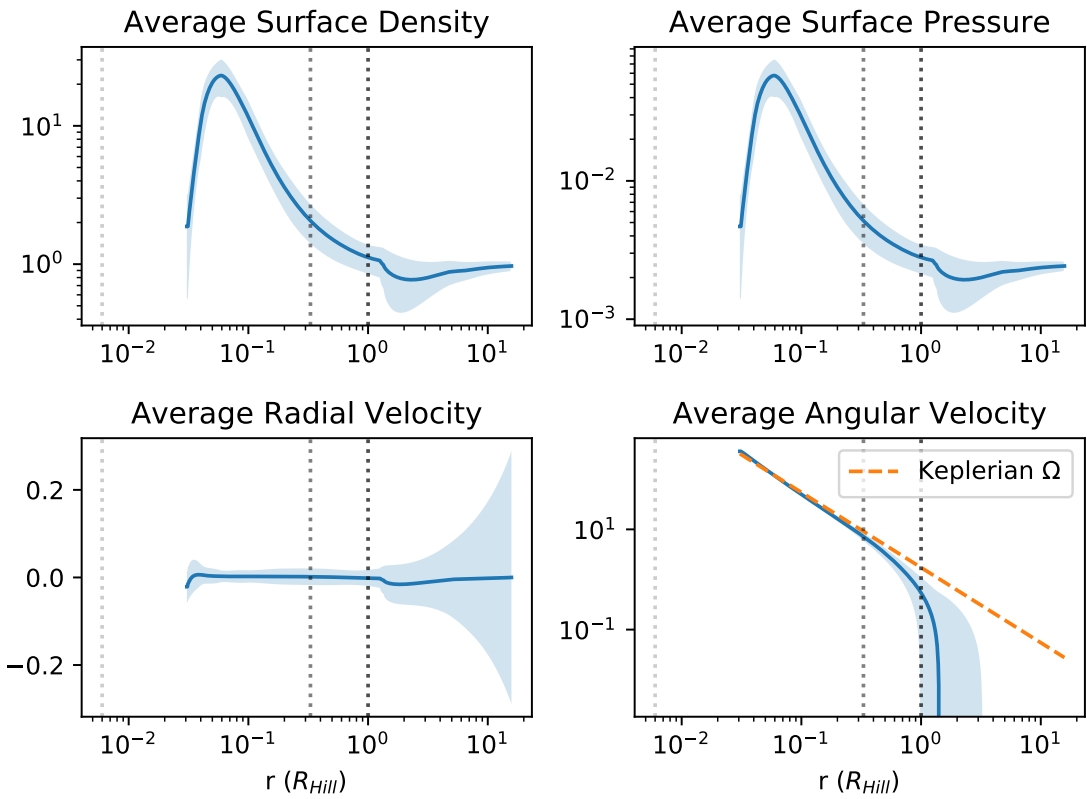
Figure 3.5: The average density, pressure, radial velocity, and angular velocity (in code units) of gas accreting onto a tenth of a Jupiter mass core as a function of Hill radii in the rotating frame. Here the planet's Hill radius (black dotted line) is 0.032 times the distance to the Sun. The gray dotted line is a rough estimate of the disk's edge ($\sim R_{\text{Hill}}/3$), and the light gray dotted line is around the centrifugal radius.
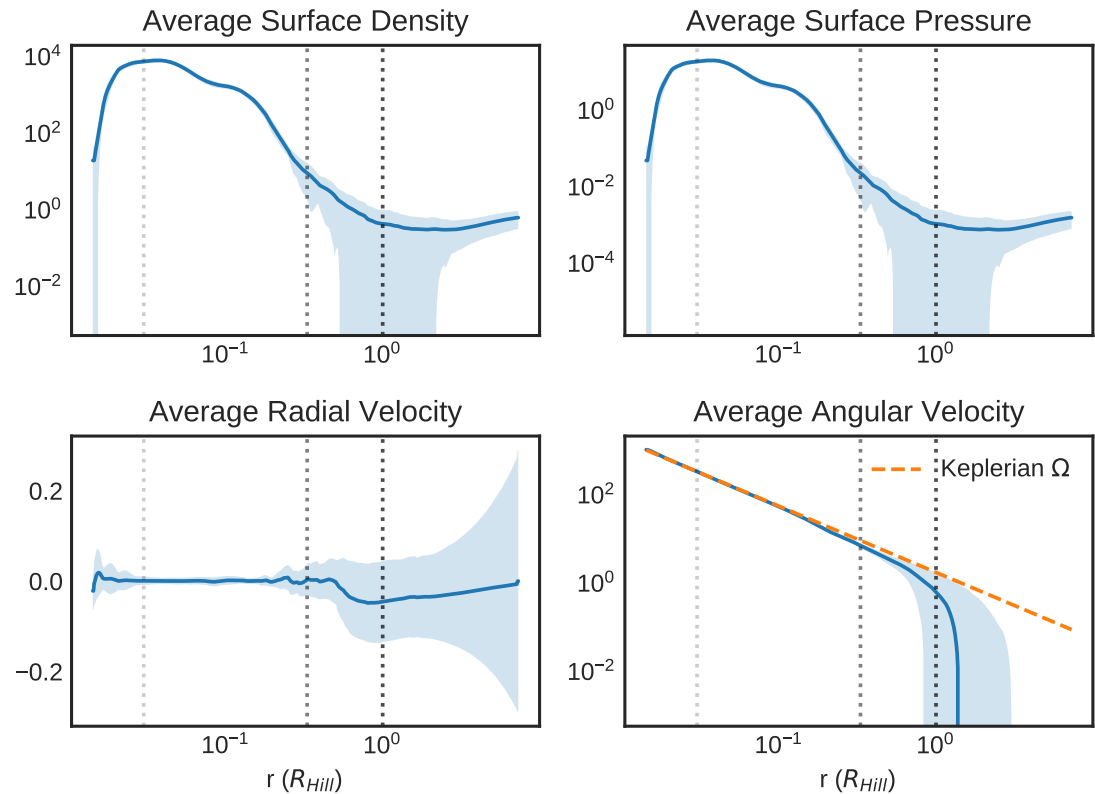
Figure 3.6: The average density, pressure, radial velocity, and angular velocity (in code units) of gas accreting onto a Jupiter mass core as a function of Hill radii in the rotating frame.

Figures 3.7 and 3.8 show the corresponding angular momentum fluxes for gas accreting onto a $0.1\,M_J$ and $1\,M_J$ core. Gas accreting onto a small core reaches a steady state in only a few orbits. Both the external torque at large distances and $F_{\dot{M}}$ are negative, so angular momentum spirals inwards towards the planet. The outwards flux, which allows accretion to take place, is driven by spiral waves (Reynolds flux), which dominates over the viscous flux by two orders of magnitude. Once the gas reaches the planet, though, the mean angular momentum flux is the only source of angular momentum and spins up the planet, as expected (Figure 3.9).

The accreting gas is more dynamic when the core is larger because the infalling speeds are faster. This is especially noticeable in the region where the gas begins to circularize. In this case, the gas becomes quite variable, partly because the Reynolds flux is stronger by about a factor of 100. The viscous flux is also equally larger, and it peaks near the centrifugal barrier and the edge of the disk. Both are positive so they drive angular momentum away from the planet, but $F_{\dot{M}}$ changes sign showing high variability in the flow. The external torque is low below $0.1\,R_{\mathrm{Hill}}$ but becomes comparable in magnitude to the Reynolds flux at large distances. We ran this simulation for 130 orbits, or about 1500 years, and the system has yet to reach a true steady state. Since the duration of runaway gas accretion is around 10,000 years (Lissauer et al., 2009), we suspect that gas accretion will never reach a steady state once the planet's mass reaches close to Jupiter's. When the gas approaches the planet's surface, though, the fluxes are more well behaved (Figure 3.10) with bulk flow still dominating gas transport near the inner boundary.
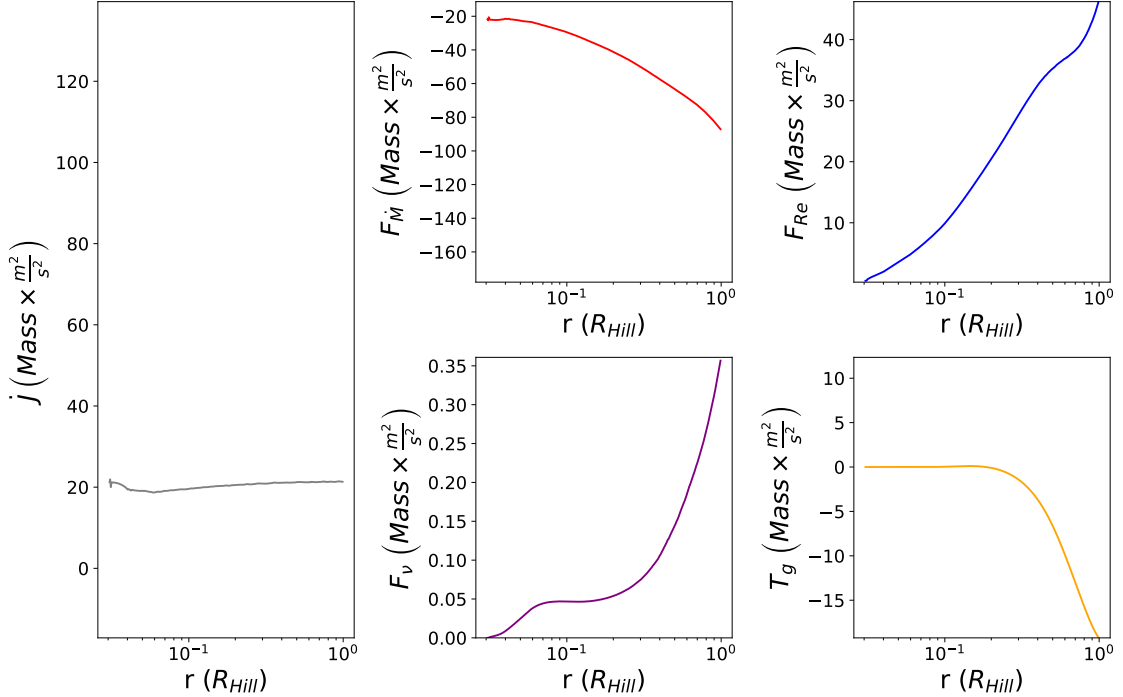
Figure 3.7: Final snapshots of the time-averaged angular momentum fluxes of gas accreting onto a 0.1 Jupiter mass core. The unit for mass in calculating the flux is arbitrary as it will be divided out when solving for the accreted specific angular momentum. The full movie can be found here: `https://github.com/zrogoszinski/Dissertation/blob/master/movies/Multiplot_small.mp4`
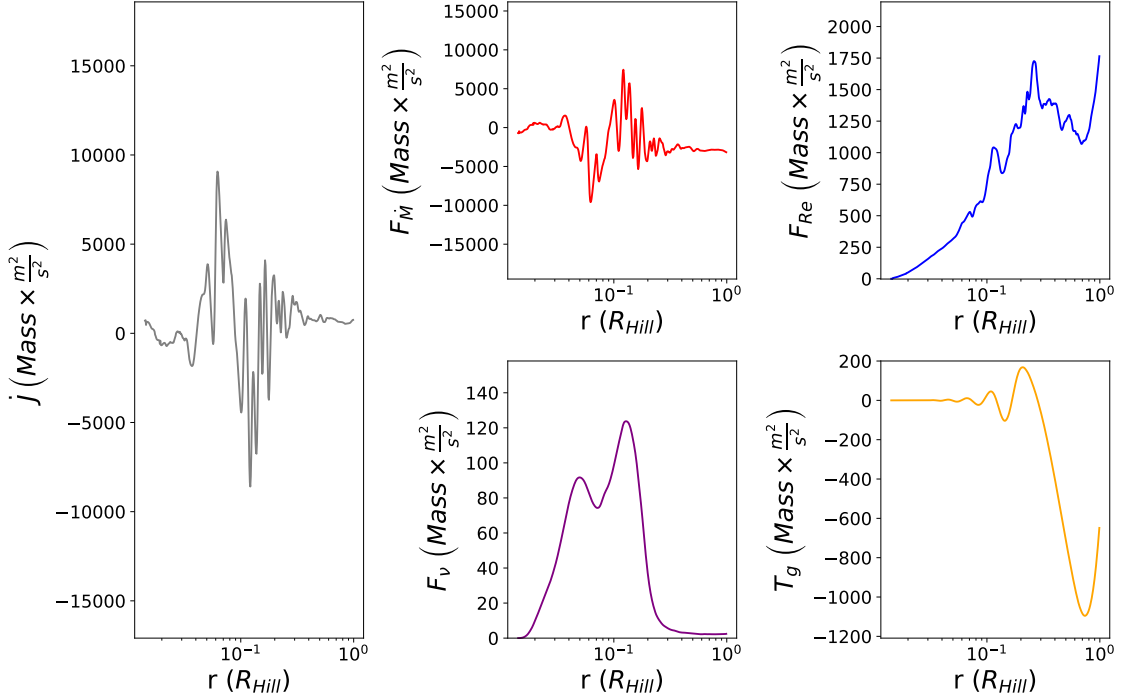
Figure 3.8: Final snapshots of the time-averaged angular momentum fluxes of gas accreting onto a Jupiter mass core. The layout is the same as in Figure 3.7. The full movie can be found here: https://github.com/zrogoszinski/Dissertation/blob/master/movies/Multiplot_large.mp4
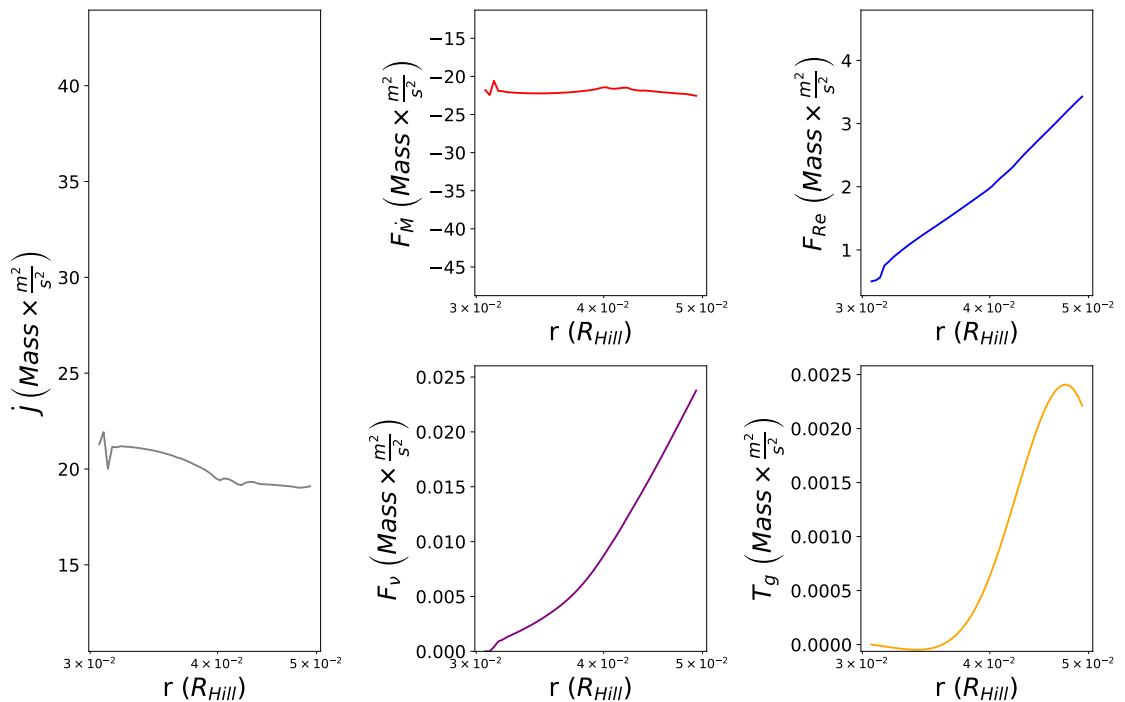
Figure 3.9: Figure 3.7 but zoomed in near the inner boundary.
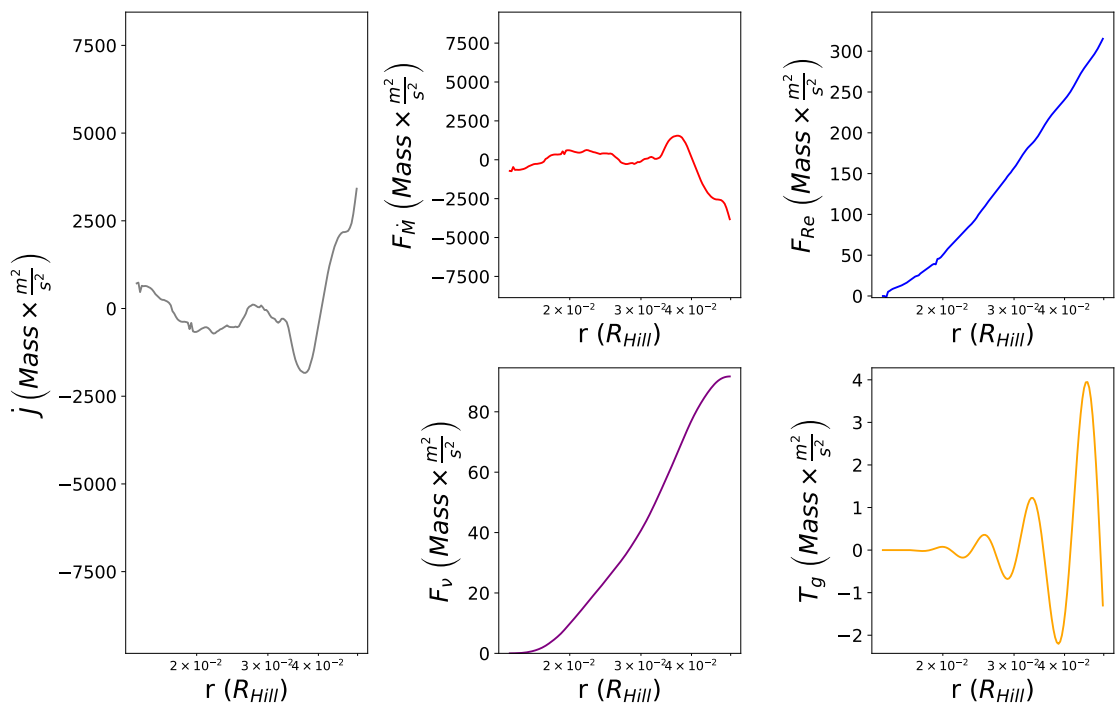
Figure 3.10: Figure 3.8 but zoomed in near the inner boundary.

3.4.2 Spinning Up a Planet

Eventually the gas spirals inwards until it reaches the planet where it deposits all of its angular momentum. If we assume the planet accretes gas from a thin disk, and the planet is the only angular momentum sink, then the analytic model for the specific angular momentum growth rate is simply

$$\frac{dJ}{dm} = \sqrt{GMR},\tag{3.26}$$

where M is the mass of the planet and R is the planet's radius. As such, we should observe the planets to be spinning near the Keplerian velocity of the innermost orbit.

Figure 3.11 shows the average specific angular momentum accreted for a growing planet. The dashed lines are the model for varying inner radii, and the data fits the model exceptionally well. The planet's corresponding spin rate for an inner radius of 10 times the planet's radius is about 0.3 hours per rotation, or ten times faster than break-up. We were not capable of simulating gas accreting onto larger mass cores at smaller inner disk radii because the simulations would be too expensive; however, we suspect that they should follow the same curve as the $10\,R_J$ case. If the inner boundary was set to Jupiter's radius, then the corresponding spin rate after accreting a Jupiter's mass worth of gas is about 1 hour. Therefore, if we expect the planet to be spinning faster than its break-up velocity, then it should be shedding mass well before it reaches its final state. Since that is not the case and we

observe gas giants to be spinning slower than break-up, there must be some other mechanism responsible for removing excess angular momentum.

3.5 Conclusion and Future Work

As expected, a 2D gas accretion model implies that gas giants should be spinning close to their break-up velocities, which is unlike what we observe today. In this case the planet is the only angular momentum sink, which is not true if we extend the model to three dimensions as polar inflow could allow gas to escape through the planet's mid-plane and (Tanigawa et al., 2012; Szulágyi et al., 2014; Batygin, 2018). This would be the first future development, followed by implementing a proper radiative cooling function, and then including the effects of magneto-hydrodynamic effects. While 3D magneto-hydrodynamics is a promising solution for gas giant formation (Batygin, 2018), it is worth checking to see how well this model applies at lower masses with ice giants.

This project's aim is to provide a baseline for future development to modeling the evolution of planetary spins. From Figure 3.11 it is clear that ice giants should also be spinning too fast if modeled with this simple 2D gas accretion flow. Furthermore, gas simply piles up near the planet's surface instead of also spreading out in contrast to better developed circumplanetary disk models (Lissauer et al., 2009; Szulágyi et al., 2018). Improvements to modeling gas accretion onto planets before they undergo runaway gas accretion and tailored specifically to ice giants could certainly provide further insights that could explain Uranus's and Neptune's
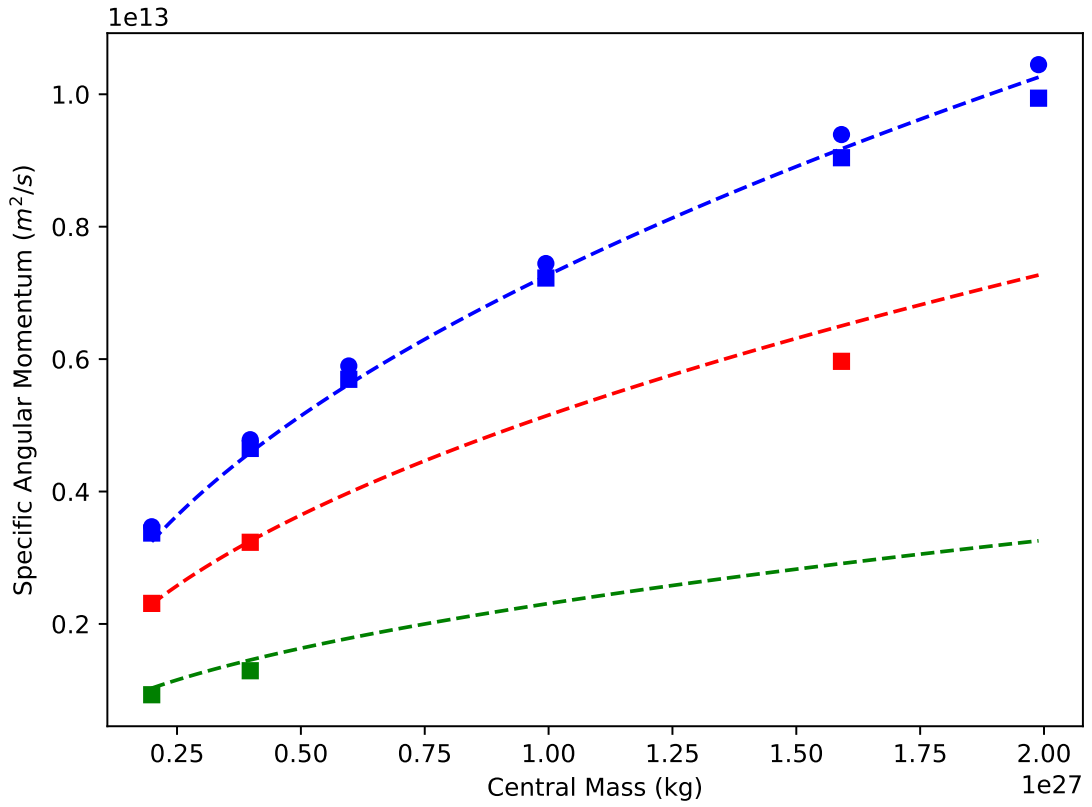
Figure 3.11: The average specific angular momentum at the disk's inner radius verses the planet's mass. The squares are the results from the simulation, the circles are the same simulations but at double the resolution, and the dashed lines are the models. Blue have the inner disk radius at $\sim 10 R_J$, red have the inner disk radius at $\sim 5 R_J$, and green have the inner disk radius at $\sim R_J$. The red square $(M_{\text{core}} = 0.8 \, M_J, \, R_{\text{in}} \sim 5 R_J)$ probably falls under the model because the resolution is too low.

distinguishing characteristics (Podolak & Helled, 2012; Helled et al., 2020; Helled & Fortney, 2020). For instance, understanding how exactly particles accrete onto and are transported inside the planet, under the constraint of the planets' spin evolution, could illuminate how the planet's interior is structured, which in turn could provide some insight to the evolution of the planets' temperatures.

Chapter 4:   Placing Uranus Closer to the Sun

In Chapter 2 we showed that a spin-orbit resonance that can tilt Uranus by more than $40°$ can improve the likelihood that a subsequent collision would reproduce the planet's current spin state. This would also halve the mass and number of required impactors to tilt the planet the rest of the way to $98°$. Uranus's current spin precession frequency, however, is too slow to match any of the planets' orbital precession rates, but that may not have been the case in the past. Boué & Laskar (2010) posit that a resonance is possible if Uranus harbored a moon large enough so that the planet's spin axis could precess sufficiently fast to resonate with its own orbit. This moon would, however, have to be larger than all known moons (between the mass of Ganymede and Mars), have to be located far from Uranus (≈ 50 Uranian radii), and then have to disappear somehow perhaps during planetary migration. In this chapter we investigate another possibility by placing Uranus closer to the Sun where tidal forces are stronger and precession timescales are shorter. Here Uranus, placed between Jupiter and Saturn, would resonate with a Neptune-like planet located beyond Saturn and tilt over as Neptune migrates outwards.

5 au   7 au   9 au   24 au
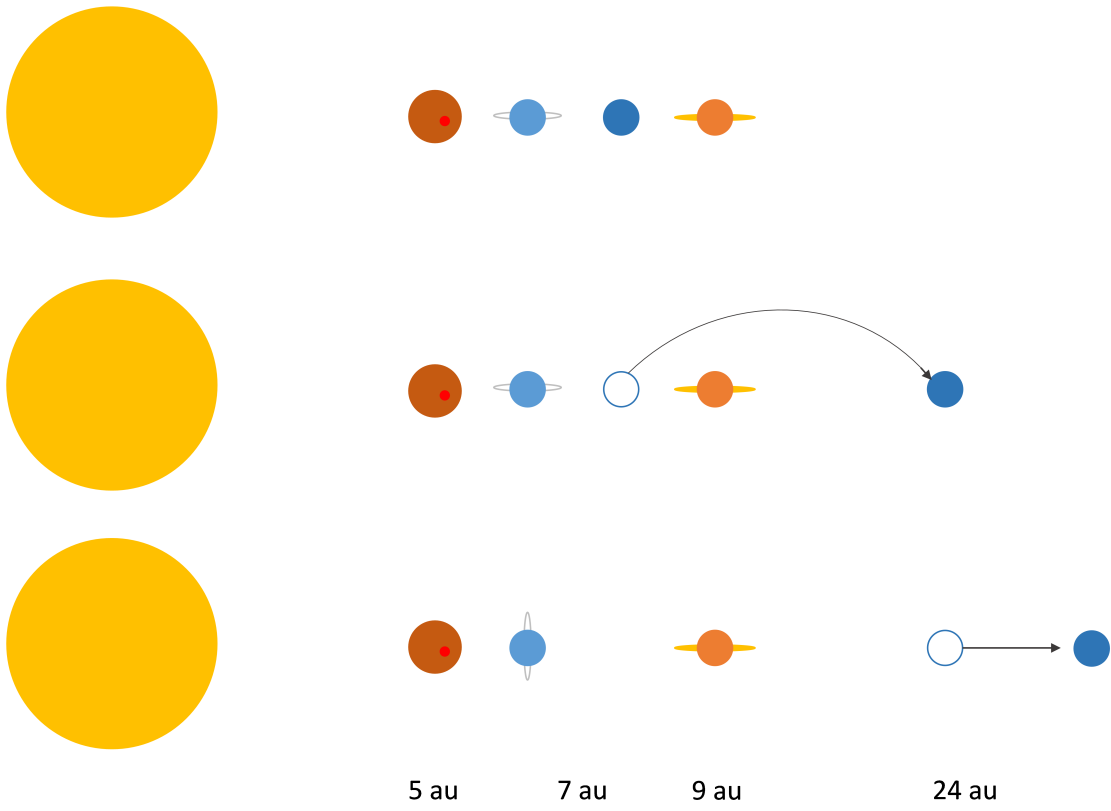
Figure 4.1: An illustration of how Uranus can be tilted over if placed closer to the Sun and if it resonates with an ice giant like Neptune that first scatters outwards. Not to scale.

4.1 Initial Conditions

Recall from Chapter 1.3 that gravitational torques from the Sun on an oblate planet cause the planet's spin axis to precess backwards, or regress, about the normal to its orbital plane (Colombo, 1966). Also, gravitational perturbations from the other planets cause a planet's inclined orbit to regress around the Sun. A match between these two precession frequencies results in a secular spin-orbit resonance (Equation 1.1).

The precession rate of Uranus's spin axis can be derived by considering the torques of the Sun and the Uranian moons on the planet's equatorial bulge. Following Colombo (1966), if $\hat{\sigma}$ is a unit vector that points in the direction of the total angular momentum of the Uranian system, then:

$$\frac{d\hat{\sigma}}{dt} = \alpha(\hat{\sigma} \times \hat{n})(\hat{\sigma} \cdot \hat{n}) \tag{4.1}$$

where $\hat{n}$ is a unit vector pointing in the direction of Uranus's orbital angular momentum, α is the spin precession rate near zero degree tilts, and t is time. Uranus's axial precession period is therefore:

$$T_\alpha = \frac{2\pi}{\alpha \cos \epsilon}, \tag{4.2}$$

where ϵ is the obliquity, and $\cos \epsilon = \hat{\sigma} \cdot \hat{n}$. The precession frequency near zero obliquity, α, incorporates the torques from the Sun and the moons on the central

body (Tremaine, 1991):

$$\alpha = \frac{3n^2}{2} \frac{J_2(1 - \frac{3}{2}\sin^2\theta_p) + q}{K\omega\cos\theta_p + l}. \tag{4.3}$$

Here $n = (GM_\odot/r_p^3)^{1/2}$ is the orbital angular speed of the planet, G is the gravitational constant, $M_\odot$ is the Sun's mass, r_p is the Sun-planet distance, ω is the planet's spin angular speed, J_2 is its quadrupole gravitational moment, and K is its moment of inertia normalized by $M_p R_p^2$. For Uranus today, $M_p = 14.5\,M_\oplus$, $R_p = 2.56 \times 10^9$ cm, $K = 0.225$ and $J_2 = 0.00334343$.[1] The parameter

$$q \equiv \frac{1}{2}\sum_i (M_i/M_P)(a_i/R_P)^2 \tag{4.4}$$

is the effective quadrupole coefficient of the satellite system, and

$$l \equiv R_P^{-2}\sum_i (M_i/M_P)(GM_P a_i)^{1/2} \tag{4.5}$$

is the angular momentum of the satellite system divided by $M_p R_p^2$. The masses and semi-major axes of the satellites are M_i and a_i, $\cos\theta_p = \hat{s}\cdot\hat{\sigma}$ and $\cos\theta_i = \hat{l}_i\cdot\hat{\sigma}$, where $\hat{s}$ is the direction of the spin angular momenta of the central body and $\hat{l}_i$ is the normal to the satellite's orbit (Tremaine, 1991). Note that $M_i \ll M_p$ where M_p is the mass of the planet and, since the satellite orbits are nearly equatorial, we can take $\theta_p = \theta_i = 0$.

---

[1] All physical values of the solar system are courtesy of NASA Goddard Space Flight Center: http://nssdc.gsfc.nasa.gov/planetary/factsheet/

Torques from the main Uranian satellites on the planet contribute significantly to its precessional motion, while those from other planets and satellites can be neglected. We therefore limit ourselves to Uranus's major moons—Oberon, Titania, Umbriel, Ariel, and Miranda. We find $q = 0.01558$ which is about 4.7 times larger than Uranus's J_2, and $l = 2.41 \times 10^{-7}$ which is smaller than $K\omega$ by about a factor of 100. So from Equation 4.3, the effective quadrupole coefficient of the satellite system plays a much more significant role in the planet's precession period than the angular momentum of the satellite system. At its current obliquity, $\epsilon = 98°$, Uranus's precession period is about 210 million years (or $\alpha = 0.0062$ arcsec yr^{-1}), and reducing Uranus's obliquity to $0°$ results in a precession period 7.2 times faster: 29 million years (or $\alpha = 0.045$ arcsec yr^{-1}). This pole precession rate is much longer than any of the giant planets' fundamental frequencies (Murray & Dermott, 1999), but it can be sped up to ≈ 2 Myr by placing Uranus at around 7 AU. This is just fast enough for Uranus to resonate with a similar planet—Neptune—located beyond Saturn (Figure 4.1).

Placing Uranus's orbit between those of Jupiter and Saturn is not entirely ad hoc. Thommes et al. (1999, 2002, 2003) argue that at least the ice giants' cores might have formed between Jupiter and Saturn (4-10 au), as the timescales there for the accretion of planetesimals through an oligarchic growth model, when the large bodies in the planetary disk dominate the accretion of surrounding planetesimals, are more favorable than farther away. The Nice model (Gomes et al., 2005; Morbidelli et al., 2005; Tsiganis et al., 2005) places Uranus closer to the Sun but beyond Saturn for similar reasons; however, having the ice giants form between Jupiter and Saturn is

not inconsistent with the Nice model. If Uranus and Neptune were indeed formed between Jupiter and Saturn and later ejected sequentially, then a secular spin-orbit resonance between Uranus and Neptune is possible. Note that such close encounters would not yield any significant obliquity excitations because the perturbing torque is too weak as it depends on the planet's gravitational quadrupole moment (Lee et al., 2007). A related possibility that is also sufficient for these purposes is if the planets were formed from pebble accretion, as the pebble isolation mass can be similar everywhere in the outer solar system (Lambrechts et al., 2014) allowing Neptune to be initially formed beyond Saturn and Uranus between Jupiter and Saturn. In the following, we assume that Uranus is fully formed with its satellites located near their current configurations to derive the spin axis precession rate. We also include only the known giant planets because adding a third or fourth ice giant, as suggested by the Nice model to better reproduce the solar system (Nesvorný, 2011; Batygin et al., 2012; Nesvorný & Morbidelli, 2012), would increase the planet's orbital precession rates and make it more difficult for Uranus to obtain a spin-orbit resonance. If this configuration can tilt Uranus reasonably, then we could begin to introduce more giant planets to the model.

4.2   Method

Calculating Uranus's obliquity evolution requires tracking the planets' orbits while also appropriately tuning Neptune's nodal precession rate. We use the HN-Body Symplectic Integration package (Rauch & Hamilton, 2002) to track the motion

of bodies orbiting a central massive object using symplectic integration techniques based on two-body Keplerian motion, and we move Neptune radially with an artificial drag force oriented along the velocity vector using the package HNDrag. These packages do not follow spins, so we have written an integrator that uses a fifth-order Runge-Kutta algorithm (Press et al., 1992) and reads in HNBody data to calculate Uranus's axial orientation due to torques applied from the Sun (Equation 4.1). For every time step, the integrator requires the distance between the Sun and Uranus. Since HNBody outputs the positions and velocities at a given time frequency different from the adaptive step that our precession integrator uses, calculating the precessional motion requires interpolation. To minimize interpolation errors, we use a torque averaged over an orbital period which is proportional to $\langle r_p^{-3} \rangle = a_p^{-3}(1 - e_p^2)^{-\frac{3}{2}}$, where a_p is the planet's semi-major axis and e_p is its eccentricity. This is an excellent approximation since Uranus's orbital period is $10^5 - 10^6$ times shorter than its precession period. We tested the code for a two-body system consisting of just the Sun and Uranus and recovered the analytic result for the precession of the spin axis (Figure 4.2).

For these simulations we place Jupiter and Saturn near their current locations (5 au and 9 au respectively), Uranus at 7 au, and Neptune well beyond Saturn at 17 au. Leaving Uranus in between the two gas giants for more than about ten million years is unstable (Lecar & Franklin, 1973; Franklin et al., 1989; Gladman & Duncan, 1990; Holman & Wisdom, 1993), but eccentricity dampening from remnant planetesimals can delay the instability. Scattering between Uranus and the planetesimals provides a dissipative force that temporarily prevents Uranus from being
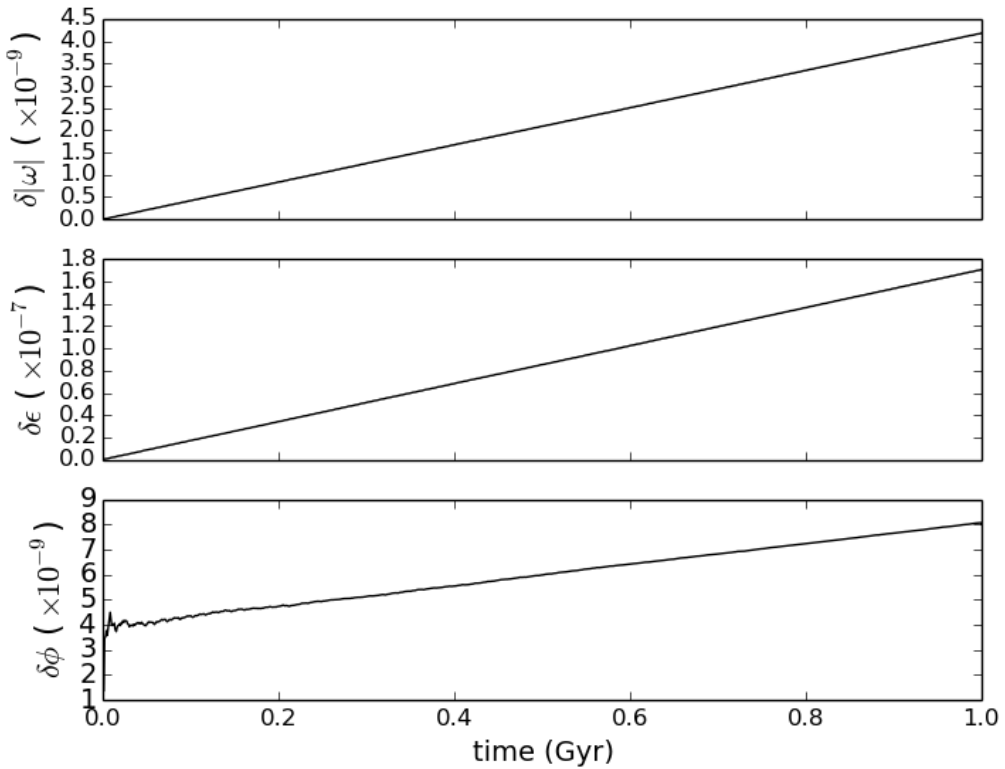
Figure 4.2: The calculated relative error of three quantities describing Uranus's spin axis. Here ω is the unit vector pointing in the direction of Uranus's spin axis. ϵ is the planet's obliquity and ϕ is the planet's spin longitude of the ascending node. All quantities should be constant with time as the system only contains the Sun and Uranus. Numerical errors at the levels shown here are sufficiently low for our purposes.

ejected, and we mimic this effect by applying an artificial force to damp Uranus's eccentricity. We apply the force in the orbital plane and perpendicular to the orbital velocity to damp the eccentricity while preventing changes to the semi-major axis (Danby, 1992). With Uranus's orbit relatively stable, we then seek a secular resonance between its spin and Neptune's orbit.

4.3   Capturing into a Spin-Orbit Resonance

Recall that capturing into a spin-orbit resonance also requires the two angular momentum vectors, the planet's spin axis and an orbital pole, and the normal to the invariable plane be co-planar. Equilibria about which the resonance angle librates are called "Cassini States" (Colombo, 1966; Peale, 1969; Ward, 1975; Ward & Hamilton, 2004), and there are multiple vector orientations that can yield a spin-orbit resonance. In this case, the resonance angle, Ψ, librates about Cassini State 2, where Uranus's spin axis and Neptune's orbital pole precess on opposite sides of the normal to the invariable plane, because it is a stable solution that can excite obliquities.

As Neptune migrates outwards away from the Sun, its nodal precession frequency slows until a resonance is reached with Uranus's spin precession rate. If the consequence of the resonance is that Uranus's obliquity increases (Ward, 1974), then its spin precession frequency slows as well (Equation 4.3) and the resonance can persist. The time evolution of the resonance angle and obliquity are given by

(Hamilton & Ward, 2004):

$$\dot{\Psi} = -\alpha \cos \epsilon - g \cos I \tag{4.6}$$

$$\dot{\epsilon} = g \sin I \sin \Psi \tag{4.7}$$

where g is the negative nodal precession rate, and I is the amplitude of the incli-
nation induced by Neptune's perturbation on Uranus's orbit. If Neptune migrates
outward slowly enough, then $\dot{\Psi}$ is small and the two planets can remain in resonance
nearly indefinitely.

Figure 4.3 shows Uranus undergoing capture into a spin-orbit resonance when
Neptune crosses $\sim$24 au en route to its current location at 30 au. Here Neptune's
migration rate is set to 0.045 au/Myr, which is within the adiabatic limit — the
fastest possible rate to generate a capture with $\epsilon_i \approx 0°$, and is compatible with
orbital migration timescales (10-100 Myr) for scattering through a planetesimal
disk (Hahn & Malhotra, 1999, 2005). The adiabatic limit occurs when Neptune's
migration takes it across the resonance width in about a libration time, which is just
$2\pi/w_{lib}$ with $w_{lib} = \sqrt{-\alpha g \sin \epsilon \sin I}$ (Hamilton & Ward, 2004). Just as slow changes
to the support of a swinging pendulum do not alter the pendulum's motion, gradual
changes to Neptune's orbit do not change the behavior of the libration. However, if
Neptune's migration speed exceeds the adiabatic limit, then the resonance cannot
be established. The top panel of Figure 4.3 shows Uranus tilting to 60° in 150 Myrs
when Neptune reaches its current location, and all the way to 90° in 600 Myr if we
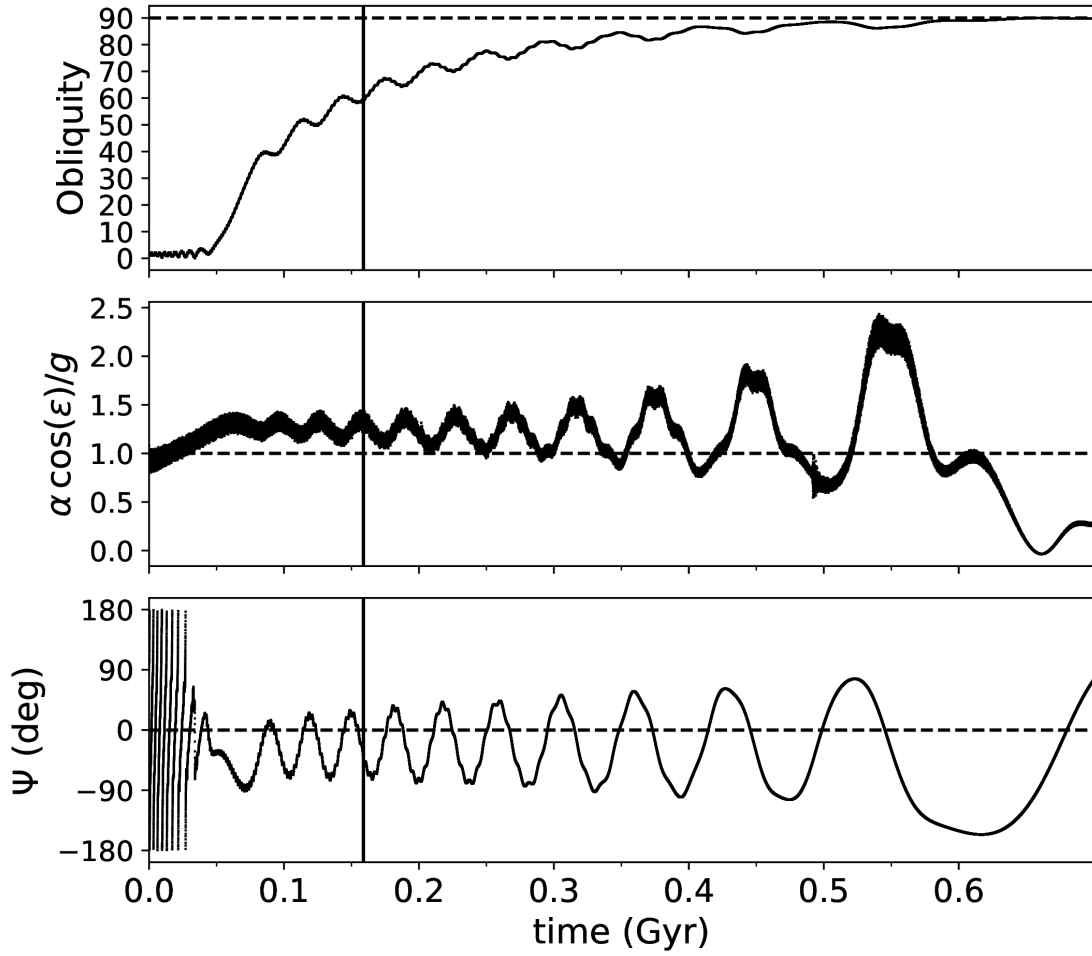
Figure 4.3: A resonance capture. The top panel shows Uranus's obliquity evolution over time. The middle panel shows the evolution of the precession frequencies with the dashed line indicating the resonance location, and the bottom panel shows the resonance angle (Ψ). The solid vertical line at $t \approx 150$ Myr indicates when Neptune reaches it current location at 30 au. In this simulation resonance is established at $t = 0.05$ Gyr when Neptune is at ≈ 24 au, and it breaks at $t = 0.85$ au with Neptune at ≈ 120 au. Stopping Neptune at 30 au, we find that this capture could account for perhaps half of Uranus's extreme tilt. Here, Uranus is located at $a_U = 7$ au, with its current equatorial radius. Neptune's inclination is set to twice its current value at $i_N = 4°$ which strengthens the resonance.
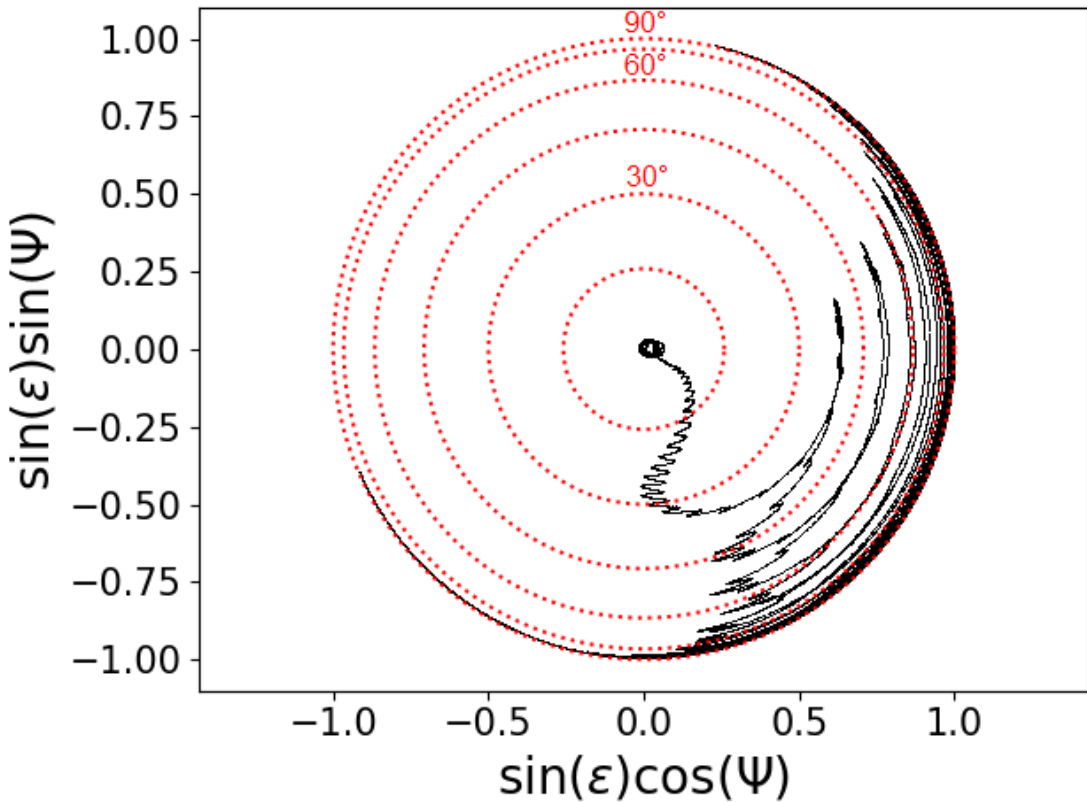
Figure 4.4: The corresponding polar plot to Figure 4.3 where Neptune is migrating well within the adiabatic limit. The short period oscillations here are at the pole precession rate while the longer oscillations are the librations about the equilibrium point which itself is moving to higher obliquities (to the right). The red dotted circles represents points of constant obliquity in increments of 15°.

allow Neptune to continue outwards. Planets migrate by scattering planetesimals, which can decrease inclinations; accordingly, we optimistically assumed an initial value for Neptune's inclination at twice its current value. Because we have increased Neptune's inclination and moved Neptune out as fast as possible and yet still allowed capture, one hundred fifty million years represents a rough lower limit to the time needed to tilt Uranus substantially.

The bottom panel of Figure 4.3 and Figure 4.4 both show the evolution of the resonance angle, and the angle oscillates with a libration period of about 30 Myr about the equilibrium point. The libration period increases as ϵ increases in accordance with Equation 4.2. The noticeable offset of the equilibrium below $\Psi = 0°$ in Figures 4.3 and 4.4 is due to the rapid migration of Neptune (Hamilton & Ward, 2004):

$$\Psi_{eq} = \frac{\dot{\alpha}\cos\epsilon + \dot{g}\cos I}{\alpha g \sin\epsilon \sin I}. \tag{4.8}$$

Recall that g, the nodal precession frequency, is negative, α is positive, and as Neptune migrates away from the Sun $\dot{g}$ is positive. Since α is constant, $\dot{\alpha} = 0$, and so Ψ_{eq} is slightly negative in agreement with Figure 4.3. We conclude that although a spin-orbit resonance with Neptune can tilt Uranus over, the model requires that Uranus be pinned between Jupiter and Saturn for an uncomfortably long few hundred million years (Holman & Wisdom, 1993). Is there any room for improvement?

Both the Thommes et al. (1999, 2002, 2003) model and the Nice model (Gomes et al., 2005; Morbidelli et al., 2005; Tsiganis et al., 2005) require the planets' migra-

tion timescales to be on the order of $10^6 - 10^7$ years. This is incompatible with this resonance capture scenario, which requires at least 10^8 years. Speeding up the tilting timescale significantly would require a stronger resonance. The strength of this resonance is proportional to the migrating planet's inclination and it sets the maximum speed at which a capture can occur (Hamilton, 1994). Although Neptune's initial orbital inclination angle is unknown, a dramatic reduction in the tilting timescale is implausible.

Another possibility is that the gas giants were once closer to the Sun where tidal forces are stronger. Some evidence for this comes from the fact that the giant planets probably formed closer to the snow line (Ciesla & Cuzzi, 2006) where volatiles were cold enough to condense into solid particles. Shrinking the planets' semi-major axes by a factor of 10% decreases the resonance location by about 3 au, and reduces the obliquity evolution timescale by about 15%. Although this is an improvement, a timescale on the order of 10^8 years seems to be the fundamental limit on the speed at which a significant obliquity can be reached (Rogoszinski & Hamilton, 2016; Quillen et al., 2018).

Less critical than the timescale problem but still important is the inability of the obliquity to exceed 90° (Figure 4.3). The reason for this follows from Equation 4.3, which shows that Uranus's precession period approaches infinity as ϵ approaches 90°. Neptune's migration speed then is faster than the libration timescale and the resonance ceases. This effect is more apparent in Figure 4.4 which shows the libration period increasing with the obliquity. The resonance breaks when the resonance angle stops librating about an equilibrium point and instead circulates a full 2π radians.

Quillen et al. (2018) show that a related resonance that occurs when the planets are also close to a mean-motion resonance could tilt the planet past 90°, but this, like the resonance considered here, is probably too weak. Keeping Uranus between Jupiter and Saturn for 10^8 years is as implausible as the planet having once had a massive distant moon (Boué & Laskar, 2010).

4.4 Obliquity Kicks

A resonance capture with Neptune may not be able to tilt Uranus effectively, but this resonance may still contribute significantly on a timescale more compatible with current planetary formation models. A *resonance kick* occurs if Neptune's migration speed is too fast to permit captures (i.e. exceeds the adiabatic limit). If $\dot{g}$, the rate Neptune's nodal precession frequency changes as the planet migrates, is large enough, then from Equation 4.6, $g \cos I$ shrinks faster than Uranus's spin precession frequency $\alpha \cos \epsilon$. Thus $\dot{\Psi} < 0$ which drives Ψ to -180°. For a capture, on the other hand, $\dot{g}$ is smaller so that the resonance lasts more than one libration cycle. A kick can also occur at slower migration speeds if the relative phase of the two precession axes are misaligned. Figure 4.5 shows an example of a resonance kick with a concurrent change in obliquity lasting 50 Myr. Overall, the magnitude of the kick depends on Neptune's orbital inclination, Uranus's initial obliquity, the migration speed, and the relative orientation of Uranus's spin axis and Neptune's orbital pole at the time the resonance is encountered. We will explore the entirety of this phase space to examine how effective Neptune's resonant kicks are at tilting
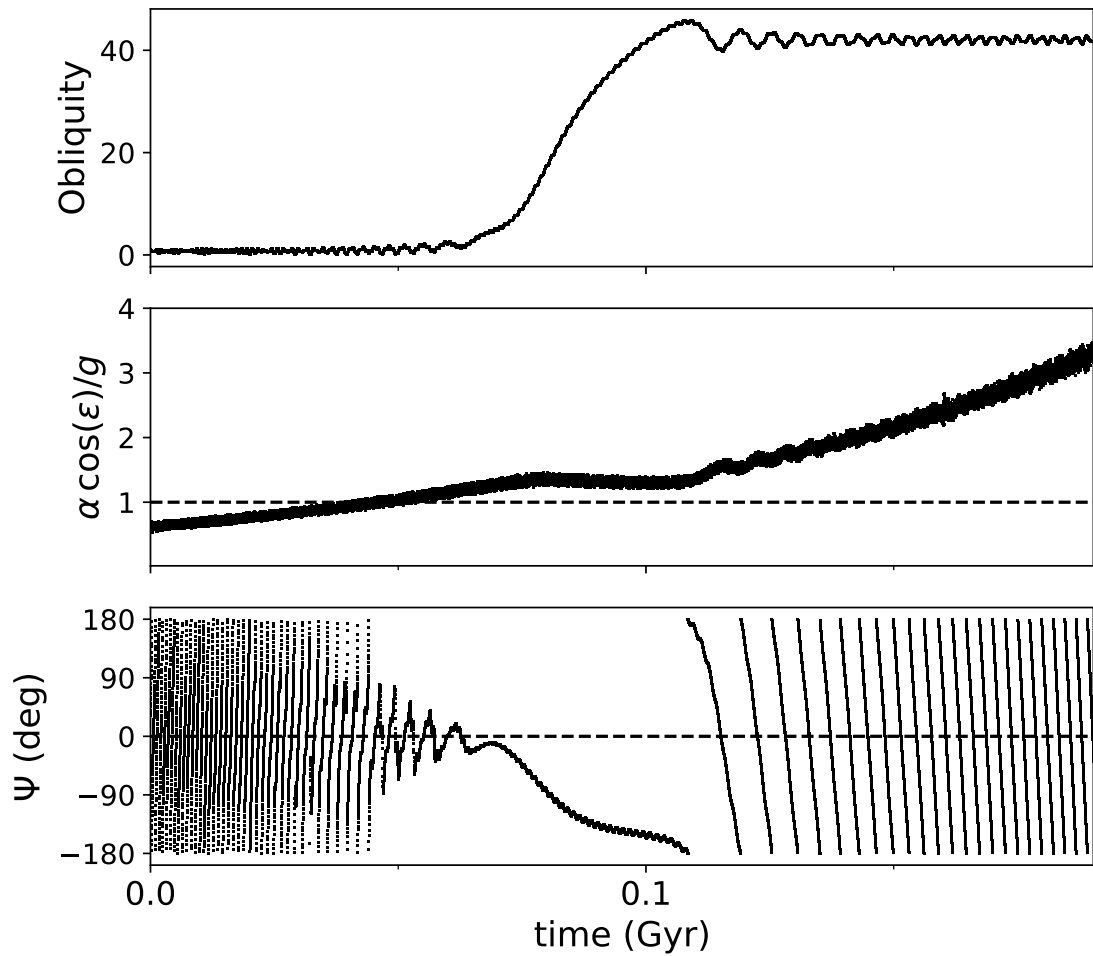
Figure 4.5: A resonance kick with a particularly large 40° amplitude. Here Neptune is migrating out rapidly at an average speed of 0.068 au/Myr, and Uranus's radius is at its current size. Jupiter, Saturn, and Uranus are located 10% closer to the Sun than today, and Neptune has an inclination of 4°.

Uranus.

For a range of seven migration speeds consistent with orbital evolution rates from planetesimal scattering (Hahn & Malhotra, 1999, 2005), we ran simulations for initial obliquities ranging from $\epsilon \approx 0°$ to $\epsilon \approx 90°$ in increments of $5°$. While Uranus may have originated with zero obliquity due to gas accretion, this does not need to be the case in general. Impacts, for example, are a source of at least small obliquities, as well as a prior spin-orbit resonance with a circumplanetary disk (Rogoszinski & Hamilton, 2020a, Chapter 5), and tidal torques onto detached circumplanetary disks (Martin et al., 2020). For each initial obliquity we sample a range of phase angles from 0 to 2π.

Distinguishing kicks from captures is more difficult when Neptune is migrating near the adiabatic limit, especially at low inclinations, so to highlight this effect we raise Neptune's inclination to $8°$ in Figure 4.6. This figure shows how the phase angle determines whether the resonance would yield a kick or a capture. Note, however, that it is actually the phase angle on encountering the resonance that matters, not the initial phase angle plotted in Figure 4.6. Also, the outlying oscillations in this figure are due to librational motion as the final obliquity is calculated only when Neptune reaches its current location at 30 au. In this case there is a clear division between captures and kicks near azimuthal angles $150°$ and $250°$. In other cases at lower inclinations, however, the boundaries between kicks and captures seem more ambiguous.

Figure 4.7 shows the corresponding polar plots for a selection of points in Figure 4.6 contrasting the difference between kicks and captures. Near the adiabatic
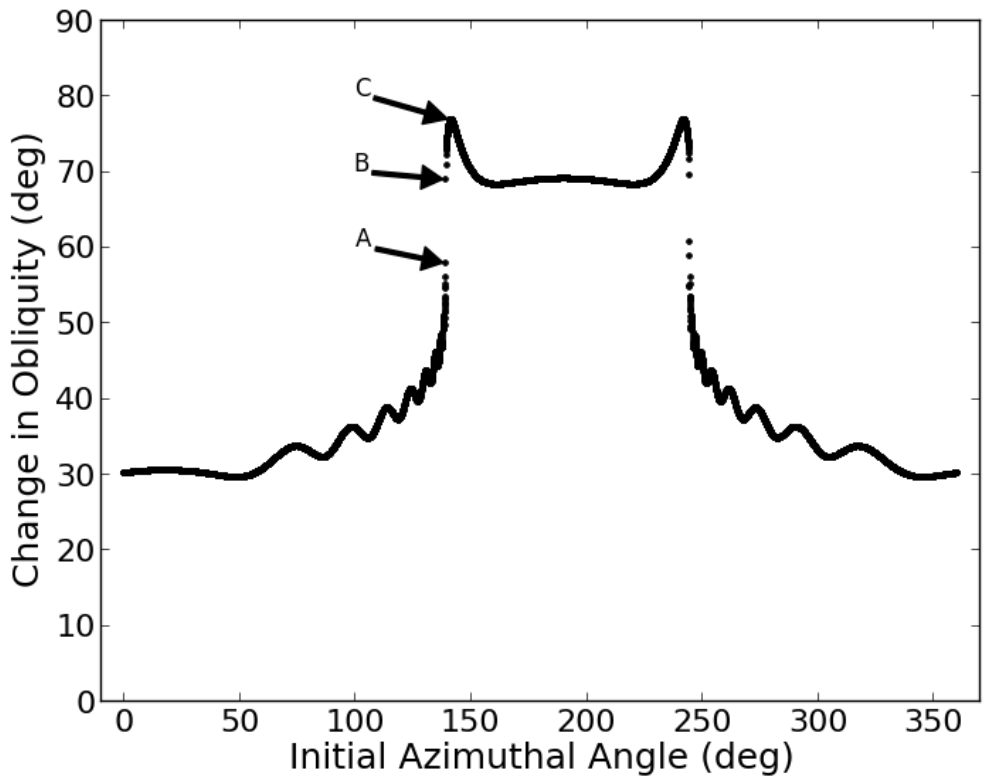
Figure 4.6: This figure shows the change in obliquity as a function of Uranus's initial azimuthal angle where $\epsilon = 1°$, $i_N = 8°$ and the system is near the adiabatic limit. Here we sampled 10,000 initial azimuthal angles from $0°$ to $360°$ and raised the inclination even further to emphasize the transition region from kicks (phases near $0°$) to captures (phases near $180°$). The annotated points (A,B,C) are discussed further in Figure 4.7.
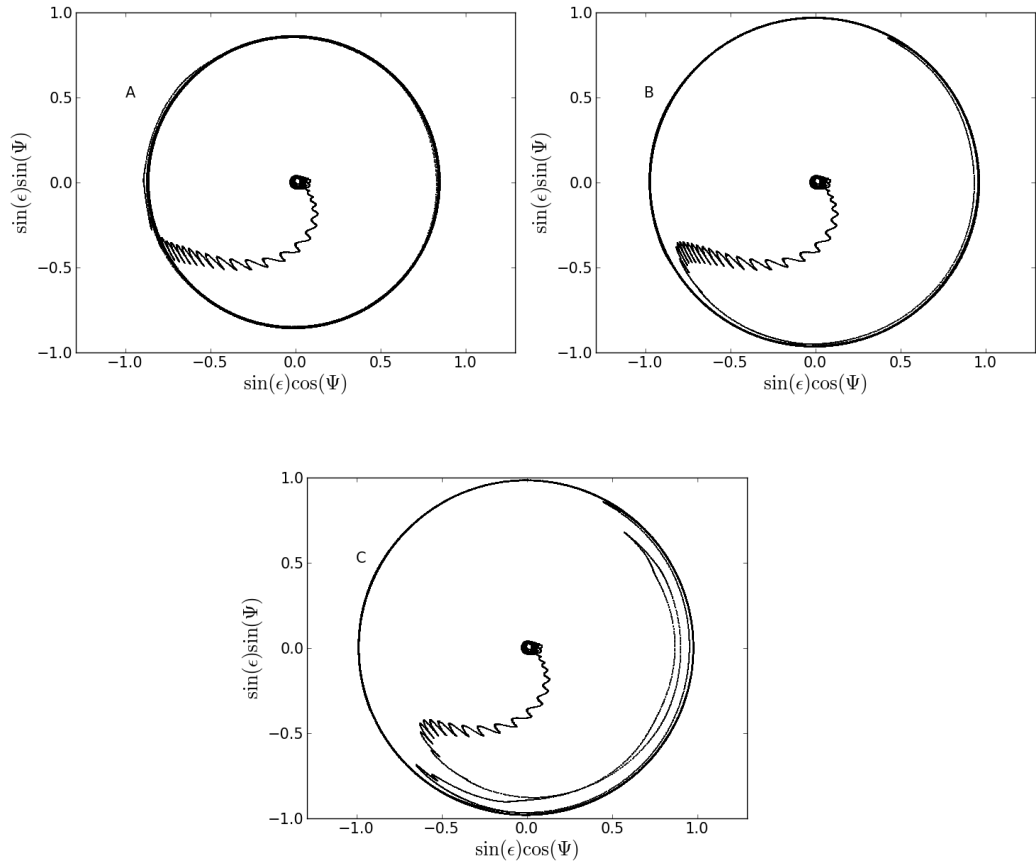
Figure 4.7: Polar plots of points A,B,C taken from Figure 4.6. (A) The largest resonance kick at the transition region in Figure 4.6. The resonance angle undergoes less than one libration cycle. It approaches 180° and then leaves the resonance. Short period oscillations in these plots are due to the effects of pole precession. (B) A very tenuous capture whose libration angle exceeds 180° for a few cycles before escaping the resonance creating the large outer circle. (C) A resonance capture well within the capture region in Figure 4.6. Here the system also breaks free from the resonance after a few libration cycles.

limit, the phase angle will not librate more than one or two cycles for captures before the resonance breaks. This is most apparent in Figure 4.7b where Uranus cycles just over one libration period before the resonance breaks. For comparison, Figure 4.4 shows a capture well within the adiabatic limit, and here the phase angle clearly librates multiple times until the planet's obliquity reaches $\epsilon \sim 90°$. We therefore only identify kicks as a resonance active for less than one libration cycle. Resonance kicks near the adiabatic limit can also generate large final obliquities, so we will focus our attention to this region in phase space. As shown in Figures 4.5 and 4.6, it is possible to generate kicks up to $\Delta\epsilon \sim 40°$ for $i_N = 4°$ and $\Delta\epsilon \sim 55°$ for $i_N = 8°$.

Figure 4.8 maps the fraction of resonances that produce captures for a range of migration speeds and initial obliquities. The transition from 100% kicks to 100% captures over migration speeds is sharpest at lower initial obliquities. This can be understood by considering the circle that Uranus's spin axis traces as it precesses; for small obliquities significant misalignments between the two poles are rare, and the outcome of a resonance is determined primarily by Neptune's migration speed. With increasing initial obliquities, large misalignments become more common and the probability of generating a resonance kick increases (Quillen et al., 2018).

We expect and find that the strongest resonant kick occurs at around the adiabatic limit because a slow migration speed gives ample time for the resonance to respond. Conversely, a rapid migration speed would quickly punch through the resonance leaving little time for the resonance to influence Uranus. Figure 4.9 depicts the distributions of kicks and captures near the $\epsilon = 0°$ adiabatic limit where Neptune's migration speed is roughly 0.068 au/Myr. Looking at the average resonance
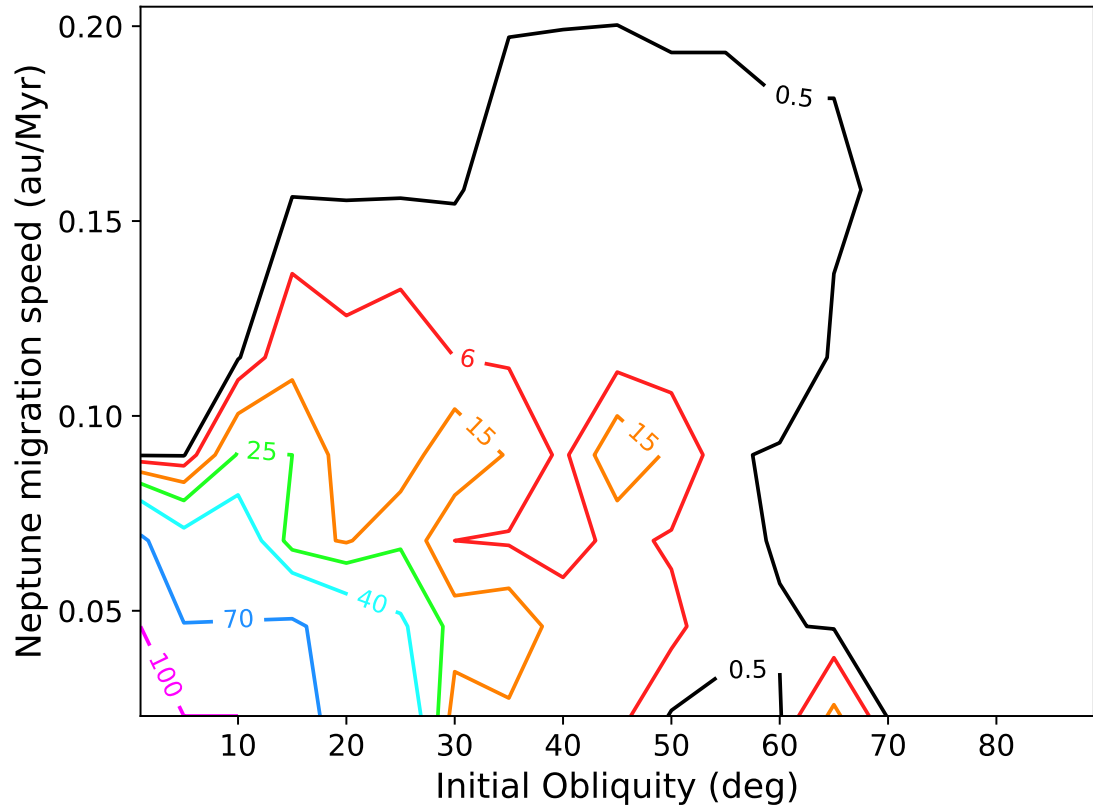
Figure 4.8: This figure shows the percentage of resonances that produce captures for a range of initial obliquities and migration speeds. Captures occur most readily in the lower left corner of the figure for small obliquities and slow migration rates. Here $i_N = 4°$.
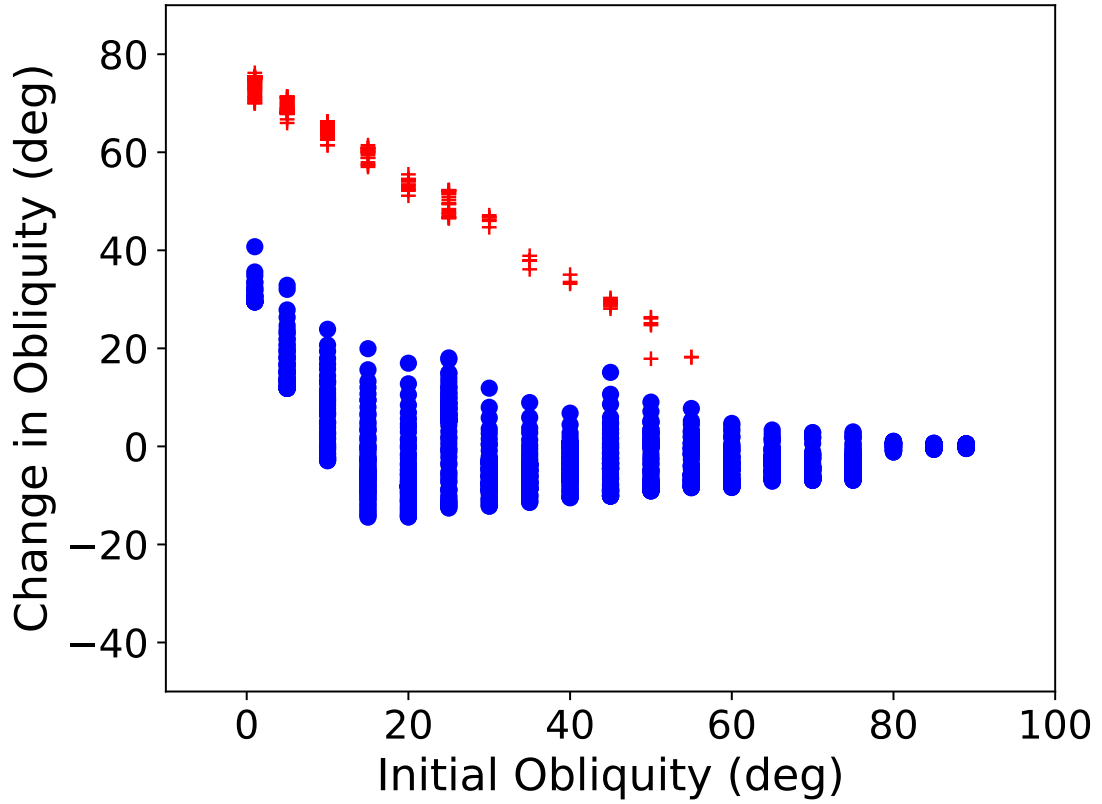
Figure 4.9: This figure depicts the change in obliquity as a function of Uranus's initial obliquity. The blue circles depict resonance kicks, while the red crosses depict resonance captures. Neptune's migration speed is 0.068 au/Myr, which is near the adiabatic limit at small initial obliquities. We set $i_N = 4°$. It should be noted that our sampling of 100 initial azimuthal angles for Uranus is too coarse to resolve any captures for initial obliquities greater than 55°. It is possible for captures to happen at larger initial obliquities but the range of favorable phase angles is very small.

kicks, we see that they can reach maximum changes in obliquities of 40° (Figure 4.5) for i_N near twice Neptune's current inclination and even greater changes in obliquity for higher assumed i_N (Figure 4.6). This looks promising, but we need to understand the probability of these large kicks. In fact, looking at Figure 4.9 shows that for high obliquities negative kicks are common. For low obliquities, kicks must be positive since ϵ itself cannot be negative. However, if Neptune is migrating quickly and ϵ is large enough, then the relative phase angle is random resulting in a range of possible obliquity kicks; in particular if $\sin(\Psi)$ is positive in Equation 4.7, then $\dot{\epsilon}$ is negative.

Figure 4.10 shows the maximum possible kicks over all initial obliquities and migration speeds, and although large kicks are possible, they are rare. Apart from resonant kicks that occur near the adiabatic limit, which can be seen in this figure as the magenta feature extending linearly up and to the right, the maximum strength of resonant kicks is typically $\Delta\epsilon \approx 10° - 20°$. On top of that, resonance kicks can also decrease obliquities, which is depicted in Figure 4.11. If Uranus's obliquity was initially large, then the percentage of positive kicks is around 50% tending towards primarily negative kicks as Neptune's migration speed decreases. Since about half of all possible resonance kicks at initial obliquities greater than 10° are negative, the average kick should be low. Figure 4.12 depicts the corresponding mean changes in obliquity, and they tend to be weak with mean resonance kicks of only a few degrees. At low initial obliquities, though, kicks tend to increase the planet's obliquity by at least 10°. Generating a large resonance kick would most commonly occur if $\epsilon_i = 0°$ with Neptune migrating no faster than 0.1 au/Myr. These figures show that, as a
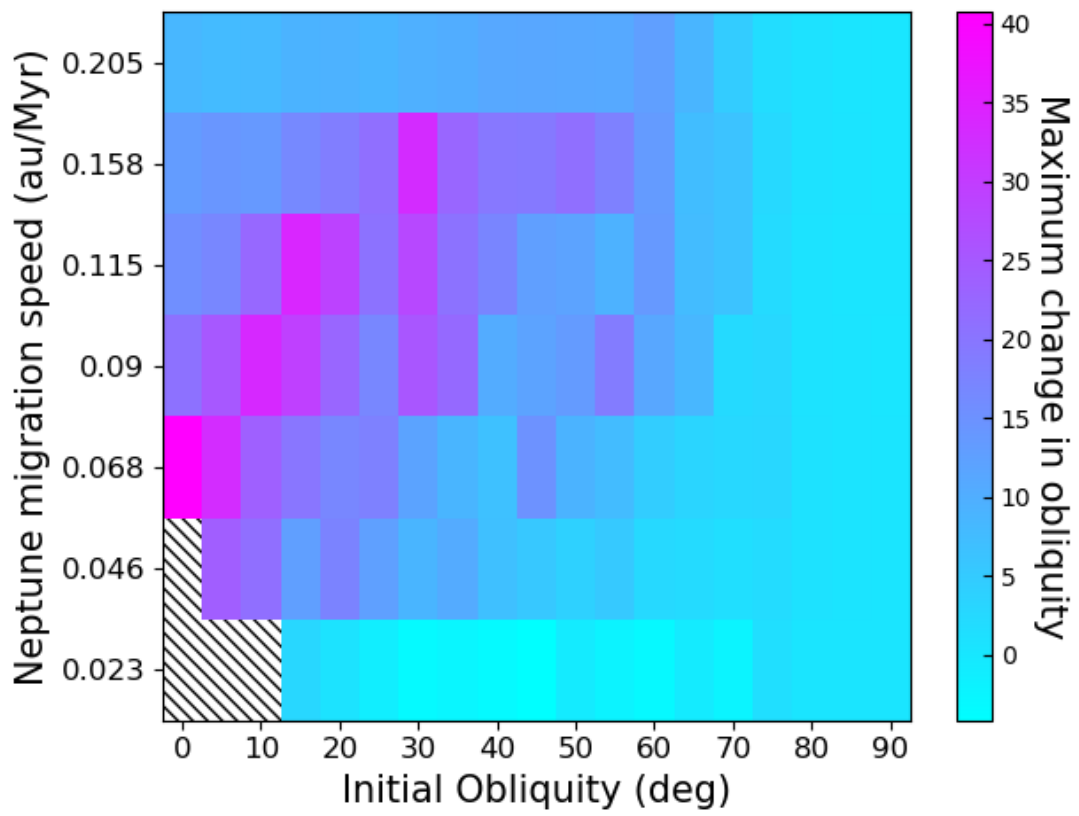
Figure 4.10: This shows the corresponding maximum change in obliquity for resonant kicks depicted in Figure 4.8. Diagonal hatching in the four boxes to the lower left in all panels correspond to captures. The scale ranges from 40° kicks (magenta) to 0° (cyan).
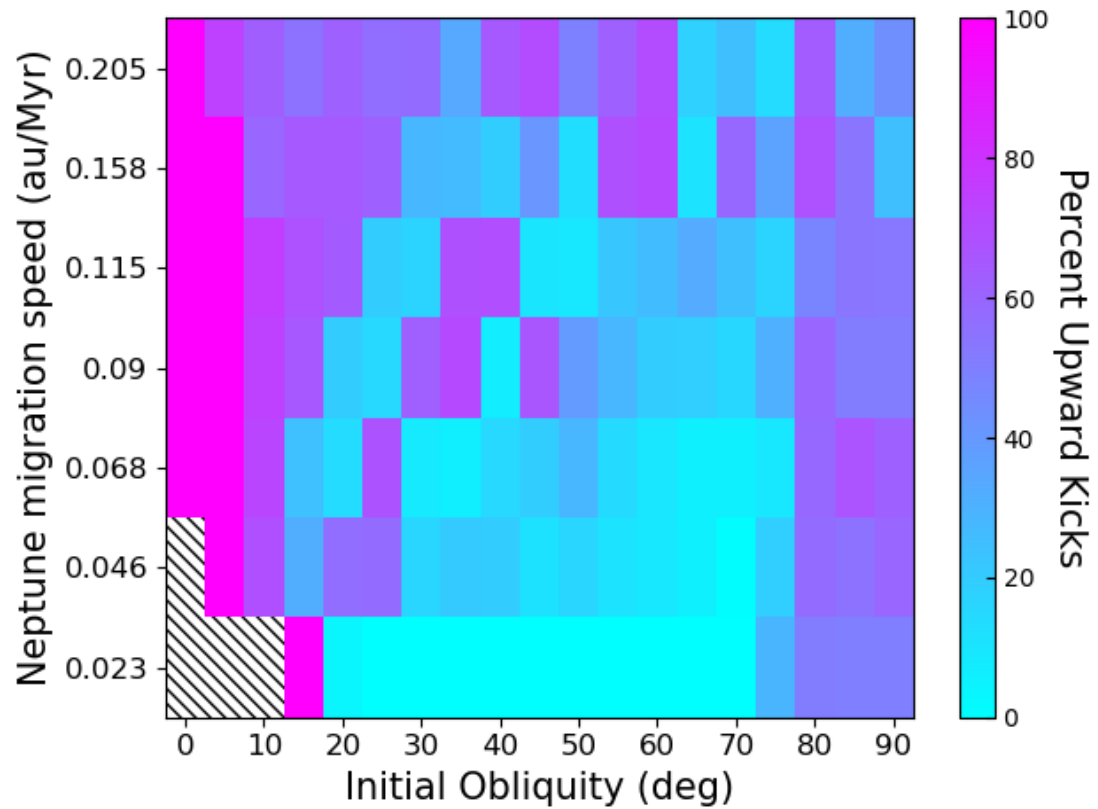
Figure 4.11: This shows the percentage of kicks that yield positive changes in obliquity. 100% positive kicks are depicted in magenta. Diagonal hatching in the four boxes to the lower left in all panels correspond to captures. The scale ranges from 100% upward kicks (magenta) to 0% (cyan).
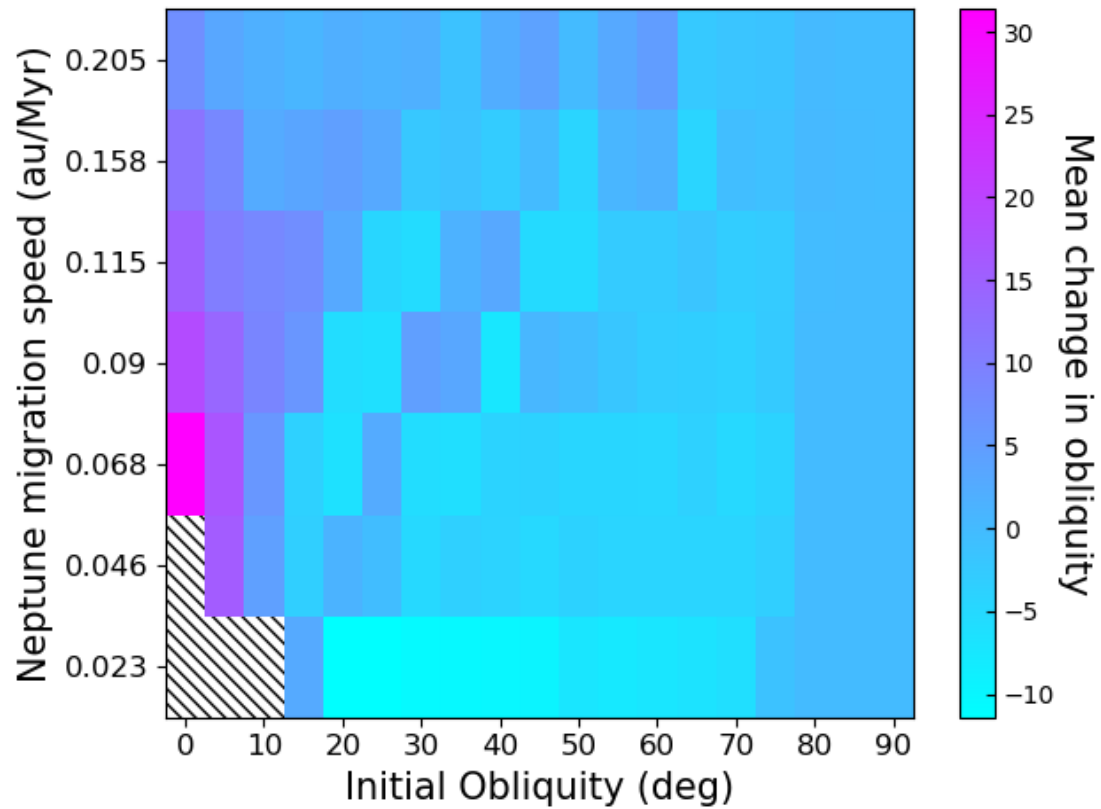
Figure 4.12: This shows the mean changes in obliquity for resonant kicks. The scale measures the change in obliquity with magenta being the maximum. Diagonal hatching in the four boxes to the lower left in all panels correspond to captures. The scale ranges from 30° kicks (magenta) to -10° (cyan).

statistical process, resonances have only a weak effect, and that one needs favorable initial conditions for large kicks.

4.4.1 A Shrinking Planet

We could increase Uranus's obliquity further if it received multiple successive resonance kicks. This might be achieved with either a resonance between Uranus and another possible ice giant that may have existed in the Thommes et al. (1999) model, a resonance with its own orbital pole after Uranus' spin precession rate was amplified by harboring a massive extended circumplanetary disk (Rogoszinski & Hamilton, 2020a), or if Uranus's precession frequency quickened as the planet cools and shrinks. The latter process is interesting and merits further discussion.

Uranus was hotter and therefore larger in the past (Bodenheimer & Pollack, 1986; Pollack et al., 1991, 1996; Lissauer et al., 2009), and conserving angular momentum requires that a larger Uranus must spin significantly slower. Both Uranus's spin angular frequency, ω, and its quadrupole gravitational harmonic, J_2, appear in Equation 4.3 and change if the planet's radius changes. Since $\omega \propto R^{-2}$ and $J_2 \propto \omega^2$ (Ragozzine & Wolf, 2009), the result is a slower precession frequency. Here, for simplicity, we have ignored the contributions of the satellites as including them would soften the response somewhat. Although this is highly dependent on Uranus's cooling rate, Bodenheimer & Pollack (1986) and Pollack et al. (1991) show that Uranus shrank by a factor of 2 on a timescale of order 10 Myr. We simulated this scenario by having Uranus's radius decrease according to an exponential function with Neptune
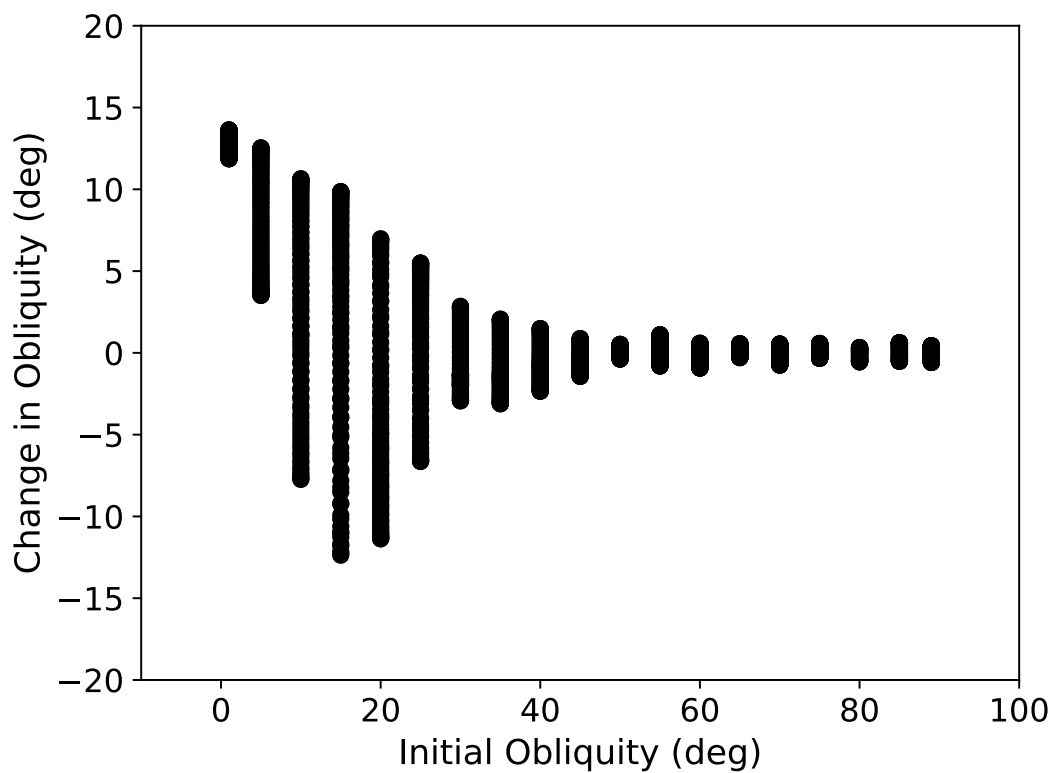
Figure 4.13: The change in obliquity as a function of Uranus's initial obliquity for a cooling and shrinking Uranus with $i_N = 4°$. There are 1900 simulations depicted here.

stationary at 25 au. Figure 4.13 shows the resulting kicks as a function of Uranus's initial obliquity, and they never exceed 15°. Scenarios that include multiple crossings of the same resonance would likely still fall short of fully tilting Uranus (e.g. Ward & Hamilton, 2004; Hamilton & Ward, 2004; Correia & Laskar, 2004).

4.5 Conclusion

The advantage of the collisionless secular spin-orbit resonance model is that it preserves both Uranus's spin rate and its moons' orbits by gently tipping the Uranian system over. Here we have investigated a resonance argument with Uranus commensurate with Neptune. We have shown that Uranus being located between Jupiter and Saturn can augment the planet's spin precession rate enough to match with Neptune located beyond Saturn. Capture into resonance can tilt the planet to near 90°, but only on unrealistic 100 Myr timescales. Resonance kicks, on the other hand, require just 10^7 years, but would produce at most a 40° obliquity under ideal circumstances. This resonance can, however, easily excite Uranus's obliquity by about 10° or 20°, which would eliminate one of the impacts required by Morbidelli et al. (2012). As seen in Tables 2.2 and 2.3, however, an initial obliquity under 40° does not provide much mass reduction or probability improvements for the subsequent collisions needed to generate Uranus's current spin state.

Chapter 5:   Tilting Uranus with a Circumplanetary Disk

An early circumplanetary accretion disk could also enhance the planetary sys-tem's bulge and speed up the planet's spin precession rate, at least for a few million years. The ice giants must have once had gaseous accretion disks, as 10% of their mass is hydrogen and helium (Podolak et al., 1995, 2000), and circumplanetary disks are thought to be the birthplaces of the planet's regular satellites (Canup & Ward, 2002, 2006; Szulágyi et al., 2018). Because the circumplanetary disk survives for only a few Myr (Ward & Canup, 2010; Szulágyi et al., 2018), a strong resonance would be required to tip Uranus in this short timespan.

5.1   Initial Conditions

The setup here is similar to Section 4.1, in that Equation 4.1 describes the evolution of the planet's obliquity when entering a secular spin-orbit resonance. The effective quadrupole coefficient of the satellite system (Equation 4.4) can be modified to describe a disk by simply replacing the summation with an integral with M_i interpreted as the mass of the ringlet with width Δa at a distance a_i. The mass of each ringlet is therefore $M_i = 2\pi a \, \Delta a \, \Sigma(a)$, with $\Sigma(a)$ as the surface density profile of the disk.

Recall that Equation 4.3 neglects the effects of other planets as they would increase α, the spin precession rate near $0°$, by only $\sim M_P/M_\odot \sim 0.1\%$. Only Uranus's major regular satellites contribute significantly to these quantities, so at the present day, we have $q = 1.56 \times 10^{-2}$ and $l = 2.41 \times 10^{-7}$ s^{-1}. Furthermore, $J_2 = 3.34343 \times 10^{-3}$ and $K\omega = 2.28 \times 10^{-5}$ s^{-1}, so $K\omega \gg l$ and $q = 4.7J_2$. At its current $\epsilon = 98°$ obliquity, Uranus's spin precession period is about $T_\alpha = 210$ Myr (or $\alpha = 0.0062$ arcsec yr^{-1}), and at near zero obliquity, $T_\alpha = 29$ Myr (or $\alpha = 0.045$ arcsec yr^{-1}). The mass of Uranus's current satellite system is about $1.05 \times 10^{-4} M_U$ or 9.1×10^{21} kg, so a more massive circumplanetary disk would increase q and α considerably, especially for a slowly spinning planet.

5.1.1 Orbital Pole Precession

Torques from neighboring planets cause a planet's orbit to precess, and Uranus's current orbital precession period is 0.45 Myr or 64 times faster than its present-day α. The orbital precession rate would be even faster in the presence of the massive circumplanetary disk. If the density profile of the circumstellar disk is the minimum-mass solar nebula, then the total mass of the disk would be about $M_d = 10M_J$ (Hayashi, 1981). Raising the total orbiting mass of the solar system by an order of magnitude should also increase the orbital precession frequencies of all the planets by a similar amount (Murray & Dermott, 1999).

A planet's orbital precession rate is determined by perturbations from sections of the disk both interior and exterior to the planet's orbit. Assuming the density

of the circumstellar disk follows a power-law profile as a function of the distance away from the planet with index β_- inside the planet's orbit and β_+ outside, the precession rate is negative and is given as $g = g_- + g_+ + g_p$ with

$$g_- = -\frac{3}{4}n\left(\frac{2-\beta_-}{4-\beta_-}\right)\left(\frac{1-\eta_-^{4-\beta_-}}{1-\eta_-^{2-\beta_-}}\right)\left(\frac{M_{d,-}}{M_\odot}\right)\left(\frac{R_{o,-}}{r_p}\right)^2, \qquad (5.1)$$

$$g_+ = -\frac{3}{4}n\left(\frac{2-\beta_+}{-1-\beta_+}\right)\left(\frac{1-\eta_+^{-1-\beta_+}}{1-\eta_+^{2-\beta_+}}\right)\left(\frac{M_{d,+}}{M_\odot}\right)\left(\frac{r_p}{R_{o,+}}\right)^3 \qquad (5.2)$$

where g_- is the orbital precession rate induced from the interior disk, g_+ is from the exterior disk (Chen et al., 2013, see Appendix C for derivation), and g_p is the contribution from the other giant planets (Murray & Dermott, 1999). Here n is the mean motion of the planet, $M_{d,-}$ and $M_{d,+}$ are the masses of the circumstellar disk interior and exterior to the planet, $R_{o,-}$ and $R_{o,+}$ are the outer radii of each respective disk, and η is the ratio of the inner and outer disk radii.

To calculate g, we set r_p, the distance to the planet, to be 19 au, and the inner and outer radii of the solar system to be 0.1 and 100 au. The index $\beta = 1.5$ for a minimum-mass solar nebula if the planets were formed near their current locations, and $\beta \approx 2.2$ if the planets abide by the Nice model (Desch, 2007). For this range of β, assuming $\beta = \beta_+ = \beta_-$ and a protoplanetary disk mass of $10\,M_J$, Uranus's orbital precession rate is faster than its current rate by a factor of 3–7. Here the contributions from the other giant planets to Uranus's orbital precession rate are minor, as the mass of the circumstellar disk is much larger than the forming giant planet cores. However, since Uranus and Neptune are categorically gas-limited, the

ice giants likely were actively accreting their atmospheres only when the circumstellar disk was significantly depleted (Frelikh & Murray-Clay, 2017). At this point in time, Jupiter and Saturn had almost finished forming, so g_p is close to Uranus's current rate. Shrinking the circumstellar disk to $1\,M_J$ would only increase Uranus's current orbital precession frequency by about 30% - 60%.

Capturing into a spin-orbit resonance requires that the orbital precession rate $g \approx \alpha \cos \epsilon$. We increase Uranus's current orbital precession rate by 30% to account for the contribution from the protoplanetary disk, and vary the planet's and circumplanetary disk's physical parameters (e.g. planet's initial spin rate and size of circumplanetary disk) to find solutions for Uranus's spin precession rate that yield resonances. If Uranus's orbital precession rate was faster, then the planet would need a more massive circumplanetary disk to increase its spin precession rate and generate a resonance. As Uranus accretes matter, its spin angular momentum will also increase, so, all else being equal, α will tend to decrease (Equation 4.3). We therefore seek cases where $\alpha \cos \epsilon$ was initially larger than g so that the system will pass through the resonance. If the masses of both circumplanetary disk and circumstellar disk deplete at the same rate, then both precession rates (g and $\alpha \cos \epsilon$) decrease at similar rates, and capturing into resonance is difficult (Millholland & Batygin, 2019). We instead expect the two frequencies to change at different rates, especially as the planet's spin precession rate will increase as it builds up its circumplanetary disk. A slow spin rate and a massive circumplanetary disk are optimal for speeding up a planet's spin precession rate, but is this enough to generate a strong and lasting spin-orbit resonance as the planet grows?

5.1.2 Evolution of Ice Giants

Recall from Chapter 3.2.1 that there are multiple competing models for ice giant formation. Uranus and Neptune probably formed closer to the Sun, but it is unclear whether they originated inside or beyond Saturn's orbit. Furthermore, the circumstellar disk could have either been massive ($\sim 10\,M_J$) and Jupiter and Saturn happened to have accreted most of the surrounding gas, or Uranus and Neptune accreted their atmospheres after they have scattered in an already depleted circumstellar disk ($\sim 0.1\,M_J$) over ~ 1 Myr (Frelikh & Murray-Clay, 2017). Regardless of how they formed, Uranus and Neptune would have had to harbor a circumplanetary disk at some point. This disk will at least initially maintain a steady state, but as the circumstellar disk dissipates, we expect the circumplanetary disk to disappear as well. In this chapter we explore these two basic scenarios.

Since Uranus and Neptune spin at about the same rate and have similar gas content, we suspect that gas accretion is the primary source of their respective spin periods. Recall from Chapter 3.2.2 that gas accretion provides a substantial amount of angular momentum; so much so, that excess angular momentum was probably carried away by a combination of polar accretion or magnetic interactions between the planet and the surrounding gas. We model the effect of gas accretion on the planet's spin state by incrementally adding angular momentum to the planet according to

$$\vec{l}_{\mathrm{gas}} = \Delta M R_P V_{\mathrm{orbit}} \lambda\, \hat{z}, \tag{5.3}$$

where ΔM is the differential mass of the gas accreted at that time step, $V_{\text{orbit}} = \sqrt{GM_P/R_P}$ is the circular speed at the edge of the planet, M_P and R_P are the mass and radius of the planet, and $\hat{z}$ points normal to the orbital plane. The planet's spin rate then grows as $L/(KM_PR_P^2)$, where K is the moment of inertia coefficient. Since gas accretion flows to the planet's poles and does not hit the planet with perfectly tangential velocity (see Chapter 3.2.2), we include the constant λ with $\lambda < 1$. The accretion efficiency is relatively unconstrained, and, in practice, we tune λ so that Uranus's final spin angular momentum matches its current value. Here we explore a range of initial spin rates, from where the planet is spinning fast enough such that its spin angular momentum is close to its current value to cases where the planet is initially spinning slower than that.

Finally, we assume that the angular momentum transport to the planet is smooth, even when the circumplanetary disk is warped at high planetary obliquities. Planets accrete gas from a circumplanetary disk driven by accretion mechanisms such as magnetorotational instability-triggered turbulent viscosity (Shakura & Sunyaev, 1973; Balbus & Hawley, 1991) or shock-driven accretion via global density waves (Zhu et al., 2016). Tilting the planet with a quadrupole torque presents unique challenges to the accretion mechanism, as additional wavelength disturbances are introduced when the disks are warped (Papaloizou & Lin, 1995). Since we fix the accretion rate to 1 $M_\oplus$ per million years, the details of the accretion mechanism are relatively unimportant. Furthermore, as the dominant accretion mechanism in these systems is unknown, we use the fiducial constant surface density profile. Tremaine & Davis (2014) showed a big dip in the disk's density near the Laplace radius if the

viscosity is low, but the disk remains unbroken if the viscosity increases. This dip is more pronounced at higher obliquities, yet the authors show that warped disks remain intact even at $\epsilon = 60°\text{--}70°$. Circumplanetary disks can also tear if the density is too low, but the resulting instabilities and momentary variations to the accretion rate occur over short timescales (Doğan et al., 2018). Global disk properties, such as the average accretion rate, remain mostly unaffected.

5.2 Laplace Radius

The outer edges of circumplanetary disks are not well known, but estimates place them somewhere between 0.1 and 0.5 Hill radii (Quillen & Trilling, 1998; Ayliffe & Bate, 2009a, 2012; Machida, 2009; Ward & Canup, 2010; Martin & Lubow, 2011; Tanigawa et al., 2012; Szulágyi et al., 2014; Zhu et al., 2016; Szulágyi et al., 2018); however, only a portion of the disk will tilt with the planet. This region is located within the planet's Laplace radius, or warping radius, which is the transition point where perturbations from the planet are comparable to those from the Sun. Orbits well beyond a planet's Laplace radius precess about the ecliptic, while orbits well inside this point precess about the planet's equator. The Laplace radius, which also discriminates regular from irregular satellites, is approximately

$$R_L \approx \left(2 J_{2,\text{tot}} \frac{M_P}{M_\odot} R_P^2 r_P^3 \right)^{1/5} \tag{5.4}$$

(Goldreich, 1966; Nicholson et al., 2008; Ćuk et al., 2016). For reference, Uranus's current Laplace radius is about 76.5 Uranian radii ($\sim 0.03\,R_{\text{Hill}}$), and without the ef-

fect of the satellite system, it reduces to 54 R_U ($\sim 0.02\,R_{\text{Hill}}$). To compare, Uranus's outermost major regular satellite Oberon is located 23 R_U away from Uranus (or $\sim 0.01\,R_{\text{Hill}}$).

Here, $J_{2,\text{tot}}$ is the total quadrupole moment of the planetary system, or the sum of the quadrupole moment of the planet (J_2) and the disk (q). The planet's J_2 depends quadratically on the planet's spin rate,

$$J_2 \approx \frac{\omega^2 R_P^3 k_2}{3GM_P} \tag{5.5}$$

(Ragozzine & Wolf, 2009), where k_2 is the Love number. The Love number is a dimensionless parameter that characterizes a planet's susceptibility to tidal deformation, and the larger the number, the greater the bulge; though, typically, k_2 is of order unity. A more slowly spinning planet has a larger α, but also a smaller J_2 and hence a smaller Laplace radius, which may limit the disk's contribution to the planet's quadrupole moment. Furthermore, the planet may have had an initially smaller K, the planet's dimensionless moment of inertia, as the planet was hot and puffy. This means also having a smaller Love number (see Figure 4.9 of Murray & Dermott (1999)) but also a larger spin rate for a given mass, radius and angular momentum.

The disk mass contained within the Laplace radius determines the disk's gravitational quadrupole moment q. If the surface density profile of the disk falls as a

power law and $q \gg J_2$, then we can transform Equation 5.4 to be approximately

$$R_L \approx \left(\frac{2\pi \Sigma_0 R_o^\beta r_P^3}{(4 - \beta) M_\odot} \right)^{1/(1+\beta)} \tag{5.6}$$

where Σ_0 is the surface density at the outer edge of the disk, R_o is the outer radius of the disk, and $\beta > 0$ is the power-law index (see Appendix D for derivation). The Laplace plane transition from the planet's equator to the ecliptic is actually a continuous curve, but a sharp transition at R_L where everything inside it tilts in unison is a sufficient approximation. The disk's contribution to q has a stronger dependence on a than the disk's mass, and we find that q can be dozens of times larger than J_2 for a range of disk sizes (See Appendix D). Therefore, we can easily excite the planet's spin precession frequency to values much greater than the planet's nodal precession rate, and as the disk dissipates, we can achieve a spin-orbit resonance.

5.3 Changing the Obliquity of a Growing Protoplanet

A massive circumplanetary disk is capable of increasing a planet's spin precession rate and generating a resonance, and in this section, we investigate how massive this disk needs to be. We first explore how the spin precession frequency changes for different disk profiles and then expand the model by having the planet also evolve with the disk.

109

5.3.1 Constant Surface Density Profile

After the planet opens up a gap, gas flows from the circumstellar disk and concentrates near the planet's centrifugal barrier. This is the gas's pericenter distance, where the centrifugal force is balanced by the planet's gravitational pull. The gas then heats up and spreads, forming a compact Keplerian rotating disk (Machida, 2009). Calculations for the average specific angular momentum of the gas are calibrated for Jupiter and Saturn, but when adopting Lissauer's (1995) analytic estimate of the disk's specific angular momentum to Uranus, the disk extends to about $60\,R_U$. This fiducial radius for Neptune is $100\,R_N$ because the planet is located farther away from the Sun. To simplify, we assume a constant surface density profile within this boundary, which is possible for a low planetary accretion rate $\dot{M}$ (Zhu et al., 2016). A portion of the disk extends beyond the centrifugal barrier, puffing up to smoothly connect with the circumstellar disk. The surface density in this outer region falls off with increasing distance as a power law. If the planet is larger than its centrifugal barrier, then this is the only part of the disk.

We track the motions of the planets using HNBody (Rauch & Hamilton, 2002) and then evaluate Equation 4.1 using a fifth-order Runge-Kutta algorithm (Press et al., 1992; Rogoszinski & Hamilton, 2020b). If Uranus is placed at its current location and we set its physical parameters to its current values, then a disk of constant density extending to $54\,R_P$, which is also the Laplace radius without the disk's influence, needs more than 20 times the mass of its satellite system (where $M_s = 10^{-4}M_U$) to generate a spin-orbit resonance (Figure 5.1). Here the amplitude

of the resonance angle increases for increasing disk masses, and, similar to first-order mean-motion resonances, the resonance center shifts locations as the distance from the resonance changes (Murray & Dermott, 1999). Larger disks will require less mass to generate a resonance, but they could extend beyond the classical Laplace radius, which will be discussed later. If Uranus's orbital precession rate is faster by a factor of 2 due to torques from a remnant solar nebula, then we will need twice as much mass to generate a spin-orbit resonance (Equation 4.3). For comparison, Szulágyi et al. (2018) favored slightly smaller satellite disk masses of $M_d \approx 10^{-3} M_U$.

5.3.2   A Shrinking Disk

The circumplanetary disk will evolve as the planet accretes, and the spin precession rate will vary depending on how the disk changes. The ice giants need to accrete about $1\,M_\oplus$ of gas in 1 Myr, so at a constant accretion rate of $1\,M_\oplus$ Myr^{-1} the lifetime of the gas for a disk mass of $M_d = 10^{-3}\,M_U$ is $\tau_d = M_d/\dot{M} \sim 10^4$ yr, or a tiny fraction of the accretion time span. We can therefore expect a sharp initial rise to the mass of the disk, and then either the disk maintains that mass in a steady state (Zhu et al., 2016; Szulágyi et al., 2018) or it steadily decreases as the circumstellar disk dissipates. Also, since the lifetime of the gas is so short compared to the precession timescale ($\sim 10^5 - 10^6$ years), the portion of the disk inside the Laplace radius can couple to the planet's spin. Figure 5.2 shows the evolution of the resonance for both cases. In this set of figures, Uranus's physical parameters are tuned to their current values, and we place a $50\,M_s$ disk around the planet to
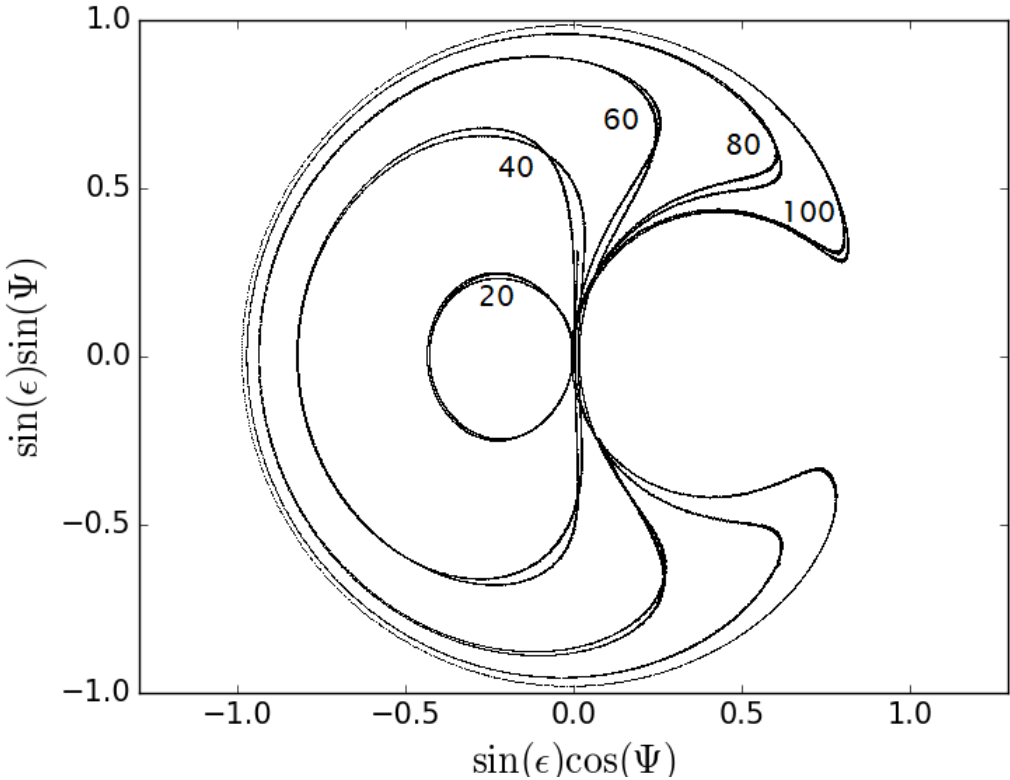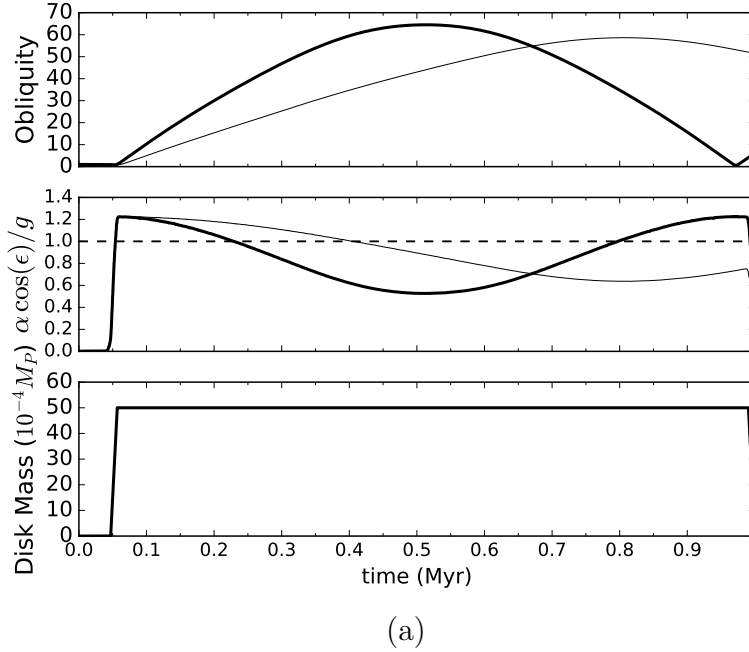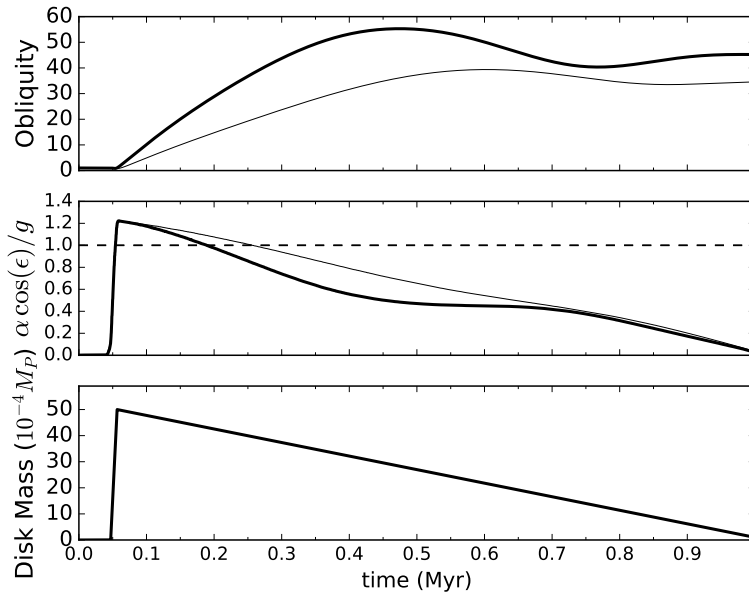
Figure 5.1: Evolution of the resonance angle Ψ and obliquity ϵ for static disks with different disk masses. The resonance angle librates about the equilibrium point indefinitely when trapped into resonance; otherwise, the resonance angle circulates through a full 2π radians. Each contour corresponds to a resonance trapping for different disk masses displayed in units of M_s, where $M_s = 10^{-4}M_U$. Uranus's orbital precession rate in a solar system that includes a depleted circumstellar disk is about 2×10^{-5} yr^{-1}, and the planet's spin precession rates near $0°$ with 20 M_s and 100 M_s circumplanetary disks are $\alpha = 1.4 \times 10^{-5}$ yr^{-1} and 3.8×10^{-5} yr^{-1}, respectively. If the mass of the disk increases well beyond $100\,M_s$, the planet's spin precession frequency will be too fast to allow a resonance capture.

Figure 5.2: (a) Uranus at its current state but surrounded by a $50\,M_s$ constant density disk for a duration of about 1 Myr. The disk extends all the way to $54\,R_U$. Thick black lines assume that Uranus's inclination is $i_U = 10°$ while thin lines indicate $i_U = 5°$. The top panel shows the evolution of the planet's obliquity in degrees; the middle panel shows the evolution of the precession frequencies, with the dashed line indicating the resonance location; and the bottom panel shows the evolution of the mass of the disk. (b) Same scenario, but the disk's mass decreases over time.

113

augment the planet's spin precession rate to generate a spin-orbit resonance. Here we see that a circumplanetary disk in steady state is capable of driving obliquities about 15% higher than disks that deplete over time. This is because the resonance frequency decreases as the disk shrinks, which limits the amount of time the planet can be nearly resonant. Finally, a larger orbital inclination can drive obliquities to higher degrees on shorter timescales as the resonance is stronger.

5.3.3 Setting the Orbital Inclination

The strength of the resonance is proportional to the planet's orbital inclination (Hamilton & Ward, 2004), so it takes longer to drive Uranus to higher obliquities in a resonance capture for low i_U. The evolution of the planets' orbital inclinations are unknown, but planet-planet interactions (Nagasawa et al., 2008) or mean-motion resonances (Thommes & Lissauer, 2003) can amplify a planet's inclination, which can then damp through dynamical friction as the planet migrates outward. Scattering small particles, such as circumstellar gas or planetesimals, places them on high-velocity orbits, and in response, the planet's orbit circularizes and flattens. For simplicity, we require the planet to maintain a constant orbital inclination for the entire duration of the simulation. This is justified because the damping timescale in a depleted gaseous disk is greater than 1 Myr, and it is even longer for planetesimal scattering.

Figure 5.3 summarizes the maximum change in Uranus's obliquity for a suite of numerical simulations like that displayed in Figure 5.2 with different assumed
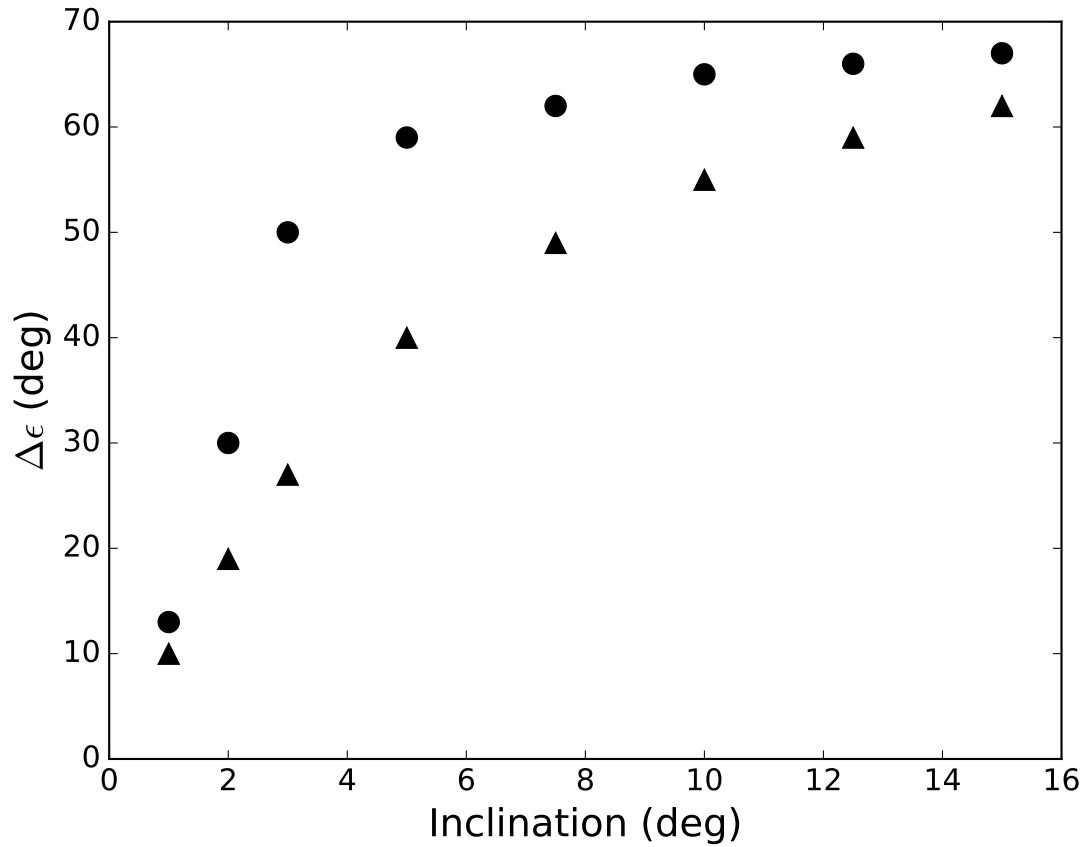
Figure 5.3: Maximum degree of tilting for a range of orbital inclinations if the disk's mass remains constant (circles) or is decreasing (triangles). The planet and disk possesses the same physical characteristics as described in Figure 5.2, and the duration of each simulation is 1 Myr. For reference, Uranus's current inclination relative to the solar system's invariable plane is about $1°$.

inclinations. If the disk maintains a constant mass, then the planet can undergo a resonance capture for inclinations above about 5°. Extending the duration of the simulation in Figure 5.3 from 1 to 10 Myr can yield resonance captures for orbits with inclinations closer to 2°. While resonance captures are capable of driving obliquities to higher values, the planet's final obliquity could be less than maximum. This is because while the resonance is active, the planet's obliquity oscillates as the spin axis librates. The resonance for a depleting disk, on the other hand, will last only briefly as a resonance kick, and in this case, the planet's final obliquity will remain fixed after the resonance terminates. Regardless, we find that we can achieve substantial tilts if the planet's orbital inclination was greater than 5°. Moderate initial eccentricities and inclinations are plausible, at least for Neptune, and may be required to dynamically heat the inclinations of the hot TNOs to $\sim 15°$ (Ward & Hahn, 1998a,b; Petit et al., 2011).

5.3.4 Growing Uranus and Tilting It Over

In the last section, we investigated how to generate a resonance by changing disk properties. Here we explore how the planet's spin precession rate and obliquity evolve as Uranus accretes its atmosphere and grows. After core accretion stops, Uranus acquires a $1M_\oplus$ atmosphere over roughly 1 million yr. Its radius is initially large ($\sim 80\,R_U$), as the planet is hot from the energy added to it from accreting planetesimals (Bodenheimer & Pollack, 1986; Pollack et al., 1996; Lissauer et al., 2009). The radius grows exponentially and terminates at around $120\,R_U$, when the
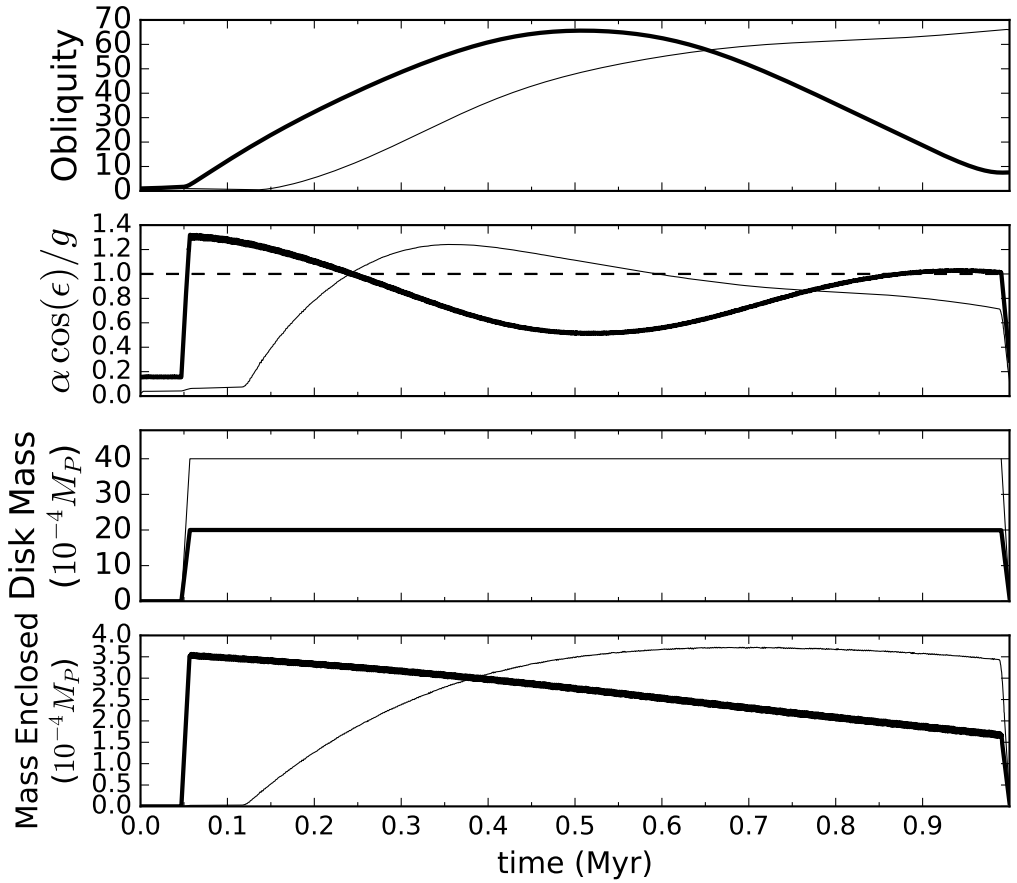
Figure 5.4: Evolution of Uranus's obliquity for a growing planet where the Laplace radius is determined by only by the evolution of the planet's J_2. The planet's mass grows from 0.9 to 1.0 M_U, and the radius grows from 80 to 120 R_U. The circumplanetary disk extends to 0.5 Hill radii, and the surface density falls by 3 orders of magnitude. The thick bold lines have a Uranus initial angular momentum L_0 of approximately the planet's current value, $L_U = 1.3 \times 10^{36}$ kg m^2 s^{-1}, and the thin bold lines have $L_0 \approx 0.25\, L_U$. In the former case, R_L ranges from 130 to 140 R_U, while for the latter, it ranges from 80 to 140 R_U. The results for having $L_0 \approx 0.25\, L_U$ do not noticeably change if the planet's initial spin angular momentum is lower. In both cases, Uranus's orbital inclination is set to 10°. The bottom panel shows the disk mass contained within Uranus's Laplace radius, which contributes to the pole precession rate α.
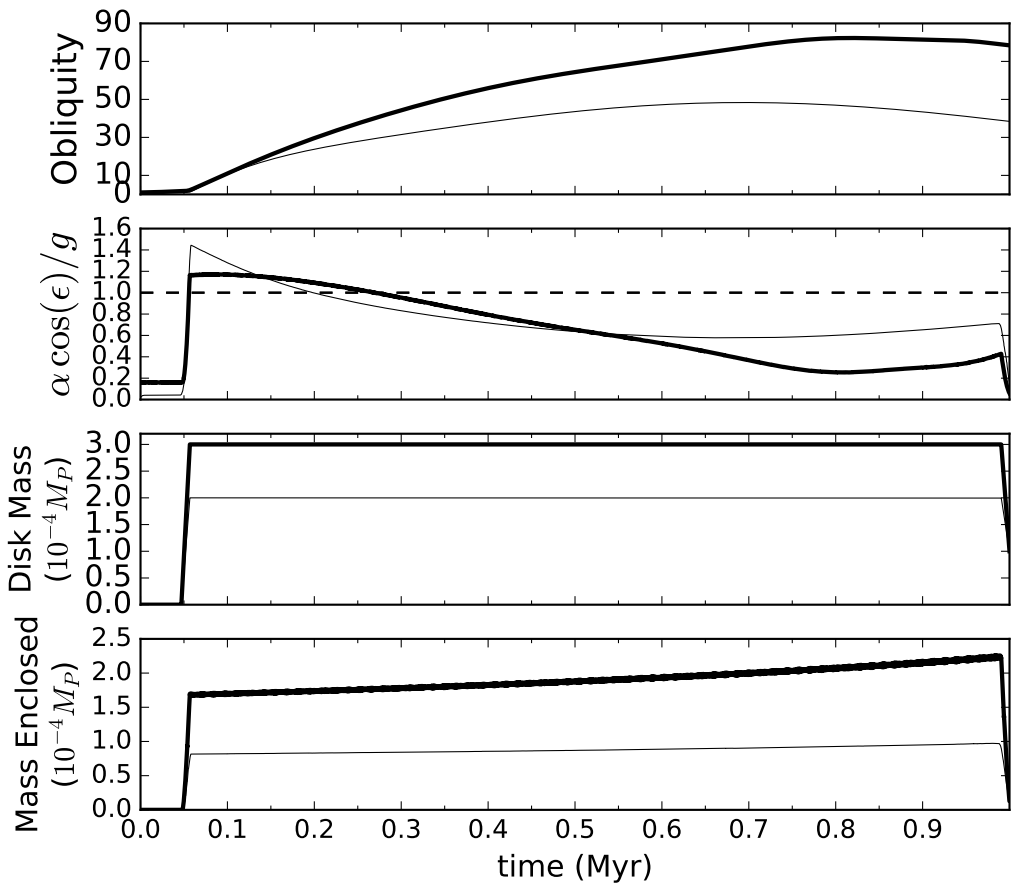
Figure 5.5: Same situation as in Figure 5.4, but R_L grows according to Equation 5.6. Here the circumplanetary disk extends to 0.1 Hill radii, consistent with Szulágyi et al. (2018), and $R_L \approx 200\,R_U$.

gas fully dissipates. The angular momentum of the planet also grows as the planet accretes gas, so the planet's spin rate varies as $L/(KMR^2)$, with the caveat that the planet's final angular momentum does not exceed its current value (Equation 5.3). Finally, a disk with an extended density profile will mostly contribute to the planetary system's quadrupole moment, and R_L increases according to Equation 5.6. The other physical limit is a thin disk in which R_L depends only on the planet's J_2, which results in a much smaller Laplace radius. We will display both cases in the following runs.

With a growing planet, even a constant disk mass lasting over 1 Myr can generate a resonance capture (Figures 5.4 & 5.5), and, for a planet with an initial spin angular momentum close to its current value, the disk needs to have $M_d = 3 \times 10^{-4} - 2 \times 10^{-3} M_U$ to tilt the planet. Recall that Szulágyi et al. (2018) calculated a circumplanetary disk around Uranus of about $10^{-3} M_U$ which falls comfortably within this mass range. In the case where R_L changes according to Equation 5.6 (Figure 5.5), a less massive disk is needed if the planet's spin rate was slower since $\alpha \propto q/K\omega$. Here we can tilt Uranus's obliquity all the way to 80°, though in most cases, it reaches about 50°.

If we instead artificially keep the Laplace radius small by having it depend only on the planet's J_2, as in Figure 5.4, then the size of the Laplace radius eventually decreases relative to the size of the planet. Assuming angular momentum is conserved, the spin rate falls as R_P^2 as the planet grows, and using Equations 5.4 and 5.5, we find $R_L/R_P \propto R_P^{-4/5}$. As a result, for an initially fast-spinning planet, both the quadrupole moment of the disk and the planet's spin precession rate shrink.

A more massive disk is needed if the planet was initially spinning slowly in order to compensate for a small Laplace radius earlier in the planet's evolution. In this case, the Laplace radius initially grows as the planet spins up, and, as represented by the thin bold line in the bottom panel of Figure 5.4, more of the disk's mass is enclosed. At around 0.6 Myr, the size of the Laplace radius compared to the size of Uranus begins to shrink because the planet's spin angular momentum is nearing its current value. These figures show that the quadrupole moment of the disk cannot be neglected; its primary effect is to reduce the amount of mass needed in the disk by about an order of magnitude. We find that a disk mass of $4 \times 10^{-3} \, M_U$ is more than sufficient to generate a spin-orbit resonance.

Figures 5.6 and 5.7 instead depict a depleting circumplanetary disk with an initial mass $M_d = 2.5 \times 10^{-4} - 4 \times 10^{-3} \, M_U$, and the planet evolves similarly to those shown in Figures 5.4 and 5.5. Regardless of how large R_L is, the planet's spin precession frequency will decrease as M_d decreases, and we can tilt Uranus to as high as 70° for similarly sized disks, as in the constant disk mass case. As in Figure 5.5, we see that the disk's effect on the Laplace radius reduces the disk mass required for resonance by about a factor of 10. How the disk evolves for an already depleted circumstellar disk is likely more complicated than these idealized scenarios, but in the realistic scenarios depicted in Figures 5.5 and 5.7 Uranus requires a disk a few times the mass of the satellite system to be contained within R_L to generate spin-orbit resonance. As such, a resonance is very possible, even with a circumplanetary disk concentrated close to the planet.
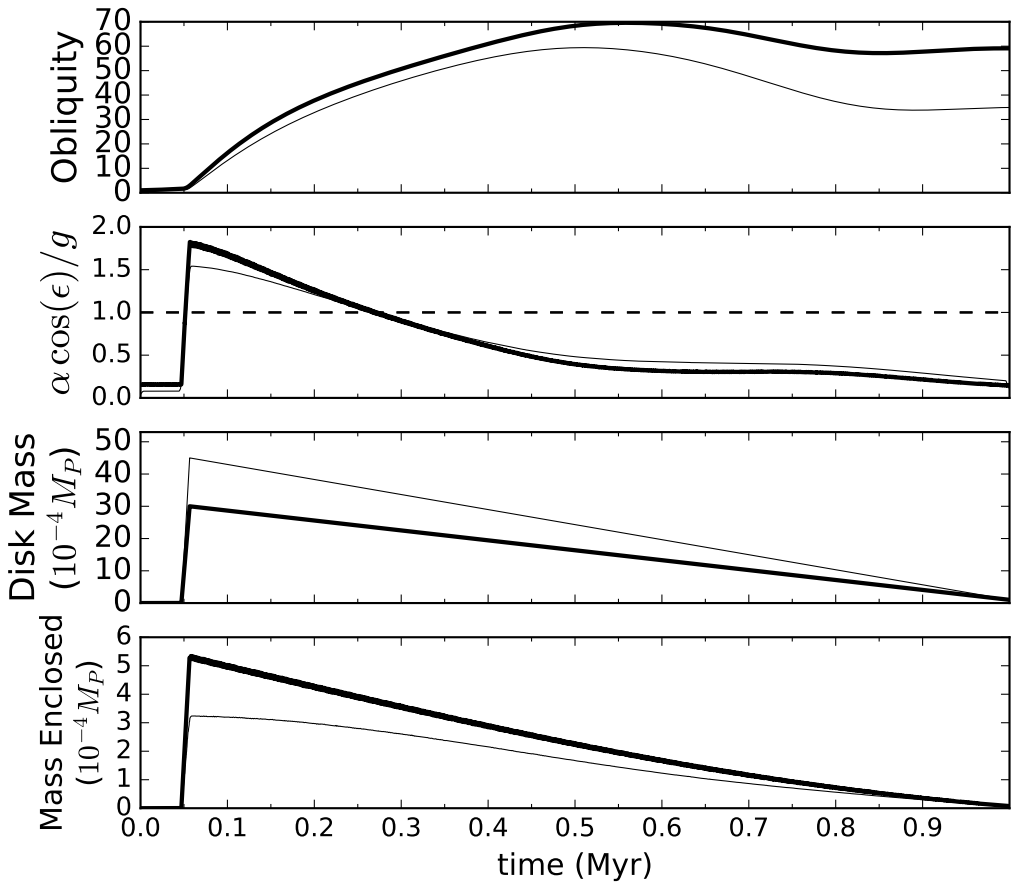
Figure 5.6: Same situation as in Figure 5.4 but with the circumplanetary disk's mass decreasing over time. Here the thick bold lines have a Uranus initial angular momentum L_0 of approximately the planet's current value, while the thin bold lines have $L_0 \approx 0.5\, L_U$. For the $L_0 \approx L_U$ case, R_L ranges from 130 to 145 R_U, while for $L_0 \approx 0.5\, L_U$ it ranges from 80 to 140 R_U.
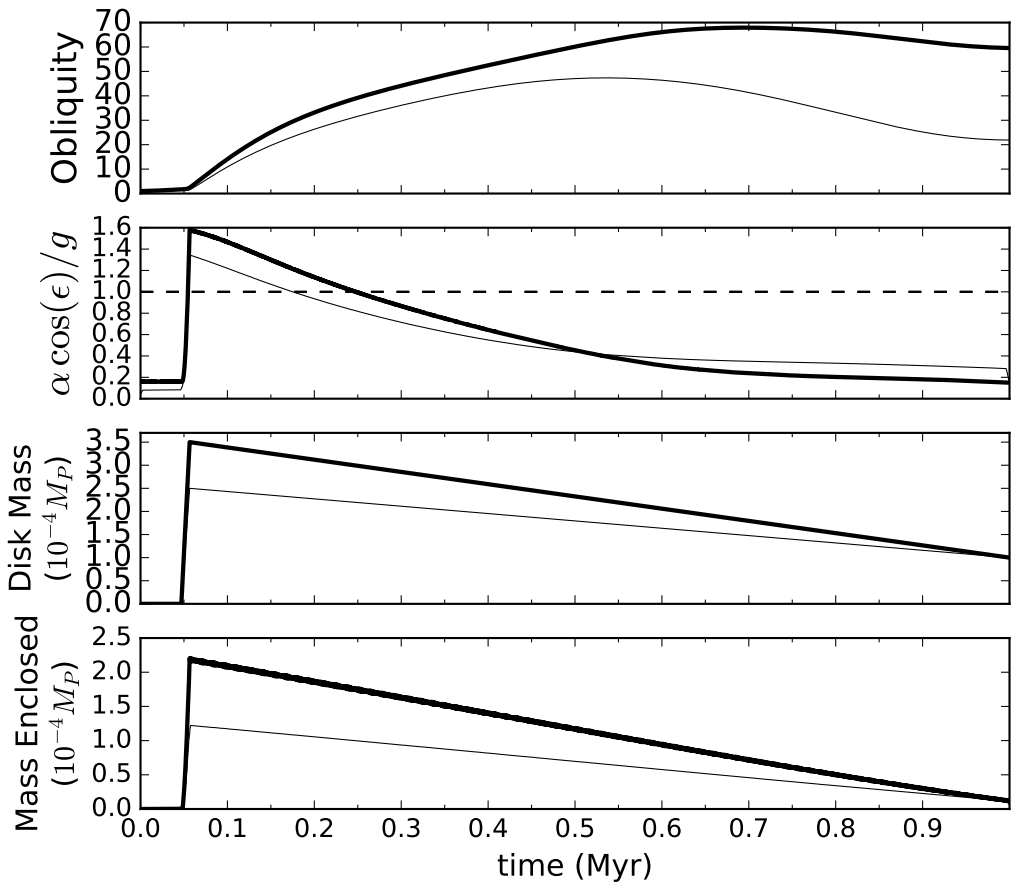
Figure 5.7: Same situation as in Figure 5.6, but R_L grows according to Equation 5.6, and $R_L \approx 200\,R_U$.

5.4 Tilting Neptune

Tilting Neptune is easier, since its obliquity needs only to be driven to $30°$. If Neptune accreted its gas while located inside Uranus's current orbit in accordance with the Nice model (Gomes et al., 2005; Morbidelli et al., 2005; Tsiganis et al., 2005) and grew similarly to Uranus as described previously, and we consider the two limiting scenarios for varying a planet's Laplace radius, then a disk with $M_d \approx 7 \times 10^{-4} - 4 \times 10^{-3} M_N$ can speed up its spin precession rate to generate a spin-orbit resonance and tilt Neptune assuming a primordial $i_N = 3°$. Alternatively, if Neptune is located at 28 au with an inclination of $10°$, then, as seen in Figure 5.8, the disk needs at least $3.5 \times 10^{-4} M_N$ of gas to generate a spin-orbit resonance. The resonance drives Neptune's obliquity more weakly than Uranus's because libration rates are slower farther away from the Sun. In this figure, we set Neptune's initial spin angular momentum to be near its current value, and the disk's mass changes by only about 10% if we reduce the planet's initial spin rate by a factor of 4. In the unphysical limiting case, where R_L depends only on the planet's J_2, the disk needs to be twice as large to generate a resonance; regardless, a $30°$ tilt can be attained in ~ 1 Myr. If Neptune's inclination is instead $5°$, then the accretion timescale needs to be 2 Myr to tilt the planet to $\sim 30°$.
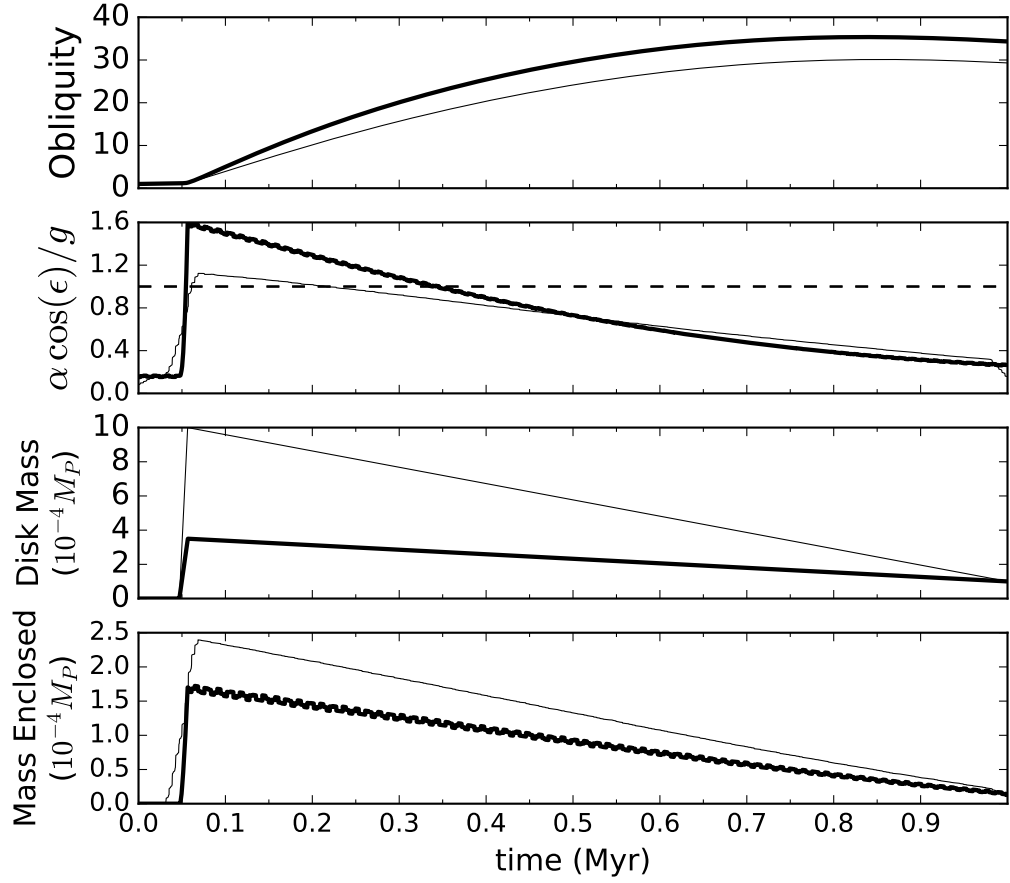
Figure 5.8: The evolution of Neptune's obliquity via a spin-orbit resonance if the planet harbored a massive disk. Here $M_0 = 0.9 M_N$, $R_0 = 80 R_N$, $a_N = 28$ au, $i_N = 10°$, and Neptune's initial angular momentum is approximately the planet's current value. The thick bold lines have R_L evolve according to Equation 5.6, while the thin bold lines have R_L depend only on the planet's quadrupole moment. The Laplace radius for the former case shrinks from $250 - 150 \, R_N$, while in the latter case the Laplace radius increases from $180 - 195 \, R_N$.

5.5 Conclusion and Future Work

Uranus and Neptune are not capable of entering a spin-orbit resonance today, as their spin axis precession rates are far too slow to match any of the planets' orbital precession frequencies. We have demonstrated that it is possible for both Uranus and Neptune to generate spin-orbit resonances if surrounded by a circumplanetary disk. Mass extending well beyond the classical Laplace radius can contribute to pole precession, meaning that the mass required to trigger a resonance is a modest 3-10 times the mass of their current satellite systems. Regardless of whether the disk remains in a steady state or is depleting, Uranus can be tilted up to 70° if its orbit is inclined by more than 5°, and Neptune can be tilted all the way to 30° with less inclined orbits. As per the conclusion from Chapter 2, an initial obliquity this high would provide an order of magnitude improvement to the collision model for tilting Uranus. Therefore, a hybrid model that includes both resonance and collisions is the most likely scenario, as it can eliminate the collision responsible for tilting Neptune, eliminates at least one of the impactors required to tilt Uranus (Morbidelli et al., 2012), requires less massive impactors which were probably more abundant than Earth-mass cores in the early solar system (Levison et al., 2015a,b), and, most importantly, preserves the near equality of Uranus's and Neptune's spin rates.

To reiterate, though, this strong resonance argument (Equation 1.1) is not capable of tilting planets beyond 90° because the resonance will break as the planet's spin precession frequency nears zero (Equation 4.2). Quillen et al. (2018) showed that a different resonant argument that includes mean motion terms and is not

sensitive to orbital inclinations can push obliquities beyond 90°. Since the circumplanetary disk model requires Uranus to have an orbital inclination greater than 5° to generate large tilts, exploring these other resonance arguments would be a natural extension for future work. This class of resonances requires additional planets potentially arranged in resonant chains. The forming giant planets may have started in or entered into such resonance chains, and in certain configurations, these mean-motion resonances can drive planets into a spin-orbit coupling (Millholland & Laughlin, 2019). Thommes & Lissauer (2003) also argued that inclination growth can occur when planets are trapped into certain low order eccentricity-exciting mean-motion resonances, so an orbital evolution scenario that can simultaneously explain the configuration and tilts of the ice giants may exist. Ice giant formation models, however, do not require them to be placed into mean motion resonances as they acquire their gaseous atmospheres. There are a lot of potential scenarios, too many to pursue in this work. As for the cases discussed in this chapter, we find that an additional collisional kick to Uranus's obliquity is inescapable.

Chapter 6: The Role of Collisions in Determining Irregular Satellite Spins

6.1 Introduction

6.1.1 The Origin of Irregular Satellites

Satellites around giant planets are thought to form after the planet accretes its gaseous atmosphere from the remnant circumplanetary disk (Lunine & Stevenson, 1982; Canup & Ward, 2002), which explains the equatorial circular prograde motion of the regular satellites. Phoebe's discovery, however, exposed the possibility of an additional avenue to satellite formation (Pickering, 1899). Since Phoebe is located far away from Saturn and orbits retrograde to the planet's spin, it was classified as the first observed irregular satellite. More of these moons have since been discovered around each giant planet, especially within the past twenty years, totaling to about 145 and vastly outnumbering the total regular satellite populations[1] (Gladman et al., 1998, 2001; Sheppard & Jewitt, 2003; Holman et al., 2004; Kavelaars et al., 2004; Sheppard et al., 2005, 2018). The term 'irregular' is therefore a byproduct of past observational bias, an historical anomaly, and does not indicate any particularly

---

[1] See here for a full updated list by Scott Sheppard: `https://sites.google.com/carnegiescience.edu/sheppard/moons?authuser=0`

perceived peculiarities. Formally, with the exception of our Moon and Triton, irregular satellites are rock-ice objects located on stable orbits around the giant planets at distances where gravitational perturbations from the Sun dominate over those from the central planet's quadrupole (Burns & Matthews, 1986, See Section 5.2). They differ from regular satellites not only by their large distances, but by also having a larger range of orbital eccentricities (Figure 6.1) and inclinations (Figure 6.2). In fact, most known irregular satellites travel on retrograde orbits, in striking contrast to their better-behaved neighbors. This may be a result of detection bias since prograde satellites tend to be located closer to the planet making them harder to spot, but regardless, retrograde satellites are numerous.

The existence of these large populations of retrograde satellites and the wide range of eccentricities suggests that these outer moons were likely captured from the protoplanetary disk, though scattering between inner regular moons may excite satellites to higher eccentricities and inclinations (Perets & Payne, 2014). Effective capture mechanisms require the incoming bodies to lose enough energy to be placed on bound orbits. The pull-down mechanism, where the sudden growth of a gas giant as it undergoes runaway gas accretion increases its Hill radius enough to place surrounding bodies on stable orbits, is one proposed formation channel for irregular satellites around Jupiter and Saturn (Heppenheimer & Porco, 1977; Vieira Neto et al., 2004, 2006); however, this method may not explain Uranus's and Neptune's irregular satellite populations as these ice giants are not massive enough to undergo runaway growth. Dissipation via gas-drag as the body passes through a growing giant planet's extended envelope is another possible mechanism, but cap-
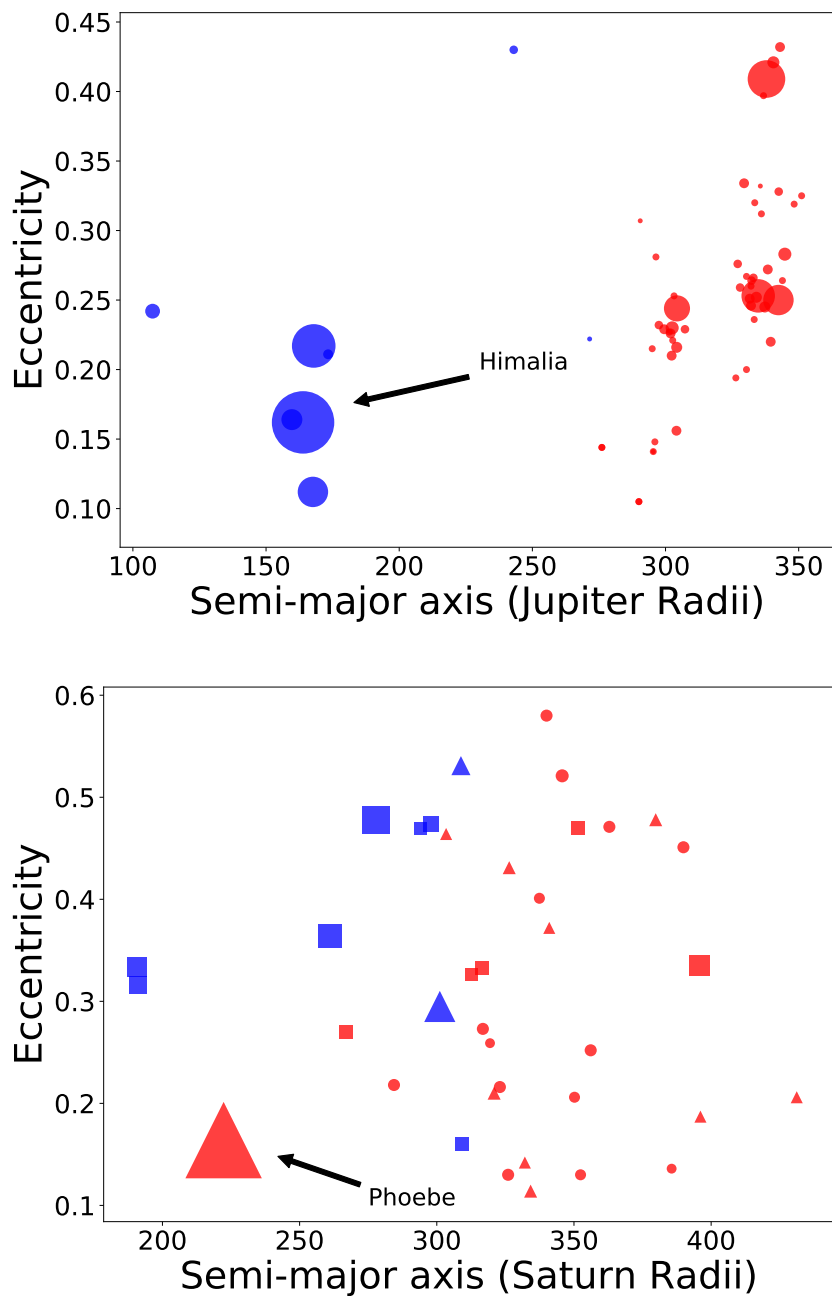
Figure 6.1: The eccentricities of Jupiter's and Saturn's irregular satellites vs. their semi-major axes. For Saturn, square points have slower than average (median) spin-rates, while triangles indicate faster spin rates. Those with unknown spin rates are circles. The number of irregular satellites around Jupiter with known spin periods is low, and so their spins are not shown here. Blue are prograde orbiting satellites, while red are retrograde orbiting satellites.
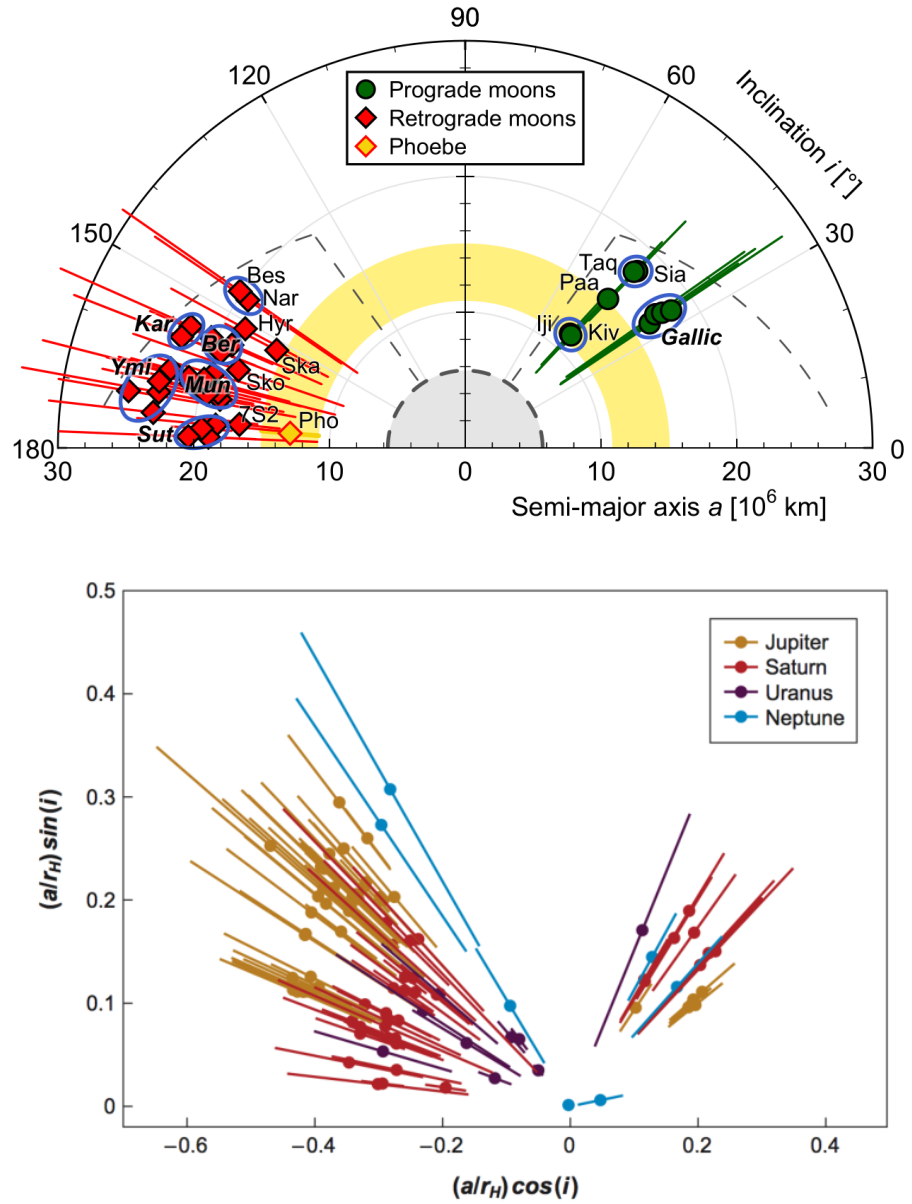
Figure 6.2: (top) A plot of Saturn's irregular satellites' inclinations verses their semi-major axes taken from Denk et al. (2018). The thin bars crossing through each satellite in both plots are the total radial extent of their orbits from pericenter to apocenter. The light-yellow band is the extent of Phoebe's sphere-of-influence, and the dashed line is the apparent outer boundary of the satellites' semi-major axes and inclinations. Families and pairs are circles, and their family names are in bold text. (bottom) A polar plot of the inclinations of all the giant planets' irregular satellites taken from Jewitt & Haghighipour (2007).

ture efficiency is size dependent and the lifetime of this envelope is short (Pollack et al., 1979; Ćuk & Burns, 2004). In addition, since an abundance of Kuiper Belt Objects are postulated to be in binaries (Stephens & Noll, 2006; Noll et al., 2008), three-body interactions, where the pair splits due to tidal disruption leaving one body bound to the planet and the other free carrying with it excess energy, works with all giant planets (Agnor & Hamilton, 2006). Finally, capture efficiency can increase during close encounters when the giant planets' orbits are disrupted in the early stages of planetary migration (Nesvorný et al., 2007; Vokrouhlický et al., 2008; Nesvorný et al., 2014; Li & Christou, 2020; Li et al., 2020), and the presence of a circumplanetary disk can also provide a dissipative force to stabilize larger captured irregular satellites around Jupiter and Saturn (Philpott et al., 2010). Regardless of the capture mechanism, we expect the satellites to possess a wide range of orbital parameters, yet there are clear gaps in these systems' orbital architectures.

The structures of these satellites' orbits as depicted in Figures 6.1 and 6.2 are byproducts of a rich variety of dynamical interactions. For example, the lack of satellites with inclinations between 50° and 130° can best be described by instabilities due to Lidov-Kozai resonances (Kozai, 1962; Lidov, 1962; Gladman et al., 2001; Carruba et al., 2002; Nesvorný et al., 2003), where perturbations from the Sun excite eccentricities of highly inclined orbits resulting in either collisions with inner bodies or ejections. Also, satellites that orbit retrograde are typically found farther away from the planet because they are more stable to perturbations from solar tides (Hamilton & Krivov, 1997; Nesvorný et al., 2003). This can be roughly explained by evection resonances, a match between the precession rate of a satellite's apsis and

the planet's orbital period (Yoder & Kaula, 1976; Touma & Wisdom, 1998), which causes the satellite's apocenter to be tidally locked with the Sun. In this configuration the satellite's eccentricity increases until it strikes the planet (Spalding et al., 2016). There are several numerical and semi-analytic solutions to these stability boundaries, but typically prograde orbits enter into these evection resonances at around half the planet's Hill radius, while retrograde orbits are stable to $\sim 0.7\,R_{\mathrm{Hill}}$ (Saha & Tremaine, 1993; Hamilton & Krivov, 1997; Nesvorný et al., 2003; Domingos et al., 2006; Yokoyama et al., 2008; Frouard et al., 2010). Jupiter's Hill radius is about 740 planetary radii, so the clear segregation between prograde and retrograde satellites in Figure 6.1 is consistent with this model.

Saturn's irregular satellite population, despite its retrograde satellites dominating at farther distances, is more mixed as dynamical timescales are slower. In addition to the previously mentioned instabilities, these crossing orbits suggests that collisions were once common. Furthermore, many irregular satellites share similar orbital elements and are grouped into families, as they may have previously been parts of a larger satellite that was broken up. Nesvorný et al. (2007) argue that the original satellite system was at least 10 times more massive after the giant planets captured them during planetary migration, and over hundreds of Myr the satellites ground down to their current population. Bottke et al. (2010) instead posit that the original satellite system was 100 times more massive because the current size frequency distribution of satellites larger than 8 km is the shallowest out of all populations of small bodies. In this case, if the original size frequency distribution was steeper and similar to the Trojan asteroids (Dohnanyi, 1969), then there would be

more available small bodies to collide with the satellites. Over time the number of available smaller satellites capable of disrupting the larger ones will deteriorate, and this disparity trickles down to smaller satellites until all that remains is an overabundance of larger moons (Kennedy & Wyatt, 2011). While extrapolating backwards from an exponential decay of a dynamical system is prone to inaccuracies, these satellite systems with typical orbital speeds of 1.5 km/s were still likely to be more massive and highly collisionally active.

Collisions can therefore shape the orbital architecture of a satellite system, but they can also alter a satellite's spin state. The Cassini–Huygens spacecraft has taken photometric lightcurves of 25 irregular satellites, and Denk & Mottola (2019) have cataloged their rotation rates; however, their obliquities, apart from Phoebe's, are still unknown. Saturn's smaller retrograde satellites spin on average faster $(2.7\,\mathrm{day}^{-1})$ than their prograde counterparts $(1.5\,\mathrm{day}^{-1})$ (Figure 6.1). As discussed in Chapter 2, giant impacts yield fast spin rates while a large number of smaller collisions can slow down a body's spin (Dones & Tremaine, 1993a). Strong-enough impacts would also alter the satellite's orbits, which may also explain Phoebe's and Himalia's relatively circular orbits and smaller semi-major axes (Figure 6.1). In this chapter we explore the possibility that the satellite's spin rates were a byproduct of collisions, and whether these collisions were powerful enough to change their orbits.
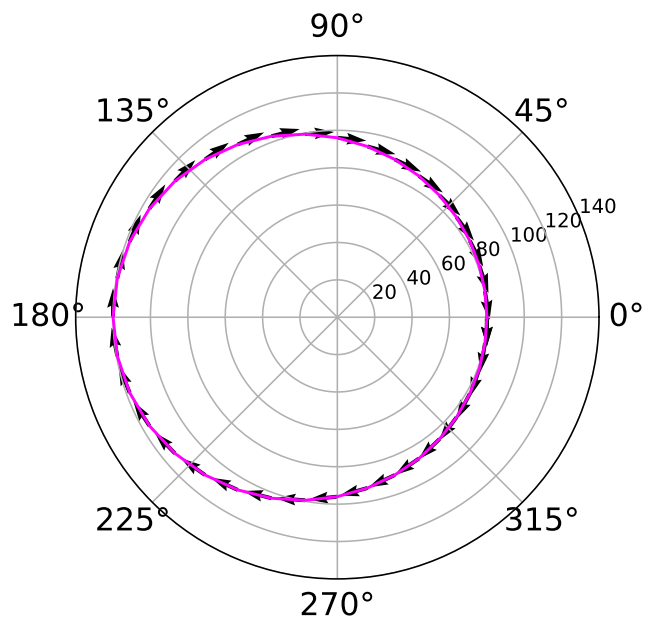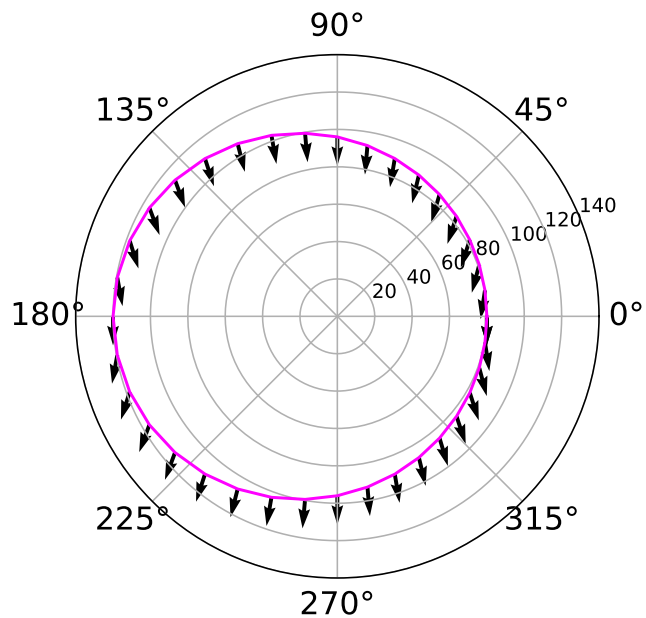
Figure 6.3: (top) A satellite orbiting counter-clockwise being struck by particles orbiting in the same direction on circular orbits. Here $a = 100$, and $e = 0.2$. The vectors point in the impact direction of $\bar{J}$. (bottom) The same vector plot but with the particles orbiting clockwise.

6.1.2 Orbital Migration and Evolution from Collisions

A projectile colliding with a satellite supplies an impulse, a change in linear momentum, that subsequently changes the satellite's orbit. The corresponding impulse is given as

$$\mathbf{J} = m_p(\mathbf{v_2} - \mathbf{v_1}) \tag{6.1}$$

where $\mathbf{v_2}$ is the velocity of the projectile, $\mathbf{v_1}$ is the velocity of the satellite, and m_p is the projectile mass. If the satellite revolves on an eccentric orbit, and the projectiles' orbits are circular, then the polar form of equation 6.1 is

$$\mathbf{J} = m_p\sqrt{\frac{GM}{a}} \left(-\frac{e\sin(\nu)}{\sqrt{1-e^2}}\hat{r} + \left(1 - \frac{1 + e\cos(\nu)}{\sqrt{1-e^2}}\right)\hat{\phi} \right), \tag{6.2}$$

where M is the mass of the planet, a is the semi-major axis, e is the eccentricity, and ν is the true anomaly.

Figure 6.3 shows the direction of the impulse at each point of a satellite's prograde orbit if it was struck by a particle revolving on a circular orbit in either the prograde (top) or retrograde direction (bottom). For prograde-prograde collisions near the satellite's pericenter, the impulse points in the direction of decreasing orbital energy. Collisions near apocenter instead increases the target's orbital energy, but on average over the entire orbit the satellite's semi-major axis decreases. This is also true for its eccentricity and inclination. Head-on collisions, on the other hand, are much more violent, so the satellite loses more orbital energy. Its eccentricity and inclination, however, tend to increase. The equations describing changes to a
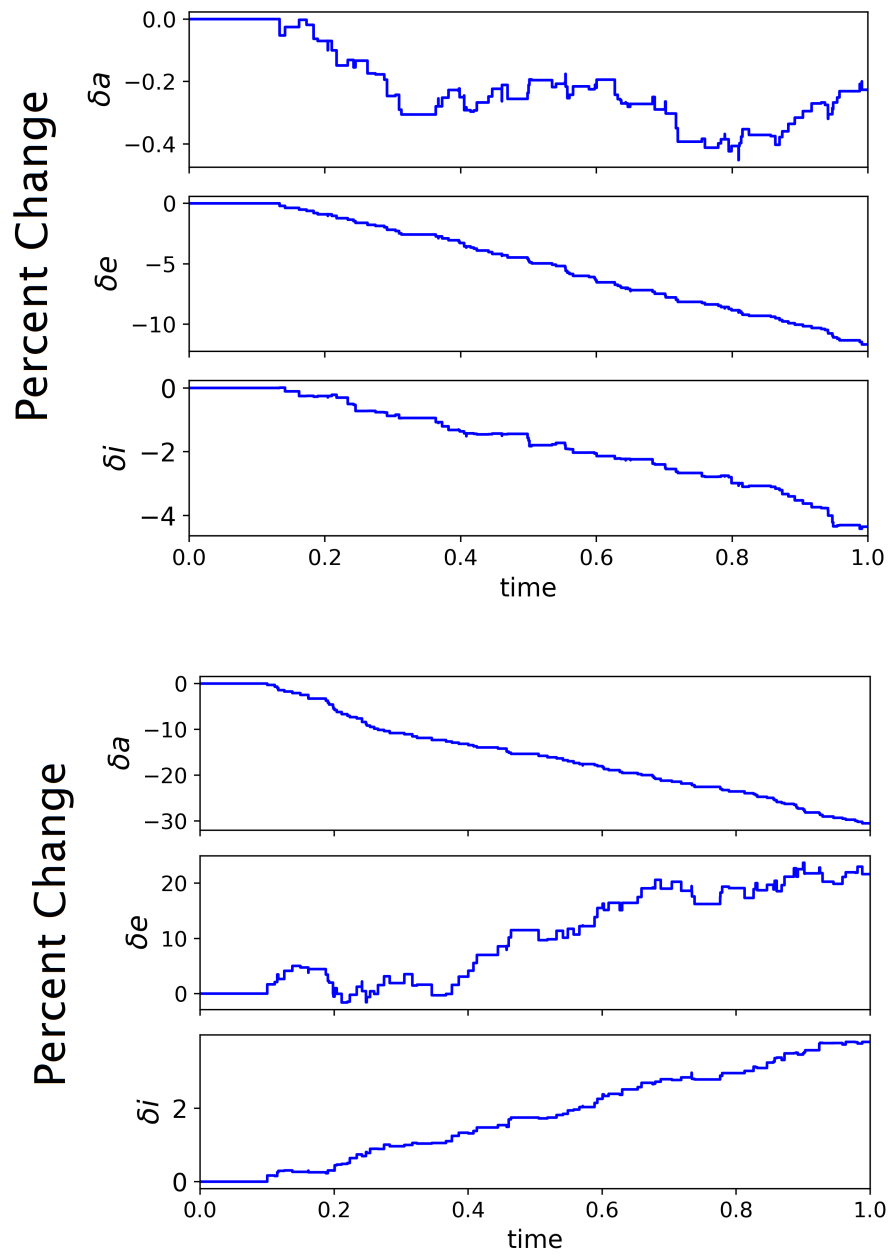
Figure 6.4: These figures show a satellite orbiting Saturn with an initial semi-major axis of 1.3×10^7 km, eccentricity of 0.2, and inclination of 5° after being struck by 100 objects each 0.1% of the satellite's mass. The Y-axes show the relative percent changes of the orbital elements, and the unit for time is arbitrary. (Top) Prograde-prograde collisions. (Bottom) Prograde-retrograde, or head-on, collisions.

satellite's orbital elements from isolated impulses are given in Danby (1992)[2], and are rewritten here

$$\frac{da}{dt} = \frac{2na^2}{\mu} \left(R\frac{ae}{\sqrt{1-e^2}} \sin\nu + B\frac{a^2}{r}\sqrt{1-e^2} \right) \tag{6.3}$$

$$\frac{de}{dt} = \frac{na^2}{\mu}\sqrt{1-e^2} \left(R\sin\nu + B(\cos\nu + \cos E) \right) \tag{6.4}$$

$$\frac{di}{dt} = \frac{nar}{\mu\sqrt{1-e^2}} N\cos u, \tag{6.5}$$

where R, N, and B are components of the impulse $\bar{J} = R\hat{r} + N\hat{h} + B\hat{h} \times \hat{r}$, and E is the eccentric anomaly. $\hat{r}$ points radially outwards and $\hat{h}$ points in the direction of the body's orbital angular momentum. Also, $u = \omega + \nu$ where ω is the argument of pericenter, n is the orbital angular speed, r is the satellite's distance, and μ is the standard gravitational parameter.

In the following simulations we use HNBody (Rauch & Hamilton, 2002) to calculate the motion of a test satellite's trajectory, and we use the package HNDrag to calculate the impulses imparted. The impactors possess a range of possible orbital and physical characteristics, so we need to control the magnitude of these impulses using a code built around HNDrag. Calculating the impactor's velocity, which is a function of its position and six orbital elements, upon impact requires making a few assumptions. The impactors' position vector is identical to the satellite's, and this is provided by HNBody. The impactor's eccentricity and inclination are drawn randomly from 0 to an average value from present day orbits, its semi-major axis is

---

[2]pg. 327

137

drawn randomly between $r/(1+e)$ and $r/(1-e)$, and we calculate the other angles using equations found in Chapter 2 of Murray & Dermott (1999). The velocity of an orbiting body as a function of orbital elements is the derivative of the position vector (Murray & Dermott, 1999)

$$
\begin{aligned}
V_x &= \tfrac{x}{r}\tfrac{he}{p}\sin\left(\nu\right) - \tfrac{h}{r}\left(\cos\left(\Omega\right)\sin\left(u\right) + \sin\left(\Omega\right)\cos\left(u\right)\cos\left(i\right)\right) \\
V_y &= \tfrac{y}{r}\tfrac{he}{p}\sin\left(\nu\right) - \tfrac{h}{r}\left(\sin\left(\Omega\right)\sin\left(u\right) - \cos\left(\Omega\right)\cos\left(u\right)\cos\left(i\right)\right) \qquad (6.6) \\
V_z &= \tfrac{z}{r}\tfrac{he}{p}\sin\left(\nu\right) + \tfrac{h}{r}\left(\cos\left(u\right)\sin\left(i\right)\right)
\end{aligned}
$$

where Ω is the longitude of the ascending node, $p = a(1 - e^2)$, and $h = \sqrt{\mu p}$ is the specific angular momentum. The satellite's mass also increases after each impact, and Figure 6.4 shows the corresponding simulations for a satellite increasing in mass by 10% after 100 inelastic collisions. The difference between changes to a satellite's semi-major axis in the two cases is the most dramatic as head-on collisions can cause significant inward migration.

6.2   Striking Satellites

The objective here is to narrow down the possible fractions of head-on collisions, total mass imparted, and number of impactors that could reproduce the observed spin distributions. To do this we apply the spin code discussed in Chapter 2 to track the satellite's spin state in the impulse code.
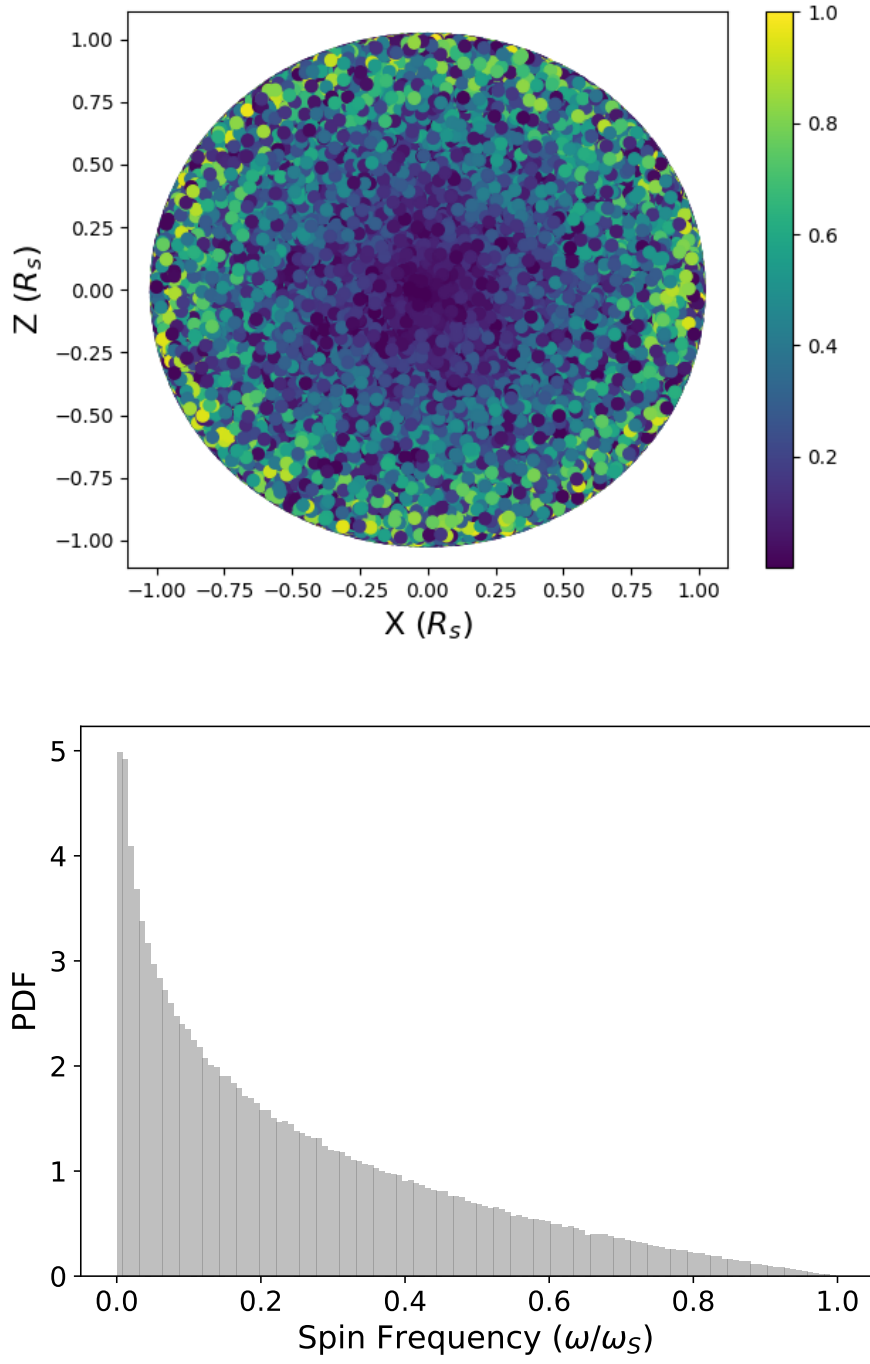
Figure 6.5: (top) A scatter plot of the angular momentum imparted over the satellite's surface with the axes in units of the satellite's radius. The target has a mass of 2.3×10^{15} kg, and a radius of 7.5 km. The colorbar is the angular momentum imparted normalized by $m_i R_s (0.3 v_{\mathrm{circ}})$. (bottom) This is the corresponding spin distribution after being struck by an impactor one-thousandth of the satellite's mass for 5×10^5 realizations. The satellite is initially non-spinning, and the impactor's eccentricity ranges from 0–0.3 striking the satellite at a speed of $e v_{\mathrm{circ}}$.

6.2.1 Spin Conditions

An irregular satellite around Saturn orbits with a speed between 1.2 km/s and 1.8 km/s, while Phoebe's escape speed is less than 6% of this; therefore, gravitational focusing is not important here as it was for Uranus in Section 2.1. The impulse code calculates the impactor's velocity directly given the target's distance and a range of possible orbital elements the satellite may have, and we use that speed to calculate the spin angular momentum imparted. Note that the relative velocity for small eccentricities for two particles traveling in the same direction with similar semi-major axes is $v_{\text{rel}} \sim e v_{\text{circ}}$ (Hamilton & Burns, 1994), so the satellite's spin distribution depends on the impactor's orbital eccentricity. Figure 6.5 is an example of the spin probability distribution of a prograde orbiting satellite if struck by one prograde impactor whose orbital eccentricities can be any value from 0 to 0.3. Since the velocity upon impact is dominated by the satellite's relative velocity, the angular momentum imparted at each annulus ranges from 0 to $m_i R v_\perp$, where R is the distance away from the center of the moon's target plane and $v_\perp$ is the component of v_{rel} perpendicular to the radius vector; therefore, the spin distribution decreases with R^{-1}. If the impactor instead orbits retrograde, then $v_{\text{rel}} \approx 2 v_{\text{circ}}$ and the spin distribution increases with R.

In these runs we assume the satellites' moment of inertia factor is 0.4. Since they are small rock-ice bodies, their density distributions should be fairly uniform (e.g. Anderson & Schubert, 2007) and we do not expect a series of small impacts to significantly alter a satellite's moment of inertia. We also assume their radii

vary with a constant density profile. The mass imparted is generally much less than 10% of the satellite, so we do not expect the satellite's radius to noticeably change. The target's initial spin rate is initially set to zero for simplicity. It is possible, however, that the satellites' initial spin rates were not slow. The average rotation rate of transneptunian objects is about 2.8 cycles/day (Sheppard et al., 2008; Thirouin et al., 2014), which is consistent with the spin rates of Saturn's retrograde population. If these satellites were captured transneptunian objects and the observed spin rates were indeed primordial, then it would be difficult to explain the differences between the prograde and retrograde populations. In this Chapter we explore an alternative possibility for the origin of their spin rates, and seek the conditions required to reproduce the satellites' spin distributions from collisions with other irregular satellites. We will leave the possibility that these satellites may have been captured with faster spin rates for future work.

An approximation to the mass of the impactor required to generate a satellite's spin rate, assuming that the initial spin and added momentum are parallel, is

$$m_i = \frac{0.4 M_s R_s^2 \omega}{R v_\perp} - \frac{L_0}{R v_\perp}, \tag{6.7}$$

where L_0 is the satellite's initial spin angular momentum. In the initially non-spinning case, $L_0 = 0$ and the angular momentum imparted by the impactor dictates the satellite's spin period. If the impact location is the satellite's radius $R = R_s$, then for a typical prograde satellite with mass 2.3×10^{15} kg, the mass of the impactor needs to be on the order of 10^{12} kg. Assuming a constant density of 1.3 g/cm^3,
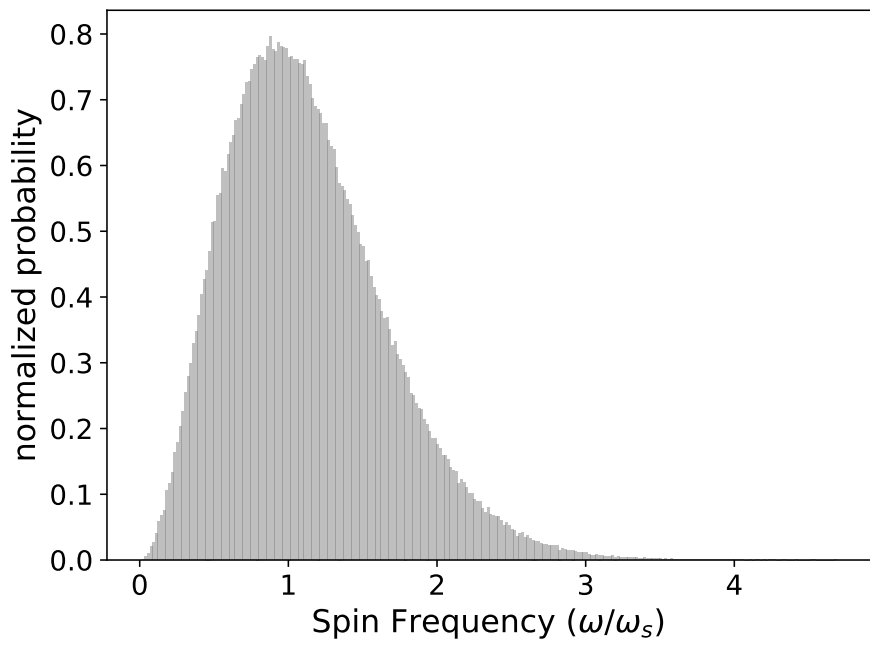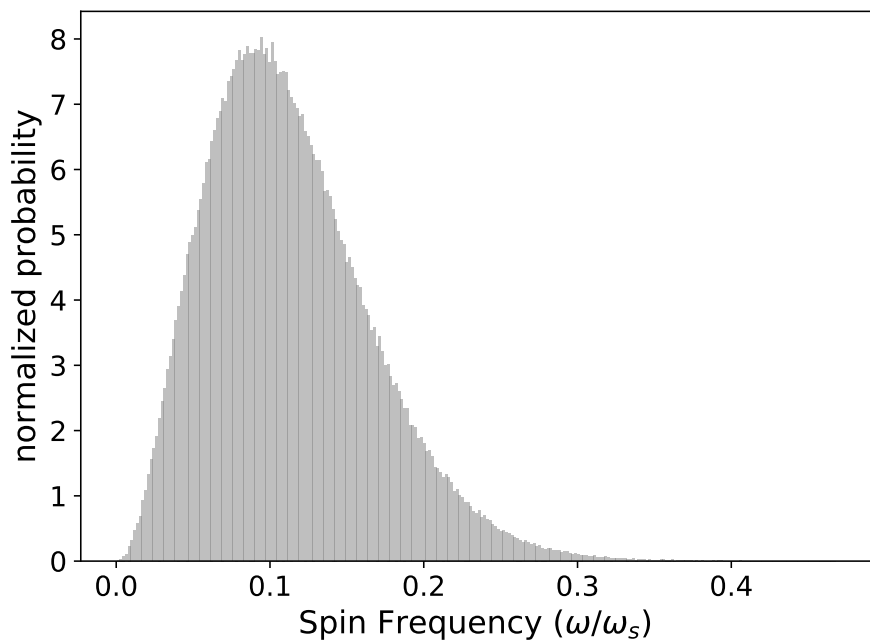
Figure 6.6: (top) The same case as in Figure 6.5 but with ten equally massive impactors totaling to one-thousandth of the satellite's mass. (bottom) The satellite being struck by ten equally massive impactors totaling to one-hundredth of the satellite's mass.

we can simplify this expression for a grazing impact on an initially slow spinning satellite to

$$m_i = 1.7 \times 10^{12} \left(\frac{M_s}{2.3 \times 10^{15}\,\mathrm{kg}} \right)^{4/3} \left(\frac{16\,\mathrm{hr}}{T} \right) \left(\frac{0.45\,\mathrm{km/s}}{v_{\mathrm{rel}}} \right)\,\mathrm{kg}, \qquad (6.8)$$

where T is the satellite's current spin period.

Figure 6.5 shows the spin distribution of a 2×10^{12} kg impactor striking a satellite with mass of 2.3×10^{15} kg, and 7.5 km radius. The relative speed of the impactor is 0.45 km/s, which is 70 times faster than the target's escape velocity. However, if that satellite's spin rate was a byproduct of multiple impacts totaling to 2×10^{12} kg, then the spin distribution would peak at a slower spin rate (Figure 6.6). Ten times more mass is needed, in this case, for the spin distribution to peak near the satellite's current spin rate if struck by about ten prograde orbiting impactors. If the impactors were instead striking the planet head-on, then their relative velocities are now closer to twice the circular speed at around 3 km/s. Accordingly, smaller impactors by about an order of magnitude are required in this case to impart the same angular momentum.

A typical retrograde satellite is 1.5×10^{14} kg with radius 2.5 km, so a single impactor traveling in the same direction needs to be at least 5×10^{10} kg to reproduce the satellite's spin period, and the total mass imparted for multiple strikes needs to be 10 times that. Again, the total mass imparted reduces by about a factor of 10 if the impactors were orbiting in the prograde direction and striking the target head-on. Recall that the peak of the corresponding spin distribution shifts to slower spin

143

rates if the number of impactors increases, and increasing the total mass imparted shifts the peak to faster spin rates. We will need to explore different combinations of imparted mass, number of impactors, and relative velocities to understand which initial satellite populations can reproduce the observed spin rates.

6.2.2 Collision Rates

We calculate the impactor's velocity using information provided by HNBody and some inputted parameters, but determining whether the impactors are prograde or retrograde depends on their respective collision probabilities. There are a number of different derivations for collision timescales between orbiting bodies (e.g. Greenberg, 1982; JeongAhn & Malhotra, 2017), but for simplicity, and since each derivation yields similar results, we use the particle-in-a-box approximation of a satellite's collisional timescale modified for inclined bodies. It is given as

$$T_{\text{coll}} \approx \pi \left(\sin^2 i_{\text{imp}} + \sin^2 i_{\text{moon}} \right)^{0.5} \left(\frac{a_{\text{moon}}}{R_{\text{moon}}} \right)^2 \left(\frac{U_r}{U} \right) T_{\text{orb}} \qquad (6.9)$$

where T_{orb} is the moon's orbital period, a_{moon} is the moon's semi-major axis, R_{moon} is the moon's radius, i_{imp} and i_{moon} are the moon's and impactor's inclinations, U_r is the impactor's relative radial velocity, and U is the relative velocity between the moon and the impactor (Opik, 1976; Kessler, 1981; Hamilton & Burns, 1994). The collision rate per orbit is therefore: $r_{\text{coll}} = T_{\text{orb}}/T_{\text{coll}}$.

If the two objects' inclinations are nearly co-planar, then the vertical phase space that the particles sweep is small, as is the collisional timescale. This equation

is valid for either prograde or retrograde collisions as only the relative velocity varies between the two cases. If the impactor is orbiting in the opposite direction to the satellite, then it will sweep through the satellite's orbit with the same radial velocity as if it were orbiting in the other direction. For prograde-prograde impacts the relative velocity is approximately $U \approx eV_{\mathrm{circ}}$ for small eccentricities, and the ratio U_r/U is close to unity (Hamilton & Burns, 1994). For head-on collisions the relative velocity is about $U \approx 2V_{\mathrm{circ}}$, so the collision rate here is about 10-100 times faster. For a typical 7.5 km prograde orbiting satellite around Saturn, the collision rate for a prograde impact is about $r_{\mathrm{coll}} \approx 10^{-13}$. This translates to about $\sim 10^{-4}$ collisions over the age of the solar system, so the odds of one prograde impact is highly unlikely.

However, if there is a reservoir, N, of potential impactors crossing the satellite's orbit, then, assuming the satellite orbits prograde, the collisional probability that the impactor is also prograde is Nfr_{coll}, where f is the fraction of the disk of particles that orbit prograde. The total number of impacts over the age of the solar system is therefore $(4.5 \times 10^9 \, \mathrm{years}) \, Nfr_{\mathrm{coll}}/T_{\mathrm{orb}}$. Since retrograde impactors have a higher chance of striking the satellite, for each batch of simulations we choose the direction of the impactor by comparing the prograde collision rate to the total for a a given f: $p = fr_{\mathrm{pro}}/\left(fr_{\mathrm{pro}} + (1-f)r_{\mathrm{retro}}\right)$. Notice that this comparison is independent of the total number of available impactors.

6.2.3   Probabilities

To better understand the orbital diversity of the initial population and the number of impacts required to reproduce the observed spin rates, we compare the simulated cumulative distribution of spin rates to the observed data (Figure 6.7) using a two sample Kolmogorov–Smirnov (KS) test. A KS test checks whether the two samples are drawn from the same distribution, so failing the KS test means the conditions for collisions do not reproduce the observed spin rates. The p-value is the associated probability that gauges the level of significance that these two distributions are sampled from the same distribution, and we use this value when comparing runs.

Figure 6.8 shows cumulative distributions of an average-sized prograde orbiting satellite's spin rates for different fractions of head-on impacts. The satellite is initially non-spinning in order to understand the approximate amount of angular momentum imparted to reproduce the moon's spin rates. The impactors are all equally sized totaling to 0.1% of the satellite's mass (2×10^{15} kg), and a greater fraction of retrograde impacts can speed up a satellite to faster spin rates. To counteract these fast speeds, we require a greater number of smaller sized impactors to generate the observed spin distributions (Dones & Tremaine, 1993a; Lissauer & Kary, 1991, Chapter 2). Figure 6.9 shows a density plot of p-values where we vary the number of impacts incident on the satellite and the fraction of the total population that orbit prograde. The magenta feature that decreases to the right is the collection of simulations that pass the KS test because, as expected, a greater
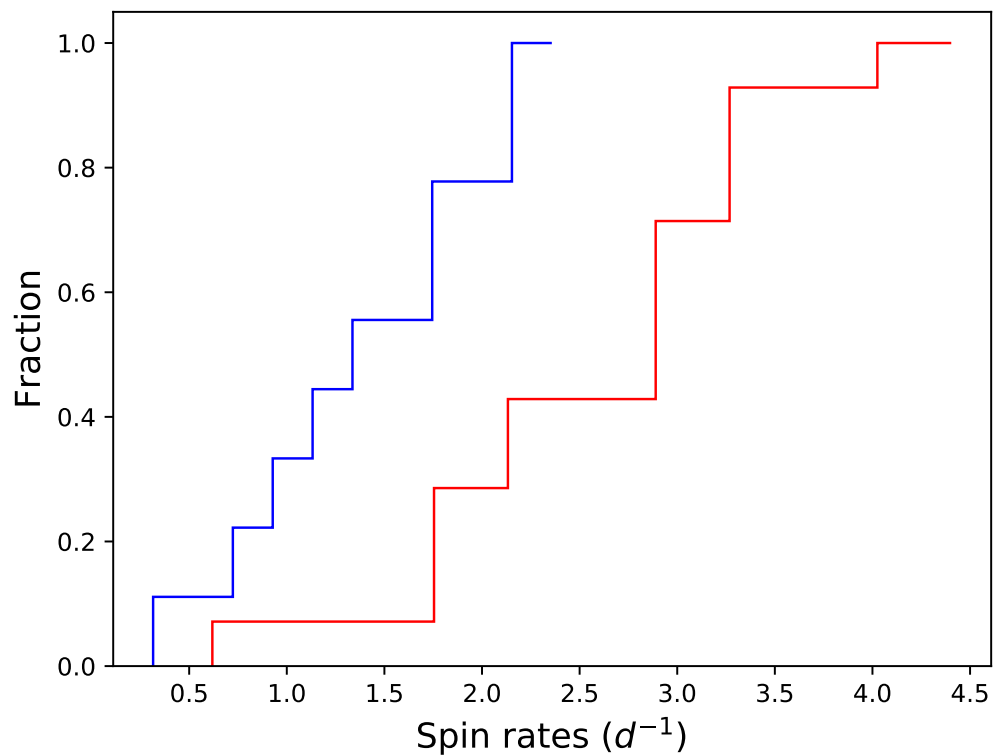
Figure 6.7: The cumulative distribution of the known spin rates (revolutions per day) of the prograde (blue) and retrograde (red) orbiting irregular satellites around Saturn.
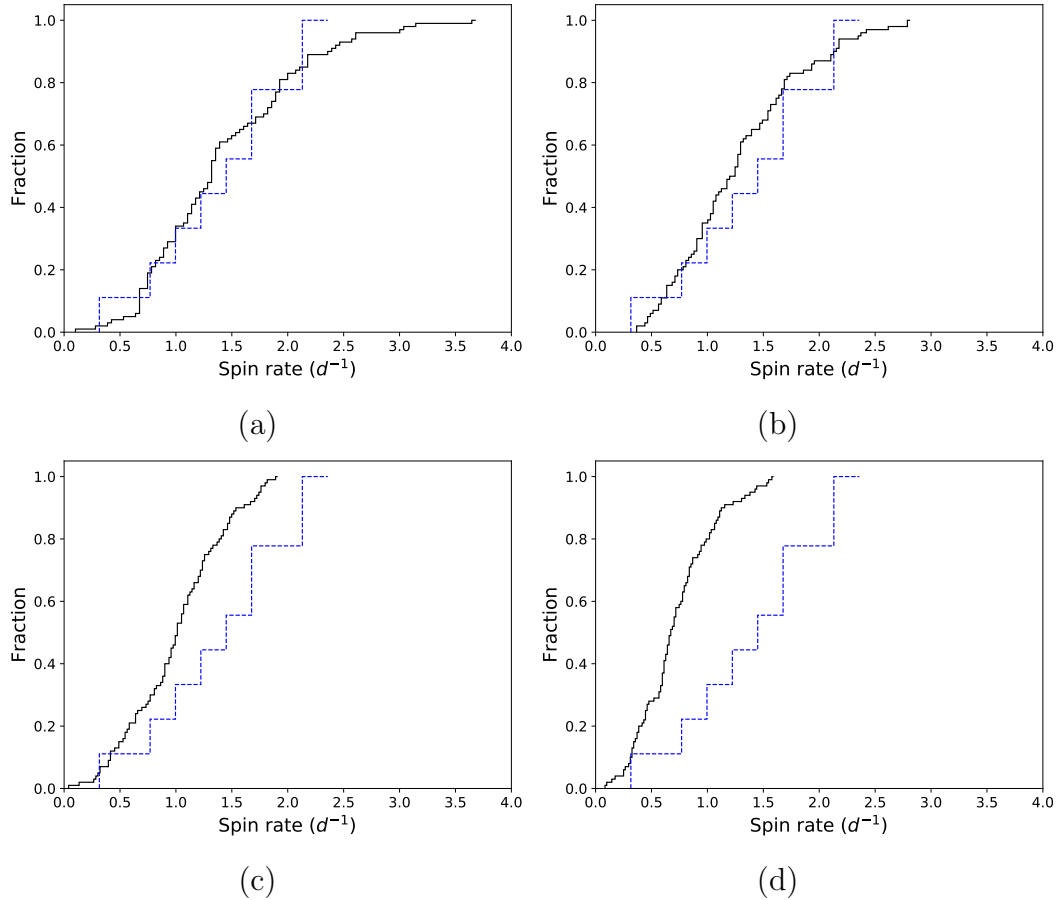
Figure 6.8: Cumulative distributions of the target prograde satellite's spin rate after 50 equal mass collisions totaling to 0.1% of the satellite's mass. The blue dashed distribution is the current observed spin distribution of the prograde irregular satellites around Saturn. (a) 100% retrograde impactors. (b) 60% retrograde impactors. (c) 40% retrograde impactors. (d) 20% retrograde impactors.
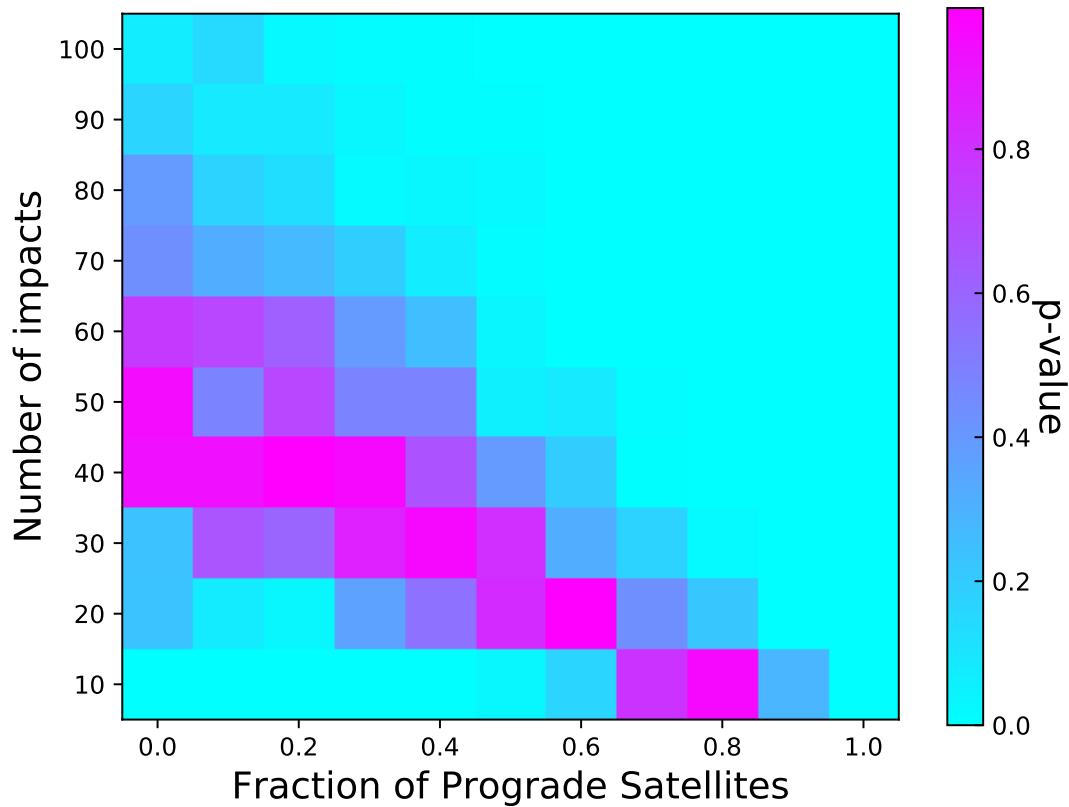
Figure 6.9: A density plot of p-values over the parameter space of the number of same-sized impacts (growing the satellite by 0.1%) incident on a prograde orbiting satellite verses the fraction of the total population that orbit prograde. The target satellite here is an average-sized prograde orbiting satellite around Saturn. It has an inclination of 10°, an eccentricity of 0.1, a mass of 2.3×10^{15} kg, a radius of 7.5 km, and a semi major axis of 1.5×10^7 km. Its initial spin rate is near zero. The impactors can have inclinations from 0° to 10°, and eccentricities from 0 to 0.1. Here each simulation is iterated 100 times.

number of smaller mass retrograde impactors are required as their relative speeds are faster. If the spin distribution was a byproduct of entirely prograde strikes, then fewer more massive impactors are required given our assumption of 0.1% total mass imparted.

6.2.4   Equal Sized Initial Satellite Populations

We will now look at different equal sized initial satellite populations to see which conditions can reproduce both spin distributions of Saturn's prograde and retrograde irregular satellites. In this subsection, we strike a target satellite representing a typical prograde or retrograde moon with equal sized impactors. The prograde target has a mass of 2.3×10^{15} kg and a radius of 7.5 km, and the retrograde target is smaller with a mass of 10^{14} kg and radius of 3 km. The prograde satellite is located 1.5×10^7 km away from Saturn, while the retrograde target is located 2×10^7 km away. Both targets revolve on orbits near the planet's mid-plane ($1°$ and $179°$) with eccentricities of 0.1, and are struck by impactors revolving on similar orbits. We explored whether we should compare the simulated and observed spin distributions for a range of satellite sizes for both prograde and retrograde populations, but Figure 6.10 shows that there is little to no correlation between the moons' sizes and spin rates. There may be a correlation with the prograde population in that the larger satellites tend to spin faster, but the variance is large and there are insufficient data to warrant such a detailed analysis.

Figures 6.11 and 6.12 show density plots of p-values for a range of total pop-
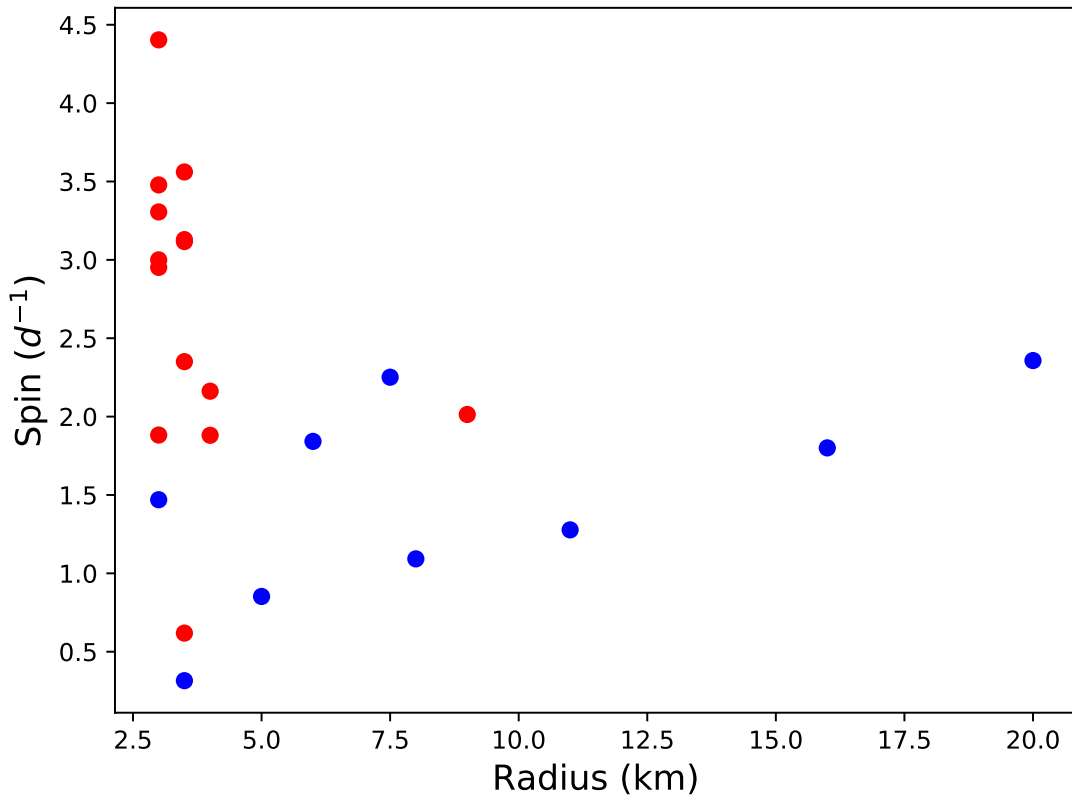
Figure 6.10: Size vs. spin rate for Saturn's prograde (blue) and retrograde (red) irregular satellites. Phoebe not included.

ulation of satellites and the fraction of satellites that orbit prograde. The scale of the x-axis is not increasing linearly in order to highlight the top and bottom 10%. For a typical prograde collision rate of $r_{\mathrm{coll}} \approx 10^{-13}$ and a retrograde collision rate ten times faster than that, f needs to be about 90% for the target to be struck by an equal amount of prograde and retrograde impactors; therefore, we should expect larger variations for simulations that pass the KS test for fractions greater than 90% (or less than 10% if the target satellite orbits retrograde). The target satellite in Figure 6.11 represents a typical prograde satellite, while the target satellite in Figure 6.12 orbits retrograde. Note that m is the relative mass of the incident impactors for each target satellite, and since the prograde satellites are about 10 times larger than the prograde satellites (excluding Phoebe) the impactors striking the prograde target are about 10 times larger than those striking the retrograde satellite. In the prograde case, the fraction of prograde impacts that can reproduce the observed spin rates increases as the mass of the impactors increase because the larger masses compensate for the slower relative speeds. Also, since the collision rate for retrograde impacts are at least 10 times that of prograde impacts for a prograde target, we should also expect more collisions overall for low f. The opposite is true if the target satellite orbits retrograde.

Overlaying the plots for each prograde-retrograde pair yields the simulations that can reproduce both populations. If the prograde and retrograde target satellites were located in an environment of potential impactors of similar mass, then we need to compare the top figure of Figure 6.11 and the bottom figure of Figure 6.12. Here each impactor is about 10^{10} kg, and the simulations that can produce both plots

152
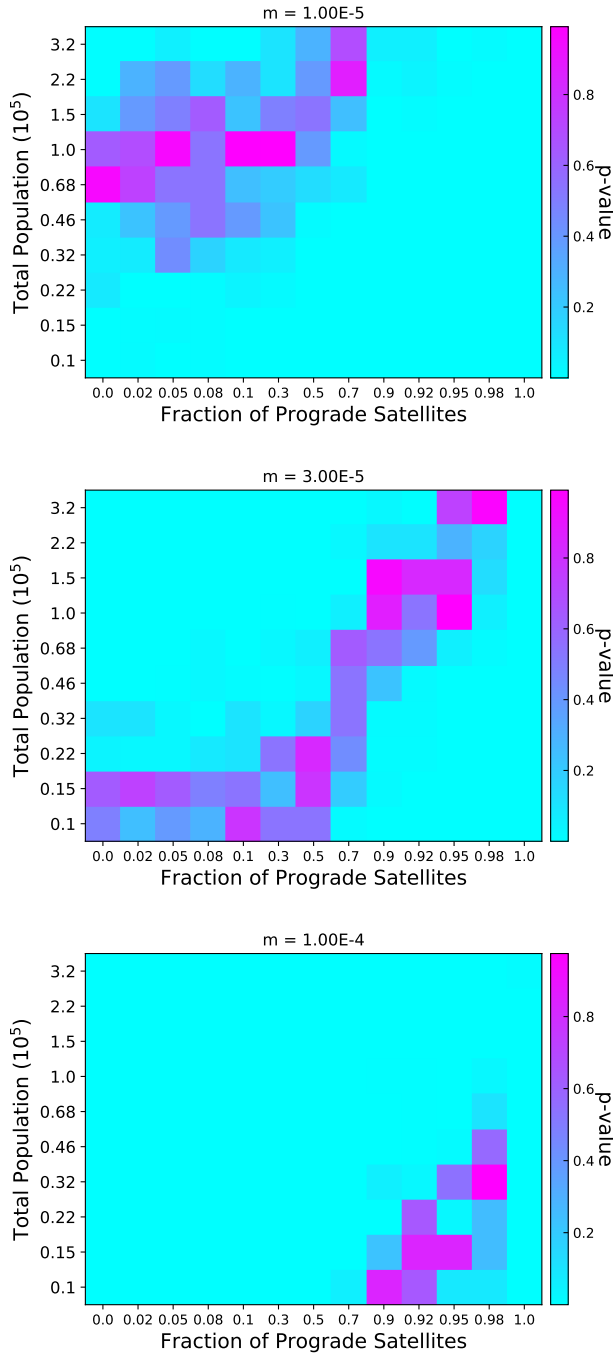
Figure 6.11: Density plots of p-values over the parameter space of equal sized impactors. From top to bottom, the relative mass of the impactors (m) increases from 10^{-5} to 10^{-4} times the mass of the satellite. The target satellite represents a typical prograde satellite similar to Figure 6.9 with a mass of 2.3×10^{15} kg, radius of 7.5 km, semi-major axis of 1.5×10^{7} km, eccentricity of 0.1, and inclination of $1°$. The impactors can have inclinations from $0°$ to $1°$, and eccentricities from 0 to 0.1. The satellites' spin rates are initially near zero, and each simulation is iterated 10 times.

153
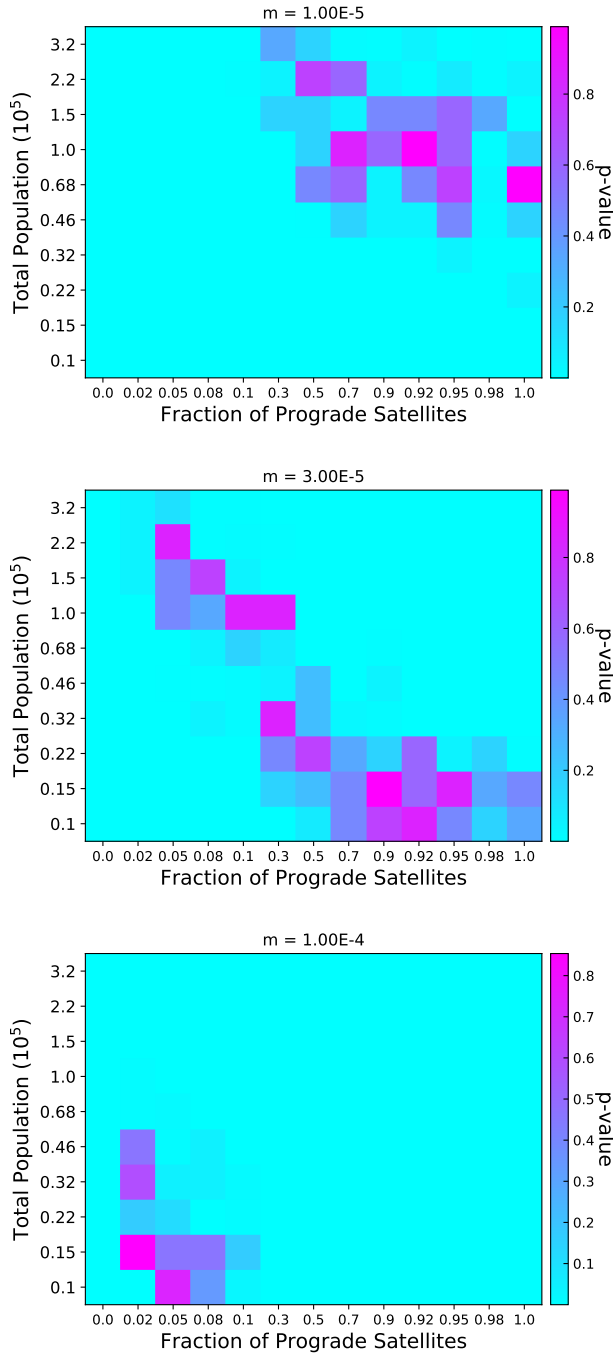
Figure 6.12: Density plots of p-values over the parameter space of equal sized impactors. From top to bottom, the relative mass of the impactors (m) increases from 10^{-5} to 10^{-4} times the mass of the satellite. The target satellite orbits retrograde (i=179°) with a mass of 10^{14} kg, radius of 3 km, semi-major axis of 2×10^7 km, and eccentricity of 0.1. The impactors can have inclinations from 0° to 1°, and eccentricities from 0 to 0.1. The satellites' spin rates are initially near zero, and each simulation is iterated 10 times.

154

requires an initial population of 40,000 satellites with 2% of them orbiting prograde. If the impactors were more massive, then there are no solutions that can reproduce the spin rates of both prograde and retrograde satellites. This is because the high p-values for the retrograde case in Figure 6.12 shift further towards the bottom left to smaller initial populations and lower f. If the impactors' masses decrease, then the high p-values for the prograde case in Figure 6.11 shift further towards the top left to larger initial populations and lower f. Since the retrograde satellites are typically smaller than the prograde satellites (excluding Phoebe), collisions for any given impactor mass will tend to be more violent for retrograde satellites. An impactor population that can reproduce the observed spin states for both prograde and retrograde populations should therefore be biased towards smaller masses. The higher relative velocities from impactors traveling retrograde onto a prograde target would account for their smaller masses and impart the same amount of angular momentum. Encouraged by our success with a population of single sized impactors, we now turn to more realistic size distributions.

6.2.5   Satellites Drawn from a Power-Law Distribution

Realistically, the disk population should resemble a power law rather than an ensemble of equally massive bodies. In the following simulations we draw satellites from a differential mass-frequency distribution that falls as a power law with indices

(γ) ranging from 1.5 to 2.5:

$$N(m)dm = N_0 \left(\frac{m}{m_{\min}} \right)^{-\gamma} dm. \tag{6.10}$$

Dohnanyi (1969) showed that the power-law for the differential mass distribution from debris from prograde-prograde collisions in the asteroid belt is about 2, but this can be different for irregular satellites experiencing a greater fraction of retrograde impacts. These distributions obviously do not extend to infinity, so we need to choose a maximum and minimum mass ($m_{\max}$ and $m_{\min}$) to bound the distribution.

This power-law distribution decreases with increasing mass, so there are more available small objects than big objects to strike the satellites. We want to ignore the effect of a series of impacts from really small objects because they would impart little angular momentum to the satellite, so we set the lower bound to that which can just reproduce the spin rates for a typical retrograde satellite. The top figure of Figure 6.12 shows that many 10^9 kg prograde impactors can reproduce the retrograde population's spin rates, so we set the lower bound to that. To set the upper bound we ran a series of simulations by varying $m_{\max}$ with $\gamma = 2$, and observed how the resulting p-value plots change with increasing $m_{\max}$. We chose $m_{\max}$ to be the point where the p-value plots converged, which is around 10^{12} kg (Figure 6.13). For example, if the upper bound was instead set to 10^{13} kg, then the odds of sampling such a large impactor is almost zero. With the bounds set, we vary the power-law index and compare the p-value plots for both prograde and retrograde target satellites.

Figure 6.13: Density plots of p-values over the parameter space of impactors drawn from a mass distribution. The maximum bound of the power-law distribution (Equation 6.10) varies in the three panels as follows: 10^{11} kg (top), 10^{12} kg (middle), 10^{13} kg (bottom) . The minimum bound is set to 10^9 kg, and $\gamma = 2$. The target satellite represents a typical prograde satellite similar to Figure 6.9 with a mass of 2.3×10^{15} kg, radius of 7.5 km, semi-major axis of 1.5×10^7 km, eccentricity of 0.1, and inclination of $1°$. The impactors can have inclinations from $0°$ to $1°$, and eccentricities from 0 to 0.1. The satellites' spin rates are initially near zero, and each simulation is iterated 100 times.

157

Figure 6.14 shows the p-value plots for the prograde satellites as we increase the power-law index from 1.5 to 2.5. The simulations that can reproduce the observed spin rates shift towards larger satellite populations and lower f for increasing γ because a steeper power-law index suggests an abundance of smaller impactors. Smaller projectiles need to strike the satellite at greater velocities to impart the necessary angular momentum, so a greater fraction of these should be traveling in the retrograde direction. Figure 6.15 shows the same plots for a retrograde target satellite, and the p-value plots evolve similarly for increasing γ.

Figure 6.16 shows the geometric mean of p-values for each pair of plots for prograde and retrograde target satellites over a range of γ, and the maximum shows the simulations that can best reproduce both populations. In these sets of simulations the collision rates for head-on (prograde impactors onto a retrograde satellite and retrograde impactors onto a prograde satellite) and non-head-on (prograde-prograde and retrograde-retrograde) impacts are the same for either target satellites. This is possible if the retrograde satellites were initially confined to low inclined orbits. The total population of satellites vary between $10^4 - 10^5$ objects depending on the distribution's power-law index, but there is a clear bias towards an initial population with an abundance of retrograde satellites. This is because it is easier to spin up the smaller retrograde satellites with 10^9 kg strikes than the larger prograde satellites. As such, the prograde satellites need more head-on impacts than the retrograde satellites to compensate for the abundance of small impactors and supply the proper amount of angular momentum.

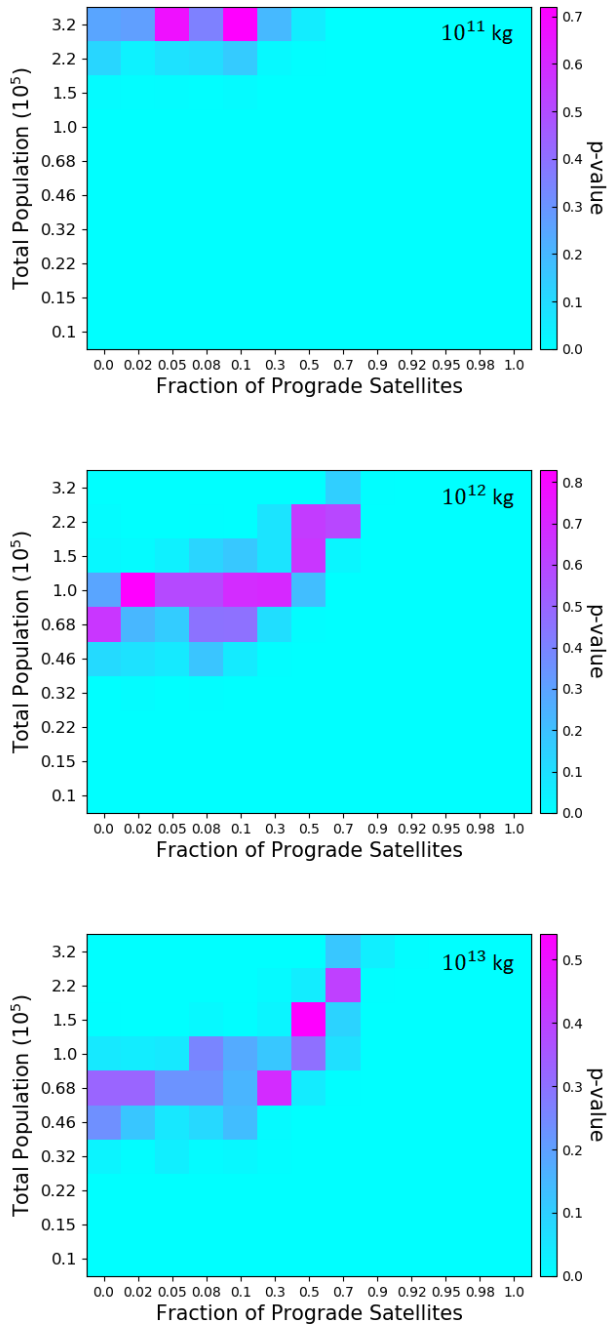Figure 6.17 shows the same plots but with the collision rates a factor of ten
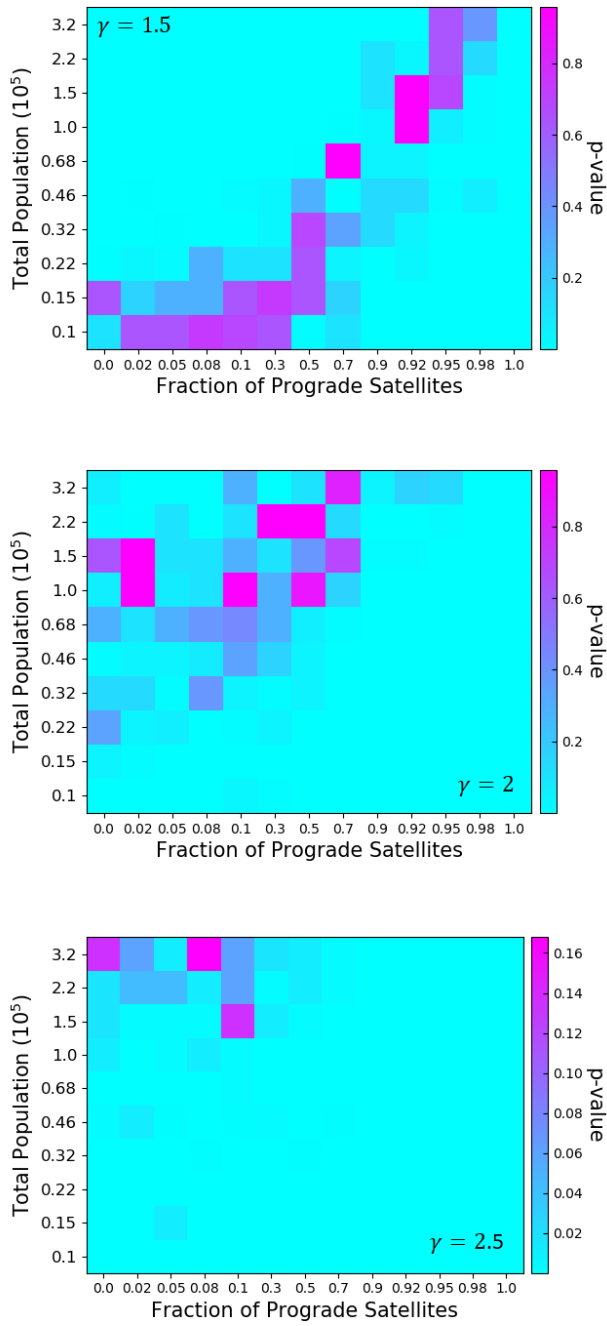
Figure 6.14: Density plots of p-values over the parameter space of impactors drawn from a mass distribution. From top to bottom, the power-law index increases from 1.5 to 2.5. The target satellite represents a typical prograde satellite similar to Figure 6.9 with a mass of 2.3×10^{15} kg, radius of 7.5 km, semi-major axis of 1.5×10^7 km, eccentricity of 0.1, and inclination of $1°$. The impactors can have inclinations from $0°$ to $1°$, and eccentricities from 0 to 0.1. The satellites' spin rates are initially near zero, and each simulation is iterated 10 times.
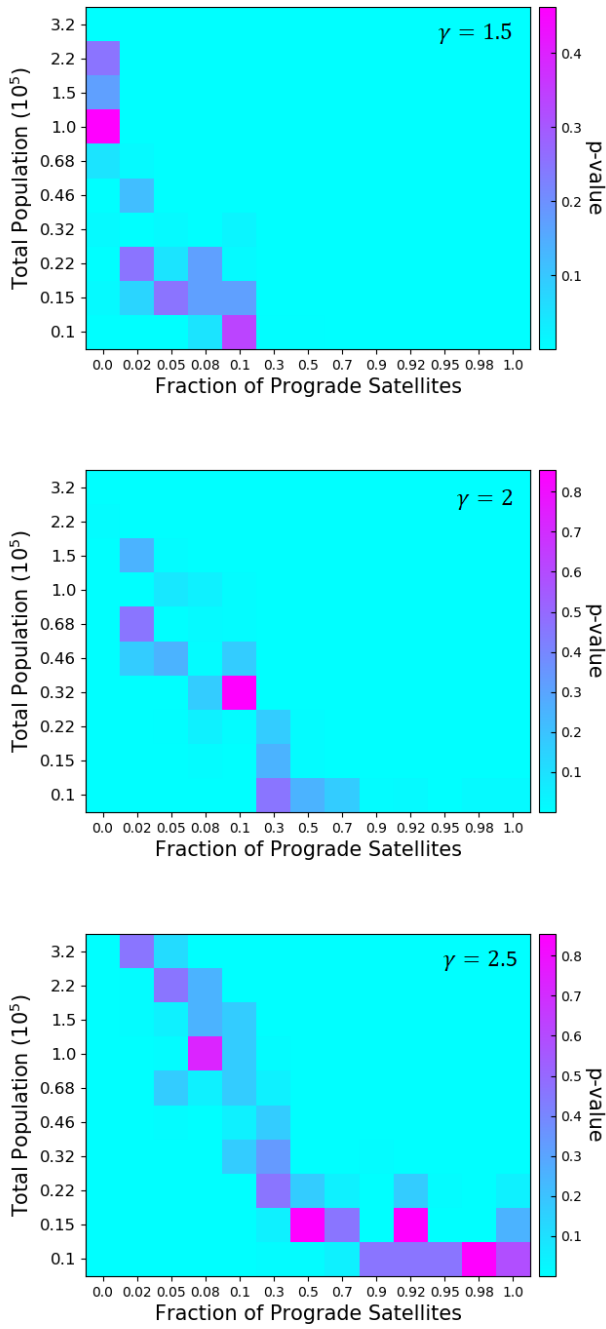
Figure 6.15: Density plots of p-values over the parameter space of impactors drawn from a mass distribution. From top to bottom, the power-law index increases from 1.5 to 2.5. The target satellite orbits retrograde (i=179°) with a mass of 10^{14} kg, radius of 3 km, semi-major axis of 2×10^7 km, and eccentricity of 0.1. The impactors can have inclinations from 0° to 1°, and eccentricities from 0 to 0.1. The satellites' spin rates are initially near zero, and each simulation is iterated 10 times.

smaller for the retrograde target satellite. This is because the retrograde satellites are typically smaller than the prograde satellites and revolve on more distant orbits, and from Equation 6.9 we can expect about an order of magnitude decrease in their collision rates. In this case there are fewer impactors striking the target satellite. A greater fraction of these impactors should orbit in prograde direction because they are more frequent and their faster relative velocities mean that they impart more angular momentum per strike. Thus, Figure 6.17 shows similar solutions to Figure 6.16 with a total initial population between $10^4 - 10^5$ satellites, but shifted towards a higher concentration of prograde satellites. In this case, where the collision rates for the retrograde satellites are slower than their prograde counterparts, half of the initial satellite population should orbit in the prograde direction and the other half orbit retrograde. To compare, if the collision rates for the retrograde satellites were instead an order of magnitude greater, as shown in Figure 6.16, then we require over 90% of the initial irregular satellite population to be orbiting retrograde in order to reproduce the observed spin rates.

6.2.5.1 Increasing the Range of Eccentricities and Inclinations

The previous plots have the target satellites revolving on nearly circular low inclined orbits, when in fact Saturn's irregular satellites possess a wide array of orbital inclinations and eccentricities (Figures 6.1 and 6.2). Here we place the target satellites on orbits with greater inclinations and eccentricities, and sample the impactors from a wider array of eccentricities and inclinations. Figure 6.18 shows that
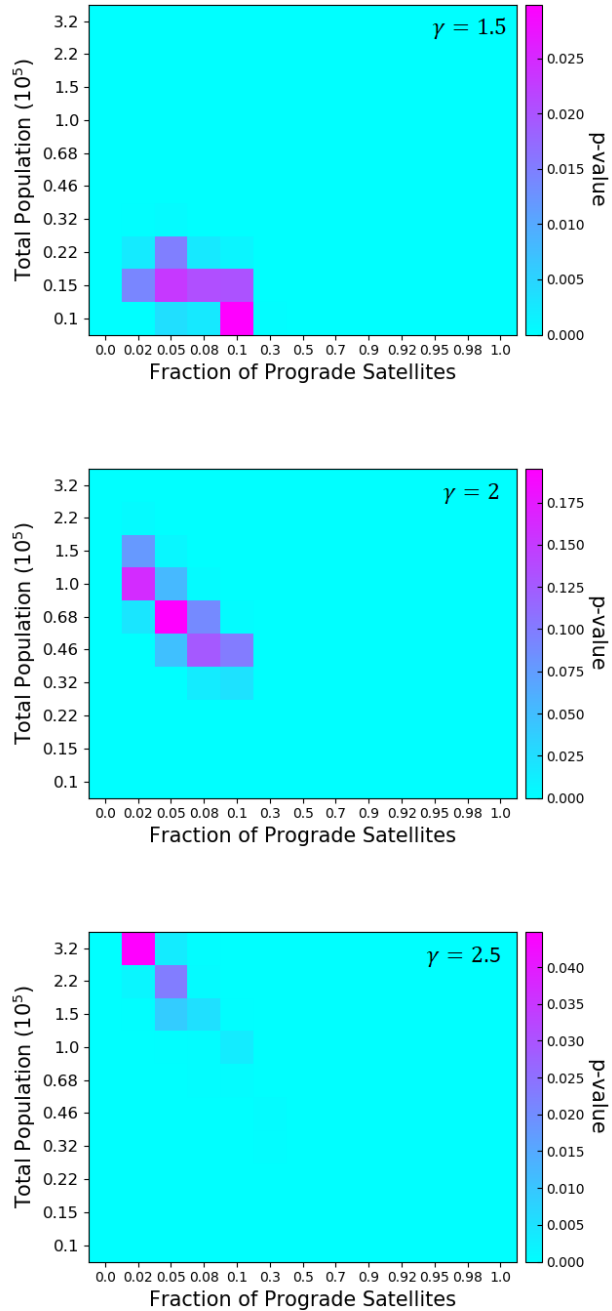
Figure 6.16: The geometric mean of p-values for each pair of plots of equal power-law index from Figures 6.14 and 6.15. The collision rates for both prograde and retrograde target satellites are the same. We ran each simulation 100 times.
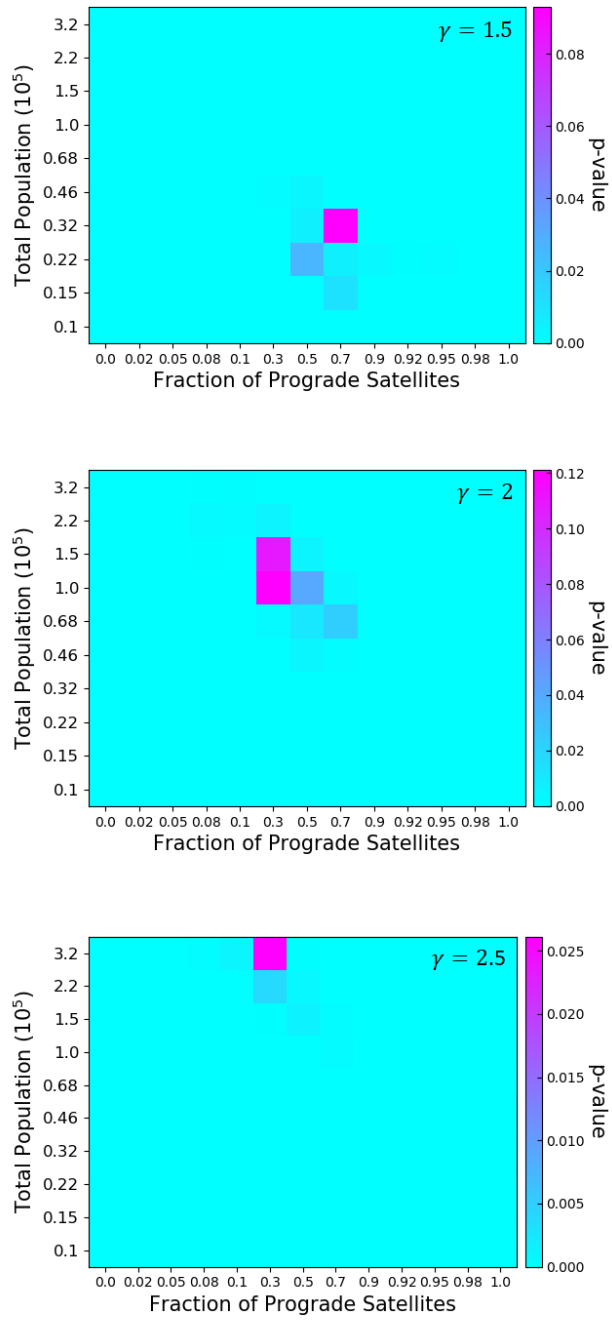
Figure 6.17: The same as Figure 6.16 but the collision rates for the retrograde target satellite are an order of magnitude smaller. We ran each simulation 100 times.

the population of impactors that can best reproduce the spin rates of both prograde and retrograde satellite populations is similar to Figure 6.17. The collision rates, therefore, play a more important role in determining the fraction of initial satellites that orbit prograde than their distribution of orbital elements.

6.3   Application to Himalia and Phoebe

Himalia and Phoebe are Jupiter's and Saturn's largest irregular satellites. Although they orbit prograde and retrograde to the planet's spin, respectively, they share similar orbital properties. Both satellites are situated closer to the central planet than their neighboring moons, and both revolve on more circular orbits. If collisions were responsible for the evolution of their orbits, then it is possible that these large satellites share a similar formation history (Hamilton, 2001, 2003).

Phoebe spins at a rate of 2.6 revolutions per day, which falls right in line with the other retrograde satellites; however, Phoebe is 10^4 times more massive than the next largest retrograde irregular satellite. If Phoebe grew by accreting some of the intermediary mass satellites, then its spin period could be a byproduct of those giant impacts. From Equation 6.8, we can estimate that a single giant impact totaling to about 5% of the satellite's mass would reproduce the moon's spin rate. If Phoebe was struck by more than one impactor, then more mass is needed to account for strikes that spin the satellite down. Figure 6.19 shows that the spin distribution peaks near its current value if it was struck by a few retrograde impactors totaling to 10% of its mass. If the impactors instead orbited prograde, then the total mass
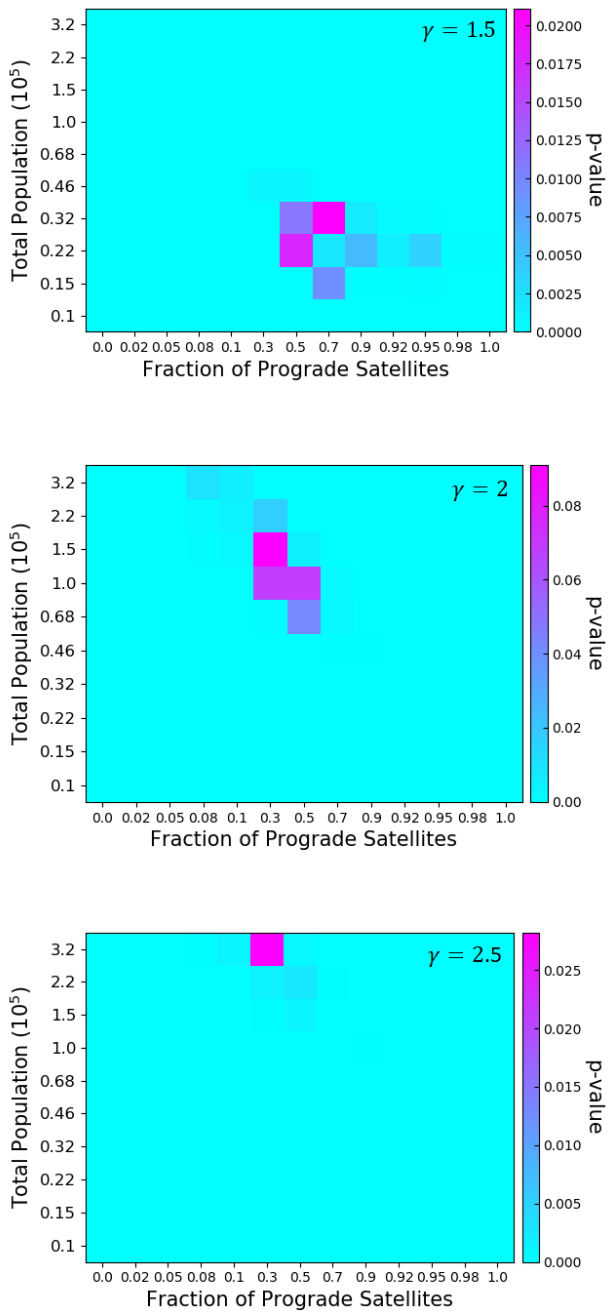
Figure 6.18:   The same as Figure 6.17 but the impactors can possess a wider range of orbital eccentricities (0 to 0.6) and inclinations (up to 40° above the mid-plane). The target satellites also orbit with eccentricities and inclinations similar to that of the observed population with the prograde target satellite possessing an eccentricity of 0.3 and inclination of 45°, and the retrograde target satellite having an eccentricity of 0.3 and inclination of 165°. We ran each simulation 100 times.
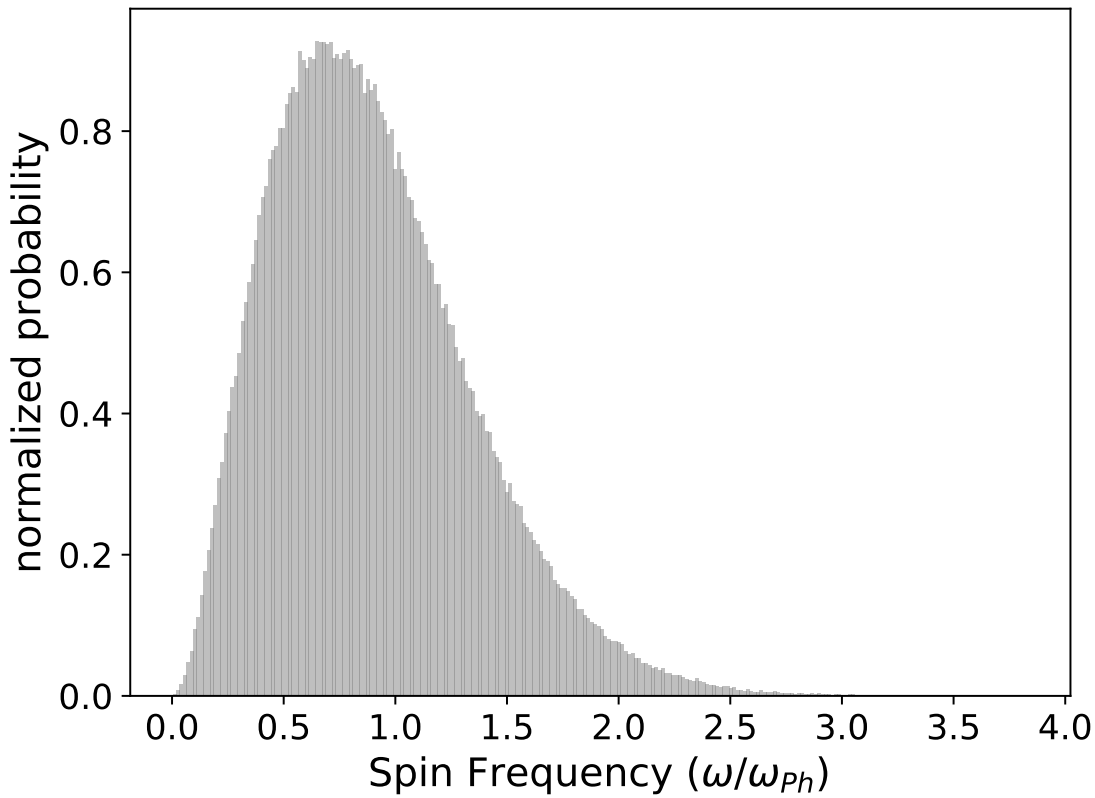
Figure 6.19: A spin distribution of Phoebe, orbiting retrograde, after being struck by five retrograde $0.02\,M_{\text{Phoebe}}$ impactors.

imparted shrinks to about 1%. A 10% mass increase happens to be about the amount required to significantly vary the satellite's orbit (Figure 6.4). In this case, Phoebe's eccentricity and inclination will only change by a few percent, but if it was struck head-on by a series of massive prograde orbiting moons, then its semi-major axis could shrink by a few percent. Himalia would have evolved similarly if there were an abundance of retrograde satellites located within its vicinity.

Scattering between these larger satellites and their neighboring moons can also be described by dynamical friction (Chandrasekhar, 1943), in that Phoebe and Himalia trade kinetic energy with the smaller scattered satellites. Here, the smaller satellite would gain orbital energy and angular momentum, while Phoebe's and Himalia's orbits would shrink and circularize. From Figure 6.1 it would seem that Phoebe and Himalia have been settling into a thermodynamic equilibrium with their environment, as they orbit closer to the central planet on more circular orbits than their surrounding neighbors. To check whether this model is a valid description of these satellite systems, we must compare the kinetic energies of the satellites using the orbital average of the square of their radial velocities. A satellite's radial velocity is linearly proportional to its eccentricity,

$$v_R = \sqrt{\frac{GM}{a(1-e^2)}} e \sin(\nu) \tag{6.11}$$

which would be minimized for the larger satellites. The orbit average of the square

167
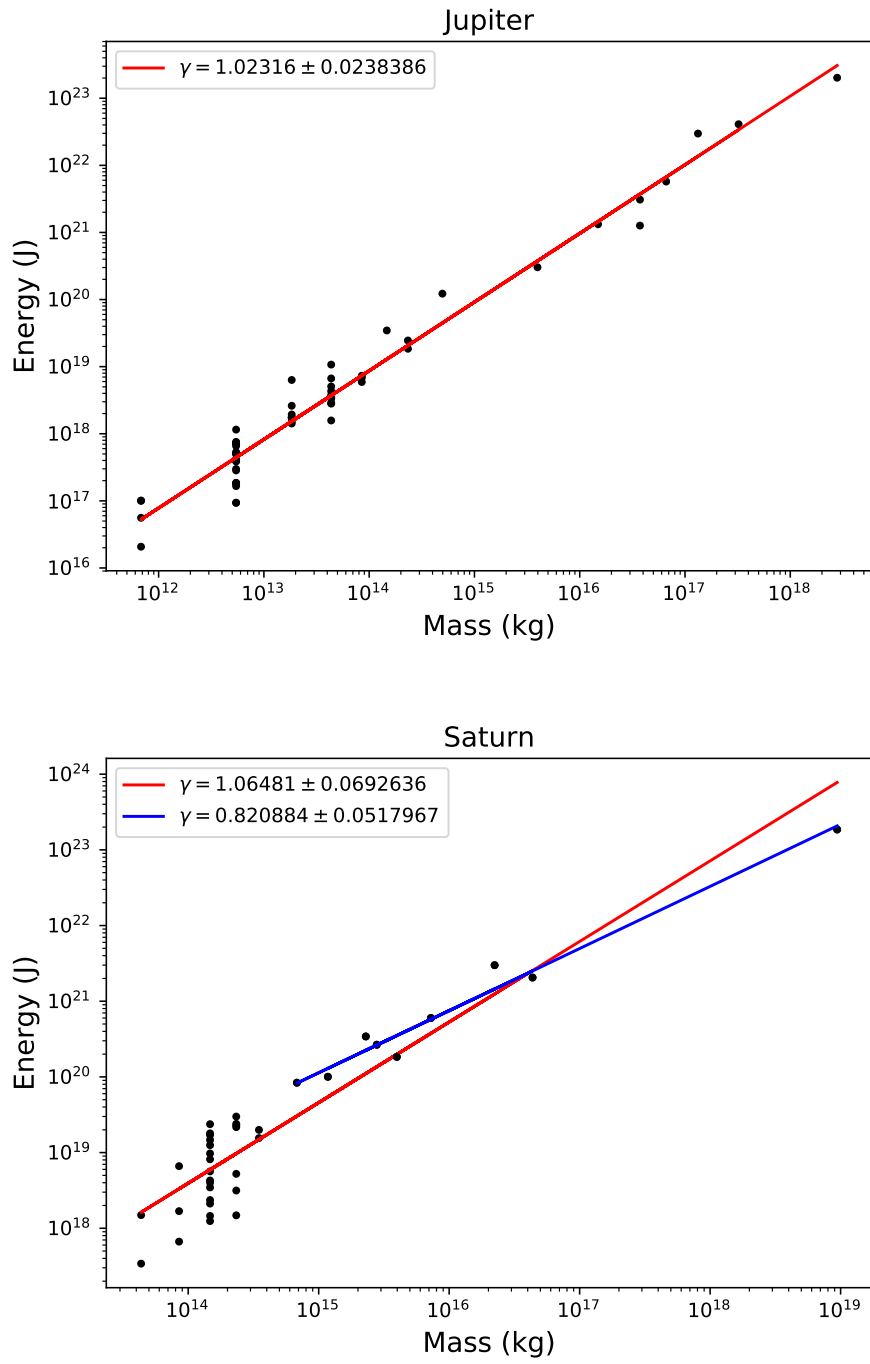
Figure 6.20:   (top) The kinetic energy corresponding to the irregular satellites'
radial motion around Jupiter as a function of their mass. A negative linear relation-
ship would suggest that dynamical friction dominated their orbital evolution as the
satellites scattered. (bottom) An equivalent plot for satellites around Saturn.

of the radial velocity is

$$\langle v_R^2 \rangle = \frac{1}{T} \int_0^T v_R^2 dt = \frac{1}{T} \int_0^{2\pi} v_R^2 \frac{dt}{d\nu} d\nu \tag{6.12}$$

where T is the orbital period,

$$\frac{d\nu}{dt} = \frac{h}{R^2} = \frac{2\pi}{T(1-e^2)^{1.5}} (1 + e\cos(\nu))^2, \tag{6.13}$$

h is the specific angular momentum, and R is the orbital distance.

$$\langle v_R^2 \rangle = \frac{1}{2\pi} \int_0^{2\pi} \frac{(1-e^2)^{1.5}}{(1 + e\cos(\nu))^2} \frac{GM}{a(1-e^2)} e^2 \sin^2(\nu) d\nu \tag{6.14}$$

$$\langle v_R^2 \rangle = \frac{e^2 v_{\text{circ}}^2 \sqrt{1-e^2}}{2\pi} \int_0^{2\pi} \frac{\sin^2(\nu)}{(1 + e\cos(\nu))^2} d\nu \tag{6.15}$$

For eccentricities less than 0.6, the integral is approximately equal to π (the integral diverges to ∞ as the eccentricity nears 1), so for small eccentricities

$$\langle v_R^2 \rangle \approx \frac{e^2 v_{\text{circ}}^2}{2}. \tag{6.16}$$

Figure 6.20 shows the radial component of the kinetic energy of the satellites around Jupiter and Saturn verses their mass. Here the kinetic energy increases linearly with the satellite's mass, indicating that the eccentricities of these satellites are random and that dynamical friction did not play an important role to satellites' evolution. Satellites greater than 4×10^{14} kg around Saturn, however, can be de-

scribed by a power law with index $\gamma = 4/5$, with Phoebe falling under the $\gamma = 1$ curve. If there once existed more massive satellites that have since disappeared, then this relationship may be artificial; however, if this relationship is real, then Phoebe's orbital eccentricity shrank by a factor of a few as it scattered the less massive prograde satellites.

6.4 Conclusion and Future Work

The most collisionally evolved systems in the solar system are probably Jupiter's and Saturn's irregular satellites. These small rock-ice bodies, captured isotropically from the circumstellar disk, revolve with orbital speeds of around 1.5 km/s on highly eccentric and inclined orbits. Crossing orbits lead to collisions, which should shape the orbital and spin architecture of the satellite system. In this Chapter we explored the possibility that Saturn's irregular satellites' spin rates were a byproduct of impacts, and have shown different disk populations that could reproduce the satellites' spin rates.

Here we assumed that the prograde satellites are larger than their retrograde counterparts, and that the distribution of the initial irregular satellite system follows a power-law. If the collision rates are comparable between the prograde and retrograde satellites, then the initial population of satellites needs to be biased towards retrograde satellites to reproduce the spin rates of both prograde and retrograde populations (Figure 6.16). Smaller satellites need fewer impacts to spin them up, so reproducing the retrograde satellites' spin rates requires that the initial population

have a greater fraction of retrograde satellites. If the collision rates for the retrograde satellites were instead slower by placing a greater emphasis on their smaller than average sizes, then the number of impacts overall decreases. Increasing the number of collisions to reproduce the retrograde satellites' spin rates in this case requires a greater fraction of prograde satellites, which we calculate to be about half in order to reproduce both prograde and retrograde satellites' spin rates (Figure 6.18). Regardless, we require a total initial irregular satellite population of $10^4 - 10^5$ objects greater than 10^9 kg, which is in between what Nesvorný et al. (2007) and Bottke et al. (2010) posit. The corresponding total mass of this satellite population is between $10^9 - 10^{12}$ kg, and is comparable to the mass of the massive target satellites.

Spinning up Phoebe and Himalia is more difficult than reproducing the smaller satellites' spin rates because these satellites are much larger than their neighbors. Both satellites would need to accrete between 1%-10% of their mass in giant impacts to retrieve spin distributions that peak at their current rates. This could explain the large gap of massive objects between Phoebe and the next largest satellite, as Phoebe may have simply accreted these satellites as it migrated inwards closer to Saturn. Such violent impacts would also shrink the satellite's orbit if the collisions were head-on, which is likely considering that Phoebe is located closer to the prograde orbiting satellites. There are no retrograde satellites orbiting close to Himalia today, however, so it is uncertain if Phoebe and Himalia have shared a similar formation history (Hamilton, 2001, 2003).

Chapter 7:   Conclusion and Future Work

The overall theme of this thesis is exploring spin dynamics in the solar system from giant planets to tiny satellites. We have demonstrated a number of different methods that are capable of spinning and tilting planetary objects, and studied the ones that are more capable of altering a particular body's spin state. In general, the spin states of rocky bodies are mostly influenced by collisions, so we should, and do, observe a variety of tilts and spins for terrestrial planets and satellites. Gas accretion, though, provides a substantial amount of angular momentum pointing normal to the orbital plane, so we expect to find untilted fast-spinning gas giants. We instead observe the giant planets to possess a wide range of obliquities and spin rates well below break up speeds. In this thesis we focus on ice giant formation, and explore how collisions and spin-orbit resonances can explain Uranus's and Neptune's high obliquities and similar spin rates.

We showed that placing Uranus closer to the Sun between Jupiter and Saturn can speed up its spin precession rate enough to resonate with a planet like Neptune located beyond Saturn, but leaving Uranus here for over 100 Myr is unstable and we can only achieve 40° kicks under ideal conditions (Rogoszinski & Hamilton, 2020b). More likely, Uranus and Neptune were formed beyond Saturn and harbored

massive circumplanetary disks as they accreted their gaseous atmospheres. These disks would augment the planets' gravitational quadruple moment and speed up their spin precession rates enough to resonate with their own orbit. We discovered that disks about 10 times the mass of their satellite system could lead to obliquity excitations as high as 70° (Rogoszinski & Hamilton, 2020a). This would eliminate any impactor required to tilt Neptune, and halve the mass of the subsequent impactor responsible for tilting Uranus the rest of the way to 98°. When comparing the likelihoods between this hybrid scenario and a pure collision model, the probability of generating Uranus's current spin state also increases by as much as an order of magnitude. While this latter method seems to be the more feasible model, each spin-orbit resonance argument we tried fails to drive Uranus all the way to 98°. We conclude that not only are giant collisions capable of generating Uranus's spin state, but they are required at some point during Uranus's formation to tilt the planet at least partially.

Giant collisions are therefore an integral part of solar system evolution, with the implication that such rogue massive cores were likely more common during the earlier stages of planetary formation (Levison et al., 2015a,b). Recently, spin-orbit resonances have been getting more attention in the context of exoplanet formation. There is currently very little data on the spin architecture of exoplanet systems (Snellen et al., 2014; Bryan et al., 2020), but efforts have been taken to map out likely combinations of orbital parameters that could indicate strong possibilities of such resonances (Saillenfest et al., 2019). Also, possible signatures of spin-orbit resonances have been discovered elsewhere with regard to the abundance of giant

planets at close proximities to their host stars and near first-order mean-motion resonances. Here, obliquity excitations can raise the tidal force from the host star, drain the planet's orbital energy, and cause these giant planets to migrate out of mean motion resonance (Millholland & Laughlin, 2019). As such, spin-orbit resonances may very well play as an important role in planetary formation and evolution as giant impacts with regards to shaping their spin architectures.

We would therefore like to know how big a role spin-orbit resonances play in shaping the orbital architecture of solar systems, and how our solar system fits into this paradigm. One future direction we can take from the work described in this thesis is to incorporate mean-motion resonances into the spin-orbit resonance arguments outlined here. The forming giant planets may have started in or entered into such resonance chains, and Quillen et al. (2018) showed that including mean-motion terms yields resonance arguments that are not sensitive to orbital inclinations and can push obliquities beyond 90°. Also, Thommes & Lissauer (2003) argue that inclination growth can occur when planets are trapped into certain low order eccentricity-exciting mean-motion resonances. Since we require Uranus with an extended circumplanetary disk to have an orbital inclination greater than 5° in order to tilt the planet substantially, exploring alternative resonance arguments could yield promising results.

Circumplanetary disk formation around ice giants is also an emerging field of study, and we would like to understand how gas accretion supplies spin angular momentum to the forming planet. In this thesis we explored disk formation around a Jupiter analogue using a two dimension gas accretion model, and showed that

such a simple model will generate giant planets that spin several times faster than what we observe today. The next step would be to expand these simulations to include the third dimension and polar inflow. Expanding to 3D will allow gas to instead flow onto the planet's polar regions rather than the planet's equator, which would supply less angular momentum and spin the planet to sub-break-up speeds. Batygin (2018) posit that polar inflow coupled with magnetic braking will produce the observed giant planet spin rates, and so including magneto-hydrodynamics to these simulations would help gauge the significance each mechanism plays in transporting angular momentum during gas accretion. We will also need to include a proper radiative cooling mechanism since the circumplanetary disk will have some scale height, and we may also need to resolve how the gas interacts with the planet's surface. All this will require overcoming some serious computation hurdles. After we develop a solid framework for how a gas giant's spin rate evolves, we can then extend this model to gas accreting onto ice giants, which have smaller atmospheres relative to the size of their cores. However, our lack of data for Uranus and Neptune, their unique physical characteristics (Helled et al., 2020; Helled & Fortney, 2020), and their possibly different formation history with respect to Jupiter and Saturn will make this transition all the more complicated.

We have also shown that the spin rates of Saturn's irregular satellites may be a byproduct of collisions after they have been captured from the protoplanetary disk. We calculated that an initial population of $10^4 - 10^5$ satellites more massive than 10^9 kg with more than half of them orbiting retrograde can lead to collisions and produce their present-day spin rates. For simplicity, we assume the satellites were

initially non-spinning, but this may not have been the case since transneptunian objects spin with an average rate of 2.8 rev/day (Thirouin et al., 2014), which is comparable to the spin rates of Saturn's retrograde population. For future work, we would like to explore collision scenarios that can preserve the spin rates of initially fast spinning retrograde satellites, while also slowing down the spin rates of the prograde population to their current average spin rates of 1.8 rev/day.

In these sets of simulations we assume the collisions are entirely inelastic and that all the mass imparted is absorbed by the target satellite. More realistically, collisions among irregular satellites produce debris, and in the more violent cases can disintegrate them. Some of the observed irregular satellites share orbital elements suggesting that they may have originated from a larger proto-satellite that has since broke apart. It would be helpful to simulate collisions between irregular satellites using smoothed-particle hydrodynamics simulations, and measure the resulting distribution of spin rates. We would also like to incorporate Phoebe, Saturn's largest irregular satellite, into our models and explore how Phoebe would interact with its neighbors. We have presented evidence that Phoebe might have scattered the larger prograde moons onto more eccentric orbits, and so Phoebe may have played an important role in the satellites' collisional evolution. This study can then be contrasted with Himalia's orbital evolution (Jupiter's largest irregular satellite), as both satellites possibly share a similar formation history (Hamilton, 2001, 2003). Collisions play an important role in both planetary and satellite formation, and understanding the origin of their spin and orbital architectures can provide a clearer picture of these systems' dynamical histories.

Appendix A: Angular Momentum and Obliquity Distributions

This section shows the derivation for the angular momentum and obliquity distributions from accreting multiple small particles. This is similar to the approach of Dones & Tremaine (1993a). If these particles are isotropically distributed, then they possess a wide range of eccentricities and inclinations, and so there is no preference to any spin direction. This isotropy breaks down if particles instead orbit within the planetary disk at low inclinations and eccentricities.

A.1   Angular Momentum Distributions

The calculation for the angular momentum distribution of a planet from multiple strikes at random locations on the planet's surface is a random walk scenario. Lets start with the magnitude of the spin angular momentum of a planet:

$$L = \sqrt{L_X^2 + L_Y^2 + L_Z^2} \tag{A.1}$$

where the probability distribution $(f_{L_k}(l_k))$ of each component (L_k) of the angular momentum vector is described by a normal distribution as a byproduct of the central

limit theorem:

$$f_{L_k}(l_k) = \frac{1}{\sigma_k\sqrt{2\pi}}e^{-l_k^2/2\sigma_k^2}. \tag{A.2}$$

As such, to find the distribution of the magnitude of the angular momentum we will first need to determine the square of each distribution, then the sum of three squares, and finally take the square root of the sum as seen in Equation A.1.

The distribution of the square of each component (L_k^2) can be calculated by assuming that X and Y are continuous random variables (i.e. 'variates' as depicted in upper case), with x and y as specific elements in the ranges of their corresponding variates (i.e. also called 'quantiles' depicted here in lower case)(Grinstead & Snell, 2006). X and Y have cumulative distribution functions F_X and F_Y, and Y is described by a strictly increasing function as a function of X: $Y = \phi(X)$. $F_Y(y) = P(Y \leq y)$, where the right hand side describes the probability that the variate Y is less than or equal to a number y, which is equal to $P(\phi(X) \leq y) = P(X \leq \phi^{-1}(y)) = F_X(\phi^{-1}(y))$.

So for the variate X^2 and its corresponding quantile x^2:

$$F_{X^2}(x^2) = P(X^2 \leq x^2) = P(-x \leq X \leq x). \tag{A.3}$$

The right hand side can be rearranged accordingly:

$$P(-x \leq X \leq x) = P(X \leq x) - P(X \leq -x) \tag{A.4}$$

so that:

$$F_{X^2}(x^2) = F_X(x) - F_X(-x). \tag{A.5}$$

The corresponding density distribution function for an arbitrary variate Y is: $f_Y(y) = \frac{d}{dy}F_Y(y)$. Starting with $F_Y(y) = F_X(\phi^{-1}(y))$, we take the derivative of each side and employ the chain rule to obtain: $f_Y(y) = f_X(\phi^{-1}(y))\frac{d}{dy}\phi^{-1}(y)$.

So:

$$f_{X^2}(x^2) = \frac{f_X(x) + f_X(-x)}{2x}. \tag{A.6}$$

Since the normal distribution is centered at zero and is symmetric, the density distribution for L_k^2 is then:

$$f_{L_k^2}(l^2) = \frac{1}{\sigma_k l \sqrt{2\pi}} e^{-l^2/2\sigma_k^2} \tag{A.7}$$

which is the distribution for a chi squared with one degree of freedom.

Next, the density distribution of the sum of two independent random variables is their convolution. Let $L_{XY}^2 = L_x^2 + L_y^2$ and its corresponding density distribution:

$$f_{L_{XY}^2}(l_{xy}^2) = \int_0^{l_{xy}^2} f_{L_X^2}(l_{xy}^2 - l_y^2) f_{L_Y^2}(l_y^2) dl_y^2 \tag{A.8}$$

where L_Y^2 ranges from 0 to L_{XY}^2. Note that the standard deviations for both f_{L_X} and f_{L_Y} are equal with $\sigma = \sigma_x = \sigma_y$. Thus, combining Equation A.7 and A.8:

$$f_{L^2_{XY}}(l^2_{xy}) = \frac{1}{2\pi\sigma^2} \int_0^{l^2_{xy}} \left(e^{-(l^2_{xy}-l^2_y)/2\sigma^2} (l^2_{xy} - l^2_y)^{-0.5} \right) \left(e^{-l^2_y/2\sigma^2} (l^2_y)^{-0.5} \right) dl^2_y = \frac{e^{-l^2_{xy}/2\sigma^2}}{2\sigma^2}$$

(A.9)

Now let $L^2 = L^2_{XY} + L^2_Z$ and repeat the above process. The probability distribution $f_{L^2}(l^2)$ describes the probability that L^2 takes the value l^2, and $f_{L^2_Z}(l^2_z)$ describes the probability that L^2_Z takes the value l^2_z. We explicitly treat the general case $\sigma \neq \sigma_z$.

The density distribution for L^2 is:

$$f_{L^2}(l^2) = \int_0^{l^2} f_{L^2_{XY}}(l^2 - l^2_z) f_{L^2_Z}(l^2_z) dl^2_z = \frac{1}{2\sqrt{2\pi}\,\sigma^2\sigma_z} \int_0^{l^2} e^{-(l^2-l^2_z)/2\sigma^2} e^{-l^2_z/2\sigma^2_z} (l^2_z)^{-0.5} dl^2_z$$

(A.10)

let $\beta = \frac{\sigma^2 - \sigma^2_z}{2\sigma^2\sigma^2_z}$, $\gamma = \beta l^2_z$, and $d\gamma = \beta dl^2_z$, and so

$$f_{L^2}(l^2) = \frac{e^{-l^2/2\sigma^2}}{2\sqrt{2\pi}\,\sigma^2\sigma_z} \frac{1}{\sqrt{\beta}} \int_0^{\beta l^2} e^{-\gamma} \gamma^{-0.5} d\gamma$$

(A.11)

Equation A.11 is of similar form to Equation 109 found in Dones & Tremaine (1993a). Applying Equation A.6 to f_{L^2} and noting that since L is the magnitude of the planet's angular momentum, $f_L(-l) = 0$. We find $f_L(l) = f_{L^2}(l) \cdot 2l$. The probability distribution describing the angular momentum of the planet for $\beta > 0$, or $\sigma_x = \sigma_y > \sigma_z$ is then:

$$f_L(l) = \frac{l e^{-l^2/2\sigma^2}}{\sqrt{2\pi}\,\sigma^2\sigma_z} \frac{1}{\sqrt{\beta}} \gamma(0.5, \beta l^2)$$

(A.12)

180

where $\gamma(0.5, \beta l^2)$ is the lower incomplete gamma function. For $\beta < 0$ ($\sigma_x = \sigma_y < \sigma_z$):

$$f_L(l) = \frac{le^{-l^2/2\sigma^2}}{\sqrt{2\pi}\,\sigma^2\sigma_z} \frac{1}{\sqrt{-\beta}} (2l\sqrt{-\beta})\,\Phi(0.5; 1.5; -\beta l^2) \qquad \text{(A.13)}$$

where $\Phi(0.5; 1.5; -\beta l^2)$ is the confluent hypergeometric function of the first kind.

For $\beta = 0$, where $\sigma = \sigma_x = \sigma_y = \sigma_z$ (isotropic case), the form is particularly simple:

$$f_L(l) = \frac{2l^2 e^{-l^2/2\sigma^2}}{\sqrt{2\pi}\,\sigma^3}. \qquad \text{(A.14)}$$

A.2   Obliquity Distributions

The obliquity angle (ϵ) is defined by $\tan(\epsilon) = \frac{\sqrt{L_x^2+L_y^2}}{L_z} = \frac{L_{XY}}{L_z}$. To find the distribution of the quotient of two independent variants we let $Q = X/Y$ where X and Y are independent random variables. Then $F_Q(q) = P(Q \le q) = P(X/Y \le q)$. If $Y > 0$, then $X \le yq$, while if $Y < 0$, then $X \ge yq$. Therefore, $P(X/Y \le q) = P(X \le yq, Y > 0) + P(X \ge yq, Y < 0)$. These constraints determine the integral limits in the corresponding cumulative distribution:

$$F_Q(q) = \int_{y=0}^{\infty} \int_{x=-\infty}^{yq} f_{XY}(x, y)dxdy + \int_{y=-\infty}^{0} \int_{x=yq}^{\infty} f_{XY}(x, y)dxdy. \qquad \text{(A.15)}$$

and density distribution:

$$f_Q(q) = \int_0^{\infty} y f_{XY}(yq, y)dy + \int_{-\infty}^{0} (-y)f_{XY}(yq, y)dy. \qquad \text{(A.16)}$$

So for calculating the obliquity distribution, let $\sigma \neq \sigma_z$, and $U = \tan(\epsilon)$ with $u = \tan(\varepsilon)$ as the corresponding quantile. Thus:

$$f_U(u) = \int_0^\infty l_z f_{L_{XY}}(ul_z) f_{L_z}(l_z) dl_z + \int_{-\infty}^0 -l_z f_{L_{XY}}(ul_z) f_{L_z}(l_z) dl_z \qquad (A.17)$$

which becomes:

$$f_U(u) = 2 \int_0^\infty \frac{|u| l_z^2}{\sigma^2 \sigma_z \sqrt{2\pi}} e^{-l_z^2 u^2/(2\sigma^2)} e^{-l_z^2/(2\sigma_z^2)} dl_z. \qquad (A.18)$$

If $\alpha = \frac{u^2}{2\sigma^2} + \frac{1}{2\sigma_z^2}$, then the equation is now of the form:

$$\int_0^\infty t^2 e^{-\alpha t^2} dt = \frac{\sqrt{\pi}}{4\alpha^{1.5}} \qquad (A.19)$$

and so when normalized:

$$f_U(u) = \left| \frac{u}{4\sqrt{2}\,\sigma^2 \sigma_z \alpha^{1.5}} \right|. \qquad (A.20)$$

We can change variables to obliquity (ϵ) by setting $f_\epsilon(\varepsilon) = \frac{du}{d\varepsilon} f_U(u)$ where $\frac{du}{d\varepsilon} = \sec^2(\varepsilon)$. We find:

$$f_\epsilon(\varepsilon) = \left| \frac{1}{4\sqrt{2}\,\sigma^2 \sigma_z} \frac{\tan(\varepsilon)}{\cos^2(\varepsilon)} \left(\frac{\tan^2(\varepsilon)}{2\sigma^2} + \frac{1}{2\sigma_z^2} \right)^{-3/2} \right|. \qquad (A.21)$$

This is equivalent to the obliquity distribution given in Dones & Tremaine (1993a) (Equation 111). For the isotropic case, $\sigma_z = \sigma$, the distribution reduces to:

$$f_\epsilon(\varepsilon) = \left| \frac{1}{2} \sin(\varepsilon) \right|. \qquad\qquad \text{(A.22)}$$

Appendix B: Rotating into a Planet's Reference Frame

Since we are interested in the angular momentum accreting onto the planet, the simulations will take place within the planet's reference frame. Assuming the planet and gas revolve on circular orbits, we can set up the following prescription for rotating the gas's velocity into the planet's reference frame. As shown in Figure B.1, a cloud of gas is initially located at a distance R away from the Sun, and the planet is located at a corresponding distance a. As such, $\dot{R} = 0$, $\dot{\Psi}(R)$, and $\dot{\Psi}_p = \sqrt{GM_\odot/a^3}$, but in the absence of other planets $\dot{\Psi} = \sqrt{GM_\odot/R^3}$. In the planet's frame of reference, though, the gas possess both a radial and angular speed. Here we seek the velocities $\dot{r}$ and $\dot{\Phi}$ in the planet-centric frame by transforming the known heliocentric frame R and Ψ with inertial velocities $\dot{R}$ and $\dot{\Psi}$.

The position the gas is from the planet, a distance r at an angle Φ, is a function of the gas's position from the Sun and time: $r = r(R, \Psi, t)$, $\Phi = \Phi(R, \Psi, t)$. The corresponding radial and angular speeds are therefore

$$\dot{r} = \frac{\partial r}{\partial R}\dot{R} + \frac{\partial r}{\partial \Psi}\dot{\Psi} + \frac{\partial r}{\partial t} \tag{B.1}$$

Figure B.1: A diagram of a cloud of gas (purple cloud) and a planet (black circle) orbiting the Sun (white circle). a is the distance from the planet to the Sun, R is the distance a particle of gas is from the Sun, and r is the distance the gas is away from the planet. Ψ is the angle between the gas and a reference direction (x-axis), Ψ_p is the angle between the planet and the x-axis, and Φ is the angle between the planet and clump of gas. Here both the planet and gas orbit the Sun on circular orbits.

and

$$\dot{\Phi} = \frac{\partial \Phi}{\partial R}\dot{R} + \frac{\partial \Phi}{\partial \Psi}\dot{\Psi} + \frac{\partial \Phi}{\partial t}. \tag{B.2}$$
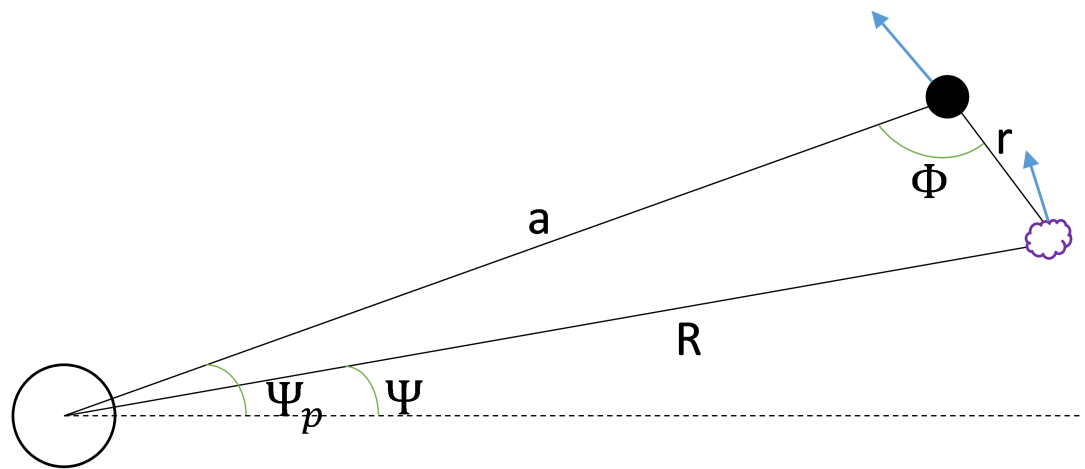
$\dot{R} = \dot{a} = 0$ since both the planet and gas are revolving on circular orbits. We can also extract the following trigonometric relations from Figure B.1 using the sine and cosine rules

$$\frac{\sin(\Psi_p - \Psi)}{r} = \frac{\sin(\Phi)}{R} \tag{B.3}$$

$$r^2 = a^2 + R^2 - 2aR\cos(\Psi_p - \Psi) \tag{B.4}$$

To solve for $\dot{r}$ and $\dot{\Phi}$ we take the derivatives of the previous three equations. First, the $\partial/\partial\Psi$ terms. Taking the derivative of Equation B.4 while holding R and t constant yields

$$\frac{\partial r}{\partial \Psi} = -\frac{aR}{r}\sin(\Psi_p - \Psi) = -a\sin(\Phi), \tag{B.5}$$

while taking the derivative of Equation B.3 gives

$$\cos(\Phi)\frac{\partial \Phi}{\partial \Psi} = -\frac{R}{r^2}\sin(\Psi_p - \Psi)\frac{\partial r}{\partial \Psi} - \frac{R}{r}\cos(\Psi_p - \Psi). \tag{B.6}$$

After a little rearranging and substituting in Equation B.4 yields

$$\frac{\partial \Phi}{\partial \Psi} = 1 - \frac{a}{r}\cos(\Phi). \tag{B.7}$$

Now the time derivative terms. If we take the derivative of Equation B.4 while

holding R and Ψ constant, we get

$$\frac{\partial r}{\partial t} = \frac{aR}{r}\sin(\Psi_p - \Psi)\dot{\Psi}_p = a\sin(\Phi)\dot{\Psi}_p = -\dot{\Psi}_p\frac{\partial r}{\partial \Psi}. \tag{B.8}$$

Taking the derivative of Equation B.3 with respect to time yields

$$\frac{\partial \Phi}{\partial t} = \frac{1}{\cos(\Phi)}\left(-\frac{R}{r^2}\sin(\Psi_p - \Psi)\frac{\partial r}{\partial t} + \frac{R}{r}\cos(\Psi_p - \Psi)\dot{\Psi}_p\right) = -\dot{\Psi}_p\frac{\partial \Phi}{\partial \Psi}. \tag{B.9}$$

Therefore, the gas's velocity with respect to the planet's reference frame is

$$\dot{r} = (\dot{\Psi} - \dot{\Psi}_p)\frac{\partial r}{\partial \Psi} \tag{B.10}$$

$$\dot{\Phi} = (\dot{\Psi} - \dot{\Psi}_p)\frac{\partial \Phi}{\partial \Psi}. \tag{B.11}$$

Appendix C: Nodal Precession Within a Protoplanetary Disk

Torques from neighboring planets cause a planet's orbit to precess. This precession rate is given as the sum of perturbations exterior and interior to the planet:

$$g_+ \simeq -\frac{3}{4}\mu_2 n_1 \alpha^3 \qquad \text{Exterior Perturber} \qquad (C.1)$$

$$g_- \simeq -\frac{3}{4}\mu_1 n_2 \alpha^2 \qquad \text{Interior Perturber} \qquad (C.2)$$

(Murray & Dermott, 1999). Here μ is the mass ratio of the perturber to the star, n is the mean motion of the planet, and $\alpha = a_1/a_2$, where a is the semimajor axis and the subscripts 1 and 2 refer to the inner and outer perturbers. These equations can be transformed to instead describe perturbations from disks, as disks are made up of a series of concentric rings. For a surface density given by $\Sigma(r) = \Sigma_0(r/R_o)^{-\beta}$, the mass of a protoplanetary disk can be described by

$$M_d = \int_{R_i}^{R_o} \Sigma_0 \left(\frac{r}{R_o}\right)^{-\beta} 2\pi r \, dr \qquad (C.3)$$

which can be integrated and solved for the constant reference surface density

$$\Sigma_0 = \frac{(2 - \beta) \, M_d}{2\pi \, (1 - \eta^{2-\beta}) \, R_o^2} \tag{C.4}$$

where $\eta = R_i/R_o < 1$, R_i is the inner radius of the disk, and R_o is its outer radius. Note that in the special case where $\beta = 2$, the expression for Σ_0 is

$$\Sigma_0 = \frac{M_d}{2\pi R_o^2 \log (R_o/R_i)}. \tag{C.5}$$

Setting r_p as the planet–Sun distance that divides the interior and exterior disks, for an outer disk, we can integrate Equation C.1 radially over the disk, and use Equation C.4 to eliminate Σ_0. Setting $R_i = a_1 = r_p$ and integrate $r = a_2$ out to R_o to find

$$g_+ = -\frac{3}{4} \frac{2\pi\Sigma_0}{M_\odot} n_1 r_p^3 \int_{R_i}^{R_o} \left(\frac{r}{R_{o,+}} \right)^{-\beta} r^{-2} dr \tag{C.6}$$

$$g_+ = -\frac{3}{4} n \left(\frac{2 - \beta_+}{-1 - \beta_+} \right) \left(\frac{1 - \eta_+^{-1-\beta_+}}{1 - \eta_+^{2-\beta_+}} \right) \left(\frac{M_{d,+}}{M_\odot} \right) \left(\frac{r_p}{R_{o,+}} \right)^3. \tag{C.7}$$

Similarly, for an interior disk, we use Equation C.2, set $R_o = r_p = a_2$ and integrate $r = a_1$ from the inner boundary R_i to find

$$g_- = -\frac{3}{4} \frac{2\pi\Sigma_0}{M_\odot} \frac{n_2}{r_p^2} \int_{R_i}^{R_o} \left(\frac{r}{R_{o,-}} \right)^{-\beta} r^3 dr \tag{C.8}$$

$$g_- = -\frac{3}{4} n \left(\frac{2 - \beta_-}{4 - \beta_-} \right) \left(\frac{1 - \eta_-^{4-\beta_-}}{1 - \eta_-^{2-\beta_-}} \right) \left(\frac{M_{d,-}}{M_\odot} \right) \left(\frac{R_{o,-}}{r_p} \right)^2. \tag{C.9}$$

Typically, we take $\beta_- = \beta_+$, but $M_{d,-}$ and $M_{d,+}$ can be quite different depending

on the geometry. The expression for g_+ agrees with that obtained by Chen et al. (2013) using a different method, while g_- is first given in Rogoszinski & Hamilton (2020a).

Appendix D: Laplace Radius with a Circumplanetary Disk

Orbits located within a planet's Laplace radius precess about the planet's equator, while orbits located beyond the Laplace radius precess about the ecliptic plane. The transition between the two Laplace planes is gradual, and an approximation for this location is given as

$$R_L \approx \left(2J_{2,\text{tot}} \frac{M_P + M_d}{M_\odot} R_P^2 r_P^3 \right)^{1/5} , \tag{D.1}$$

where $J_{2,\text{tot}} = J_2 + q$ is the total quadrupole of the planetary system, and r_P is the planet's distance from the Sun. We can neglect M_d since the mass of the circumplanetary disk or satellite system is usually much less than that of the planet, but the corresponding gravitational quadrupole moment is significant. The quadrupole moment of the Uranus's current satellite system is 4.7 times larger than the planet's J_2, and that value increases for an extended massive circumplanetary disk.

A circumplanetary disk is composed of a series of nested massive rings, and those contained within the Laplace radius contribute to the disk's quadrupole moment. We can transform Equation 4.4 by substituting the mass of the satellite with the mass of a ringlet, $dm = 2\pi\Sigma(a)a\,da$, and replacing the summation with an

integral. This gives

$$q = \int_{R_P}^{R_L} \frac{\pi \Sigma(a)}{M_P R_P^2} a^3 \, da, \tag{D.2}$$

where a is the distance away from the central planet. In this derivation, we let the surface density profile of the disk fall as a power law,

$$\Sigma(a) = \Sigma_0 \left(\frac{a}{R_o}\right)^{-\beta}, \tag{D.3}$$

where Σ_0 is the surface density at the outer edge of the disk, R_o is the outer radius of the disk, and $\beta > 0$ is the power-law index. We typically compute the power-law index by assuming either a constant surface density or one that falls 3 orders of magnitude to the outer edge of the disk. The disk extends from the planet's surface to 0.3-0.5 Hill radii (Quillen & Trilling, 1998; Ayliffe & Bate, 2009a, 2012; Machida, 2009; Ward & Canup, 2010; Martin & Lubow, 2011; Tanigawa et al., 2012; Szulágyi et al., 2014; Zhu et al., 2016), but Szulágyi et al. (2018) focused specifically on ice giant formation models, and they focused their attention within 0.1 Hill radii. The disk's quadrupole moment can then be rewritten and solved assuming a Laplace radius much larger than the planet's radius

$$q = \frac{\pi \Sigma_0 R_o^\beta}{M_P R_P^2} \int_{R_P}^{R_L} a^{3-\beta} da \approx \frac{\pi \Sigma_0 R_o^\beta}{M_P R_P^2} \frac{R_L^{4-\beta}}{4-\beta}. \tag{D.4}$$

For a small disk with mass $10^{-4} \, M_P$ extending to the planet's current Laplace radius of $54 \, R_P$, the disk's quadrupole moment q is 0.033, which is 10 times larger than Uranus's current J_2. A larger and more massive disk would therefore yield a

192

much bigger value for q. So, if $q \gg J_2$, then substituting Equation D.4 into Equation D.1 gives

$$R_L \approx \left(\frac{2\pi \Sigma_0 R_o^\beta r_P^3}{(4-\beta) M_\odot} \right)^{1/(1+\beta)}.$$ (D.5)

Appendix E: Facilities and Software

The following is a list of computing facilities and software used in this dissertation.

1. Deepthought2 HPC Cluster

2. YORP Cluster

3. Department of Astronomy Public Workstation(s): aegaeon, neptune.

4. DISCO (Duffell, 2016), see section 3.3.3.

5. HNBody (Rauch & Hamilton, 2002), see chapters 4 - 6.

Bibliography

Agnor, C. B., Canup, R. M., & Levison, H. F. 1999, Icarus, 142, 219

Agnor, C. B. & Hamilton, D. P. 2006, Nature, 441, 192

Alexander, R. D., Clarke, C. J., & Pringle, J. E. 2005, MNRAS, 358, 283, arXiv:astro-ph/0501100

Alibert, Y., Mousis, O., & Benz, W. 2005, A&A, 439, 1205, arXiv:astro-ph/0505367

Anderson, J. D. & Schubert, G. 2007, Geophys. Res. Lett., 34, L02202

Ayliffe, B. A. & Bate, M. R. 2009a, MNRAS, 397, 657, arXiv:0904.4884

—. 2009b, MNRAS, 393, 49, arXiv:0811.1259

—. 2012, MNRAS, 427, 2597, arXiv:1208.5513

Balbus, S. A. & Hawley, J. F. 1991, ApJ, 376, 214

Batygin, K. 2018, AJ, 155, 178, arXiv:1803.07106

Batygin, K., Brown, M. E., & Betts, H. 2012, ApJL, 744, L3, arXiv:1111.3682

Belyaev, M. A., Rafikov, R. R., & Stone, J. M. 2013, ApJ, 770, 67, arXiv:1212.0580

Benz, W., Slattery, W. L., & Cameron, A. G. W. 1989, Meteoritics, 24, 251

Bitsch, B., Crida, A., Morbidelli, A., Kley, W., & Dobbs-Dixon, I. 2013, A&A, 549, A124, arXiv:1211.6345

Bodenheimer, P. & Pollack, J. B. 1986, Icarus, 67, 391

Bottke, W. F., Nesvorný, D., Vokrouhlický, D., & Morbidelli, A. 2010, AJ, 139, 994

Boué, G. & Laskar, J. 2010, ApJL, 712, L44, arXiv:0912.0181

Boué, G., Laskar, J., & Kuchynka, P. 2009, ApJL, 702, L19, arXiv:0909.0332

Brasser, R. & Lee, M. H. 2015, AJ, 150, 157, arXiv:1509.06834

Bryan, M. L., Benneke, B., Knutson, H. A., Batygin, K., & Bowler, B. P. 2018, Nature Astronomy, 2, 138, arXiv:1712.00457

Bryan, M. L., Chiang, E., Bowler, B. P., Morley, C. V., Millholland, S., Blunt, S., Ashok, K. B., Nielsen, E., Ngo, H., Mawet, D., & Knutson, H. A. 2020, AJ, 159, 181, arXiv:2002.11131

Bryden, G., Chen, X., Lin, D. N. C., Nelson, R. P., & Papaloizou, J. C. B. 1999, ApJ, 514, 344

Burns, J. A. & Matthews, M. S. 1986, in Satellites

Canup, R. M. & Asphaug, E. 2001, Nature, 412, 708

Canup, R. M. & Ward, W. R. 2002, AJ, 124, 3404

—. 2006, Nature, 441, 834

Carruba, V., Burns, J. A., Nicholson, P. D., & Gladman, B. J. 2002, Icarus, 158, 434

Chandrasekhar, S. 1943, ApJ, 97, 255

Chen, Y.-Y., Liu, H.-G., Zhao, G., & Zhou, J.-L. 2013, ApJ, 769, 26, arXiv:1303.6736

Ciesla, F. J. & Cuzzi, J. N. 2006, Icarus, 181, 178, arXiv:astro-ph/0511372

Colombo, G. 1966, AJ, 71, 891

Correia, A. C. M. & Laskar, J. 2004, Nature, 429, 848

Crida, A., Morbidelli, A., & Masset, F. 2006, Icarus, 181, 587, arXiv:astro-ph/0511082

Cridland, A. J. 2018, A&A, 619, A165, arXiv:1809.04657

Ćuk, M. & Burns, J. A. 2004, Icarus, 167, 369

Ćuk, M., Hamilton, D. P., Lock, S. J., & Stewart, S. T. 2016, Nature, 539, 402, arXiv:1802.03356

Danby, J. M. A. 1992, Fundamentals of celestial mechanics

de Laplace, P. S. 1796, Exposition du système du monde

Debras, F. & Chabrier, G. 2019, ApJ, 872, 100, arXiv:1901.05697

Deienno, R., Morbidelli, A., Gomes, R. S., & Nesvorný, D. 2017, AJ, 153, 153, arXiv:1702.02094

Denk, T. & Mottola, S. 2019, Icarus, 322, 80

Denk, T., Mottola, S., Tosi, F., Bottke, W. F., & Hamilton, D. P. 2018, The Irregular Satellites of Saturn, 409

Desch, M. D., Connerney, J. E. P., & Kaiser, M. L. 1986, Nature, 322, 42

Desch, S. J. 2007, ApJ, 671, 878

Dohnanyi, J. S. 1969, JGR, 74, 2531

Domingos, R. C., Winter, O. C., & Yokoyama, T. 2006, MNRAS, 373, 1227

Dones, L. & Tremaine, S. 1993a, Icarus, 103, 67

—. 1993b, Science, 259, 350

Doğan, S., Nixon, C. J., King, A. R., & Pringle, J. E. 2018, MNRAS, 476, 1519, arXiv:1801.05426

Duffell, P. C. 2015, ApJL, 807, L11, arXiv:1505.03514

—. 2016, ApJS, 226, 2, arXiv:1605.03577

—. 2020, ApJ, 889, 16, arXiv:1906.11256

Duffell, P. C., Haiman, Z., MacFadyen, A. I., D'Orazio, D. J., & Farris, B. D. 2014, ApJL, 792, L10, arXiv:1405.3711

Duffell, P. C. & MacFadyen, A. I. 2012, ApJ, 755, 7, arXiv:1202.5608

—. 2013, ApJ, 769, 41, arXiv:1302.1934

Fendt, C. 2003, A&A, 411, 623, arXiv:astro-ph/0310021

Franklin, F., Lecar, M., & Soper, P. 1989, Icarus, 79, 223

Frelikh, R. & Murray-Clay, R. A. 2017, AJ, 154, 98, arXiv:1708.00862

Frouard, J., Fouchard, M., & Vienne, A. 2010, A&A, 515, A54

Fujii, Y. I., Okuzumi, S., & Inutsuka, S.-i. 2011, ApJ, 743, 53, arXiv:1106.3528

Fujii, Y. I., Okuzumi, S., Tanigawa, T., & Inutsuka, S.-i. 2014, ApJ, 785, 101, arXiv:1402.6091

Fung, J., Shi, J.-M., & Chiang, E. 2014, ApJ, 782, 88, arXiv:1310.0156

Ginzburg, S. & Sari, R. 2018, MNRAS, 479, 1986, arXiv:1803.01868

Gladman, B. & Duncan, M. 1990, AJ, 100, 1680

Gladman, B., Kavelaars, J. J., Holman, M., Nicholson, P. D., Burns, J. A., Hergen-rother, C. W., Petit, J.-M., Marsden, B. G., Jacobson, R., Gray, W., & Grav, T. 2001, Nature, 412, 163

Gladman, B. J., Nicholson, P. D., Burns, J. A., Kavelaars, J., Marsden, B. G., Williams, G. V., & Offutt, W. B. 1998, Nature, 392, 897

Goldreich, P. 1966, Reviews of Geophysics and Space Physics, 4, 411

Goldreich, P. & Peale, S. J. 1970, AJ, 75, 273

Goldreich, P. & Tremaine, S. 1979, ApJ, 233, 857

—. 1980, ApJ, 241, 425

Gomes, R., Levison, H. F., Tsiganis, K., & Morbidelli, A. 2005, Nature, 435, 466

Gottlieb, S. & Shu, C. W. 1998, Mathematics of Computation, 67, 73

Greenberg, R. 1982, AJ, 87, 184

Gressel, O., Nelson, R. P., Turner, N. J., & Ziegler, U. 2013, ApJ, 779, 59, arXiv:1309.2871

Grinstead, C. & Snell, J. 2006, Grinstead and Snell's Introduction to Probability (Chance Project)

Guillot, T., Stevenson, D. J., Hubbard, W. B., & Saumon, D. 2004, The interior of Jupiter, Vol. 1, 35–57

Gurnett, D. A., Lecacheux, A., Kurth, W. S., Persoon, A. M., Groene, J. B., Lamy, L., Zarka, P., & Carbary, J. F. 2009, Geophys. Res. Lett., 36, L16102

Hahn, J. M. & Malhotra, R. 1999, AJ, 117, 3041, arXiv:astro-ph/9902370

—. 2005, AJ, 130, 2392, arXiv:astro-ph/0507319

Hamilton, D. P. 1994, Icarus, 109, 221

—. 2001, Nature, 412, 132

—. 2003, Nature, 423, 235

Hamilton, D. P. & Burns, J. A. 1994, Science, 264, 550

Hamilton, D. P. & Krivov, A. V. 1997, Icarus, 128, 241

Hamilton, D. P. & Ward, W. R. 2004, AJ, 128, 2510

Hanel, R., Conrath, B., Flasar, F. M., Kunde, V., Maguire, W., Pearl, J., Pirraglia, J., Samuelson, R., Cruikshank, D., Gautier, D., Gierasch, P., Horn, L., & Schulte, P. 1986, Science, 233, 70

Hayashi, C. 1981, Progress of Theoretical Physics Supplement, 70, 35

Helled, R., Anderson, J. D., & Schubert, G. 2010, Icarus, 210, 446, arXiv:1006.3840

Helled, R. & Bodenheimer, P. 2014, ApJ, 789, 69, arXiv:1404.5018

Helled, R. & Fortney, J. J. 2020, arXiv e-prints, arXiv:2007.10783, arXiv:2007.10783

Helled, R., Nettelmann, N., & Guillot, T. 2020, Space Science Reviews, 216, 38, arXiv:1909.04891

Heller, R. & Pudritz, R. 2015, ApJ, 806, 181, arXiv:1410.5802

Heppenheimer, T. A. & Porco, C. 1977, Icarus, 30, 385

Holman, M. J., Kavelaars, J. J., Grav, T., Gladman, B. J., Fraser, W. C., Milisavljevic, D., Nicholson, P. D., Burns, J. A., Carruba, V., Petit, J.-M., Rousselot, P., Mousis, O., Marsden, B. G., & Jacobson, R. A. 2004, Nature, 430, 865

Holman, M. J. & Wisdom, J. 1993, AJ, 105, 1987

Hori, Y. & Ikoma, M. 2011, MNRAS, 416, 1419, arXiv:1106.2626

Hubbard, W. B., Nellis, W. J., Mitchell, A. C., Holmes, N. C., Limaye, S. S., & McCandless, P. C. 1991, Science, 253, 648

Ida, S., Ueta, S., Sasaki, T., & Ishizawa, Y. 2020, arXiv e-prints, arXiv:2003.13582, arXiv:2003.13582

Ingersoll, A. P. & Dobrovolskis, A. R. 1978, Nature, 275, 37

Ishizawa, Y., Sasaki, T., & Hosono, N. 2019, ApJ, 885, 132, arXiv:1909.13065

Izidoro, A., Morbidelli, A., Raymond, S. N., Hersant, F., & Pierens, A. 2015, A&A, 582, A99, arXiv:1506.03029

JeongAhn, Y. & Malhotra, R. 2017, AJ, 153, 235, arXiv:1701.03096

Jewitt, D. & Haghighipour, N. 2007, ARA&A, 45, 261, arXiv:astro-ph/0703059

Ju, W., Stone, J. M., & Zhu, Z. 2016, ApJ, 823, 81, arXiv:1604.00715

—. 2017, ApJ, 841, 29, arXiv:1705.00779

Kanagawa, K. D., Tanaka, H., Muto, T., & Tanigawa, T. 2017, PASJ, 69, 97, arXiv:1609.02706

Kant, I. 1755, Allgemeine Naturgeschichte und Theorie des Himmels

Kavelaars, J. J., Holman, M. J., Grav, T., Milisavljevic, D., Fraser, W., Gladman, B. J., Petit, J. M., Rousselot, P., Mousis, O., & Nicholson, P. D. 2004, Icarus, 169, 474

Kegerreis, J. A., Eke, V. R., Gonnet, P., Korycansky, D. G., Massey, R. J., Schaller, M., & Teodoro, L. F. A. 2019, MNRAS, 487, 5029, arXiv:1901.09934

Kegerreis, J. A., Teodoro, L. F. A., Eke, V. R., Massey, R. J., Catling, D. C., Fryer, C. L., Korycansky, D. G., Warren, M. S., & Zahnle, K. J. 2018, ApJ, 861, 52, arXiv:1803.07083

Keith, S. L. & Wardle, M. 2014, MNRAS, 440, 89, arXiv:1402.1180

Kennedy, G. M. & Wyatt, M. C. 2011, MNRAS, 412, 2137, arXiv:1011.4858

Kessler, D. J. 1981, Icarus, 48, 39

Kley, W. & Nelson, R. P. 2012, ARA&A, 50, 211, arXiv:1203.1184

Korycansky, D. G., Bodenheimer, P., Cassen, P., & Pollack, J. B. 1990, Icarus, 84, 528

Kozai, Y. 1962, AJ, 67, 591

Kurosaki, K. & Inutsuka, S.-i. 2019, AJ, 157, 13, arXiv:1811.05234

Lambrechts, M. & Johansen, A. 2012, A&A, 544, A32, arXiv:1205.3030

Lambrechts, M., Johansen, A., & Morbidelli, A. 2014, A&A, 572, A35, arXiv:1408.6087

Landau, L. D. & Lifshitz, E. M. 1959, Fluid mechanics

Laskar, J., Joutel, F., & Robutel, P. 1993, Nature, 361, 615

Laskar, J. & Robutel, P. 1993, Nature, 361, 608

Lecar, M. & Franklin, F. A. 1973, Icarus, 20, 422

Lee, M. H., Peale, S. J., Pfahl, E., & Ward, W. R. 2007, Icarus, 190, 103

Levison, H. F., Kretke, K. A., & Duncan, M. J. 2015a, Nature, 524, 322, arXiv:1510.02094

Levison, H. F., Kretke, K. A., Walsh, K. J., & Bottke, W. F. 2015b, Proceedings of the National Academy of Science, 112, 14180, arXiv:1510.02095

Levison, H. F., Morbidelli, A., Tsiganis, K., Nesvorný, D., & Gomes, R. 2011, AJ, 142, 152

Li, D. & Christou, A. A. 2020, AJ, 159, 184, arXiv:2004.02512

Li, D., Johansen, A., Mustill, A. J., Davies, M. B., & Christou, A. A. 2020, arXiv e-prints, arXiv:2006.13747, arXiv:2006.13747

Lidov, M. L. 1962, P&SS, 9, 719

Lin, D. N. C. & Papaloizou, J. 1979, MNRAS, 186, 799

—. 1986, ApJ, 307, 395

Lissauer, J. J. 1995, Icarus, 114, 217

Lissauer, J. J., Hubickyj, O., D'Angelo, G., & Bodenheimer, P. 2009, Icarus, 199, 338, arXiv:0810.5186

Lissauer, J. J. & Kary, D. M. 1991, Icarus, 94, 126

Liu, S.-F., Hori, Y., Müller, S., Zheng, X., Helled, R., Lin, D., & Isella, A. 2019, Nature, 572, 355

Lovelace, R. V. E., Covey, K. R., & Lloyd, J. P. 2011, AJ, 141, 51, arXiv:1010.2463

Lozovsky, M., Helled, R., Rosenberg, E. D., & Bodenheimer, P. 2017, ApJ, 836, 227, arXiv:1701.01719

Lubow, S. H. & Martin, R. G. 2012, ApJL, 749, L37, arXiv:1203.6134

Lunine, J. I. 1993, ARA&A, 31, 217

Lunine, J. I. & Stevenson, D. J. 1982, Icarus, 52, 14

Machida, M. N. 2009, MNRAS, 392, 514, arXiv:0810.2584

Machida, M. N., Kokubo, E., Inutsuka, S.-i., & Matsumoto, T. 2008, ApJ, 685, 1220, arXiv:0801.3305

Martin, R. G. & Lubow, S. H. 2011, MNRAS, 413, 1447, arXiv:1012.4102

Martin, R. G., Zhu, Z., & Armitage, P. J. 2020, ApJL, 898, L26, arXiv:2007.05022

Millholland, S. & Batygin, K. 2019, ApJ, 876, 119, arXiv:1904.07338

Millholland, S. & Laughlin, G. 2019, Nature Astronomy, 3, 424, arXiv:1903.01386

Morbidelli, A., Brasser, R., Tsiganis, K., Gomes, R., & Levison, H. F. 2009, A&A, 507, 1041

Morbidelli, A., Levison, H. F., Tsiganis, K., & Gomes, R. 2005, Nature, 435, 462

Morbidelli, A., Szulágyi, J., Crida, A., Lega, E., Bitsch, B., Tanigawa, T., & Kanagawa, K. 2014, Icarus, 232, 266, arXiv:1401.2925

Morbidelli, A., Tsiganis, K., Batygin, K., Crida, A., & Gomes, R. 2012, Icarus, 219, 737, arXiv:1208.4685

Morbidelli, A., Tsiganis, K., Crida, A., Levison, H. F., & Gomes, R. 2007, AJ, 134, 1790, arXiv:0706.1713

Mosqueira, I. & Estrada, P. R. 2003, Icarus, 163, 198

Mousis, O. 2004, A&A, 413, 373

Murray, C. D. & Dermott, S. F. 1999, Solar System Dynamics, 153

Nagasawa, M., Ida, S., & Bessho, T. 2008, ApJ, 678, 498, arXiv:0801.1368

Ness, N. F., Acuna, M. H., Behannon, K. W., Burlaga, L. F., Connerney, J. E. P., Lepping, R. P., & Neubauer, F. M. 1986, Science, 233, 85

Ness, N. F., Acuna, M. H., Burlaga, L. F., Connerney, J. E. P., Lepping, R. P., & Neubauer, F. M. 1989, Science, 246, 1473

Nesvorný, D. 2011, ApJL, 742, L22, arXiv:1109.2949

Nesvorný, D., Alvarellos, J. L. A., Dones, L., & Levison, H. F. 2003, AJ, 126, 398

Nesvorný, D. & Morbidelli, A. 2012, AJ, 144, 117, arXiv:1208.2957

Nesvorný, D., Vokrouhlický, D., & Deienno, R. 2014, ApJ, 784, 22, arXiv:1401.0253

Nesvorný, D., Vokrouhlický, D., & Morbidelli, A. 2007, AJ, 133, 1962

Nicholson, P. D., Cuk, M., Sheppard, S. S., Nesvorny, D., & Johnson, T. V. 2008, Irregular Satellites of the Giant Planets, 411–424

Noll, K. S., Grundy, W. M., Stephens, D. C., Levison, H. F., & Kern, S. D. 2008, Icarus, 194, 758, arXiv:0711.1545

Opik, E. J. 1976, Interplanetary encounters : close-range gravitational interactions

Papaloizou, J. C. B. & Lin, D. N. C. 1995, ApJ, 438, 841

Parisi, M. G. & Brunini, A. 1997, P&SS, 45, 181

Parisi, M. G. & Brunini, A. 2002, BAAS, 34, 892

Peale, S. J. 1969, AJ, 74, 483

Pearl, J. C. & Conrath, B. J. 1991, JGR, 96, 18921

Pearl, J. C., Conrath, B. J., Hanel, R. A., Pirraglia, J. A., & Coustenis, A. 1990, Icarus, 84, 12

Perets, H. B. & Payne, M. J. 2014, arXiv e-prints, arXiv:1407.2619, arXiv:1407.2619

Petit, J. M., Kavelaars, J. J., Gladman, B. J., Jones, R. L., Parker, J. W., Van Laerhoven, C., Nicholson, P., Mars, G., Rousselot, P., Mousis, O., Marsden, B., Bieryla, A., Taylor, M., Ashby, M. L. N., Benavidez, P., Campo Bagatin, A., & Bernabeu, G. 2011, AJ, 142, 131, arXiv:1108.4836

Philpott, C. M., Hamilton, D. P., & Agnor, C. B. 2010, Icarus, 208, 824, arXiv:0911.1369

Pickering, E. C. 1899, AJ, 20, 13

Podolak, M. & Helled, R. 2012, ApJL, 759, L32, arXiv:1208.5551

Podolak, M., Podolak, J. I., & Marley, M. S. 2000, P&SS, 48, 143

Podolak, M., Weizman, A., & Marley, M. 1995, P&SS, 43, 1517

Pollack, J. B., Burns, J. A., & Tauber, M. E. 1979, Icarus, 37, 587

Pollack, J. B., Hubickyj, O., Bodenheimer, P., Lissauer, J. J., Podolak, M., & Greenzweig, Y. 1996, Icarus, 124, 62

Pollack, J. B., Lunine, J. I., & Tittemore, W. C. 1991, Origin of the Uranian satellites, 469

Press, W. H., Teukolsky, S. A., Vetterling, W. T., & Flannery, B. P. 1992, Numerical recipes in C. The art of scientific computing

Quillen, A. C., Chen, Y.-Y., Noyelles, B., & Loane, S. 2018, Celestial Mechanics and Dynamical Astronomy, 130, 11, arXiv:1707.03180

Quillen, A. C. & Trilling, D. E. 1998, ApJ, 508, 707, arXiv:astro-ph/9712033

Ragozzine, D. & Wolf, A. S. 2009, ApJ, 698, 1778, arXiv:0807.2856

Rauch, K. P. & Hamilton, D. P. 2002, BAAS, 34, 938

Reinhardt, C., Chau, A., Stadel, J., & Helled, R. 2020, MNRAS, 492, 5336, arXiv:1907.09809

Rogoszinski, Z. & Hamilton, D. P. 2016, in AAS/Division for Planetary Sciences Meeting Abstracts, Vol. 48, 318.09

Rogoszinski, Z. & Hamilton, D. P. 2020a, ApJ, 888, 60, arXiv:1908.10969

—. 2020b, arXiv e-prints, arXiv:2004.14913, arXiv:2004.14913

Rufu, R. & Canup, R. M. 2017, AJ, 154, 208, arXiv:1711.01581

Ryan, G. & MacFadyen, A. 2017, ApJ, 835, 199, arXiv:1611.00341

Saha, P. & Tremaine, S. 1993, Icarus, 106, 549

Saillenfest, M., Lari, G., & Courtot, A. 2020, A&A, 640, A11

Saillenfest, M., Laskar, J., & Boué, G. 2019, A&A, 623, A4, arXiv:1901.02831

Shakura, N. I. & Sunyaev, R. A. 1973, A&A, 500, 33

Sheppard, S. S., Jewitt, D., & Kleyna, J. 2005, AJ, 129, 518, arXiv:astro-ph/0410059

Sheppard, S. S. & Jewitt, D. C. 2003, Nature, 423, 261

Sheppard, S. S., Lacerda, P., & Ortiz, J. L. 2008, Photometric Lightcurves of Transneptunian Objects and Centaurs: Rotations, Shapes, and Densities, 129

Sheppard, S. S., Williams, G. V., Tholen, D. J., Trujillo, C. A., Brozovic, M., Thirouin, A., Devogele, M., Fohring, D., Jacobson, R., & Moskovitz, N. A. 2018, Research Notes of the American Astronomical Society, 2, 155, arXiv:1809.00700

Slattery, W. L., Benz, W., & Cameron, A. G. W. 1992, Icarus, 99, 167

Snellen, I. A. G., Brandl, B. R., de Kok, R. J., Brogi, M., Birkby, J., & Schwarz, H. 2014, Nature, 509, 63

Spalding, C., Batygin, K., & Adams, F. C. 2016, ApJ, 817, 18, arXiv:1511.09472

Sromovsky, L. A. & Fry, P. M. 2005, Icarus, 179, 459

Stephens, D. C. & Noll, K. S. 2006, AJ, 131, 1142, arXiv:astro-ph/0510130

Szulágyi, J., Cilibrasi, M., & Mayer, L. 2018, ApJL, 868, L13, arXiv:1811.06574

Szulágyi, J., Masset, F., Lega, E., Crida, A., Morbidelli, A., & Guillot, T. 2016, MNRAS, 460, 2853, arXiv:1605.04586

Szulágyi, J., Morbidelli, A., Crida, A., & Masset, F. 2014, ApJ, 782, 65, arXiv:1312.6302

Tanigawa, T., Ohtsuki, K., & Machida, M. N. 2012, ApJ, 747, 47, arXiv:1112.3706

Thirouin, A., Noll, K. S., Ortiz, J. L., & Morales, N. 2014, A&A, 569, A3, arXiv:1407.1214

Thommes, E. W., Duncan, M. J., & Levison, H. F. 1999, Nature, 402, 635

—. 2002, AJ, 123, 2862, arXiv:astro-ph/0111290

—. 2003, Icarus, 161, 431, arXiv:astro-ph/0303269

Thommes, E. W. & Lissauer, J. J. 2003, ApJ, 597, 566, arXiv:astro-ph/0308112

Toro, E. F., Spruce, M., & Speares, W. 1994, Shock Waves, 4, 25

Touma, J. & Wisdom, J. 1993, Science, 259, 1294

—. 1998, AJ, 115, 1653

Tremaine, S. 1991, Icarus, 89, 85

Tremaine, S. & Davis, S. W. 2014, MNRAS, 441, 1408, arXiv:1308.1964

Tsiganis, K., Gomes, R., Morbidelli, A., & Levison, H. F. 2005, Nature, 435, 459

Turner, N. J., Lee, M. H., & Sano, T. 2014, ApJ, 783, 14, arXiv:1306.2276

Varnière, P., Quillen, A. C., & Frank, A. 2004, ApJ, 612, 1152, arXiv:astro-ph/0306422

Vieira Neto, E., Winter, O. C., & Yokoyama, T. 2004, A&A, 414, 727

—. 2006, A&A, 452, 1091

Visser, R. G., Ormel, C. W., Dominik, C., & Ida, S. 2020, Icarus, 335, 113380, arXiv:1907.04368

Vokrouhlický, D. & Nesvorný, D. 2015, ApJ, 806, 143, arXiv:1505.02938

Vokrouhlický, D., Nesvorný, D., & Levison, H. F. 2008, AJ, 136, 1463

Wahl, S. M., Hubbard, W. B., Militzer, B., Guillot, T., Miguel, Y., Movshovitz, N., Kaspi, Y., Helled, R., Reese, D., Galanti, E., Levin, S., Connerney, J. E., & Bolton, S. J. 2017, Geophys. Res. Lett., 44, 4649, arXiv:1707.01997

Ward, W. R. 1973, Science, 181, 260

—. 1974, JGR, 79, 3375

—. 1975, AJ, 80, 64

Ward, W. R., Burns, J. A., & Toon, O. B. 1979, JGR, 84, 243

Ward, W. R. & Canup, R. M. 2006, ApJL, 640, L91

—. 2010, AJ, 140, 1168

Ward, W. R. & Hahn, J. M. 1998a, AJ, 116, 489

—. 1998b, Science, 280, 2104

Ward, W. R. & Hamilton, D. P. 2004, AJ, 128, 2501

Ward, W. R. & Rudy, D. J. 1991, Icarus, 94, 160

Warwick, J. W., Evans, D. R., Peltzer, G. R., Peltzer, R. G., Romig, J. H., Sawyer, C. B., Riddle, A. C., Schweitzer, A. E., Desch, M. D., Kaiser, M. L., Farrell, W. M., Carr, T. D., de Pater, I., Staelin, D. H., Gulkis, S., Poynter, R. L., Boischot, A., Genova, F., Leblanc, Y., Lecacheux, A., Pedersen, B. M., & Zarka, P. 1989, Science, 246, 1498

Warwick, J. W., Evans, D. R., Romig, J. H., Sawyer, C. B., Desch, M. D., Kaiser, M. L., Alexander, J. K., Carr, T. D., Staelin, D. H., Gulkis, S., Poynter, R. L., Aubier, M., Boischot, A., Leblanc, Y., Lecacheux, A., Pedersen, B. M., & Zarka, P. 1986, Science, 233, 102

Wilson, H. F. & Militzer, B. 2012, ApJ, 745, 54

Yoder, C. F. & Kaula, W. M. 1976, in BAAS, Vol. 8, 434

Yokoyama, T., Neto, E., Winter, O., Sanchez, D., & Brasil, P. 2008, Mathematical Problems in Engineering, 2008

Zhu, Z., Ju, W., & Stone, J. M. 2016, ApJ, 832, 193, arXiv:1609.09250